THERMOMECHANICAL PROCESSING OF PLAIN LOW CARBON AND MICROALLOYED STEELS

Ph.D. THESIS

by

SUNIL KUMAR RAJPUT

DEPARTMENT OF METALLURGICAL AND MATERIALS ENGINEERING
INDIAN INSTITUTE OF TECHNOLOGY ROORKEE
ROORKEE- 247 667 (INDIA)
DECEMBER, 2014

THERMOMECHANICAL PROCESSING OF PLAIN LOW CARBON AND MICROALLOYED STEELS

A THESIS

Submitted in partial fulfilment of the requirements for the award of the degree of

DOCTOR OF PHILOSOPHY

in

METALLURGICAL AND MATERIALS ENGINEERING

by

SUNIL KUMAR RAJPUT

DEPARTMENT OF METALLURGICAL AND MATERIALS ENGINEERING
INDIAN INSTITUTE OF TECHNOLOGY ROORKEE
ROORKEE- 247 667 (INDIA)
DECEMBER, 2014

INDIAN INSTITUTE OF TECHNOLOGY ROORKEE
ROORKEE

CANDIDATE'S DECLARATION

I hereby certify that the work which is being presented in the thesis entitled **"THERMOMECHANICAL PROCESSING OF PLAIN LOW CARBON AND MICROALLOYED STEELS"** in partial fulfilment of the requirement for the award of the Degree of Doctor of Philosophy and submitted in the **Department of Metallurgical and Materials Engineering** of the Indian Institute of Technology Roorkee is an authentic record of my own work carried out during a period from July, 2011 to December, 2014 under the supervision of **Dr. G.P. Chaudhari, Associate Professor,** and **Dr. S. K. Nath, Professor,** Department of Metallurgical and Materials Engineering, Indian Institute of Technology Roorkee, Roorkee.

The matter presented in this thesis has not been submitted by me for the award of any other degree of this or any other Institute.

(SUNIL KUMAR RAJPUT)

This is to certify that the above statement made by the candidate is correct to the best of our knowledge.

(G.P.CHAUDHARI)
Supervisor

(S.K. NATH)
Supervisor

Date:

Thermomechanical processing of plain low carbon and microalloyed steels

ABSTRACT

The usage and importance of structural applications of steels continue to lead in critical areas even when the availability of ceramics, polymeric and composite materials with the improved properties exists for many decades, now. There is ever increasing demand of high performance steels in many critical strategic applications such as in military applications, ship building, nuclear power, aerospace, automobiles etc. The manufacturers are always trying to reduce the cost of raw materials and production without the cost of quality. Thus, to produce quality products at low cost any scientific approach should be explored and employed to optimize the processing parameters. Further, the mechanical properties can be enhanced by the alloy design and heat treatment. Thermomechanical processing (TMP) is a technique that can control the hot deformation process parameters, which result in improved mechanical properties of the materials. Thermomechanical processing is commonly related to the hot working operations. Hot working involves controlling various processing parameters such as reheating temperatures, deformation temperature, applied strain, strain rate, and the post deformation-cooling rate, which decides the final mechanical properties of the products.

The review of literature shows that there is a need to perform more hot deformation studies in the widest range of processing parameters (deformation temperature, strain rate), and also to compare the different dynamic materials models (DMM). A new instability parameter κ_j can also be employed in the processing maps and compared with the other parameters, for the study of plain low carbon and microalloyed steels. There are some reports regarding the use of flow localization parameter, α in non-ferrous alloys but its use for plain low carbon and microalloyed steels is rarely reported. In addition, significance of Zener-Hollomon parameter, Z is not evaluated along with that of the processing maps and flow curves. Low carbon steels are important common structural steel in which high strength and good ductility is desired. Using DIFT technique in safe workable region, low carbon steels are expected to produce defect free grain refinement. This will obviate the need for expensive alloying, and improve the quality of the product at low cost.

In the present study, hot deformation behavior of three steels has been studied using thermomechanical simulator Gleeble® 3800. These are AISI 1010, AISI 1016 and low carbon Ti-Nb microalloyed steels. The microstructural evolution after hot deformation at different

deformation temperatures and strain rates is studied. Processing maps using different models, flow localization parameter, Zener-Hollomon parameter, and constitutive equations are studied and correlated. In addition, the different processing maps are compared and the safe workability region is defined. The effect of carbon content in the plain carbon steel and effect of micro alloying elements are also studied on the various processing maps, microstructural evolution and apparent activation energy of hot deformation. The grain refinement of plain low carbon (AISI 1010) and low C Ti-Nb microalloyed steel using DIFT is investigated in the safe workable region. The investigations of fine-grained metals have been mainly concerned with structural characterization, micro hardness and tensile behaviour.

This thesis consists of the eight different chapters. The first chapter consists of introduction to the topic and gives a brief idea about the hot deformation behavior, grain refinement using DIFT technique, overview of the work included in the thesis and the importance of this work.

The literature review is given in chapter two along with the history of the hot deformation, and the hot deformation behaviour of plain carbon and microalloyed steel. Various processing maps with different power dissipation efficiency and instability criterion have also been explained in the review. Significance of the present study is explained based on the research gaps found in the literature about the hot deformation processing parameters of plain low carbon steel as well as microalloyed steel. Moreover, grain refinement using the different hot deformation routes is studied.

The details of all the experimentation performed right from the determination of phase transformation temperatures up to the development of the fine-grained steel and their characterization is given in chapter three. Microstructural analysis was performed in the mid-section of the deformed specimens using optical microscopy, SEM, and EBSD. Macro and micro hardness tests were performed to determine the hardness of specimens.

Chapter four consists of theory and analysis in which the various processing maps are discussed using different criteria. Processing maps are shown in the processing space i.e. on the axes of temperature and strain rate for a given strain. Prasad et al. developed processing maps using the DMM, in which no storage of energy in the material is assumed. The modified DMM developed by Murty and Rao are also described. A new instability criterion κ_j developed by Poletti et al. is explained along with the instability criterion of Prasad et al. and Murty and Rao. The flow localization parameter and constitutive equations are explained in this chapter.

Chapter five consists of results and discussion of hot deformation behaviour and processing map of plain low carbon and Ti-Nb microalloyed steels. In all three steels the hot deformation behavior were studied using dynamic materials model (DMM) and modified DMM using different instability parameters given by Prasad el al. and Murty and Rao. A new instability criterion κ_j developed by Poletti et al. was also studied. Also the effect of increase in carbon content, and micro alloying on hot deformation behaviour were studied. This study show that as the amount of carbon content increased the values of strain rate sensitivity, m, and power dissipation efficiency, η increased and also the workability region increased. The instability parameter, κ_j predict the more accurate deformation behaviour. The value of strain rate sensitivity parameter, m, power dissipation efficiency, η_{Prasad} and $\eta_{Murty\ \&\ Rao}$ is reduced with the addition of Ti-Nb microalloying and the region of the high value of m is shifted towards the higher temperature zone. The safe and unsafe regions of workability using the processing maps were determined and verified with the microstructural study. The apparent activation energy is increased with increase in carbon contents and also increased with Ti-Nb micro alloying. This is because that in Ti-Nb microalloyed steel Nb can be present either in dissolved form where it exhibits a strong solute drag effect, or as NbC precipitates which effectively pin the grain boundaries. Drag exerted on the migrating grain boundaries by Zener pinning effect of the NbC/TiC precipitates or by the presence of dissolved Nb solute can retard the progress of recrystallization.

The Chapter six consists of results and discussion of grain refinement by thermomechanical processing of plain low C AISI 1010 and Ti-Nb microalloyed steels. In this chapter, the hot deformation was performed in order to make use of the deformation induced ferrite transformation (DIFT) technique. The effect of different processing parameters such as strain, prior austenite grain size, deformation temperatures etc. on DIFT are analyzed. In addition, the processing conditions are optimized in the safe working zone to obtain the ultra-fine ferritic (UFF) microstructure. In this study, the strain rate is kept constant and is 1 s^{-1} as reflected in the results of hot deformation (finer ferritic grains). The effects of deformation temperatures and the amount of applied strain are discussed in this chapter. Hot deformation was performed in the two steps at different temperatures with different amount of strain, and the average grain size of 3.2μm for AISI 1010 steel and 1.1μm for Ti-Nb microalloyed steel were obtained. The mechanical properties are determined using the Tabor's relation. Chapters seven and eight deal with conclusions and suggestions for future work, respectively.

ACKNOWLEDGEMENTS

First of all, I would like to express my sincere gratitude, deepest respect and heartiest thanks to my supervisors, Dr. G.P. Chaudhari, Associate Professor and Dr. S.K. Nath, Professor and Head, Department of Metallurgical and Materials Engineering (MMED), Indian Institute of Technology, Roorkee for their valuable and intellectual guidance, unwavering support and encouragement throughout the tenure of my research work. This thesis could not have attained its present form, both in content and presentation, without their active interest, timely help, painstaking efforts, direction and valuable guidance. The words prove to be insufficient to express my deep feelings and heartfelt thanks to my supervisors for their high benevolence and un-hesitated guidance throughout my doctoral work.

I express my sincere gratitude to Dr. Ujjwal Prakash, Associate Professor, MMED, IIT Roorkee (Chairman SRC) for his utmost co-operation, help and support throughout the course of my research work. I am highly obliged to the members of my SRC committee, Dr. V. Pancholi, (Internal member), Associate Professor, MMED and Dr. D.B. Karunakar (External member), Assistant Professor, MIED, IIT, Roorkee for their invaluable suggestions and encouragements to pursue this work. I extend my deep sense of gratitude to all the faculty members of MMED who have directly or indirectly facilitated for the smooth progress of my research work.

I would like to express my sincere thanks to Mr. Rajendra Sharma and Mr. R. K. Sharma, technical staff, MMED for their extended help and support during my doctoral work. I am also thankful to all the technical and administrative staff of the MMED, especially to Mr. S.M.Giri, Mr. Shakti Gupta, Mr. Naresh Kumar, Mr Sanjay and Mr. S. Sharma, who have rendered their help in all possible ways during the Ph.D. work.

I would like to thank all India council of technical education (AICTE), New Delhi for providing me the opportunity of doing Ph.D. through quality improvement program (QIP). I gratefully acknowledge QIP Centre, IIT Roorkee for providing me the complete support during entire work of PhD. I express my deep sense of admiration to the Co-ordinator and co-cordinator, QIP Centre, for his co-operation. I express my sincere thanks to all the QIP staff members especially to Mr. Anil Kumar, and Mr. Rajeev.

I am highly obliged and express my sincere thanks to Director Bundelkhand Institute of Engineering and Technology, Jhansi, U.P. for giving me an opportunity of doing Ph.D. through QIP program. I owe my sincere gratitude to Dr. N.P. Yadav Head Mechanical Engineering department, BIET, Dr. V.K Bhatt, Dr. S.K. Agarwal, Dr. T. Soota, Dr. A.K. Padap, and Mr. Vijay Verma in mechanical engineering department, BIET Jhansi. My sincere thanks to all my colleagues especially to Dr. S.K. Gupta, Dr. Yashpal Singh, Dr. S.S. Rajput in BIET Jhansi.

I wish to thank my friends and student colleagues, Mr. Yashwant Mehta, Mr. Sanjeev Kumar, Mr. Neeraj Srivastava, Mr. BrijKishor, Dr. Amerendra Hassan, Mr. Guru Prakash, Mr.

Sobhit Saxena, Mr. Sanjay Rathor, Mr. Swapn K Srivastava, Mr. Sandan Sharma, Mr. Sankalp Goel, Mr. P. Nageswar Rao, Mr. Neeraj Agarwal, Mr. Kapil Kochhar, Mr. Lalit Meena, Mr. Kuldeep Saxena, Dr. Dharmendra Kumar, Mr. P. Sudhakar Rao and all the fellows who helped me directly or indirectly during the entire period of this work.

Where would I be without my family? My family deserves special attention for their unflagging love and support throughout my life and this work would not have been possible without their support, never-ending patience and constant encouragement. I express my profound regards to my parents for their blessings and for being the main source of inspiration to succeed in my endeavors. I am indebted to my father, Mr. Vijay Bahadur Singh, for his timely valuable advices, care and love throughout the life. I express heartiest gratitude to my mother Mrs. Devki Devi, and no words could describe her everlasting love being shown to me. I would like to express my reverence and great admiration to my wife, Mrs. Kalpana Rajput for her sacrifice, help and providing me constant encouragement. I feel proud to have a wife like her for being with me always and listening to me whenever I needed the most. I would like to thank my loving daughters Anshika and Divyanshi, for beginning my each day with a great smile. I would like to dedicate this thesis to my parents and my wife for being so special and daughters Anshika and Divyanshi you made this worthwhile. I am highly appreciative of my brother Mr. Rajendra Kumar Rajput and his family for their love and encouragement throughout.

I would like to thank everyone who was important to the successful realization of thesis, as well as expressing my apology that I could not mention everyone personally.

Above all, I express my gratitude from the core of my heart to God for giving courage, strength and patience to carry out my research work.

(Sunil Kumar Rajput)

Contents

LIST OF FIGURES

LIST OF TABLES

SYMBOLS

1.	Ar_3	Temperature at which, during cooling, transformation of the austenite into ferrite starts
2.	Ar_1	Temperature at which, during cooling, transformation of the austenite into ferrite + cementite ends
3.	Ae_3	Equilibrium transformation temperatures, above which austenite is stable
4.	A_s	Serration amplitude of austenite
5.	σ	Flow stress
6.	ε	True strain
7.	ε_c	Critical strain
8.	$\varepsilon_{c,\,DIFT}$	Critical strain for deformation induced ferrite transformation
9.	$\varepsilon_{c,\,UFF}$	Critical strain for ultra-fine ferrite
10.	ε_{VM}	von Mises equivalent strain
11.	$\dot{\varepsilon}$	Strain rate
12.	Ψ	Outer angle (ECAP channel)
13.	Φ	Inner Angle (ECAP channel)
14.	α	Flow localization parameter
15.	θ	Angle of incident electron on the diffracting plane
16.	λ	Wavelength of electron
17.	γ'	Dimensionless softening coefficient at constant strain rate
18.	P	Power dissipated
19.	G	Power dissipated by plastic work
20.	J	Power dissipated by microstructural changes
21.	η	Power dissipation efficiency
22.	D	Power dissipation function
23.	ξ	Instability parameter proposed by Prasad et al.
24.	κ	Instability parameter proposed by Murty and Rao
25.	κ_j	Instability parameter proposed by Poletti et al.
26.	Z	Zener-Hollomon parameter
27.	T_γ	Austenitization temperature
28.	d_γ	Prior austenite grain size

29. m Strain rate sensitivity
30. T_{nr} Non-recrystallization temperature
31. T_m Melting point temperature
32. ΔT Degree of under-cooling
33. c Material constant
34. n Stress exponent
35. dT Maximum increment of temperature
36. T_{def1} First step deformation temperature
37. T_{def2} Second step deformation temperature
38. R Universal gas constant
39. Q Activation energy

ABBREVIATIONS

ARB	Accumulative roll bonding
CCC	Continuous cooling compression
CCT	Continuous cooling transformation
CDRX	Continuous dynamic recrystallization
CG	Coarse grained
DFT	Dynamic ferrite transformation
DIF	Deformation induced ferrite
DIFT	Deformation induced ferrite transformation
DMM	Dynamic materials model
DRV	Dynamic recovery
DRX	Dynamic recrystallization
EBSD	Electron back scattered diffraction
ECAP	Equal channel angular pressing
FEM	Finite element method
FG	Fine grain
Fig.	Figure
HAGB	High angle grain boundary
HSLA	High strength low alloy
LAGB	Low angle grain boundary
LOM	Light optical microscope
LVDT	Linear voltage differential transducer
MAE	Micro alloying element
MDRX	Metadynamic recrystallization
PTT	Precipitation time temperature
SAIL	Steel Authority of India
SEM	Scanning electron microscope
SFE	Stacking fault energy
SIDT	Strain induced dynamic transformation
SIF	Strain induced ferrite
SIFT	Strain induced ferrite transformation
SIT	Strain induced transformation

SoS	State of stress
SRX	Static recrystallization
TMP	Thermomechanical processing
UFF	Ultra-fine ferrite
UFG	Ultra-fine grain

Chapter 1

INTRODUCTION

The usage and importance of structural applications of steels continue to lead in critical areas even when the availability of ceramics, polymeric and composite materials with the improved properties exists for many decades, now. There is ever increasing demand of high performance steels in many critical strategic applications. These steels are being imported at high cost. Military applications, ship building, nuclear power, aerospace, automobiles etc. are the examples, where huge tonnage of special steels is used. The manufacturers are always trying to reduce the cost of raw materials and production. Price reduction is becoming so dominant at the cost of quality. Industries require using more effective design practices and accepting the upgraded design processes. This enabled industries to deliver the customized products and services at relatively lower cost. Historically, expensive trial and error techniques are used to optimize the metal forming processes. The behavior of the materials is often ignored whereas the capability of machine and the geometry of the piece are the main considerations. The trial and error method is unsuitable for newer materials and small batch production. Thus, to produce quality products at low cost any scientific approach should be explored and employed to optimize the processing parameters. Further the obtained mechanical properties are enhanced by the alloy design and heat treatment. Thermomechanical processing (TMP) is a technique that can control the hot deformation process parameters, which result in improved mechanical properties of the materials. The first introduction of TMP for commercial production in 1950s, was through controlled rolling of C-Mn steel plates of 40 kgf/mm^2 grade for ship building [1]. This is an important research contribution in the area of manufacturing engineering.

Thermomechanical processing is commonly related to the hot working operations. Hot working of plain low carbon and micro alloyed steels involves controlling various processing parameters such as reheating temperatures, deformation temperature, applied strain, strain rate, and the post deformation cooling rate which decides the final mechanical properties of the products. Plain low carbon and low carbon microalloyed steels are hot worked in the austenite phase (>0.6 T_m, T_m is the melting point in K) with the fine microalloyed precipitates in the latter. At low finishing temperatures low carbon microalloyed steel exhibits grain refinement

due to the presence of microalloyed carbonitride precipitation, which retards the restoration mechanism and makes it considerably stronger than the plain carbon steel [2-5]. Generally, the thermomechanical processing is focused on the metallurgical aspects to obtain the desirable microstructure which results in desired mechanical properties.

Venugopal [6] proposed an optimization procedure based on various technical parameters for the selection of safe temperature zone for processing as shown in figure 1.1. This procedure involves establishing the relationship between the properties of tool and billet materials with various processing parameters, and optimization of the process variables using the above correlation. Khun et al. [7] proposed the empirical criteria and fracture models to optimize the workability particularly in cold working. Using this approach for bulk forming processes to establish experimental fracture criteria, compression tests were performed. Cylindrical surface specimens were used for compression tests with small grid marked at the mid span. At various stages of the test, the grid displacement was measured, which is used in the calculations of principal stress and strain histories. This type of tests should be performed with the help of compression tests, by compressing a number of identical specimens in sequence with progressively larger reductions till fracture. The limit for safe working is given by the locus of principal surface stains at fracture as shown in figure 1.2 (cold deformation of AISI 1045 steel). At fracture, the straight line relationship between tensile and compressive strains is a characteristic result of ductile fracture process. This line is treated as fracture criterion which represents the workability of the material. These methods are better than the trial and error techniques, but are tedious and expensive.

The knowledge of the constitutive behavior of the material under different processing conditions is required for the optimization of workability. During deformation process, Ashby et al. [8] and Raj [9] attempted to understand the effects of temperature, strain, strain rate and microstructure on the flow behavior of metals. To describe the fracture and deformation modes during process they developed the deformation maps. Ashby plotted maps as a function of normalized shear stress and absolute temperature as shown in figure 1.3. The maps are divided into different regimes in which a particular mechanism is dominated. Two mechanisms contribute equally at the regime boundaries for the overall strain rate.

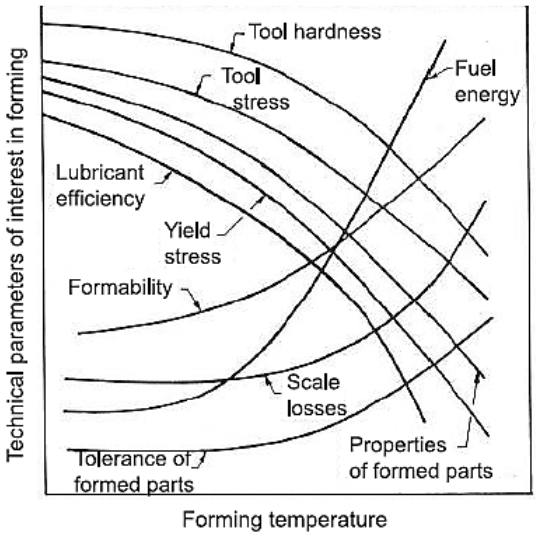

Fig. 1.1. Schematic consolidated concepts involved in selecting optimum temperature in metal forming [6].

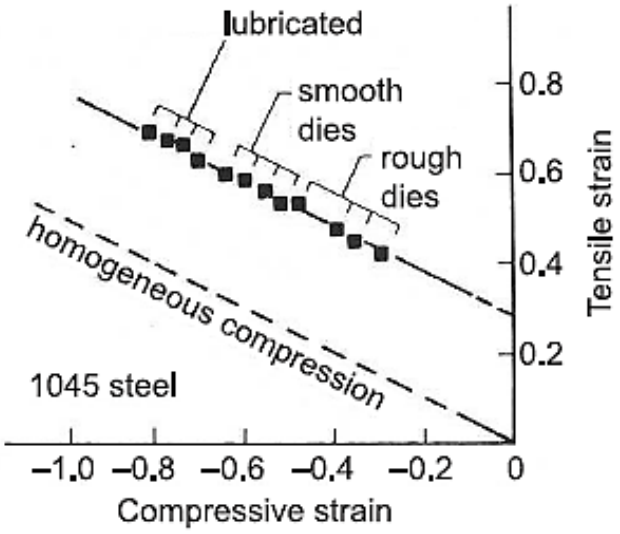

Fig. 1.2. Map of cold workability optimization using locus of surface strains at fracture [7].

Constant strain rate contours are superimposed on the fields of shear stress and temperature. There are other maps with different axes such as: (i) normalized shear stress and shear strain rate with contours of temperature, (ii) axes of temperature (or reciprocal temperature) and strain rate with contours of constant stress. These maps can ideally be plotted for any polycrystalline material and show the area of supremacy of each flow mechanism. Ashby et al. constructed similar maps, which give domains of various fracture processes.

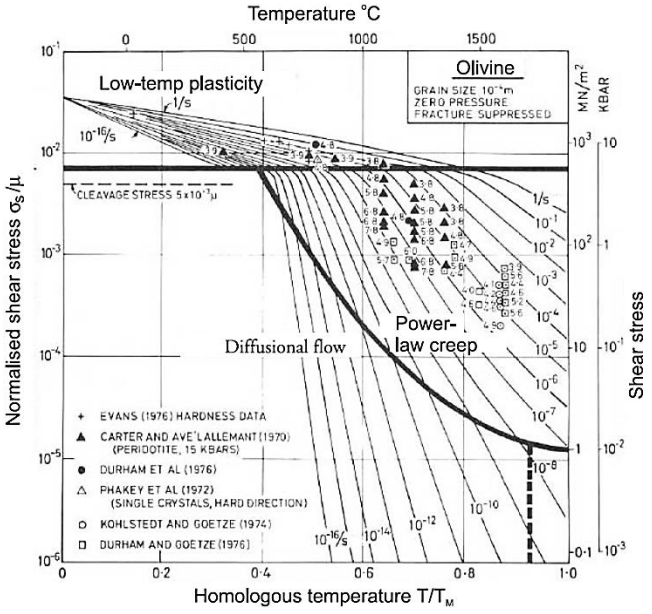

Fig. 1.3. Typical Ashby's map [8].

Considering the failure mechanisms, Raj developed the maps for a material that can operate over ranges of temperature and strain rate. These maps are useful to define the region of "safe" to process the workpiece and avoid defect nucleation. Raj map for austenitic stainless steel (AISI 316) is shown in figure 1.4.

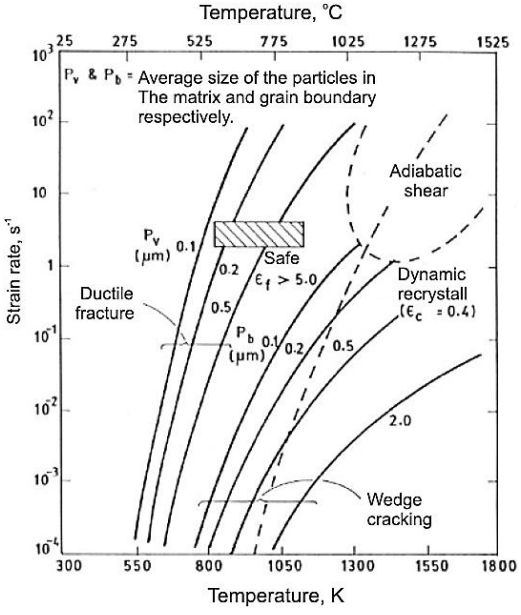

Fig.1.4. Typical Raj map for austenitic stainless steel (AISI 316).

Ashby and Raj maps use shear strain rate equations and are deterministic. These equations are valid for steady states. The number of basic atomic processes such as grain boundary sliding, dislocation motion, twinning, diffusion and phase transformation influence the equations. These maps cannot be applied for complex commercial alloys and are limited to simple systems, because it is not always possible to recognize the atomistic mechanisms of commercial alloys clearly. The maps are difficult to integrate with continuum approaches because these are based on the atomistic theory. Also, with atomistic approaches, process optimization is difficult. However these developments have directed to the knowledge of hot deformation mechanisms. For the design of deformation processes, it is difficult to use them directly. Thus, Prasad et al. [10] developed the continuum approach. This shows the potential for direct industrial application at optimum processing parameters using dynamic materials model (DMM) processing maps [11]. The workpiece is considered as power dissipator. The dissipated power is converted into two forms i.e. thermal and microstructural as described by the constitutive equations, and these are not recoverable by the system. Thus, in order to achieve the desired combination of microstructure and mechanical properties, it is essential to develop the hot working procedures on plain low carbon steels and low carbon microalloyed steel in the perspective of the recent developments in dynamic materials modeling.

Hot workability is concerned with the extent to which a material deforms plastically during shaping at high temperatures without the occurrence of fracture or flow localization. The modeling of process parameters such as strain, strain rate and temperature is required to describe the flow behavior of the material. Thus, the stress values are used to create deformation maps as a function of the process parameters, delineating the “safe” from the “unsafe” hot working conditions. To optimize the hot workability and evaluate the hot working mechanisms different approaches have been used, including evaluation of kinetic parameters, examinations of stress-strain curves and developing the processing maps using different approaches. The processing map is the superimposition of two maps i.e. power dissipation efficiency and instability map in the axes of temperature and strain rate. The power dissipation maps are formed using the approach of Prasad et al. using DMM [10], Murty and Rao using modified DMM [12]. Further, the instability maps are drawn using Prasad et al., Murty and Rao, and Poletti et al. approaches [13].

In order to obtain the desired phases in the microstructure, prior knowledge of transformation temperatures is necessary. Transformation temperatures can be determined using dilatometry or continuous cooling compression (CCC) tests. After determining the phase transformation temperatures, the effect of cooling rate on the microstructure can be ascertained using continuous cooling transformation (CCT) diagram. This represents the austenite decomposition in a particular steel during cooling.

By utilizing the safe workable window, the strength of the material processed increases with reduction in its grain size according to the well known Hall-Petch relation. High strength to weight ratio in the steel parts used in vehicles can be achieved by gauge reduction. The yield strength of the steel can be improved to the large extent by the ferrite grain refinement. The ferrite grain size of approximately 1 μm is called ultrafine ferrite (UFF). Generally, the dynamic recrystallization (DRX) of ferrite, deformation and annealing of martensite, deformation induced ferrite transformation (DIFT) and asymmetric rolling are found to be the more suitable processing routes among different studied processing routes for steel production [14-15].

Although there are many studies on hot deformation of plain low carbon and low carbon Ti-Nb microalloyed steels in literature, the systematic treatment of hot deformation, especially at high strain rates, is lacking. Thus, present work involves the investigation of hot deformation characteristics of plain low carbon and low carbon Ti-Nb microalloyed steels in a comprehensive manner in order to identify the processing windows inherent to the material. Such a study can also help in the design of microstructures for obtaining fine grained dual phase steels [16] in further thermomechanical treatment steps. In this work, hot compression experiments are performed using Gleeble® 3800 thermomechanical simulator at different temperatures ranging from 750°C-1050°C and strain rates from 0.01 to 80 s^{-1} in the case of AISI 1016 and low carbon Ti-Nb microalloyed steel, and 0.01 to 20 s^{-1} for AISI 1010 steel upto total true strain of 0.7. Efficiency of power dissipation, strain rate sensitivity and instability parameters are obtained using different approaches. The apparent activation energy and the stress exponent are determined and correlated to high temperature phenomena. Also, the relation between the Zener-Hollomon parameter with the processing maps is determined. The optimized processing parameters for grain refinement using the DIFT technique are determined.

Chapter 2

REVIEW OF LITERATURE

In this chapter, the first section gives the overview of hot working of plain low carbon and microalloyed steels. The second section reviews the hot deformation mechanisms under which the deformation, softening, and hardening phenomena occur are studied. The third section reviews workability in bulk forming processes. The fourth section reviews the materials modelling in the hot deformation. Under this section various models such as kinetic model, atomistic model, dynamic materials model (DMM), and other models (activation energy map, polar reciprocity map) are reviewed. Finally, a comprehensive literature review on the methodology for grain refinement of steels using the deformation induced ferrite transformation (DIFT) technique is presented.

2.1. HOT WORKING

Metal forming is the process to give shape by means of applied mechanical forces with the assumption that the metal retains its shape when the stress drops below the yield stress (except for elastic changes). The shaping of the components can be considered from the mechanical, industrial, microstructural and computational point of view, they are distinct but interconnected. To produce the desired shape and size of the object the tooling, machines and lubrication are selected under the industrial processing. To control the final properties of the product specific pre and/or post treatment is given [5]. To produce the product with economy, it is necessary to minimize the defects. Primary forming usually causes extensive shape and size changes to large rough work pieces. Large machinery is required to produce the large forces to give the shape and size. Therefore, hot working is employed to improve the ductility and to lower the flow stress. Generally, hot working of metals and alloys is performed above the 0.6 T_m at relatively high strain rates (10^{-1} to 10^{3} s^{-1}), where T_m is the melting point [17]. The dislocation hardening at these temperatures is relatively moderate. The ductility is increased due to quick dislocations annihilation [18].

The metal working processes have become the essential part of the manufacturing after industrial upheaval (1940). Over this period, the effect of various processing parameters such as temperature, rate of deformation, and amount of deformation on the final product has been

studied. Meanwhile, the use of high temperature thermo-mechanical processing resulting in the substantial changes in the microstructure has increased. Additionally, the use of computer based process models which predict the properties of the final product by simulating the complete process has also increased in process development [19]. This makes the production more efficient and cost effective and reduces the shop floor trials.

Initially, the steel industry used the traditional alloy development techniques which required more attention for alloy chemistry of the starting billet rather than the process route. This method was effective but not economical. Presently, there has been shift away from alloy development to the process development [20]. To achieve good quality product through process development route requires thorough knowledge of the basic metallurgy of the alloy e.g. knowledge of the temperature range for stability of a particular phase. Moreover, the knowledge of restoration processes like dynamic recrystallization (DRX) and dynamic recovery (DRV) is also required. This helps to define the workability region.

Thus, the following sections provide the comprehensive review of the existing literature on hot working behavior of the plain low carbon steel and low carbon microalloyed steels which is essential to understand the microstructural evolution after hot deformation and the deformation mechanisms.

2.1.1. HOT WORKING OF PLAIN CARBON STEEL

Rao et al. [21] performed compression tests of plain low carbon steel (C-0.06 wt %) at different deformation temperatures ranging from 900°C to 1100°C using constant strain rates of 0.1, 1 and 8 s^{-1} to total true strain of 0.8. The specimens were heated upto the austenitization temperature of 1200°C with the heating rate of 2.6°Cs^{-1} and held for 2 minutes, followed by cooling at the rate of 2°Cs^{-1} to the deformation test temperature and held for 30 s before compression. They found a hyperbolic-sine relation to represent the hot deformation behavior in the austenitic field. For any given conditions of strain rate and temperature, a constitutive relationship could describe DRX, strain hardening and DRV phenomena.

Empirical equations were determined to represent the high temperature and high strain rate flow curves after performing [22] the hot compression tests on plain low carbon and high strength low alloy (HSLA) steel at the deformation temperatures of 990°C, 1000°C and 1100°C with the constant strain rates of 2, 20 and 120 s^{-1} upto true strain of 0.7, after austenitization at 1200°C for 1 h. The empirical equations predict the stress-strain curves of plain low carbon

steel over the entire deformation zones, whereas it is not possible in the case of HSLA because it shows athermal behavior between 900°C and 1000°C.

Ultra-fine and equiaxed ferrite (1 μm) was produced upto the depth of 1/4 to 1/3 of the total thickness. To obtain this, Hodgson et al. [14] rolled the low plain carbon steel with the help of 2 high laboratory rolling mills in a single pass upto a reduction of 30% with the rolling speed of 24m/min, after the austenitization at 1250°C for 15 min. The entry temperature of specimen in the roll mill was 780°C (Ar_3). The rolled specimen was air cooled to room temperature. With large strain and high undercooling, strain induced transformation from austenite to ferrite played a major role in the refinement.

Matsumura et al. [23] hot rolled the plain low carbon steel at 800°C in two step deformations with the interpass time of 0.2 s and 5 s and the amount of strain in each deformation was 0.69, after the austenitization at 1000°C for 3 min. The results show that the second deformation just above the Ar_3 reduces the ferrite grain size and also increases the volume fraction of fine ferrite.

Eghbali et al. [24] performed two step hot deformation in plain low carbon steel (C-0.055 wt%) after austenitization at 1000°C for 2 min. The first step deformation was at 876°C with the strain rate of 1 s^{-1} and strain was 2, the specimen was cooled with the cooling rate of 1°Cs^{-1} to the second step deformation temperature of 810°C and held for 2 min followed by large deformation with strain rate of 0.1 s^{-1}. Due to large deformation of ferrite steady state dynamic flow softening is seen. In the initial stage of deformation no DRX grains are formed and the low angle grain boundaries are introduced in the original grains. With an increase in strain, the amount of high angle grain boundaries increased. Eghbali et al. [25] also observed that when the specimen was deformed with comparatively lower strain rates and with large amount of deformation, DRV and / or continuous DRX (CDRX) was the operating phenomena. The fraction of HAGB's did not decrease more than 5% during the straining from 2 to 50.

Wen et al. produced the steel plate with the ferrite grain size of 7.5 μm with the plate thickness of 8.7 mm after performing [26] hot deformation in the plain low carbon steel (C-0.15 wt%) in the temperature range of 550°C to 850°C followed by reheating to 750°C for 5 min, after the austenitizing at 900°C for 5 min. Tensile strength of plate was in the range of 465-525MPa, yield strength was 325-285MPa with elongation of 27-36% and also the toughness was not decreased.

Yang et al. [27] performed hot compression tests on the plain low carbon steel specimens at the deformation temperatures ranging from 850°C to 1100°C with the strain rates ranging from 0.1-60 s^{-1} and the applied true strain was 0.9, after austenitizing in the range of 900°C to 1300°C. The equiaxed and homogeneous ferrite of grain size 2 μm was obtained when the specimen was deformed in the temperature range of Ae_3 to Ar_3.

The fine ferrite grain size of 2 μm was obtained after performing the [15] hot compression tests on low carbon steel at Ar_3+10°C with the strain rate of 10 s^{-1} upto 70% reduction. Effect of undercooling on strain induced ferrite (SIF) transformation was studied. When the applied reduction was relatively small, the amount of SIF was increased with the increasing the undercooling (ΔT). But the amount of the SIF was nearly same with the increase in ΔT in the case of heavy deformation, while the ferrite grains became equiaxed and finer after transformation due to dynamic continuous recrystallization. Also, with increasing the ΔT the amount of reduction for the onset of ferrite formation within the austenite grains was reduced.

Cai et al. [28] hot compression tests on plain low carbon steel at Ar_3+10~15°C with the strain rate of 1 s^{-1} after reheating at 1000°C for 3 min in order to study the DIFT. The uniform ferrite grains were produced at the temperature above 845°C in Si added plain C steel. The critical stress and peak stress during hot compression decreases with the increase in the amount of Si.

Kim et al. [29] hot rolled the low carbon steel at 900°C upto 88% reduction after austenitizing at 1250°C for 2 h. Results show that retained austenite fraction increases due to the higher Mn content which deteriorates the elongation and enhances the strength. Strong banded structure was formed due to small Si:Mn ratio, which diminished the effect of ductility improvement.

Zhang et al. [30] hot compressed the plain carbon steels (C-0.08 and 0.13 wt%) between 650 and 1000°C at a strain rate of 1 s^{-1}, using 50% and 70% of length reduction. After 50% compression, cracks could not be observed whereas some micro-cracks were found in the specimens deformed at 650, 700, 750 and 900°C after 70% of compression. The initiation of these micro-cracks was strain and temperature dependent. The steel had higher hardness and lower ductility at lower temperatures. The decrease in ductility is due to the work hardening during the deformation. The flow stress decreased when the temperature was greater than 900°C, due to the recrystallization and recovery; whereas the ductility reduced in the

temperature range of 850-900°C due to the precipitates around the austenite grains and deformation induced thin ferrite films.

Sarkar et al. [31] hot deformed the low carbon steel at the deformation temperature of 820°C with the rolling speed of 4 m/min and reduction of 50 pct, 60 pct and 65 pct after austenitize at 1250°C for 30 min. They found a fine grained microstructure containing ferrite and bainite.

The strain assisted ferrite transformation was used to refine ferrite to a grain size of 3-5 μm. To achieve refined ferrite, Huang et al. [32] performed hot compression tests on plain low C steel (C-0.16 wt%) at deformation temperatures ranging from 520°C to 900°C, true strain upto 0.8 and a constant strain rate of 1 s^{-1}, after the austenitization at 900°C for 5 min. To precipitate the pre-eutectoid ferrite before deformation with different volume fractions another hot deformation test was performed. After austenitising the specimen at 900°C for 5 min, it was cooled to the deformation temperature of 770°C with the cooling rate of 50°Cs^{-1} and deformed upto true strain of 1.6 with the constant strain rate of 1 s^{-1}. The specimens were held for 8 s and 35 s after the compression, followed by in-situ water quenching.

To determine the flow softening behavior, Chung et al. [33] performed hot compression tests on plain carbon steel (C-0.15 wt%) between 700°C and 875°C at the interval of 25°C and at 0.01 s^{-1} and 1 s^{-1} using true strain of upto 0.8, after austenitization at 900°C for 10 min. The heating rate was 10°Cs^{-1} and the cooling rate was 5°Cs^{-1}. Unusual flow softening behavior was strongly dependent on the strain rate and observed at about 780°C within austenite+ferrite phase field at low strain rate 0.1 s^{-1}, whereas the usual flow behavior was observed at higher strain rate 1 s^{-1}.

To obtain the ultra-fine microstructure, Calcagnotto et al. [16] performed three hot compression tests on plain carbon steel at 860°C with strain rate of 10 s^{-1} upto true strain of 0.3, after austenitization at 912°C for 3 min to obtain (a) coarse grain (CG), (b) fine grained (FG), and (c) ultra-fined grained (UFG) structure. To obtain the CG ferritic and pearlite structure, the above processed specimen was cooled slowly. To obtain FG polygonal ferritic matrix with small islands of pearlite and globular cementite, the hot compressed specimen was further deformed at 700°C in four step compression each of true strain 0.4 (i.e. 4 x 0.4) and inter pass time of 0.5 s with the strain rate of 10 s^{-1}. To obtain UFG structure, the specimen was warm deformed in four steps having strain of 0.4 in each step at 550°C with inter pass time 0.5 s,

after the austenitization and hot deformation at 860°C with true strain of 0.3. The specimen was annealed for 2 h at the same temperature followed by air cooling. After hot deformation and large strain warm deformation at different deformation temperatures, the three low carbon dual phase steels were obtained with the martensite volume fraction of about 30% and having different ferrite grain size of viz. 12.4 μm for CG, 2.4 μm for FG and 1.2 μm for UFG. Calcagnotto et al. also observed that the tensile and yield strength also increased due to the grain refinement. The grain refinement was attributed to early dislocation interaction, results the increase in initial strain hardening [34].

To study the effect of second phase particle on the work hardening rate, Song et al. [35] hot deformed the three plain low carbon steel after austenitization at Ae_3+100°C for 3 min followed by air cooling to different deformation temperatures of 860°C (steel with C-0.15 wt%) and 870°C (steel with C-0.20 and 0.30 wt%) and applied the true strain of 0.3 with strain rate of 10 s^{-1} to obtain fully recrystallized austenite. After the first step deformation the specimens were cooled to 550°C for 2 min followed by four step plain strain compression with each step strain of 0.4 and strain rate of 10 s^{-1}. The ultra-fine ferrite of grain size ranging from 1.1μm to 1.4μm with homogeneous distributed fine cementite was obtained. Work hardening rate was increased with an increase in the amount of fine dispersed cementite particles, and it balanced the negative effect of grain refinement on ductility.

Hickson et al. [36] also performed hot rolling in order to achieve the ultrafine ferrite (UFF) in plain low carbon (C-0.06 wt pct) steel after austenitizing at 1250°C for 15 min. The entry temperatures of rolling ranged from 730°C to 835°C with the rolling speed varying from 0.2 ms^{-1} to 1 ms^{-1} and reduction varying from 20 to 60%. The temperatures of specimens during the exit were varied from 630°C to 740°C followed by air cooling. The results show that significant amount of UFF was present in the single pass of rolling due to strain induced transformation, high shear strain, and undercooling.

Ultra-fine equiaxed polygonal ferrite of less than 2 μm in diameter was produced after hot rolling of [37] two low carbon steels (C-0.095 and 0.11 wt pct) at temperatures of 800°C and 675°C with the reduction of 40% with the rolling speed of 24 m/min, after austenitizing for 15 min.

The fine ferrite with the grain size of about 2 μm was observed at the prior austenite grain boundaries on asymmetric rolling of [38] the low carbon steel done at 750°C after

austenitization at 900°C for 10 min, with the roll diameter ratio of 1.5 and the reductions were 30, 40, 50 and 60%. The yield strength and the yield ratio were increased with the increase in the deformation. Moreover the volume fraction of ferrite also increased with the rolling reduction.

Fine ferrite grains of size 2 μm was obtained by Choi et al. [39] after hot compression of plain low carbon steel (C-0.15 wt%) at the deformation temperatures ranging from 650°C to 900°C with the strain rates of 0.1 and 1 s^{-1} upto the true strain of 1.2 after austenitizing at 900°C, 1050°C and 1200°C for 1 min. The results show grain refinement in plain low carbon steel when the specimen was deformed between Ae_3 and Ae_1. Strain induced dynamic transformation (SIDT) plays a very important role to produce the fine ferrite grains. The amount of SIDT ferrite increases when the strain increases above the critical strain. As the temperature of austenitization decreases, the prior austenite grain size decreases that result in acceleration of SIDT kinetics.

In order to study the effect of carbon content on flow behavior, Escobar et al. [40] performed hot compression tests on plain carbon steels at the deformation temperatures ranging from 900°C to 1100°C with the strain rates of 10^{-4}, $3x10^{-4,}$ 10^{-3}, $3x10^{-3}$, 10^{-2}, $3x10^{-2}$ and 10^{-1} s^{-1} upto the true strain of 0.7 after austenitizing at 1100°C for 15 min. It was found that low carbon steel showed higher work hardening rate and faster DRV kinetics than high carbon steel at high temperatures and lower strain rates whereas this became reversed at low temperature and higher strain rates.

2.1.2. HOT WORKING OF MICROALLOYED STEELS

Microalloyed steels contain 0.001-0.1 (wt) % microalloying elements (MAE). The base steel typically contain (wt %) 0.05-0.25% C and 1.0-2.0% Mn with optional additions of Ni (up to 3%), Mo (up to 1%) and Cr (up to 1%). The microalloying elements include Ti (0.01-0.05%), Nb (0.03-0.1%), V (0.06-0.1%), B (0.0018-0.006%) and Al (0.03-0.08%). These may be added either individually or in combinations. The addition of alloying such as Mn, Nb, Ti, Mo, Ni and/or Cu in low carbon steel promotes the formation of acicular ferrite [41]. To achieve the high strength steel through precipitation hardening, V is one of the most potent microalloying element [42]. Addition of B improved the ductility and lowered the strain hardening exponent [43].

Due to the physical and chemical features, The MAE have different effects on recrystallization, precipitation, inclusion control, and phase transformation. The addition of MAE significantly increases the mechanical properties such as toughness, yield and tensile strength, formability etc. of the base steel. For property optimization the major alloy systems that used different thermomechanical processing may contain Nb, V-Nb, Nb-Mo, V, V-N, Ti, Ti-Nb, V-Ti, Ti-Nb-Mo and Ti-Nb-Mn-Mo. These alloy systems are used not only for precipitation hardening (V,Nb) and grain refinement (Nb,Ti), but also for other strengthening mechanisms such as solid solution hardening (Mn) and the formation of bainite/ acicular ferrite structures (Mo and Mn) by accelerated cooling.

Generally, to increase the yield strength by precipitation hardening and grain refinement, 0.02-0.04% Nb is added to steels. To retard the austenite recrystallization, strain induced precipitation of Nb (C,N) is an effective method during the hot rolling. When Nb is in the solution (at T > 1000°C), it suppresses the recrystallization by an order of magnitude, whereas it is suppressed by three orders of magnitude when it was in precipitate form (at T < 950°C) [44]. The non-recrystallization temperature (T_{nr}) significantly increases due to the carbide forming ability of Nb. To increase hardenability, the dissolved Nb is useful, which contributes to microstructural control. Whereas, Nb precipitates in ferrite increase the strength of the final product. During hot working NbC precipitates have little influence on DRX. Hence, to inhibit the austenite DRX during hot deformation, the solute drag effect of Nb is more powerful as compared to NbC precipitates. On retarding the static recrystallization, the importance of NbC precipitates is more obvious than that of solute Nb [45].

Titanium prevents the grain growth of the austenite due to the precipitation ability with N to form stable TiN precipitates. To prevent the grain growth up to temperature of 1300°C, Ti up to 0.025% is most effective. Dissolved or precipitated Ti has a similar but less effective role to retard the austenite recrystallization as compared to Nb. To control the shape of sulphide particles, high amount of Ti is added which forms (Mn, Ti) S and globular $Ti_4C_2S_2$ along with the TiC precipitate in ferrite. This further aids in strengthening of the final product [46].

Steels with maximum 0.1% Vanadium are widely used in the structural application with the maximum yield strength of 415 MPa in the hot rolled, accelerated cooled, controlled cooled, normalized or quenched and tempered conditions. During hot rolling, V remains in the solution, and it does not strong impact in the austenite recrystallization. However, the

precipitate VN in ferrite during cooling substantial strengthening the base steel and it depends upon the cooling rate [46].

Hong et al. [47] hot compressed the plain low carbon and V-Nb microalloyed steel in two steps: (a) rough rolling (b) finishing rolling, after austenitization at 1100°C for 2 min with the heating rate of 20°Cs^{-1} followed by cooling at the rate of 1°Cs^{-1} to the deformation temperatures. The roughing reduction was 50, 30, 10 and 0% at 1000°C whereas the finishing temperature was Ar_3+10°C and the reduction was 30, 50, 70 and 80% respectively with the strain rate of 1 s^{-1}. Total deformation was 80%. The Ar_3 temperatures of low C and microalloyed steel measured by dilatometry were 725°C and 741°C whereas by continuous cooling compression (CCC) were 740°C and 755°C, respectively. Results show that more amount of deformation at finishing temperature induced more deformation induced ferrite (DIF) in austenite matrix. It was found that more DIF was formed by applying high strain rates and with the smaller austenite grain size due to the increase of γ grain boundary.

The optimum domains of hot working with the high power dissipation efficiency is in the temperature ranging from 1050°C to 1150°C and strain rates ranging from 0.01 s^{-1} to 3 s^{-1} as reported by Lin et al. [48]. Hot compression tests were performed on commercial 42CrMo high strength low alloy steel at four different temperatures ranging from 850°C to 1150°C with the interval of 100°C with the strain rates of 0.01, 0.1, 1, 10 and 50 s^{-1} with the different amount of deformations (10%, 20%, 30%, 40% and 60%) on Gleeble 1500 thermomechanical simulator machine. The specimens were heated at the heating rate of 10°Cs^{-1} and held for 5 min for austenitization. The results show that for a given temperature, with the increasing strain rate the deformation resistance increases. Also, with the decrease in the deformation temperatures the deformation resistance increases for a given strain rate. The values of power dissipation efficiency increase with the increase in strain at the relatively small strain rates whereas at higher strain rates (10 s^{-1} and 50 s^{-1}) the results were contrary. Lin et al. [49] also performed hot deformations at temperatures 850°C, 950°C and 1050°C with the strain rates of 0.1 s^{-1}, 0.5 s^{-1}, 1 s^{-1}, and 2 s^{-1}. The amount of deformations was 5%, 10%, 12% and 15%. Based on experimental results, the grain size model for static recrystallization was developed. The microstructural evolution during static recrystallization was influenced by processing parameters like deformation temperature, strain rate, amount of deformation.

Deva et al. [50] hot rolled the Nb microalloyed steel and found the ferrite grain size less than 3 μm. Wei et al. found that the DRX behavior depends on strain rates, and the deformation

temperature. They concluded this after [51] performing hot compression tests on 0.23C, 1.50Mn, 1.79Al (wt %) based microalloyed high strength steel at different temperatures ranging from 900-1100°C and at constant strain rates ranging from 0.01-30 s^{-1}. The activation energy of hot working was 310 kJ/mol.

Wei et al. [52] hot compressed low carbon vanadium microalloyed and medium carbon vanadium microalloyed steels in the temperature range from 900°C to 1100°C at an interval of 50°C at constant strain rates of 0.005, 0.01, 0.1, 0.5, 1 and 10 s^{-1} upto strain of 1, after austenitization at 1150°C for 5 min. The heating rate was 10°Cs^{-1}. The hot deformation activation energy decreased as the carbon content in vanadium microalloyed steel increased from 0.055 wt% to 0.37 wt%. Further, it also decreases the flow stress and work hardening rate at lower strain rates due to expansion of austenite lattice and increase in self diffusivity whereas flow stress is higher at higher strain rates due to effect of carbon on stacking fault energy. The DRX rate increases with increasing the carbon content in vanadium microalloyed steel which shows that DRX process accelerated due to increase in carbon addition.

Wei et al. performed hot compression tests on Nb microalloyed steel in order to determine the effect of Nb and C on the flow behavior [53] at the deformation temperatures ranging from 900°C to 1100°C at an interval of 50°C with the strain rates of 0.005, 0.01, 0.1, 0.5, 1 and 10 s^{-1} and the applied total true strain was 1.0. The results show that at the same hot deformation conditions the flow stress of Nb-microalloyed steel is higher than that of C-Mn steel due to the high solute strengthening and precipitation strengthening effect of Nb. The peak strain and the steady state strain increases due to Nb addition which delays DRX. However, C addition in Nb microalloyed steel diminishes the characteristic strains which promote the DRX.

To observe the DRX behavior of the HSLA 100 alloy, Momeni et al. [54] hot compressed the alloy after reheating the specimens at 1200°C for 1 h followed by the cooling to the deformation temperatures in the range 850°C to 1150°C with the strain rate of 0.001 to 1 s^{-1} and the total true strain was 0.8. Before deformation, the specimens were held for 10 min at the deformation temperatures. Results show that at temperatures higher than 950°C, DRX behavior was observed whereas at lower temperatures no indication of DRX was observed. This indicates that this temperature is recrystallization-stop temperature of the alloy. The apparent activation energy for DRX is 377 kJ/mol.

DRX is the main microstructural phenomenon in the temperature range of 900°C to 1150°C with the strain rates of 10^{-3} to 1 s^{-1}, and the apparent activation energy was found to be 435 kJ/mol for VCN200 medium carbon low alloy steel. To observe this Momeni et al. [55] hot compressed the steel in the temperature range of 850°C to 1150°C at an intervals of 50°C with strain rates of 10^{-3} to 1 s^{-1}, after the reheating at 1200°C for 30 min. To estimate the fractional softening due to DRX, a model based on Avrami's equation was developed for any given strain in the flow curve.

Jorge et al. [56] performed hot compression on low carbon Nb-microalloyed steel in 20 deformation steps during cooling in the temperature range of 1200°C to 630°C with the interval of 30°C, after the austenitization at 1200°C for 5 min. The strain in each step was 0.3. The physical simulations of multi-step deformations revealed information about the work hardening, softening, phase transformations and microstructural evolution and a grain size of about 1 μm is obtained.

Mirzaee et al. [57] investigated the hot working behavior of 26NiCrMoV 14-5 steel by performing hot compression tests in the temperatures range of 850°C to 1150°C with the strain rate of 0.001-1 s^{-1} after austenitization at 1200°C for 10 min. The results show that at temperatures higher than 1000°C DRX behavior is observed whereas at lower temperatures there was work hardening without any sign of DRX. The apparent activation energy was determined to be 437 kJ/mol with the help of sinh type law.

In order to observe the grain refinement, Ueki et al. [58] performed hot torsion tests on plain low carbon and low carbon V-Nb microalloyed steels in the temperature range of 900°C to 1200°C with the strain rates of 10^{-3} to 10 s^{-1}. Results show that when the microalloyed steel was deformed at 800°C, grain refinement was observed. In this steel, the grain fragmentation was observed due to subgrain formation whereas the austenite recrystallized at the grain boundaries.

To study the influence of thermomechanical processing parameters on ferrite grain refinement, Eghbali et al. [59] hot compressed Nb-microalloyed steel at deformation temperatures of 760°C, 810°C and 850°C with the strain rate of 0.01 s^{-1} after austenitizing at 1000°C for 5 min. The applied true strains were 0.8 and 1.5. The ultrafine and equiaxed ferrite of grain size 2 μm was obtained when the specimen was deformed at 760°C with true strain of 1.5.

For grain refinement, Eghbali et al. [60] performed hot deformation of low carbon Nb-Ti microalloyed steel at the temperatures 830°C, 845°C, 950°C and 1100°C after holding for 20 s at the deformation temperature. Strain rate was 0.01 s^{-1} and the applied strain was 0.8. The specimens were solutionized at 1150°C for 5 min prior to the deformation. The equiaxed and ultra-fine ferrite of grain size 1.8-3 μm was obtained when the specimen was deformed at about Ar_3 ± 10°C. In this temperature range, strain induced transformation (SIT) mechanism is responsible for ferrite refinement.

Eghbali et al. [61] performed hot compression tests on low carbon microalloyed steel at 845°C, 950°C and 1100°C with the strain rates of 0.001 and 0.1 s^{-1} up to the strain of 0.8 in order to obtain grain refinement. SIT plays a stronger role in grain refinement as compared to the deformation in non-recrystallization or recrystallization temperatures zones. The equiaxed and fine grain ferrite of 1.5 μm is obtained when the deformation was performed at 845°C with strain rate of 0.1 s^{-1} due to SIT mechanism.

In order to obtain the ultra-fine ferrite grained structure [62] hot compression tests were performed in low carbon Nb-Ti microalloyed steel at 845°C (just above the Ar_3) with the strain rates of 0.001, 0.01 and 0.1 s^{-1} up to the true strains of 0.25, 0.4 and 0.8 after austenitizing at 1150°C for 5 min. Equiaxed, homogeneous and ultrafine ferrite of grain size 2 μm with little amount of deformed pro-eutectoid ferrite was obtained after deforming the specimen at 845°C with strain rate of 0.1 s^{-1} upto true strain of 0.8.

Eghbali et al. [63] performed hot deformation of microalloyed steel with the strain rate of 0.1 s^{-1} at 750°C with different amount of strains after the austenitizing at 1200°C for 2 min. The results show that DIFT and CDRX were promoted with increasing strain, and ultra-fine ferrite of 1.8 μm grain size was obtained.

To study the recrystallization kinetics, Kwon et al. [64] hot compressed a low carbon Nb-microalloyed steel in the temperature range from 900°C to 1100°C with the constant strain rates of 0.1 and 10 s^{-1} up to the true strain of 0.3, after the austenitizing at 1300°C. Mechanical softening was seen and it was nonlinearly related to recrystallization. The retardation of recrystallization kinetics is greater when precipitates were formed in Nb-microalloyed steel as compared to the dissolved Nb.

Chun et al. [65] reported that due to hot deformation of HSLA steel, austenite to ferrite transformation is accelerated and refined ferrite grains were obtained upon hot compression of low carbon HSLA steel at 875°C and strain rate of 10 s^{-1}.

Opiela et al. [66] stated that the flow stress increased with strain rate during hot compression of Ti-V-B microalloyed steel at temperatures ranging from 900 to 1100°C and constant strain rates of 1-50 s^{-1}, and the deformation was controlled by DRX.

In a medium carbon V microalloyed steel, at low strain rates (0.1-1 s^{-1}), the activation energy value is 287.4 kJ/mol with dislocation climb as the rate controlling mechanism whereas for high strain rates (10-30 s^{-1}) the activation energy value is 500.6 kJ/mol and cross slip is the rate controlling mechanism. Zhao et al. obtained these conclusions after [67] performing hot compression tests at temperatures ranging from 750-1050°C and at constant strain rates of 0.005-30 s^{-1}, after austenitizing at 1200°C for 10 min.

In order to study the different recrystallization kinetics, Cho et al. [68] performed hot deformation on Nb micro alloyed steel in the temperatures range of 850°C-1050°C with the strain rates ranging from 0.05 to 5 s^{-1} after austenitizing at 1200°C. The results show that the kinetics of SRX increased with the increasing temperature and strain, whereas the kinetics of metadynamic recrystallization (MDRX) depends on strain rate. The rate of MDRX was higher than that of SRX. Cho et al. [69] also performed continuous and interrupted torsion tests on microalloyed steels in the temperatures range from 950°C to 1050°C with the strain rates of 0.05 s^{-1} to 5 s^{-1}, after austenitizing at 1200°C for 15 min. The rate of static recrystallization (SRX) increases rapidly with the temperature and strain whereas the rate of MDRX was twice as high with the increase in strain rate.

The DRX is delayed due to the addition of high level of Nb as reported by Xu et al. [70] after performing single and double hit hot compression tests on HSLA steel in the deformation temperatures ranging from 900°C to 1200°C with the strain rates of 0.1 s^{-1} to 10 s^{-1}. The deformation activation energy of high Nb steel is 373 kJ/mol.

In order to study the influence of chemical composition on the peak strain [71] hot deformation tests were performed on the low alloyed and microalloyed steel specimens at the deformation temperatures of 900°C, 1000°C and 1100°C with the strain rates of 0.544, 1.451, 3.628 and 5.224 s^{-1} after austenitizing at 1230°C for 10 min. The microalloying elements, such as V, Ti and especially Nb increase the peak strain due to the delay in DRX whereas C, Mn and

Si do not show any effect. The peak strain value also increases when approx. 0.2-0.3 wt% Mo is added.

In order to determine the DRX fraction Medina et al. [72] performed hot deformation tests on the microalloyed steels at the deformation temperatures of 900°C, 1000°C and 1100°C with the strain rates of 0.544, 1.451, 3.628 and 5.224 s^{-1}. The results show that all the alloying elements, especially Nb retards the DRX.

Zhang et al. [73] performed hot compression tests on plain low carbon and low carbon Nb-microalloyed steel at the deformation temperatures ranging from 900°C to 1100°C with the strain rates ranging from 0.01 to 40 s^{-1}, after austenitizing at 1200°C for 5 min. The results show that the apparent deformation activation energy increases and the DRX retards due to the presence of Nb in solution. The energy required to induce recrystallization of austenite of plain carbon steel is smaller than that of Nb-steel.

To study the recrystallization behavior [74] hot compression tests were performed on Nb-microalloyed steel specimen at the deformation temperatures of 950°C, 1000°C, 1050°C and 1100°C with the strain rates of 0.1, 1, 5 and 15 s^{-1} after the austenitizing at 1200°C for 10 min. The results show that at higher temperatures and lower strain rates DRX occurs more easily and the deformation activation energy is 379.29 ± 23.56 kJ/mol.

To determine the DRX kinetics [75], hot deformation tests were performed tests on the low carbon Nb-Ti microalloyed steel at 900°C, 1000°C and 1100°C with the strain rates of 0.01, 0.1 and 1 s^{-1} up to the strain of 2.0 after austenitizing at 1200°C for 2 min. The relationship between DRXed grain size and Zenner-Hollomon parameter *Z*, critical strain and *Z*, and the steady state strain and *Z* were determined.

Maruyama et al. [76] performed double hit compression test on microalloyed steels at 1000°C with the strain rate of 10 s^{-1} after austenitizing at 1250°C for 20 min. The applied strains were 0.18 and 0.36 for first and second hit, respectively. The results show that microalloying solute atoms retard the onset of austenite recovery. Nb had larger retarding ability as compared to other alloying elements Ti and V.

In order to analyze the DRX behavior of low carbon microalloyed steel [77], the hot deformation tests were performed at 1000°C, 1100°C and 1200°C with the strain rates ranging from 0.02-5 s^{-1} after austenitizing in the temperatures ranging 1000°C to 1420°C. The DRX is

largely retarded by Nb as compared to Ti. The dynamic recrystallized grain size increases as the value of *Z* decreases.

The peak stress and steady state stress significantly increases with the addition of Nb and Ti. The solute dragging and dynamic precipitate pinning of Nb and Ti retards the onset of DRX, and therefore results higher peak strain values as reported by Qiang et al. [78]. They performed hot compression of the plain low carbon and low carbon microalloyed steels at the deformation temperatures ranging from 850°C-1150°C with the constant strain rates of 0.1 to 5 s^{-1} upto the strain of 1.2.

Mukherjee et al. [79] performed hot strip rolling on plain low carbon and low carbon microalloyed steels at 25°C to 50°C above the Ar_3 temperature with different amounts of strain i.e. 0.2, 0.4 and 0.6 with the constant strain rate of 1 s^{-1}, followed by helium quenching, after austenitization for 2 min. The results show that the potential of deformation induced ferrite transformation (DIFT) increases with the increasing the amount of strain, results the finer ferrite structure of 1 μm to 2 μm in grain size.

The potential of ferrite grain refinement in low carbon microalloyed steel was increased due to the heavy deformation as reported by Priestener et al. [80]. They observed this phenomenon after hot deformation at the deformation temperatures of 1000°C and 1100°C upto the strain of 1.25, after austenitizing at 1250°C for 5 min.

Bakkaloğlu [81] performed hot deformation in V-Nb microalloyed steel in the temperature range of 740°C-820°C with the interval of 20°C in two step deformations after austenitization at 1150°C for 1 h. Total amount of reduction was 35-40%. Results show that due to control rolling in two phase region the tensile and the impact properties were improved and the mechanical properties was comparable to those of highly alloyed or heat treated steels. The yield and tensile strength of steels increased with the lowering of deformation temperature.

Hot deformation characteristics of microalloyed steels are also influenced by precipitation processes. In order to study the precipitation kinetics of TiC during deformation, two stage hot compression tests were performed on Ti-microalloyed steel at the deformation temperatures ranging from 875°C to 975°C with the strain rate of 1 s^{-1} after austenitizing at 1150°C for 3 min [82]. The applied reduction in each stage was 20%. The nose of the precipitation time temperature (PTT) diagram is at the temperature 910°C and about 3 s and strain induced TiC was observed at the dislocation and dislocation sub-structures.

In order to study the precipitation kinetics two stage interrupted compression tests were [83] performed at the deformation temperatures ranging from 850°C to 975°C with the strain rate of 10 s^{-1} after austenitizing at 1250°C for 400 s. The strain in each step was 0.3. The precipitation start time of strain induced NbC in Nb-microalloyed steel is earlier as compared to the Nb-Ti microalloyed steel.

In order to study the effect of Nb on hot deformation behavior [84], hot deformations were performed on Nb microalloyed steels after austenitizing at temperatures of 1150°C and 1200°C for 3 min. The specimens were cooled to the deformation temperatures in the range of 950°C to 1100°C and deformed with the strain rates ranging from 0.005 s^{-1} to 0.1 s^{-1} and the reduced up to 60%. The results show that the undissolved precipitates increase the peak stress more effectively than that of solute Nb. The peak strain and the DRX are also influenced by the undissolved precipitates. During deformation at the lower strain rates, the strain induced precipitation occurs.

Kostryzhev et al. [85] performed single and double hit compression tests on Nb-Ti microalloyed steel at the deformation temperatures of 825°C, 975°C, 1075°C and 1100°C with the strain rate of 5 s^{-1} up to the true strain of 0.75, after austenitizing at 1250°C for 5 min. The effect of deformation temperature on Nb clustering and precipitation was determined. The results show that the amount of Nb in solid solution decreased due to the formation of (Ti, Nb)(C, N) and this reduces the grain boundary pinning effect expected due to the Nb clustering or precipitation.

In order to study the DRX behavior [86] hot compression tests were performed on Nb-Ti microalloyed steels at the deformation temperatures ranging from 900°C to 1150°C with the strain rates ranging from 0.1 to 5 s^{-1} up to the strain of 1.2 after austenitizing. At low temperature, the DRX was retarded due to the onset of dynamic precipitation of Nb, Ti (C,N) which result in higher value of peak strain. To determine the activation energy of deformation an expression was developed as a function of the alloying elements Nb and Ti.

Hong et al. [87] performed hot compression tests on plain low carbon and Nb-microalloyed steel at Ar_3+10°C with the strain rate of 5 s^{-1} up to the true strain of 1.6 in order to see the effect of Nb on DIFT. When the NbC precipitates pre-existed, the DIFT kinetics behaves like C-Mn steel whereas the ferrite grain size was finer in Nb steel.

In order to determine the recrystallization-precipitation interaction, [88] double deformation tests were performed at 1000°C with the strain rates of 0.5 s^{-1} with different inter pass time after austenitizing at 1250°C for 5 min. The applied strain was 0.2 in each compression steps. The yield strength and tensile strength were higher in the Nb steel at the temperatures 900°C-1025°C (below NbC solubility temperature). The strain induced precipitates grow as the inter pass time increased.

Zadeh et al. [89] performed deformation on low carbon Nb microalloyed steel at 950°C with the strain rate of 1 s^{-1} using strain up to 1 after austenitizing at 1000°C for 2 min, in order to study the grain refinement mechanism. The results show that low angle grain boundaries (LAGB) were changed to high angle grain boundaries (HAGB) as the strain increased. This happened due to the continuous DRX (CDRX).

Jie et al. [90] hot compressed the low carbon microalloyed steel in the temperature range of 750°C to 800°C with the strain rate of 10 s^{-1} up to true strain of 1, after the austenitization at 900°C. DIFT and the dynamic austenite grain growth were detected when the specimen was deformed above the Ar_3 i.e. at 800°C. Moreover, as the deformation preceded the dynamic inverse ferrite to austenite was detected.

In order to study the effect of Nb on DIFT, Qing et al. [91] hot compressed the Nb-Ti microalloyed steel in two steps i.e. in first step deformation at 880°C with the strain rate of 0.1 s^{-1} and the strain was 0.51, whereas in second step at 780°C with the strain rate of 10 s^{-1} and the applied strain was 0.693. The results show that the DIFT is promoted by Nb (precipitates) in the multi pass deformation. The large amount of Nb precipitation is beneficial for DIFT.

In order to obtain the ultrafine ferritic structure, [92, 93] hot deformation of C-Mn-V steel was performed at 775°C with the strain rate of 1 s^{-1} with different amount of strain after austenitizing at 900°C or 1200°C for 3 min. The ultrafine ferrite of grain size 1-3 μm was obtained through the DIFT.

In order to study the effect of multiple deformations on grain refinement low carbon microalloyed steel [94] hot deformation was performed in the temperature range of 775°C to 900°C with the strain rate of 1 s^{-1} after austenitizing and the applied true strain varied from 0 to 4. The deformation in the Ae_3-Ar_3 reduced the ferrite grain size by factor of about 2 as compared to that of between T_{nr} (non-recrystallization temperature) and Ae_3.

In order to study the microstructural evolution during metadynamic recrystallization in a low-alloy steel Lin et al. [95] performed hot compression tests in the temperatures ranging from 850°C to 1150°C in the interval of 100°C using the strain rates of 0.01 s^{-1}, 0.1 s^{-1}, 0.5 s^{-1}, and 1 s^{-1} after austenitizing at 1200°C for 5 minutes. They observed that the microstructural evolution during metadynamic recrystallization is influenced by strain rate and deformation temperatures significantly. Also, with decreasing strain rates and increasing deformation temperatures, the deformed austenite grain size increased.

2.2. HOT DEFORMATION MECHANISMS

The key feature of hot deformation is that the large strains can achieved with little or no strain hardening. This indicates that strain hardening processes are balanced sufficiently with the softening processes. Generally, the commercial hot working operations in metals and alloys are defined as that when the deformation is performed at the relatively higher strain rates ranging from 0.1 to 100 s^{-1} and the deformation temperatures above 0.6 T_m [5], where *Tm* is melting temperature (K). In various metals and alloys, the softening processes are dynamic recrystallization (DRX) and/or dynamic recovery (DRV). Creep experiments establish the various basic characteristic of restoration phenomena. Due to restoration, the flow stress of the materials lowers resulting in easy deformation, and has an influence on grain size and texture of the material. To avoid the defects in finished parts and developing correct processing sequence in hot working, the knowledge of various strain hardening and softening mechanisms are helpful. To understand the strain hardening and softening mechanisms, a review of the independent deformation mechanisms and knowledge of deformation mechanism maps (DMMs) of the metals shall help.

2.2.1. DEFORMATION MECHANISMS

There are numerous basic atomic processes in which a polycrystalline can be deformed and yet remain crystalline [96]. There are six independent and distinguishable way to deforms by which the crystallinity can preserved. First, over a broad range of temperatures the glide of dislocations can proceed to extensive plastic flow. The ability of dislocations to climb as well as cross slip at high temperatures introduces the second mechanism i.e. dislocation creep. The third and fourth mechanisms are based on the diffusion of point defects through the grains and along their boundaries and these are called Nabarro-Herring creep and Coble creep,

respectively. Finally, the fifth mechanism is twinning that result in low temperature plasticity. The distinctive deformation mechanisms are given by these independent processes. The deformation mechanisms are power law creep, Nabarro-Herring creep, Coble creep and superplastic flow. Each mechanism has an equation which relates stress, strain rate and temperature and structure. Based on basic atomic processes, Ashby (1972) developed and constructed the DMMs. Theses maps were represented in the axes of stress divided by Young's modulus and homologous temperature (T/T_m), where T_m is the melting point (K). Further, Frost et al. [8] suggested the deformation mechanism maps provides the overall perspective of high temperature deformation phenomena, though it was limited to simple alloys, pure materials and steady state conditions.

2.2.2. STRAIN HARDENING MECHANISMS

Plastic deformation in crystalline materials in the temperatures range of about 0.1 to 0.5 T_m occurs by the glide of dislocations apart from the effects associated with diffusion. When the dislocations are inhibited in their movement through the crystal because of work hardening or strain hardening, higher stress must be applied to continue the plastic deformation. Many obstacles exist that hinder the dislocation movement. These are: other dislocations, grain and sub-grain boundaries, solute atoms, and second phase particles [97]. As the deformation proceeds, the dislocation density gradually increased through the fact that some fraction of mobile dislocations produces the strain that does not exit through the surface, are stored in the crystals, but are not absorbed in grain boundaries, and do not annihilate each other. Due to increased dislocation density and mutual interaction between dislocations, the stress necessary to force a passage for the later dislocations is increased.

The flow stress of solid solutions arises due to the frictional force caused by the movements of dislocations. The difference in elastic properties and atomic size difference between solute and solvent atoms influence the magnitude of the frictional force. If an atom of the matrix is substituted by the different elastic constants and same size impurity atom, there is no pre-existing lattice distortion due to the solute atom. If the dislocation moves close to the elastically harder impurity atom it must do more work, results the interaction between the solute atom and the dislocation.

An additional barrier for the movement of dislocations is the formation of fine precipitate in a solid solution, which lies across the slip planes in the dislocations movement

path. The dislocation cross the fine precipitates in one of the two ways viz cut through the particles or take a path around the obstacles.

2.2.3. SOFTENING MECHANISMS

When the polycrystalline materials deformed at the elevated temperatures, the increase of strain hardening (dislocation density) is continuously counteracted by the restoration processes (softening processes). The main restoration mechanisms are dynamic recovery (DRV) and dynamic recrystallization (DRX). In DRV, the dislocations have adequate mobility to permit attractive interactions to attain annihilation and a rearrangement into regular sub-boundaries and sub-grains. To decrease the strain hardening, the climb of dislocations and cross slip plays an important role [98, 99]. The flow curve of a material undergoing DRV during hot working increases continuously up to the steady state flow stress. No peak is observed in this process. The high stacking fault energy (SFE) materials shows the DRV behavior e.g. b.c.c. α-Fe, ferritic steels, β-Ti and also in the h.c.p. α-Ti, α-Zr, and Al and its dilute alloys [5, 100]. In moderate to low SFE f.c.c. metals and alloys like Ni, Cu and γ-Fe, since the recovery precedes more slowly, results high dislocation density. The nucleation of recrystallization during deformation permits due to the high difference in local dislocation density. In DRX, the flow curve exhibits a peak followed by steady state with the condition that $\sigma_p > \sigma_s$, where σ_p is peak stress and σ_s is steady state stress. At low strain rates and high temperatures, the flow curves have several maxima and minima before attaining the steady state [101]. This phenomenon occurs due to the multiple cycle of DRX.

2.3. WORKABILITY IN BULK FORMING PROCESSES

Workability is defined as the degree of deformation that can be achieved in a particular metalworking process (rolling, forging, and extrusion etc.) without creating an undesirable condition such as cracking or fracture, poor surface finish, buckling, or the formation of laps, which are the defects created during metalworking [102]. If such operations are conducted at the elevated temperatures, they are called “bulk forming processes”. There are huge changes in thickness due to the bulk forming processes which changes the shape [103]. In this section basic concepts and previous work related to workability will be reviewed.

2.3.1 EVALUATION OF WORKABILITY

Generally, the temperature, stress and strain rate along with material characteristics such as crystal structure, grain size and alloying elements influence the workability. The better understanding of material behavior during deformation results in improved metal working procedures.

At different temperatures and strain rates, the true stress-true strain curves can be obtained using actual or simulation of metal working operations such as forging, extrusion, and rolling either in the plant or in laboratory. Using these methods for a particular amount of reduction at various temperatures and strain rates the average stress values are obtained which are quite complex and non-uniform [5]. To evaluate the workability of a material tension, torsion, compression and bend tests are widely used in the laboratory. The well-defined states of stress and strain are the key feature of each of these tests. Each test has its own merits and demerits, which is discussed by Rao et al. [104] and Dieter [102, 105]. However, only the uniaxial compression test will be described in detail in the following sections.

Since the stress values obtained after compression test is close to those obtained in the bulk deformation processes, therefore it is usually considered as a standard workability test [106]. To perform the compression tests cylindrical specimens are used and compressed between flat parallel dies or anvils. To avoid the buckling of specimens, dimensions are kept within upper limit of aspect ratio (height-to-diameter). The upper limit of aspect ratio is 2.0. If the specimen is much deformed in the central plane as compared to the other contact surface due to the friction between the platens and the specimen, barreling or bulging results (figure 2.1).

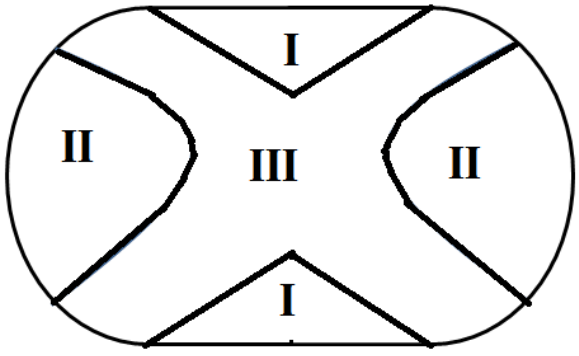

Fig. 2.1. Deformation zones of a hot compression specimen.

Due to inhomogeneous metal flow three distinct deformation zones can be identified [102]: The top and bottom surfaces of the specimen which are in contact with the dies or anvils remain almost stationary. These areas are called dead-metal zones (shown by region I in figure 2.1).

(a) The metal near the outer surface of the compressed specimen, results in bulged surface (shown by region II in figure 2.1).

(b) The zones just outside the dead-metal zones near the contact surfaces, experience most severe deformation (shown by region III in figure 2.1).

To determine the deformation resistance (flow stress) of the material, the deformation tests should be conducted under isothermal conditions (no die chilling) at the constant strain rate with minimum friction. To minimize the frictional constraints the specimens are lubricated depending upon the test temperature, with graphite, oil, molykote, glass etc. At high temperature, the frictional effects on non-lubricated specimen are insignificant with the aspect ratios of 2.0 to 1.2 and up to the true strain 0f 0.7 as reported by various researchers [107-109].

Other reasons behind the popularity of hot compression tests are as follows: specimen cross sections are suitable for optical microscopy, it is possible to obtain high strain rates and large strain values, and smaller specimens which can be easily cut from the as-received materials in order to determine the flow stress [106].

To achieve high productivity, bulk deformation processes are conducted at high temperature and high strain rates with large strain. High temperatures help to obtain final product without the onset of fracture when the large strain is applied in a single step. Furthermore, the hot deformation influences the microstructure change. Thus, to control the product microstructure without micro or macro defects or flow instability, hot deformation plays an important role. Materials processing requires the fundamental knowledge of the constitutive behavior of different elements to develop a robust control system [110, 111]. The physical model has sources, stores, and dissipators of power. Source generates the energy that is transmitted to the tools, which elastically store the power and transmit to the workpiece through the interface (lubricant). The power is dissipated by the workpiece while it undergoes plastic flow in the deformation zone. Since the system is dynamic, therefore the energy transactions occur in terms of power. Workability consists of two independent parts:

(a) Intrinsic workability

(b) State of stress (SoS) workability

The intrinsic workability depends on the constitutive behavior of the material i.e. material chemistry, initial microstructure, processing history, temperature, strain rate, and strain whereas SoS depends on the deformation zone geometry and the nature of the applied state of stress and it exist in the deformation zone.

The work piece experiences six independent stress components in three dimensional SoS system during plastic flow through the deformation zone. They consist of three hydrostatic stress components and three shear stress components. The plastic flow of the material is due to the shear stress components whereas SoS workability will be decided by the hydrostatic components. For example, if the stresses are tensile, weak interface in the microstructure will be opened and it promotes the fracture or damage [112]. On the other hand, workability is improved by the compressive hydrostatic components. Since the SoS workability depends upon the geometry of the deformation zone and the applied SoS in the process, therefore to control the particular process specific techniques are needed. For example, in extrusion it may be optimized by the die cavity design or in forging by blocker die design or preform, or in rolling by the roll pass design (geometry, the reduction per pass and the sequence of the roll pass). Though, the available variations in the preform geometry or in the roll pass are somewhat limited due to the geometry of the component. Whereas, there is substantial scope to design the die cavity geometry so that the SoS is essentially compressive in the deformation zone for a given product and container geometry. To reduce the lead time in design and manufacturing of dies without resorting expensive trial and error methods, the finite element method (FEM) modeling techniques are generally used [113]. It is generally accepted that the SoS workability does not depend on the constitutive behavior of the material and can be optimized independently. Moreover, numerical simulation techniques are beneficial for evaluating the die designs without the expensive and time consuming shop floor trials.

The intrinsic workability of the material is sensitive to the constitutive behavior which is the response of the work piece to the applied processing conditions such as strain, strain rate, and temperature. The constitutive equations indirectly show the response. The constitutive equations depict mathematically the trend of the flow stress with the process variables [114]. However, distinctly the response of the material is in two complementary ways i.e. as the temperature increase, and change in the microstructure of the material. The intrinsic workability is decided by the microstructural changes. Thus, to predict and optimize intrinsic workability during hot working, modelling techniques are developed.

2.4. MATERIALS MODELING IN HOT DEFORMATION

The materials models for hot deformation are expected to predict (1) microstructural evolution i.e. the response of the material, (2) the optimum process parameters, and (3) the process limits for controlling the process in a manufacturing environment. If the model is based on scientific principles and applicable to a wide range of materials and simple, it makes an added advantage. Prasad [115] and Rao et al. [116] reviewed the available hot deformation models which are of the following types: (1) kinetic model, (2) atomistic model, (3) dynamic materials model, and (4) others.

2.4.1. KINETIC MODEL

In hot deformation, the steady state flow stress is related to the temperature and strain rate through an Arrhenius type of rate equation [117].

$$\dot{\varepsilon} = A\sigma^n \exp\left(-Q/RT\right) \tag{2.1}$$

where $\dot{\varepsilon}$ is the strain rate, σ is steady state flow stress, A is a constant, Q is the activation energy, n is the stress exponent, T is the temperature (K), and R is the universal gas constant. Detailed discussion follows in the upcoming chapter entitled “theory and analysis”.

2.4.2. ATOMISTIC MODEL-RAJ MAPS

Raj [9] developed several atomistic models to calculate the limiting conditions of strain rate and temperature that can be responsible for microstructural damage during hot deformation. If these boundaries are recognized, it is possible to hot work in the ‘safe’ regime without onset of fracture processes which damage the microstructure. Raj considered four different processes: (1) void formation at hard particles (at higher strain rates and lower temperatures), (2) wedge cracking at grain boundary triple junctions (at lower strain rates and higher temperatures), (3) adiabatic shear band formation (at very high strain rates), and (4) DRX (higher temperatures). The first three mechanisms are damage mechanisms whereas fourth one is the safe mechanism for hot working.

The critical strain rate is calculated for the void formation (ductile fracture) at hard particles. Due to deformation of soft matrix the stress is concentrated around the particles which would be relaxed more rapidly than is produced by creep or diffusional processes. The

regime of the ductile fracture will dominate at the temperatures where recovery processes are slow and above the critical strain rate [11]. On the other hand wedge cracking damage at grain boundary triple junction occurs at higher temperatures and slower strain rates which promotes grain boundary sliding. If the strain rate is high, wedge cracking will not occur because the matrix deforms faster as compared to the grain boundary sliding. If the strain rate is very slow, the wedge cracks get repaired because at grain boundary triple junctions the high stresses will be relaxed by diffusional flow. Raj modeled the DRX which is the safe process for hot working using the kinetic approach to determine the onset of DRX. Raj also determined the strain rate regime (generally very high) where adiabatic shear bands occur.

Raj maps were developed for dilute alloys and pure metals [118] for which the required fundamental data are available. There is serious limitation due to the lack of data on fundamental parameters for the calculations of commercial alloys; also for safe processing, a broader regime is represented by the map. Additionally, for adequate modeling of a given material, it is not possible to know a priori among all atomistic mechanisms. However, to model the constitutive behavior of material, the atomistic maps are a revolutionary attempt for hot processing.

2.4.3. DYNAMIC MATERIALS MODEL (DMM)

Prasad et al. [10] developed the DMM to introduce the constitutive behavior of the material, based on the continuum mechanics of large plastic flow [119], irreversible thermodynamics [120], and physical systems modeling [121]. DMM may be worked as a bridge between the developed dissipative microstructures and the continuum mechanics of large plastic deformation for describing the dynamic response of the material in the hot working. In DMM, the work piece is considered with the following properties:

1. Dissipative: The work piece does not store the energy, it dissipates the power during hot deformation. There are four different types of stress-strain curves that can represent the dissipative nature. (i) Flat type stress-strain curve (i.e. stress does not vary with the strain e.g. aluminium) (ii) steady state due to flow softening after a critical strain at large strains (e.g. Ni and Cu) (iii) oscillated stress-strain curve which becomes damped at large strains, and (iv) continuous flow softening curves without any critical strain (i.e. Widmanstätten or spheroidisation of acicular structures and in flow localization).

2. Dynamic: During hot working, the constitutive response of the material depends on the strain rate for a given temperature. It also somewhat depends on the strain, thus it is viscoplastic.
3. Non-linear: The response of the specimen (e.g. flow stress) is non-linear for a given set of variables such as temperature, strain rate, and strain.
4. Away from equilibrium: Since the applied strain on the work piece is not infinitesimally small increments, therefore at high temperature the work piece undergoes the large plastic flow which is away from equilibrium.
5. Irreversible: The extremum principles of irreversible thermodynamics are applicable to the work piece that undergoes large plastic flow at high temperature which causes the major changes in the microstructure [119].

The above characteristics of the workpiece make it an ideal candidate for the occurrence of deterministic chaos which leads to specific or strange attractors in a given state space [122].

2.4.4. OTHER MODELS

ACTIVATION ENERGY MAPS

The activation energy and strain rate sensitivity depends upon the strain rate and temperature when considered over wide ranges. The apparent activation energy remains constant and hence possible to apply linear controls, if the deformation is controlled by single rate controlling process. The microstructure variations will be small and less sensitive to the fluctuations in the process parameters in the activation energy plateau regime.

On the basis of Lyapounov functions four different criteria were developed which are based on the combination of activation energy maps and the 'stability' maps.

1. $0 < m < 1$: This criterion is based on the principle the power is not dissipated by the material when $m = 0$ or negative, and the material will undergo fracture. With the increasing the value of strain rate sensitivity *m*, the flow localisation reduces and leads to super-plasticity.

2. $\partial m / \partial \log \dot{\varepsilon} \equiv \dot{m} < 0$: if the strain rate sensitivity decreases with the increasing the strain rate, the material flow will be stable. Whereas, catastrophic fracture occurs, if the function is positive.

3. $\left[\partial \log \sigma / \partial (1/T)\right] \equiv S > 1$: For an irreversible process the rate of entropy production is

always positive. The processes that have high temperature dependence of flow stress are likely to develop stable flow whereas with lower temperature dependence of flow stress develops the flow instability.

4. $\partial S/\partial \log \dot{\varepsilon} \equiv S < 0$: for stable flow, with the increasing the strain rate the temperature dependence flow stress decreases. If the temperature dependence of flow stress is less at the higher strain rate, flow localization results. The flow will be more stable as the temperature increases in the adiabatic shear bands which results in less localisation [11].

To identify the stable flow regime, all the above criteria have necessary conditions, which are not sufficient to confirm that the flow instabilities occur in the remaining regimes. To avoid the unnecessary restriction due to instability, flow stability criteria are used. The microstructural correlation and considerable validation will have to be made before the use for industrial process design.

POLAR RECIPROCITY MODEL

This model was considered with the purpose of including history dependence of flow stress which is required in the work hardening material, whereas at the same time the flow characteristics of the work piece is represented by the strain rate dependence of flow stress [116]. In this model power is divided into two complementary components with dual potential functions using the flow rule of classical plasticity [123]. The intrinsic workability parameter is given by equation 2.2.

$$\zeta = 1 - \left[2m'/\left(m'+1\right)\right]\left[\left\{S - H\left(E^p\right)\right\}/\sigma\right] \qquad (2.2)$$

where m' is strain rate sensitivity exponent, and $H\left(E^p\right)$ is a function of strain history. If the material shows ideal viscoplastic flow, the history dependent term will be equal to unity and $m' = m$ and $\zeta = \left(1-\eta\right)$. The hills in the efficiency maps will be the basins in the ζ map and vice versa. Thus, in the absence of strain history, the predictions of polar reciprocity model and the DMM are identical. This model has not added anything regarding the strain effects in the hot deformation at large strains. For predicting the instabilities, this model does not have any criteria.

2.5. GRAIN REFINEMENT TECHNIQUES

There are various methods for grain refinement in steels, which can produce the ultra-fine grained ferritic structure. These are as follows:

(1) asymmetric rolling
(2) equal channel angular pressing (ECAP)
(3) deformation and annealing of martensite
(4) DRX of ferrite
(5) accumulative roll bonding (ARB)
(6) deformation induced ferrite transformation (DIFT)

A brief description of all the above methods to produce the ultra-fine ferrite steel will be given subsequently. The other severe plastic deformation processes to produce the nanostructured surface layer on the metallic materials are ball milling, ultrasonic shot penning, high energy shot peening, surface nanocrystallization and hardening, severe plastic torsion, shot peening, laser peening. These processes produce nanostructured surface layer [124-127].

2.5.1. ASYMMETRIC ROLLING

There are two ways to perform the asymmetric rolling.

(i) using two rolls of the same diameter but having different velocities
(ii) using two rolls of different diameter

Using these methods the rolled material experiences the severe plastic deformation by simultaneous action of compression and shear deformation [128]. Morimoto et al. reported the fine grained steel with the grain sizes of 2-5 μm by applying asymmetric hot rolling in 2 mm thick plain carbon steel strip, in the industrial production at Nakayama Steel (Osaka, Japan) [129].

2.5.2. EQUAL CHANNEL ANGULAR PRESSING (ECAP)

Equal channel angular pressing (ECAP) is one of the severe plastic deformation technique to produce the nanoscale microstructure in bulk metals and alloys [130-132]. The material is subjected to heavy plastic deformation (straining) in a specifically designed die in the equal channel angular pressing (ECAP) process as shown in figure 2.2. The arc of curvature (ψ) and the inner contact angle (ϕ) influences the strain per pass.

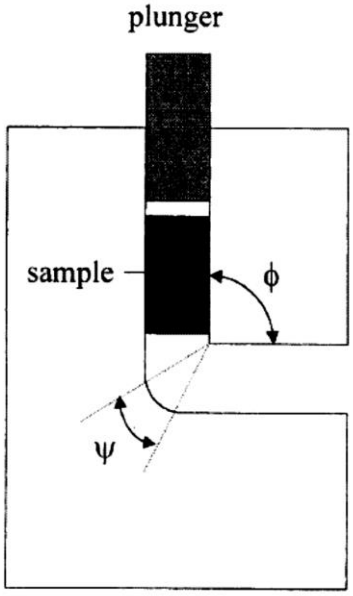

Fig. 2.2. Schematic diagram of an Equal Channel Angular Pressing die.

Shin et al. [133] performed severe plastic deformation on plain low carbon steel using the equal channel angular pressing method at 350°C and the strain was close to 8. The ultrafine grains with the average grain diameter of 0.3 μm were obtained. Zhang et al. [134] produced ultrafine grains of size 200 nm, after performing severe plastic deformation at 400°C using ECAP on plain low carbon steel. Whereas, fine grained material of grain size 350 nm was produced after 12 ECAP passes of plain low carbon steel at 400°C [135]. Hwang et al. produced the ultra-fine grained steel using ECAP and studied the mechanical properties. They reported the ultra-fine grained ferrite-pearlite steel having ferrite grain size of 0.5 μm with total elongation and tensile strength of 11% and 943 MPa, respectively [136]. Son et al. [137] used the ECAP method followed by annealing on low carbon steel to produce ultra-fine grained dual phase steel . The applied effective strain during ECAP was 4 at 500°C. The deformed specimen was inter-critically annealed at 730°C for 10 min. The results show that ultra-fine ferrite grain of 1 μm along with almost similar size of martensite islands. However, the major drawback of the ECAP technique is that it is not capable to produce the flat products.

2.5.3. DEFORMATION AND ANNEALING OF MARTENSITE

Ueji et al. [138] reported a process route for a plain low carbon steel in which the martensite microstructure is deformed followed by annealing to produce ultra-fine ferritic

microstructure. Ueji et al. also studied the effect of annealing temperature and deformation on the refinement of ferrite grain using this process [139]. The material was rolled with the different rolling reductions such as 25%, 50%, and 70% with different annealing temperatures. It was found that 50% rolling reduction with the annealing at 500°C for 30 min give the optimum fine grained structure and mechanical properties. Ueji et al. [138] performed another set of experiments to study the effect of annealing temperature on the final microstructure. For this purpose, the 50% cold rolled specimens were annealed in the temperatures ranging from 200°C to 700°C (annealing time: 30min). The ultra-fine equiaxed ferrite grains with the mean grain size of 180 nm were observed at the annealing temperatures ranging from 450°C-500°C, due to the recrystallization of martensite. The main merit of this process is that it does not require heavy straining. Hence, this process will be comparatively easy to adapt without any new metal working facilities for practical use.

Initially Dual phase steel was produced using the tubular vertical furnace by intercritical heat treatment [140-142]. But using this treatment, it is not possible to produce the fine grained DP steel with the improved quality. Thus, To develop the UFF grained DP steel in low carbon microalloyed steel Karmakar et al. [143] performed the thermomechanical processing using two different routes (i) intercritical deformation and (ii) warm-deformation and intercritical annealing using Gleeble 3500 with the strain rate of 1 s^{-1} up to the strain of 1.0. They observed the ferrite grain size ranging from 1.5 μm to 4 μm, along with uniformly distributed fine martensitic islands ranging from 1.5 μm to 3 μm with the volume fraction 15 to 45 pct. Karmakar et al. [144] performed two step rolling in low carbon steel with the reduction of 30 pct and 80 pct at the deformation temperatures of 1050°C and 550°C, respectively after austenitization at 1200°C for 1 h. They observed fine ferritic grains of size ranging from 2 μm to 4 μm.

2.5.4. DRX OF FERRITE

The ferrite grain refinement in the ferrite region is the possible path of grain refinement of steel during deformation. However, ferrite grain refinement due to rolling in the ferritic region of steel (warm rolling) can vary for different deformation conditions and steel chemistries. Najafi-Zadeh et al. [145] warm rolled at 850°C with the strain rate of 2 s^{-1} on the interstitial free steels and found the ferrite grain refinement of grain size of 1-2 μm due to the DRX.

2.5.5. ACCUMULATIVE ROLL BONDING (ARB)

Accumulative roll bonding (ARB) is one of the promising severe plastic deformation techniques for grain refinement. This involves the repeated application of conventional rolling and has potential for mass production. To obtain bulk material, the rolled sheets are stacked and then bonded together during rolling process. Hence, this involves simultaneous deformation and bonding. In this method, the rolled material is cut, bonded together to initial thickness and rolled again. Owing to this approach, huge strain can be applied on the material. Bulk material with ultra-fine grain can be produced by using this method [146-149].

2.5.6. DEFORMATION INDUCED FERRITE TRANSFORMATION (DIFT)

When a metal is deformed mechanically most of the energy is dissipated as heat and approximately 1% of the energy is stored as defects (mainly as dislocations) in the metal. But when the metal is hot deformed ($T > 0.6T_m$), the stored energy is also dissipated during deformation in recrystallization, recovery, and/or phase transformation.

The thermo-mechanical path to achieve the DIFT is schematically shown in figure 2.3. After austenitizing, the steel specimen is heavily undercooled and metastable austenite is present that is deformed. Generally, the deformation of steel is carried out at 25°C to 100°C above the Ar_3 i.e. the temperature where the transformation starts for the same cooling path but without the deformation. This superheat above the Ar_3 temperature is referred as ΔT in this study.

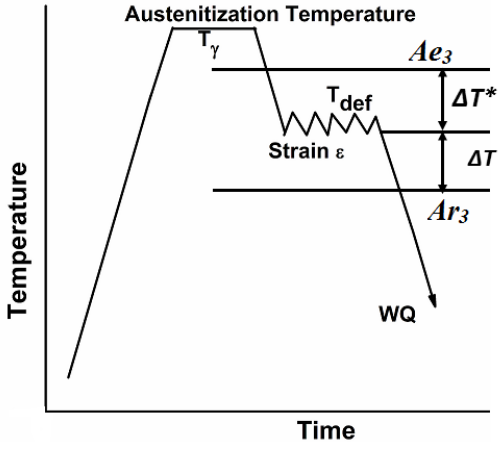

Fig. 2.3. Schematic diagram showing the procedure to obtain deformation induced ferrite transformation (DIFT).

Austenite to ferrite transformation is more beneficial as compared to the recrystallization of austenite at this high undercooling (ΔT^*). The high undercooling below the temperature Ae_3 offers sufficiently high driving pressure for ferrite nucleation. The hot deformation of steel at this temperature enhances the ferrite nucleation and results in finer ferrite grains. There are some other names used in the literature for DIFT. These are strain induced transformation (SIT), dynamic ferrite transformation (DFT), strain induced ferrite transformation (SIFT), strain induced dynamic transformation (SIDT). It is assumed that in DIFT, during the deformation the austenite to ferrite transformation, so called dynamic transformation, starts [94].

Yada et al. [150] deformed the C-Mn steel in the temperature ranging from of Ar_3+50°C to Ar_3+100°C and applied the reduction of more than 50% in less than 1 s. The results show the ferrite grain size of 2-3 μm. Niikura et al. [151] performed the deformation on low carbon Nb-microalloyed steel at 700°C up to a strain of 1.5, and obtained ferrite grain size of 1.8 μm from DIFT. Whereas, Huang et al. reported somewhat higher ferrite of grain size 3-5 μm of low carbon steel by using the same technique [32]. Though, Niikura et al. and Huang et al. used the same idea and deformed the undercooled austenite, they have not performed systematic investigation on the role of deformation temperature. Many researchers [14, 37,152] produced equiaxed ferrite grains of size 1 μm in the low carbon steel by using DIFT technique in the laboratory, however the ultra-fine ferrite layer was present only at the surface of the layer.

The ferrite nucleates within the substructures, which are formed in the work hardened austenite grains as suggested by Hurley et al. [37]. Once the ferrite was formed, it followed by deformation and dissipates the stored energy by DRX. Some researchers reported that in ferrite grain refinement, DRX plays an important role [15, 153]. However, this is not quantified in the literature.

Hodgson et al. reasoned that after deformation of the dynamically formed ferrite, it would have been elongated in shape if the DRX of ferrite had not happened [154]. But, in the final microstructure Hodgson et al. did not find any change in the aspect ratios of the ferrite grains and concluded that during the DIFT process, the DRX of ferrite also occurred.

For DIFT, high amount of deformation is required but most of the existing hot strip mills do not offer such high strains in a single pass. Therefore it is necessary to develop the new processing method to implement this technique commercially. High undercooling and high shear strain is produced at the surface due to hot rolling of thin strip and thus the ultra-fine

ferrite grains are observed only at the surface. Morimoto et al. [155] suggested an efficient way to produce the ultra-fine ferrite grained steels using asymmetric rolling which leads to DIFT. The high shear zone can be extended up to the center of the strip by using asymmetric rolling. Therefore, for industrial application of DIFT the asymmetric rolling of strip could be a feasible method. The combination of DIFT from asymmetric rolling produced the ultra-fine grained steels.

Patra et al. [156] performed hot deformation of low carbon microalloyed steel in the temperature ranging from 700°C to 1050°C after austenitizing at 1200°C for 5 minute using different routes and found the UFF with the average grain size varying from 2-3 μm.

In order to achieve the fine grained DP steel Karmakar et al. [157] performed single pass compressive deformation on low carbon microalloyed steel in the temperature range of 600°C to 900°C with the constant strain rate of 1 s^{-1} up to the true strain of 1.0. They observed the UFF grained structure of the average grain size of 3 μm.

Numerous researchers explained the necessary amount of deformation and deformation temperature which are required to introduce the DIFT in the different steel chemistries. The other processing parameters which affect the final microstructure are prior austenite grain size, strain rate, and cooling rate (from austenitization temperature to the deformation temperature).

2.5.7. ADVANTAGES OF DIFT

The asymmetric hot rolling used to produce the fine grained steel strip is an extrapolation of the thermomechanically controlled processing (TMCP) of steel. Though, the finer ferrite grains were produced by this process than TMCP of steel use of DIFT process further refined the ferrite grains. The suitable route to produce ultra-fine grained dual phase steel is the combination of DIFT and the rapid cooling of hot rolled steel. Such straight forward processing route for grain refinement is not possible by any other techniques. For example, using DRX of ferrite technique for grain refinement is possible if the working is in the ferrite phase region. To obtain the fine grained dual phase steel, the fine grained ferritic steel obtained from the DRX of ferrite was reheated to the intercritical region, followed by water quenching. In industrial application, the reheating of flat steel product intermediately is difficult. As compared to DIFT, the major drawback of the ECAP route is that the flat steel products are not processed using this process. The disadvantage of cold rolling and annealing of martensite technique over the DIFT is that the former requires the supplementary annealing step.

As the deformation induced ferrite transformation technique is used for grain refinement of studied steel, the processing parameters for DIFT and the grain refinement mechanisms in DIFT are described in the upcoming sections.

2.6. PROCESSING PARAMETERS FOR DIFT

The processing parameters that influence the DIFT are strain, strain rate, prior austenite grain size, and the deformation temperature. It is difficult to discuss the effect of one parameter on DIFT independently, because they are interrelated.

To obtain the ultra-fine ferrite (UFF) grained structure using the DIFT technique, strain is one of the most important parameter. Two strain conditions were defined by Beladi et al. [93] for DIFT. The strain required to start of the DIFT is known as critical strain of DIFT ($\varepsilon_{c,DIFT}$). But the strain required to produce the ultra-fine ferrite microstructure using DIFT technique is higher than the critical strain ($\varepsilon_{c,DIFT}$), and is known as the critical strain for ultra-fine ferrite formation ($\varepsilon_{c,UFF}$). If the imposed strains is higher than the $\varepsilon_{c,UFF}$, the obtained microstructure does not change significantly. Choi et al. reported that the rate of austenite to ferrite transformation accelerates during the deformation in terms of nucleation (i.e. transformation start) and growth [39]. Hong et al. [15] reported that with the increase in ΔT^*, the value of $\varepsilon_{c,UFF}$ decreases. This behavior is expected because with the increase in ΔT^*, the driving force for austenite to ferrite transformation increases. With the increase in strain the volume fraction of ferrite formed due to DIFT is increased for C-Mn-V steel [93].

Hickson et al. studied DIFT in different deformation modes such as rolling, torsion, and compression in C-Mn steel after austenitizing at 1250°C [152]. They found different critical strains for the formation of UFF for different modes of deformation. In rolling, to form complete UFF structure at the surface of the rolled sheet, the required nominal strain of 0.3 and 0.4 was sufficient (ε_{VM} for rolling $= \frac{2}{\sqrt{3}}$ nominal strain = 0.35 and 0.45, where ε_{VM} is the Von Mises equivalent strain). To form ultra-fine ferritic structure using torsion test, a Von Mises equivalent strain of 3 was inadequate. In compression test, to form large volume fraction of UFF, even a Von Mises equivalent strain of 0.5 was not sufficient. However, to form the UFF using torsion and compression tests Hickson et al. did not mention the required strains. The strain in the surface layer was up to 2.8 times higher than the nominal strain as observed by the

finite element modeling for rolling. This might be the reason for the formation of UFF microstructure at the surface.

The effect of strain rate on DIFT for C-Mn-V steel was studied by Beladi et al. [93]. They reported that the mean ferrite grain size was increased together with decrease in polygonal ferrite fraction as the strain rate was lowered from 1 s^{-1} to 0.1 s^{-1}. They observed the ferrite grains contain a number of sub-grains at the lower strain rate. At higher strain rate, the time between the finish of deformation and the start of quench plays an important role. There are contradictory views regarding the effect of prior austenite grain size on DIFT. Larger prior austenite grains have less potential for DIFT as compared to the finer prior austenite grain size [92, 93]. However, Hurley et al. reported that the formation of grain boundary pro-eutectoid ferrite was suppressed by the larger prior austenite grains and hence it promotes DIFT [37].

The deformation temperature was selected in between Ae_3 and Ar_3 by Beladi et al. and Hurley et al. But there was no specific relation with Ar_3 and the deformation temperature, for selecting these deformation temperatures [37, 92, 93]. However several researchers used the deformation temperatures which were having the relation with the Ar_3. For example, the deformation temperature Ar_3+10°C were used by the Hong et al. [87].

To characterize the effect of pre-deformation cooling rate on DIFT, Hong et al. performed a systematic study [15]. They reported that with increasing the pre-deformation cooling rate, the Ar_3 temperature decreases. Additionally, with the decrease in Ar_3 temperature the deformation temperature also decreases accordingly. They observed the finer ferrite grains (2 µm in size) for the faster pre-deformation cooling rate (5°Cs^{-1} and 10°Cs^{-1}) as compared to lower cooling rates (0.5°Cs^{-1} and 2°Cs^{-1}) with the same 20% compressive reduction. This statement is also supported and discussed by Xiao et al. [158]. As the amount of deformation increases, the influence of cooling rate on the final microstructure became negligible. The similar final microstructure in terms of grain size and ferrite fraction was observed for all cooling rates when the specimen was 70% deformed. Since, the cooling rate affects the Ar_3 which in turn affects the deformation temperature; hence it is difficult to separate the effect of deformation temperature from the effect of pre-deformation cooling rate.

The prior austenite grain size and the alloying elements influence the Ar_3 temperature which also affects the deformation temperature. The effect of Nb on Ar_3 temperature was studied by Hong et al. [87]. They reported that with the increase in prior austenite grain size (due to the increase in reheating temperature), the Ar_3 temperature decreases. When the prior

austenite grain size was increased from 20 μm to 240 μm, the Ar_3 temperature is decreased by 20°C for the C-Mn steel. Whereas, the Ar_3 temperature is decreased by 60°C as the prior austenite grain size was increased from 20 μm to 200 μm for the Nb-steel. This is due to the fact that the amount of Nb in solution is increased with the increasing the reheat temperature, results the delay in ferrite transformation due to solute drag.

The effect of undercooling (ΔT^*) on the amount of ferrite formed by DIFT is studied by Hong et al. [15]. It is observed that the amount of ferrite increased with increasing undercooling at lower strain. They applied the maximum stain of 1.2 (i.e. 70% reduction) and the strain rate of 10 s^{-1}. However, the time gap between the end of deformation and the start of water quenching is more and this was about 1 s. Thus, after deformation a significant amount of ferrite could also form.

Beladi et al. [93] reported the influence of post deformation cooling rate on UFF formation in C-Mn-V steel. They concluded that ferrite grain refinement and $\varepsilon_{c,UFF}$ are influenced by the post deformation cooling rate. Decrease in cooling rate enhanced the $\varepsilon_{c,UFF}$ significantly. Whereas, with increasing the cooling rate, the grain refinement increased for a given strain. They suggest that for the formation of UFF microstructure the time duration between deformation and cooling, and as well as initial cooling stages in ferrite region are significant.

Different prior austenite grain sizes altered the growth of ferrite grains during post deformation cooling as reported by Beladi et al. [92]. This results in the different ferrite grain size distribution produced by DIFT due to coarse and fine austenite grains. Both the intragranular ferrite and ferrite grain boundary are coarsened in similar way results the homogeneous final ferrite grain size distribution in the case of finer prior austenite grain. But, at the austenite grain boundary, the coarsening rate of ferrite grains formation was faster as compared to that of in the austenite grain interior, in the case of coarse prior austenite grain. This gives ferrite grain size distribution more inhomogeneous as compared to fine prior austenite grain.

Hong et al. [47] deformed the V-Nb microalloyed steel up to 80% at 751°C and studied the effect of post deformation isothermal holding time. They found that both the mean ferrite grain size and ferrite volume fraction was increased with increasing the isothermal holding time. The formation of new ferrite grains during isothermal holding increases the ferrite volume fraction. Moreover, the growth of dynamically formed ferrite may increase the final ferrite

grain size and the final ferrite volume fraction. The low angle grain boundary (LAGB) fraction decreases and high angle grain boundary (HAGB) fraction increases as the isothermal holding time increases.

Similarly, Kelly et al. [153] deformed the plain carbon steel at 760°C and studied the effect of post deformation isothermal holding. They found that due to isothermal holding, the mean ferrite grain size and ferrite volume fraction was increased. Also, the fraction of LAGB's decreased due to the isothermal holding.

However, Cho et al. [159] argued that at elevated temperature, the dynamically formed ferrite grains were very stable against grain growth. They deformed the plain low carbon steel and V-microalloyed steel up to the true strain of 0.7 followed by isothermal holding at 700°C for 10 min. A mixture of fine ferrite grains (2-3 μm) and coarse ferrite grains (7-8 μm) resulted. They reported that coarse ferrite grains (7-8 μm) nucleated and grew during the isothermal holding, whereas fine ferrite grains nucleated and grew during the deformation. A detailed study to distinguish of statically and dynamically formed ferrite, and the critical strain for DIFT was not performed.

Since, all the processing parameters are interlinked to each other; therefore the systematic analysis of various processing parameters is a major challenge. Generally, large value of undercooling (ΔT^*) below Ae_3 temperature and high amount of strain enhances the DIFT. However, the strain rate and the amount of deformation are not independent parameters for DIFT. The amount of deformation to introduce DIFT is influenced by the size of the prior austenite grain.

2.7. MECHANISMS OF DIFT

2.7.1. FERRITE NUCLEATION SITE IN DEFORMED AUSTENITE

When undeformed austenite transforms to ferrite, the ferrite nucleates at typically heterogeneous nucleation sites like edges, grain corners, and surfaces [160]. But in deformed austenite, the ferrite nucleates inside the austenite grains (i.e. due to presence of microshear bands, microbands, and also high angle misorientation boundaries), and at the grain boundaries (i.e. due to pancaking and increment in grain boundary area) [161, 162]. The prior austenite grain size, mode of deformation, and amount of deformation influences the activation of intragranular ferrite nucleation sites.

Hurley et al. rolled a Ni-30% Fe alloy and a 0.095 wt % C-1.6 wt% Mn-0.22 wt% Si-0.27 wt% Mo steel at 800°C and studied the nucleation sites for DIFT using prior austenite grain size of 200 μm [162]. They reported that at the surface of the rolled strip, the highest amount of strain was achieved. Inside the austenite grain boundary micro shear bands formed, and the ferrite nucleated at their cell boundaries. The micro shear band planes are within 20° to the rolling direction. To obtain the ultra-fine ferritic microstructure using DIFT technique, the high density of the potential ferrite nucleation sites are responsible. Ferrite embryos form along the boundaries of the dislocation cells and at the cell boundary.

To predict the ferrite nucleation sites for DIFT, Suh et al. [163] deformed the Ni-30 Fe alloy in order to study the effect of strain on the final microstructure. They found that at deformation temperature of 700°C, strain rate of 10 s^{-1}, and the austenite grain size of 20 μm, the high angle misorientation boundary spacing varies with the strain. They reported that the ferrite nucleation occurred at the high angle misorientation boundary. Additionally, they reported that for austenite grain size of 20 μm and at 700°C and at the strain of 2.1, the geometric DRX occurred Unlike discontinuous DRX (DDRX), geometric DRX does not occur due to the nucleation of strain free grains. The interpenetration of serrated grain boundaries results in geometric DRX. The geometric DRX does not affect the recovered structures such as deformation bands and dislocations cells. If the geometric recrystallized structure is developed, further deformation does not change the high angle boundary spacing. Suh et al. implemented this concept in the DIFT and anticipated that as the geometrically recrystallized austenite grains approaches the smallest possible size, the finest ferrite grains are formed. The smallest size of geometrically recrystallized austenite grain is of subgrain size (0.6 μm) [163], therefore the smallest possible high angle misorientation boundary spacing will be 0.6 μm and hence smallest grain size is 0.6 μm.

The strain required at 700°C for geometric DRX in Ni-30 Fe alloy is calculated by the Suh et al. [164]. They reported that if the thickness of the deformed austenite grain is reduced to the amplitude of the grain boundary serrations, geometric DRX occurs. It is assumed that the serration amplitude of the austenite (A_s) grain boundary is 5.5 μm. Thus, for prior austenite grain size (d_γ) of 20 μm, the critical strain for geometric DRX was $\ln(A_s/d_\gamma)=1.3$.

Beladi et al. performed torsional deformation of Ni-30 Fe alloy at 700°C with the prior austenite grain size of 110 μm and studied the microstructural evolution [94]. Microshear bands

are formed within the strain of 1. The angle between the direction of macroscopic shear and the microshear bands is 45°, and it was predicted that the potential ferrite nucleation sites are microbands.

2.7.2. GROWTH OF DIFT FERRITE

The post deformation cooling rate influence the $\varepsilon_{c,UFF}$ [93]. Beladi et al. reported that with a decrease in post deformation cooling rate, the $\varepsilon_{c,UFF}$ significantly increases. This could be explained by the fact that, a substantial amount of ferrite forms after deformation for the slower cooling rate. On the other hand, the time available for austenite to ferrite transformation is less because of the faster cooling rate. Therefore, the $\varepsilon_{c,UFF}$ is higher for the higher post deformation cooling rate as a substantial amount of ferrite has to be formed during deformation. To determine the amount of dynamically ferrite formed during DIFT, Cho et al. [159] suggested a simple procedure. They assumed that strain energy had not considerably influenced the equilibrium fraction of each phase. They suggested that the ferrite formed dynamically during deformation is deduced as the dilations between deformed and undeformed specimens during isothermal holding. They found that during deformation at 700°C about 60 pct ferrite was formed. Additionally, they reported that after deformation the transformation rate of the remaining austenite was accelerated as compared to that of undeformed austenite. However, various researchers reported that ferrite was not formed from austenite during post deformation treatment but it formed dynamically [23, 165]. The stored energy of the work hardened austenite enhances the austenite to ferrite driving force [166, 167]. However, Beladi et al. argued that there is insignificant effect of deformation on the diffusion of elements and the free energy of austenite to ferrite transformation [94].

2.7.3. DRX OF AUSTENITE VS. DIFT

Choi et al. argued that DRX and DIFT both are dynamic softening mechanisms of deformed austenite, therefore these are similar phenomenon [39]. Thus, to determine the critical strain for DIFT, they used the method developed by Poliak et al. [168] for DRX. This method is based on the principles of non-equilibrium of thermodynamics and analyzed the onset of the DRX in terms of kinetics and thermodynamics. Two conditions are required for the initiation of DRX. These are minimum dissipation rate and local maximum stored energy. Choi et al. used this approach and determined the critical strain for DRX/DIFT of austenite using

their stress-strain data [39]. Figure 2.4 shows the change of critical strain as a function of temperature for DIFT or DRX of austenite using the results of microstructural investigations. In this figure the open symbols represents the DRX of austenite, half solid symbols represents the DIFT after ferrite transformation starts, and the solid symbols indicates the DIFT

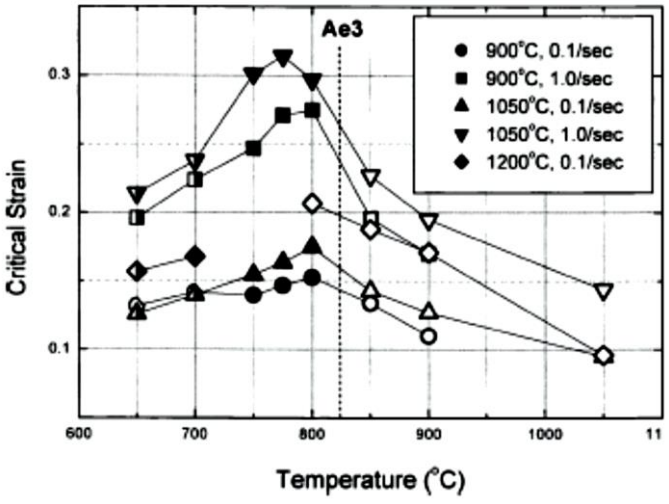

Fig. 2.4. Change of critical strain for DIFT (or DRX of austenite) as a function of deformation temperature. Results of microstructural investigation are indicated: open marks-DRX of austenite, half solid marks- DIFT after ferrite transformation start, and solid marks- DIFT [39].

It is seen from the figure 2.4 that DIFT takes place below the Ae_3 temperature in preference to the DRX of austenite (except for T_γ of 1200°C and strain rate of 0.1 s^{-1}). With decreasing temperature the critical strain for DIFT decreases. Further, with decreasing the austenitization temperature, the critical strain for DIFT also decreases. Whereas, with increasing the strain rate the critical strain significantly increases. Also, with increasing the Zener-Hollomon parameter the critical strain for DRX of austenite increases. The temperature has an opposite effect for DIFT, i.e. at a constant strain rate as the temperature decreases the Zener-Hollomon parameter increases, but the critical strain for DIFT is decreases with the temperature.

2.7.4. EFFECT OF MICROALLOYING ELEMENTS ON DIFT

Although by using suitable processing parameters, DIFT is observed in all steel chemistries, but different alloying elements have some interesting effects on DIFT. For example, in the case of the Nb-microalloyed steel, effect of Nb on the DIFT varies depending

upon whether it is in the form of precipitates (NbC) or it is in the solution [87]. DIFT was hardly observed even after 80% reduction, when the Nb is in the form of solution. This was due to the retarding effect of Nb on austenite to ferrite transformation. The DIFT kinetics was similar to that of plain carbon steel if the Nb was present in the form of precipitate. However, the observed ferrite grain size was smaller than that of plain carbon steel. Hutchinson et al. studied the effects of NbC precipitates in the austenite and Nb in solid solution in austenite on the delay of austenite recrystallization during the hot working of steel [169]. For retarding the recrystallization of austenite the fine NbC precipitates (2-10 nm in size) were more effective as compared to the solute drag for most of the conventional hot working temperatures (i.e. > 900°C). Whereas, the solute drag was more effective to retard the austenite recrystallization than the NbC precipitates at the low temperatures (i.e < 900°C) [169]. Thus, when the austenite has deformed at low temperature to achieve the DIFT, NbC precipitates are chosen over Nb in solid solution in austenite. This does not affect the austenite to ferrite transformation and at the same time retards the recrystallization of austenite. Medina performed hot torsion test after austenitizing at 1230°C for 10 min with strain rate of 3.63 s^{-1} and reported that dissolved Nb delays the recrystallization kinetics and also increases the activation energy as compared to the plain carbon steel [170]. The effect of V addition in DIFT was studied by Cho et al. and reported that the DIFT is enhanced by the addition of V on low carbon steel, this is due to the presence of V(C,N) particles [159]. Hickson et al. studied the effect of microalloying chemistry with Mo, B low carbon steel microalloyed steel on DIFT. They reported that the ultrafine ferrite formation was not enhanced by the austenite stabilizers like Mo and B [171].

2.8. RESEARCH GAP

The following research gaps which were found after the vast literature review.

1. Many literatures was found on the hot compression tests of plain carbon and microalloyed steel but the systematic treatment of hot deformation especially at high strain rates is lacking.
2. Literatures of the hot deformation were lacking in which were used wide range of processing parameters (deformation temperature, strain rate) and discussed them.
3. Researchers discussed the hot deformation processing maps using different models but they are not compared.
4. The flow localization parameter, α is not used and discussed for the steel, it was only discussed for non-ferrous alloys.
5. No literature was found in which the Zener-Hollomon parameter, Z is compared with the processing map and flow curves.
6. Researchers did the grain refinement using DIFT, but no one take the help from processing map to work in safe workable region, so that the final product will be defect free and long lasting. This will be beneficial for the industry.

2.9. PROBLEM FORMULATION

The present work is mainly concerned with the thermo-mechanical processing of plain low carbon and microalloyed steels. The aim of hot working of the plain low carbon steel and low carbon Nb-Ti microalloyed steel is to establish the better understanding of the material behavior, metallographic structure, and the safe working zone. Such understanding is necessary for users and metal workers, which will help to develop the good materials products and will increase the scope of application.

By conducting the uniaxial isothermal compression experiments the workability of the selected materials has been investigated using the data obtained from the uniaxial compression tests. Based on the flow curves, constitutive equations have been determined. The dynamic materials model (DMM) and modified DMM with various instability parameters available in the literature are used to determine the optimum processing conditions in terms of temperature and strain rate. The specific objectives of this research of the hot deformation section are as follows:

(1) To establish the hot deformation behavior and study the microstructural evolution of the selected materials over a wide range of deformation temperatures and strain rates.

(2) To plot the processing maps using the DMM and modified DMM approach with different instability parameters viz. instability parameter given by the Prasad et al., instability parameter of Murty and Rao, and the instability parameter approach of Poletti et al.

(3) To describe accurately the flow behavior over a wide range of temperatures and strain rates constitutive equations are developed and the microstructural mechanism of deformation are identified.

(4) Using the processing maps, the safe and unsafe region of workability is determined and verified with the microstructural study.

(5) Zener-Hollomon parameter Z is plotted as a function of deformation temperatures and strain rates, and is related with the flow curves and microstructural evolution.

Based on the results of hot deformation experiments, a processing schedule can be defined for optimum grain refinement by using thermomechanical treatment in the safe workability region.

In order to produce fine grained steel structure a potential processing route is studied in this section of the research work. DIFT method is used to achieve ferrite grain refinement. The effect of different processing parameters such as strain, deformation temperature, and austenitization temperatures on DIFT is studied in the plain low carbon AISI 1010 steel and low carbon Ti-Nb microalloyed steel.

Chapter 3

MATERIALS & EXPERIMENTAL METHODOLOGY

In this chapter the experimental methodology used in the present investigation is discussed in detail. The experimental work involved a series of laboratory hot compression tests of plain low carbon steels and low carbon Nb-Ti microalloyed steel at elevated temperatures using different processing variables. The experimental materials, procedures, microstructural characterization, and equipments used to perform the experiments are explained.

3.1. PROCUREMENT OF THE EXPERIMENTAL MATERIALS

The plain low carbon steel AISI 1016 and low carbon Nb-Ti microalloyed steel were procured in the form of bars of thickness 30 mm and 20 mm, respectively from the Steel Authority of India (SAIL). Another plain low carbon AISI 1010 steel is procured in the form of a rod having 12.5 mm diameter. The chemical compositions of these steels as determined from Thermo-Jarrell Ash spark emission spectroscope are given in the Tables 3.1.

Table 3.1. Chemical composition (in wt %) of different steels used in the present work.

Elements	C	Mn	Si	P	S	Fe
AISI 1010 steel	0.09	0.32	0.073	0.019	0.012	Balance
AISI 1016 steel	0.15	0.87	0.21	0.024	0.012	Balance

	C	Mn	Si	P	S	Nb	Ti	Fe
Nb-Ti microalloyed steel	0.13	1.52	0.28	0.028	0.009	0.05	0.052	Balance

3.2. SPECIMEN PREPARATIONS

Specimens for the hot compression testing and dilatometry were machined from the steel bars and rods by cutting and turning operations with the help of a lathe machine. The

dimensions of the compression specimen were 10 mm in diameter and 15 mm in length as shown in figure 3.1. The aspect ratio was 1.5, in order to promote the homogeneous deformation without buckling. The dimension of the dilatometry specimen was 10 mm in diameter and 85 mm in length.

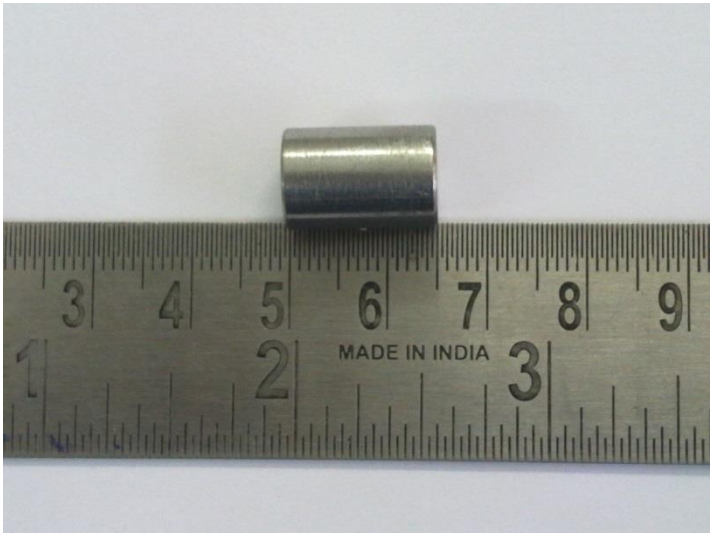

Fig.3.1. Geometry and dimensions of the steel specimens used for compression tests.

3.3. EXPERIMENTAL PROCEDURE

In this section, a general description of the experimental methods and equipments used for dilatometry and uniaxial compression tests is given.

3.3.1. DILATOMETRY TEST

To define the phase fields for each material and also to provide the basis for selecting the deformation temperatures for hot compression tests, the dilatometry tests were conducted with the help of CCT dilatometer with LVDT (Figure 3.2) in the thermomechanical simulator Gleeble® 3800. K-type thermocouple was welded at the mid span of the specimen to measure temperature variations. For dilatometric measurement, the specimen was heated at the heating rate of $5°Cs^{-1}$ upto the austenitizing temperature. This is used to determine the Ac_1 and Ac_3 temperatures of the respective steel. The austenitization time was 5 min for plain low carbon steel (AISI 1010 and AISI 1016), and 2 min for low carbon Nb-Ti microalloyed steel. The specimen further cooled to the room temperature at the cooling rate of $1°Cs^{-1}$. The Ar_1 and Ar_3 temperatures were measured in the cooling path, so it also called continuous cooling

transformation (CCT). Phase transformation in the respective steel can be detected by accurately measuring the small changes in the diameter of the specimen, due to the phase transformation. Then a plot of change in length versus temperature is produced which shows all the critical temperatures. The complete measuring head was enclosed in the chamber under the vacuum, during the operation.

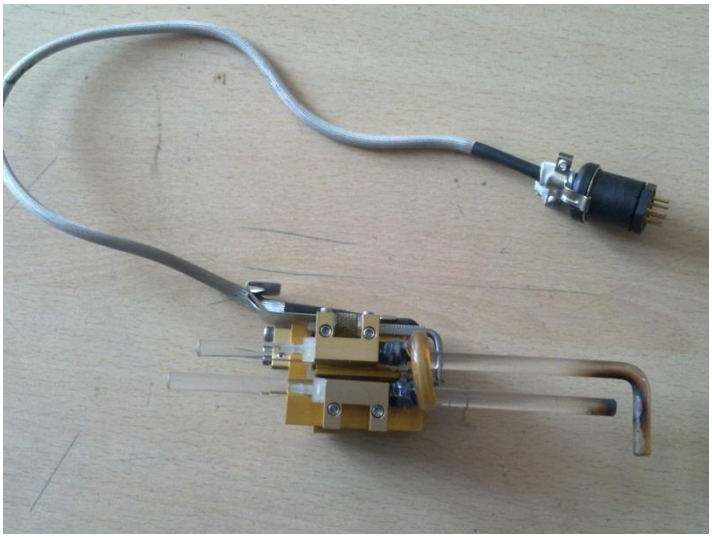

Fig.3.2. External view of the CCT dilatometer with LVDT.

The phase transformation temperatures Ar_3 and Ar_1 were also determined from the continuous cooling compression (CCC) curve with the help of Gleeble® 3800. The CCC test was used to determine the austenite to ferrite transformation temperature (Ar_3) at a given strain rate during cooling to observe the effect of plastic deformation [47,172]. The specimen of 10 mm diameter and 15 mm length was heated with heating rate of $5°Cs^{-1}$ to austenization temperature of 1050°C for 5 min in the Gleeble® 3800, followed by cooling at the rate of $1°Cs^{-1}$ to 1000°C. Further, the specimen was cooled from 1000°C to 500°C along with continuous compression at the constant strain rate of 10^{-3} s^{-1}. The Ar_3 and Ar_1 temperatures are represented by the first and second deviation points in the CCC curve.

3.3.2. UNIAXIAL COMPRESSION TEST

Uniaxial compression or upset test is the most common and simplest test to determine the workability. The hot compression tests were carried out in Gleeble® 3800 under vacuum (pressure of 1Pa). A K-type thermocouple was spot welded in mid span of the specimen to

control the temperature during the experiment. A nickel based lubricant and a 5 mil thick graphite foil were used between the sample and the ISO-T anvil to reduce both the temperature gradient and the friction. All the specimens were heated up to the austenitization temperature with the heating rate of $5°Cs^{-1}$ and soaked for 5 or 2 minutes. They were then cooled down at $1°Cs^{-1}$ to each compression test temperature in the range of 750°C-1050°C, at increments of 50°C. The specimens of AISI 1016 and low carbon Nb-Ti microalloyed steel were deformed at constant strain rates of 0.01 s^{-1}, 0.1 s^{-1}, 1 s^{-1}, 10 s^{-1} and 80 s^{-1}, whereas the specimens of AISI 1010 steel were deformed at the constant strain rates of 0.01 s^{-1}, 0.1 s^{-1}, 1 s^{-1}, 10 s^{-1} and 20 s^{-1} up to a total logarithmic deformation (true strain) of 0.7. Finally, in-situ water quenching was employed to freeze the microstructure and avoid any metadynamic or static phenomena that could occur after hot deformation.

True strain for compressive deformation is defined by equation 3.1.

$$\varepsilon = \ln\left(\frac{h_o}{h_i}\right) \qquad (3.1)$$

where h_i is the instantaneous height of the specimen and h_o is the initial height of the specimen.

3.3.3. GLEEBLE® 3800 TESTING SYSTEM

The thermomechanical simulator Gleeble® 3800 is a testing machine which can work even at the high temperature and high strain rate that can be used to study the behavior of material under hot working conditions. The external view of the thermomechanical simulator Gleeble® 3800 is shown in figure 3.3a. It consists of: (a) the main control console, (b) the testing unit, (c) the hydraulic power unit, and (d) the vacuum pump unit. The schematic representation of the compression testing chamber is shown in figure 3.3b.

A K-type thermocouple is spot welded on the mid span of the specimen to provide accurate temperature measurement and control by a closed loop feedback system during the experiments. The specimen is resistance heated by the flow of alternating current. The heat is extracted from the specimen by radiation and conduction with the water-cooled jaws and the specimen ends, and the temperature of the specimen is balanced by heat input by electrical resistance. Graphite foil of 5 mil thickness was placed between the ISO-T anvils and the specimen to avoid welding and to reduce the thermal gradient and friction during the test.

(a)

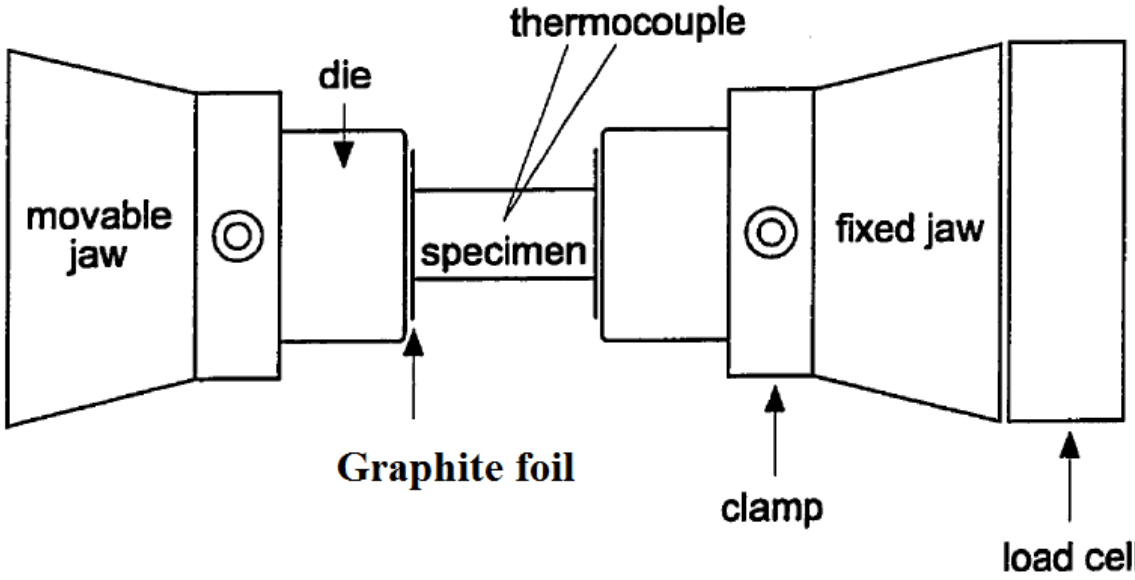

(b)

Fig. 3.3. (a) External view of thermomechanical simulator Gleeble® 3800, and (b) schematic diagram of compression testing chamber.

The force and displacement are generated by the hydraulic actuator which is measured by the load cell and a linear voltage differential transducer (LVDT), respectively. According to the amount of applied force, the load cell provides an output voltage of a proportional magnitude. The LVDT is attached in the base of the actuator and the movable core is positioned by the piston of the actuator. As the piston is displaced from its mid stroke position

the output voltage increases linearly. The stroke (closed loop mechanical displacement control system) provides the capability to provide the constant strain rate deformation during the compression. The LVDT and load cell are accurate to ± 0.25% of the full scale. In the present study, the load cell of 50kN capacity was used. The gauge length of the LVDT is 100 mm.

The specimen is placed between the fixed and the movable jaw. The movable jaw is operated by an integrated, hydraulic-pneumatic system. All processing parameters are controlled by the computer program with the help of the QuickSim. The compatible computer collects the processing data at the real time. The data acquisition rate was so selected that 1000-4000 data points were recorded during each test.

3.4. MICROSTRUCTURAL CHARACTERIZATION

Microstructural characterization of metals using various techniques has been an inevitable tool to observe the advancement of material science for more than a century. The microstructure of metals affected by numerous processing conditions is revealed by various metallography techniques. In the present work, the microstructural evolution after hot working using different sets of processing parameters was studied using light optical microscopy (LOM), scanning electron microscopy (SEM), electron backscattered diffraction (EBSD).

(a) OPTICAL MICROSCOPY

Optical microscopy was used to characterize the microstructure of the studied materials in the as-received condition and before and after the deformation. A properly prepared specimen may provide an accurate interpretation of a microstructure. The small section of the material has to fulfill the following criteria to obtain a properly prepared surface for the metallographic study.

(1) All the non-metallic inclusions should be intact with the section.

(2) The section must be flat and free from stains, scratches, and other imperfections which tend to ruin the surface.

(3) Section must be free from all traces of the disturbed metal.

(4) Galling or chipping of the hard and brittle intermetallic compounds should not show on the section.

A Leica DMI 5000M microscope was used for light optical microscopy (Figure 3.4). The

amount of different phases was determined using Material Plus 4.1 image analysis software. The sample preparation consists of the conventional metallographic polishing procedures. It consists of the following steps:

(i) SECTIONING

The hot deformed specimens were cut from the center along the compression axis using high speed diamond saw "IsoMet 4000" (Figure 3.5) to observe the microstructure at the center. The sectioned specimen was embedded in resin for metallographic preparation.

(ii) GRINDING OR PRE-POLISHING

Grinding or pre-polishing is required to prepare the embedded specimen flat and also to remove the strained surface formed during the sectioning process. It consisted of a sequence of polishing on P120, P320, and P600 grit SiC polishing papers. The specimen was rotated 90° after polishing on each paper.

(iii) PAPER POLISHING

After getting the strain free flat surface from the pre-polishing step, the embedded specimen was paper polished using P800, P1200, P1500, and finally P2000 polishing papers. The specimen was rotated through 90° and washed with cold water after polishing on each paper.

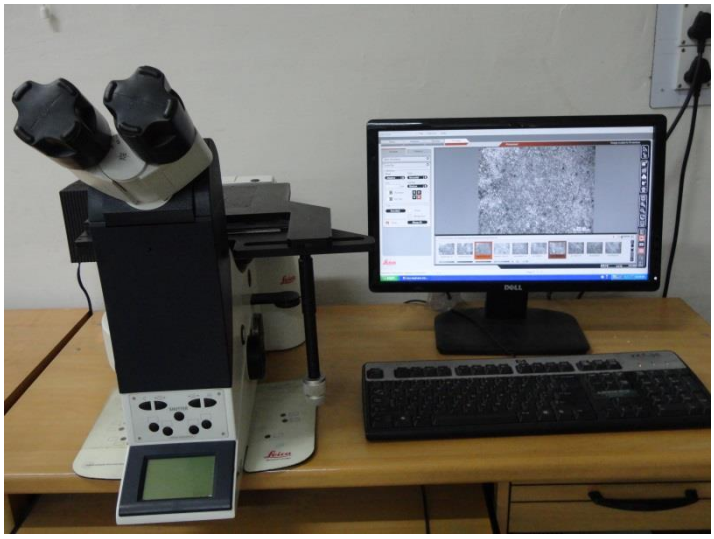

Fig. 3.4. Leica DMI 5000M light optical microscope.

Fig. 3.5. High speed diamond saw "IsoMet 4000".

(iv) CLOTH POLISHING

After paper polishing, the embedded specimen was cloth polished using the lavigated alumina grade-I of size 0.014 µm on the fine valvet cloth until the paper scratches disappeared.

(v) CLEANING AND DRYING

To prevent contamination between the each stage of preparation, running cold water and/or acetone were used as per the requirement for cleaning the specimens. Proper drying the specimen after cleaning is very necessary to prevent the corrosion or stains.

(vi) ETCHING

The properly prepared specimens were etched with the 2% nital solution to reveal the microstructure. Etched specimens were air dried quickly to prevent corrosion or staining.

(b) **SEM**

A EVO18 Zeiss scanning electron microscope (SEM) equipped with the LaB6 filament was used to examine the microstructural features of the hot deformed specimens of each steel. Some of the hot deformed specimens were analyzed using the EBSD (electron back scatter diffraction) technique. In the present study, EBSD analysis was performed using HKL channel 5 system software with the help of EVO18 Zeiss scanning electron microscope (Figure 3.6). The beam of electrons is directed at a point of interest on a 70° tilted crystalline sample in the SEM for the EBSD measurements (Figure 3.7). The mechanism by which the diffraction

patterns are formed is complex, but the following model describes the principal features. It satisfy the Bragg law (equation 3.2).

$$2d \sin\theta = n\lambda \tag{3.2}$$

where d is the spacing of the diffracting plane, n is an integer, λ is the wavelength of the electrons, and θ is the angle of incident electrons on the diffracting plane.

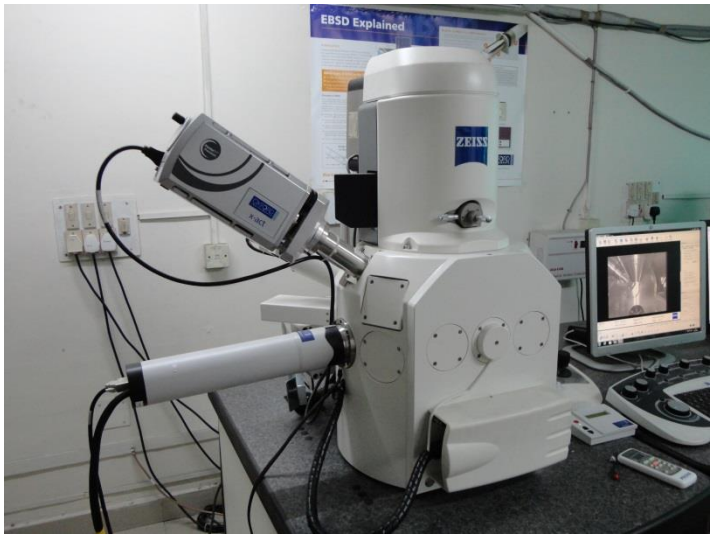

Fig. 3.6. EVO18 Zeiss scanning electron microscope (SEM)

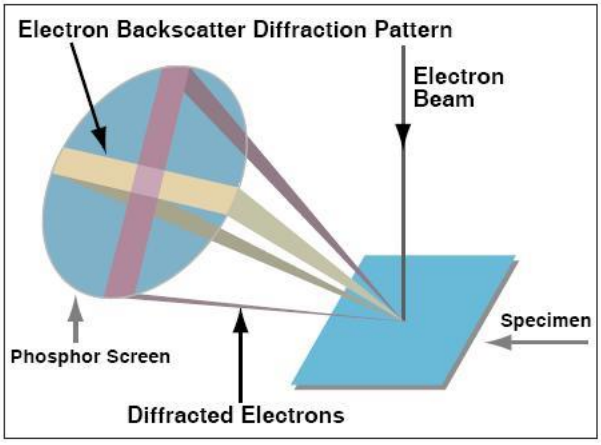

Fig.3.7. Schematic of Scanning Electron Back Scattered Diffraction Pattern [173].

A set of paired large angle cones are formed by diffraction of these electrons corresponding to each diffracting planes. When it is used to form an image on the fluorescent

screen, the characteristic Kikuchi bands of the electron backscatter diffraction pattern are produced by the regions of the enhanced electron intensity between the cones (Figure 3.8).

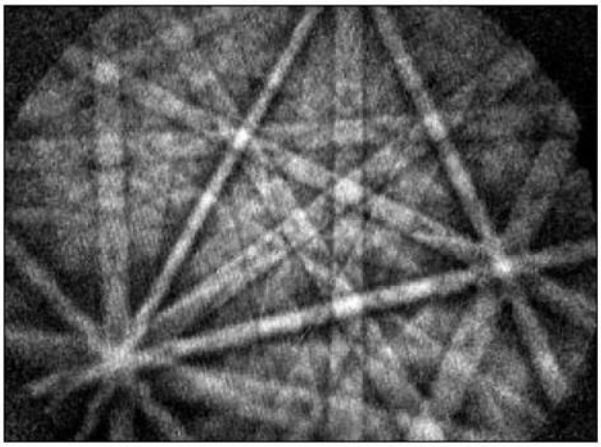

Fig.3.8. Characteristic Kikuchi bands of the electron backscatter diffraction pattern [173].

EBSD is the surface characterization technique because the diffraction pattern signal is coming from the few nanometers of depth. Therefore the sample preparation for the EBSD analysis is very critical. The EBSD pattern will be worsen/ prevent if there are any damages of the crystal lattice in the specimen surface layer. The surface which is parallel to the compression axis of the hot deformed specimen of all steels was analyzed. The preparation steps for SEM and EBSD specimens consisted of conventional mechanical polishing as discussed above for the light optical microscopy followed by either electropolishing or polishing in final step with 0.05 μm colloidal silica suspension (OPS) for 30 min duration. The specimens were electropolished in an electrolyte of 20% perchloric acid in methanol at -40°C using 21V for 50 s. The step size used for the EBSD analysis was 0.5μm for AISI 1010 steel and low carbon Ti-Nb microalloyed steel. Whereas in the case of AISI 1016 steel the analyzed region was about 150 mm 100 mm, and the step size was 0.15 mm.

3.5. PRIOR AUSTENITE GRAIN SIZE

The prior austenite grain size of plain low carbon steel (AISI 1010) and low carbon Nb-Ti microalloyed steel were determined by heating the specimen at a rate of $5°Cs^{-1}$ to the different austenitization temperature (i.e. 950°C and 1050°C) and isothermally holding for 10 s, 60 s and 120 s, followed by water quenching to room temperature. The specimen used for this test is of 10 mm diameter and 15 mm in length. The specimens were cut perpendicular to their

length where the thermocouples were welded, for the metallographic observations. Saturated picric acid was used to reveal the prior austenite grain boundary of both the materials. Grain size was determined by linear intercept method

3.6. DEFORMATION INDUCED FERRITE TRANSFORMATION (DIFT) TESTS

The optimum factors/thermo mechanical conditions for finer deformation induced ferrite (DIF) formation was investigated. These factors are prior austenite grain size, amount of strain, and applied strain rate. To study the effect of these factors, two steps simulated deformation were performed at different temperatures. All specimens were heated to the austenitization temperature (T_γ) at the heating rate of $5°Cs^{-1}$ and isothermally held for 10 s, 60 s, and 120 s followed by cooling at the rate of $1°Cs^{-1}$ to the first deformation temperature (T_{def1}), and same cooling rate was followed to attain the second deformation temperature (T_{def2}). At T_{def1}, the amount of true strain was either 0.6 or 1.0 followed by second step deformation at T_{def2} where the amount of true strain was either 0.8 or 0.4, respectively as shown in figure 3.9. Therefore, the total amount of true strain applied in each compression experiment was 1.4. For all these deformation experiments, the strain rate was $1\ s^{-1}$. After the two-step deformation, specimens were in-situ water quenched immediately after the deformation in order to retain and observe the DIF microstructure. The following designations are used for specimens prepared with the processing conditions as mentioned.

(i) Plain low carbon steel (AISI 1010)

S1: $T_{def1} = 875°C$, $\varepsilon_1 = 1.0$; $T_{def2} = 825°C$, $\varepsilon_2 = 0.4$;

S2: $T_{def1} = 875°C$, $\varepsilon_1 = 0.6$; $T_{def2} = 825°C$, $\varepsilon_2 = 0.8$;

S3: $T_{def1} = 875°C$, $\varepsilon_1 = 1.0$; $T_{def2} = 840°C$, $\varepsilon_2 = 0.4$;

S4: $T_{def1} = 875°C$, $\varepsilon_1 = 0.6$; $T_{def2} = 840°C$, $\varepsilon_2 = 0.8$;

(ii) Low carbon Nb-Ti micro-alloyed steel

M1: $T_{def1} = 850°C$, $\varepsilon_1 = 0.6$; $T_{def2} = 760°C$, $\varepsilon_2 = 0.8$;

M2: $T_{def1} = 850°C$, $\varepsilon_1 = 0.6$; $T_{def2} = 790°C$, $\varepsilon_2 = 0.8$;

M3: $T_{def1} = 875°C$, $\varepsilon_1 = 0.6$; $T_{def2} = 760°C$, $\varepsilon_2 = 0.8$;

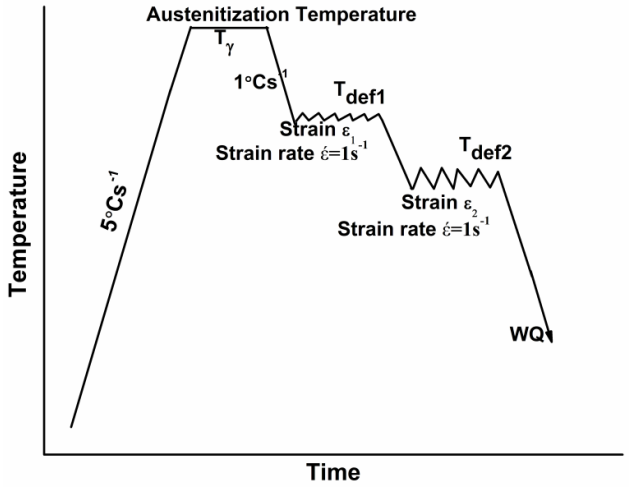

Fig. 3.9. Schematic diagram of DIFT test procedure.

3.7. MEASUREMENT OF MECHANICAL PROPERTIES

HARDNESS TESTS

Vickers hardness tests were performed to determine macro-hardness of specimen using FIE-VM50PC Vickers hardness tester by employing 10 kg load with dwell time of 10 s. The image of the hardness impression is captured on the computer screen and its diagonals were measured with the help of Vickey's^{TM} software to obtain the hardness values. Whereas, the micro-hardness tests were performed by means of VMH 104 Microhardness Tester (figure 3.10) at 10 g load using Vickers indenter, in order to verify phases such as ferrite and martensite. At least ten readings were taken and the average is reported in both the hardness tests.

Fig. 3.10. VMH 104 Microhardness Tester.

Chapter 4

THEORY AND ALALYSIS

4.1. PROCESSING MAPS

Processing maps are shown in the processing space i.e. on the axes of temperature and strain rate for a given strain. The first processing maps were developed by Ashby [8]. Lately, processing maps were conceived by Prasad et al. [10] based on the dynamic materials model (DMM), and consist of two superimposed maps i.e. the efficiency map and the instability map, at constant strain. Under this model it is stated that good hot workability is represented by a high value of dissipation efficiency and no instability.

Prasad et al. developed processing maps using the DMM, in which no storage of energy in the material is assumed [10, 174]. Murty and Rao [12, 175, 176] modified the calculation of the energy efficiency as well as the instability parameters based in the same DMM. Generally it is accepted that the power P given to a viscoplastic material during plastic deformation is expressed by the multiplication of stress times the strain rate. Prasad assumed additionally, that this power P at a given temperature T and strain ε can be separated into two contributions: G, the power dissipated by plastic work and J, the power dissipated by microstructural changes. In the DMM this separation can be expressed as [176]:

$$P_{T,\varepsilon} = G + J = \sigma\dot{\varepsilon} = \int_0^{\dot{\varepsilon}} \sigma d\dot{\varepsilon} + \int_0^{\sigma} \dot{\varepsilon} d\sigma \qquad (4.1)$$

σ and $\dot{\varepsilon}$ are the flow stress and the strain rate, respectively.

The schematic representation of stress-strain rate curve for a given strain and temperature showing the areas corresponding to G and J, as shown in figure 4.1. The area of the rectangle ($\sigma\dot{\varepsilon}$) represents the total power (P) absorbed by the workpiece material, where σ is the flow stress of the workpiece material, and $\dot{\varepsilon}$ is the applied strain rate. This partition of the input power is similar to that stated by Malvern [177] for elastic deformation which was explicitly not recommended for plastic deformations. Based on this power partition, two parameters were described: the efficiency of power dissipation η and the instability parameter ξ.

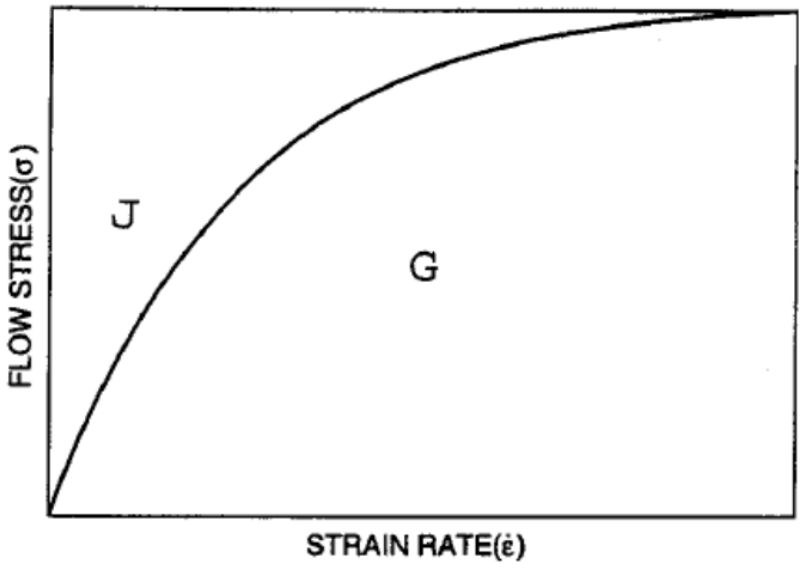

Fig. 4.1. Schematic representation of stress-strain rate curve showing the area corresponding to *G* and *J*.

The efficiency of power dissipation η, is defined as [10] and used by [178, 179]. The ratio of *J* and the maximal *J* possible, given by a linear dissipator:

$$\eta = \frac{J}{J_{\max}} = \frac{2J}{P} = \frac{2m}{m+1} \tag{4.2}$$

In previous works, the meaning of the value η was discussed and compared with the strain rate sensitivity *m* and the stress exponent *n*. It was found that all these values are high when describing diffusion controlled phenomena, such as recrystallization by grain boundary movement, recovery by climbing and gliding of dislocations, and phase transformation. Murty and Rao [12] proposed a modification that is known as the modified DMM to avoid the use of the strain rate sensitivity in the calculation of the efficiency of power dissipation. This model was shown to give useful results for multiphase materials.

In the modified DMM, η is calculated as [12]:

$$\eta = \frac{2(P-G)}{P} \tag{4.3}$$

with

$$\eta = \frac{2\left(\sigma\dot{\varepsilon} - \left(\left[\frac{\sigma\dot{\varepsilon}}{m+1}\right]_{\dot{\varepsilon}=\dot{\varepsilon}_{\min}} + \int_{\dot{\varepsilon}_{\min}}^{\dot{\varepsilon}} \sigma d\dot{\varepsilon}\right)\right)}{\sigma\dot{\varepsilon}} \tag{4.4}$$

where, $\dot{\varepsilon}_{\min}$ is the minimum strain rate tested, and m is the strain rate sensitivity for the lowest strain rate, defined as [10]:

$$m = \left[\frac{\partial \ln \sigma}{\partial \ln \dot{\varepsilon}}\right]_{\varepsilon,T} \tag{4.5}$$

In general, it can be stated that flow instabilities are related to flow concentrations. The approach developed by Ziegler [180] and expressed as in Equation (4.6) assumes that instability occurs when:

$$\frac{\partial D}{\partial \dot{\varepsilon}} < \frac{D}{\dot{\varepsilon}} \tag{4.6}$$

where D is the power dissipation function.

Considering equation 4.6, the flow instability can be calculated, depending on the formulation of the dissipation function:

i) $D = P$ considers that the total power is dissipated. Then, instabilities occur when $m < 0$ as derived [181] by Montheillet et al.

ii) $D = J$ considers only the dissipated power which is attributed to the microstructural changes by the partition proposed by DMM developers, as given in equation 4.1. This consideration results in different instability parameters depending on how they are calculated. These parameters are

a) as proposed by Prasad et al. [10] and also used by [182, 183].

$$\xi(\dot{\varepsilon}) = \frac{\partial \ln\left(m/m+1\right)}{\partial \ln \dot{\varepsilon}} + m < 0 \tag{4.7}$$

b) as proposed by Murty & Rao [12]

$$\kappa = \frac{2m}{\eta} - 1 < 0 \tag{4.8}$$

c) as developed by Poletti et al. [13, 184] to avoid the dependence on strain rate sensitivity *m*:

$$\kappa_j = \left(\frac{\partial \ln J}{\partial \ln \dot{\varepsilon}} - 1 \right) < 0 \tag{4.9}$$

Furthermore, the flow instability can be predicted from the mechanical point of view by using another approach as proposed in [185, 186]. Thus, the flow localization parameter α estimates the tendency of a material to form marked or catastrophic strain concentrations. This parameter is derived similarly to the one developed by Considère [187] for tension and modified by Hart [188] for viscoplastic materials. The flow localization parameter determines that flow instability that takes place beyond the force equilibrium and takes into account the influence of temperature, strain rate and strain on the stress values can be described independently. In this case, the instability parameter α, is given as follows [189].

$$\alpha = \frac{\gamma' - 1}{m} \tag{4.10}$$

Instability is predicted if α is positive (and especially for titanium alloys, if α > 5 [186]). The factor γ' is a dimensionless softening coefficient at constant strain rate, which is composed of the strain hardening and temperature as two independent terms:

$$\gamma' = \left(\frac{1}{\sigma} \frac{d\sigma}{d\varepsilon} \right)_{\dot{\varepsilon}} = \frac{\left(\frac{\partial \sigma}{\partial \varepsilon} \right)_{\dot{\varepsilon},T} d\varepsilon + \left(\frac{\partial \sigma}{\partial T} \right)_{\dot{\varepsilon},\varepsilon} dT}{\sigma d\varepsilon} \tag{4.11}$$

The two physical phenomena included in γ' induce flow instability by γ' > 1 when large softening is produced by strain and/or temperature increment meaning damage by wedge cracking and pores and by adiabatic flow, or when strain hardening is very large.

4.2. BASIC CONSTITUTIVE EQUATION

The steady state flow stress, strain rate, and temperature are interdependent and obey the kinetic rate equation of the form given in equation (4.12) [190].

$$\sigma = K\varepsilon^{n}\dot{\varepsilon}^{m} + Y \tag{4.12}$$

where *n* is the strain hardening exponent, *m* is strain rate sensitivity, *Y* and *K* are coefficients. For most metallic materials strain rate sensitivity is of little importance at room temperature. However, it is important at elevated temperatures. With decreasing temperatures the strain hardening exponent becomes more significant. The effect of temperature is not reflected by the equation 4.12. Zener-Hollomon parameter *Z* correlates well with the constitutive equations given below [13, 191, 192] at different deformation parameters. Sellars and Tegart [193] proposed a relationship which is known as universal constitutive equation that is used for a wide range of stresses. It correlates stress, temperature and strain rate in hot working (equation 4.13).

$$Z = A\sinh\left(c\sigma\right)^{n} = \dot{\varepsilon}\exp\left(\frac{Q}{RT}\right) \tag{4.13}$$

At low stresses ($c\sigma < 1$), the hot deformation behavior is described by the power creep law and is represented by equation 4.14.

$$Z_{p} = A_{p}\sigma^{n_{p}} = \dot{\varepsilon}\exp\left(\frac{Q_{p}}{RT}\right) \tag{4.14}$$

The exponential law equation (equation 4.15) is used for high stresses ($c\sigma > 1.2$).

$$Z_{E} = A_{E}\exp\left(\beta\sigma\right) = \dot{\varepsilon}\exp\left(\frac{Q_{E}}{RT}\right) \tag{4.15}$$

where, *R* is the gas constant and *Q* is the apparent activation energy. *A*, *c*, *β*, and *n* are material constants. Subscripts *P* and *E* are concerned with the power law and the exponential law, respectively. The activation energy is usually referred to as the apparent activation energy and is determined using the Arrhenius plot with a linear range, with the assumption that there is no

change in the microstructures. The stress exponent n obtained according to sinh type law is usually lower than that corresponding to the power law [194]. In the present treatment, the value of constant c is taken as equal to 0.014 MPa^{-1} in the case of plain low carbon steel and 0.012 MPa^{-1} for low carbon Ti-Nb microalloyed steel when using the sinh type equation [195].

Chapter 5

RESULTS AND DISCUSSION: HOT DEFORMATION BEHAVIOR AND PROCESSING MAPS

The objective of the present chapter is to study the hot deformation behavior of the plain low carbon steels and low carbon Ti-Nb microalloyed steel at different temperatures and strain rates using the constitutive equations. The relation among the true stress-true strain curves, the evolution of microstructure, and the processing maps are discussed. Also, the processing window that may be utilized to produce sound products is arrived at.

A. PLAIN LOW CARBON STEEL (AISI 1010)

The hot deformation behavior of plain low carbon steel AISI 1010 is covered into two sub-divisions named as (i) Results, and (ii) Discussion.

5.1. RESULTS

5.1.1. AS-RECEIVED MICROSTRUCTURE

The light optical microstructure in as-received condition of AISI 1010 is shown in figure 5.1a. It consists of two phases i.e. the light color phase is ferrite whereas pearlite (marked by the arrows) is of dark color. Figure 5.1b shows the SEM micrograph in secondary electron mode. Pearlitic areas are shown by arrows. Figure 5.1c shows the inverse pole figure (EBSD map) of the plain low carbon steel in as-received condition. The unindexed white region (shown by arrows) represents either a grain boundary region or a non-ferritic phase [79]. It shows randomly oriented mix of elongated and equiaxed grains.

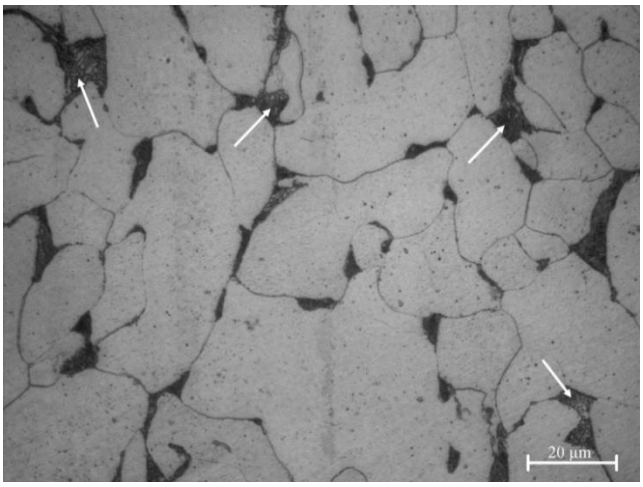

(a)

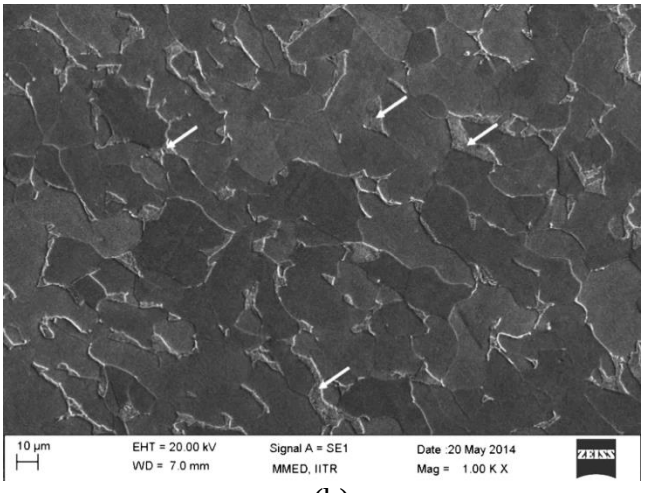

(b)

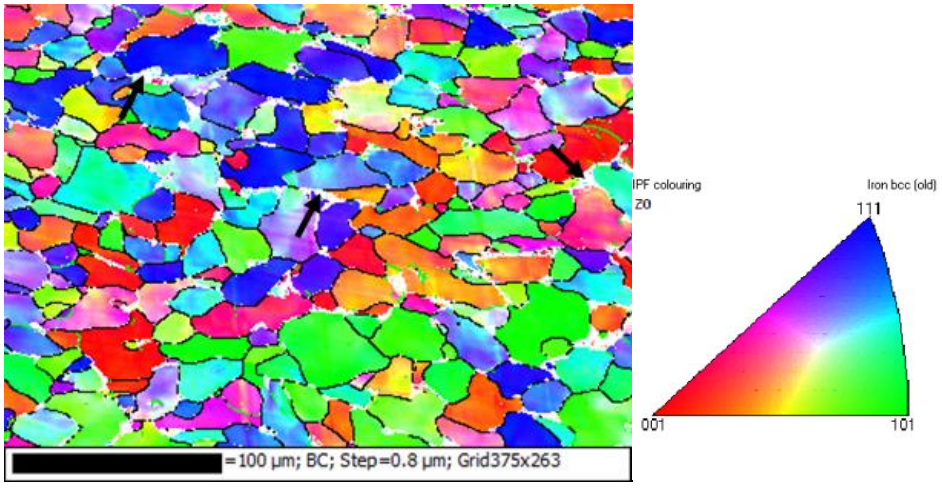

(c)

Fig. 5.1. Microstructures of as-received plain low carbon steel (AISI 1010) steel using (a) Optical microscopy (b) scanning electron microscopy (c) inverse pole figure map from EBSD. Pearlite is shown by arrows.

Microstructure of the undeformed AISI 1010 steel specimen heated up to 1050°C, soaked for 5 minutes followed by water quenching is shown in figure 5.2. It consists almost entirely of martensite, which is in agreement with its average microhardness value of 515 ± 10 VHN that is close to the value of Vickers hardness of martensite containing 0.09 wt% carbon [196]. Very small amount of ferrite is also observed at the prior austenite grain boundary (marked by arrows), which probably formed during the cooling. This is because at this level of low carbon content, the nose of the CCT curve shifts towards the left and is intercepted by the cooling curve during the cooling. In addition, the growth of grain boundary allotriomorphic ferrite is suppressed as the cooling proceeds because of shorter range of diffusion of carbon atoms and extremely retarded movement of iron atoms. Thus, Widmanstätten side plates of are nucleated and grow into austenite, which is observed in the micrograph [197].

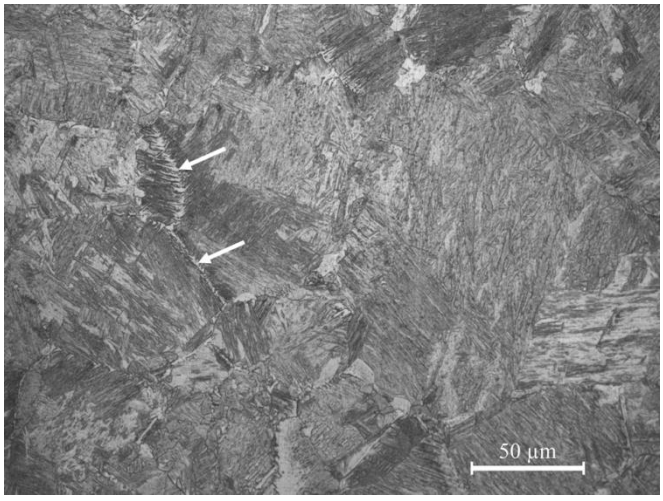

Fig. 5.2. Optical micrograph of AISI 1010 steel specimen heated up to 1050°C for 5 min followed by water quenching. Arrows show ferrite.

5.1.2. PHASE TRANSFORMATION CHARACTERIZATION

In order to analyze the phase transformations, it is necessary to determine the critical temperatures such as Ar_3 and Ar_1. Hence, for each material the Ar_3 and Ar_1 temperatures are determined from the dilatometric measurements as well as continuous cooling compression (CCC) curve obtained from the Gleeble® 3800. Figure 5.3 shows the results from the different methods used to obtain the phase transformation temperatures. The onset of phase transformation in steel is represented by the variation in the slope of the curve. The inflection points during cooling represent the Ar_1 and Ar_3 temperatures. The continuous cooling

transformation (CCT) curve is shown in figure 5.3a and the Ar_3 and Ar_1 temperatures are 791°C and 653°C, respectively. Figure 5.3b shows the compressive stress versus temperature curve obtained from CCC test and the estimated Ar_3 and Ar_1 temperatures are 828°C and 735°C, respectively.

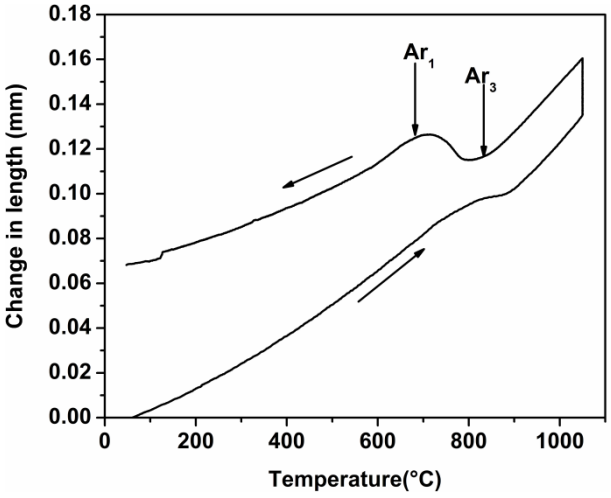

(a)

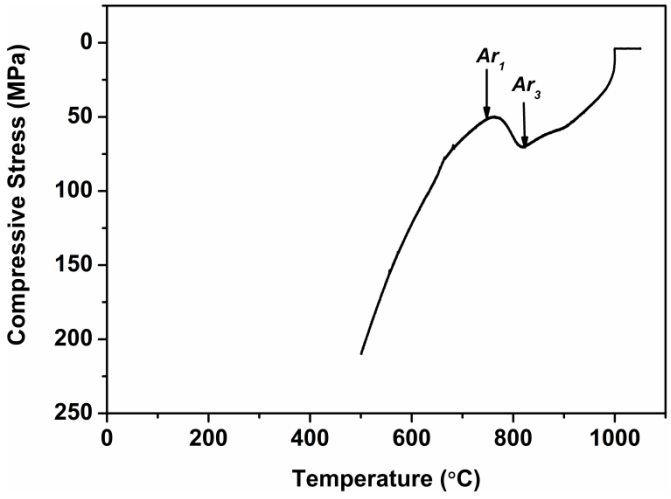

(b)

Fig. 5.3. Results of the (a) dilatometry test and (b) the continuous cooling compression test, performed on plain low carbon steel (AISI 1010). Inflection points correspond to the Ar_1 and Ar_3 temperatures.

5.1.3. TRUE STRESS-TRUE STRAIN CURVES

AISI 1010 steel specimens heated up to 1050°C, soaked for 5 minutes were compressed at different hot compression temperatures upto a true strain of 0.7. Figure 5.4 shows the flow curves corresponding to the test temperatures ranging from 750°C to 1050°C at intervals of 50°C using the true strain rates of 0.01, 0.1, 1, 10, and 20 s^{-1}. The true flow stress showed a dependence on the strain rate and temperature. For a fixed strain rate, as the temperature increased, the values of flow stress progressively decreased. The flow stress-strain curves (750°C at strain rate of 0.01 s^{-1}, 800°C-850°C at strain rates of 0.01-0.1 s^{-1}, 900°C-1000°C at strain rates of 0.01-1 s^{-1}, and at temperature 1050°C with strain rates of 0.01-10 s^{-1}) show peak after the strain hardening, followed by softening and steady state. The peak shows the onset of dynamic recrystallization (DRX). The peak shifted towards the higher strain as the hot compression temperature decreased or the strain rate increased. That is because at lower temperatures and/or at higher strain rates, the rate of work softening due to DRX slows down as compared to the work hardening rate. In other specimens, the flow stress gradually increases over the entire strain range of testing as the strain rate increases or the temperature decreases. The stress strain curves without a stress peak represent dynamic recovery (DRV) behavior in that temperatures and strain rates region. When the Zener-Hollomon parameter Z is high the DRV occurs whereas when it is low the DRX phenomenon occurs. Figure 5.5a shows that the values of flow stress progressively increase as the temperature decreases for a fixed strain rate because the work hardening phenomena plays a dominating role. Additionally, for a fixed temperature, as the strain rate increases the value of flow stress also increases as shown in figure 5.5b.

Plastic deformation of materials produces heat. Heat generated in the materials is either dissipated to the surroundings or it results in an increase in its temperature. The later occurs when the rate of heat generation is higher than the rate of heat dissipation. Significant heating of the sample is caused usually when deformation is performed with high strain rates, by nearly adiabatic conditions. Here, heat exchange with the surroundings is insignificant due to the short time of the deformation. The values of measured maximum increment of temperature (dT) due to adiabatic heating are summarized in Table 5.1 as a function of the strain rate and the temperature. The largest values of dT are observed at low temperatures and high strain rates. These values are used in the calculation of flow instability parameter c in equation 4.11.

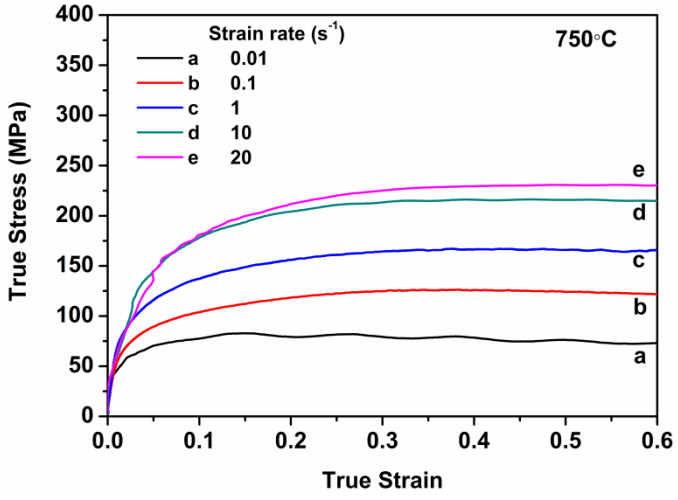

(a)

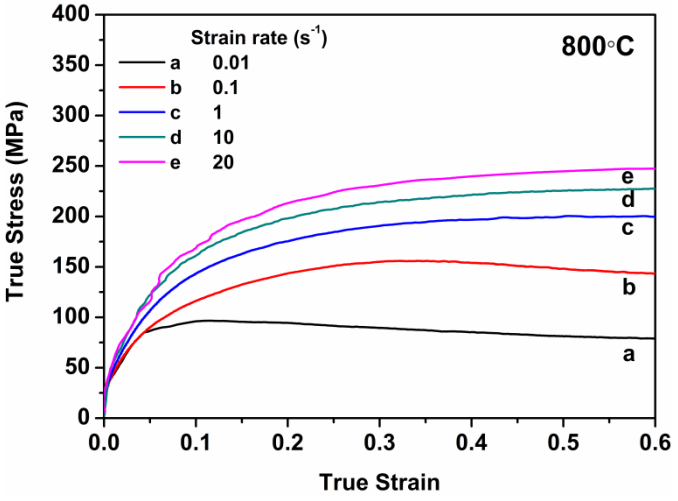

(b)

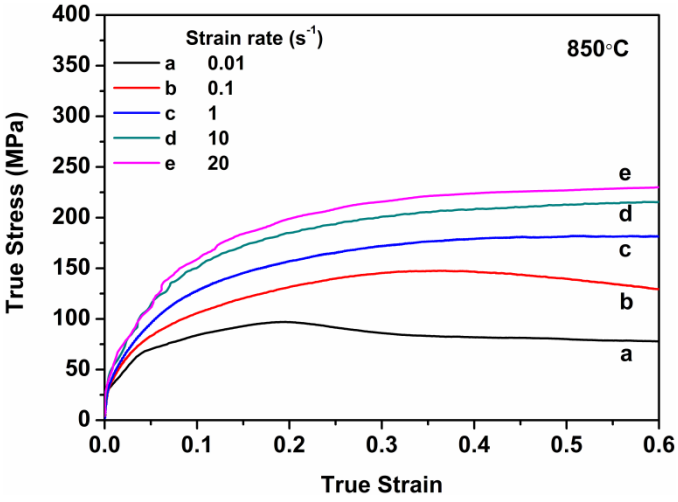

(c)

Fig. 5.4. Contd..

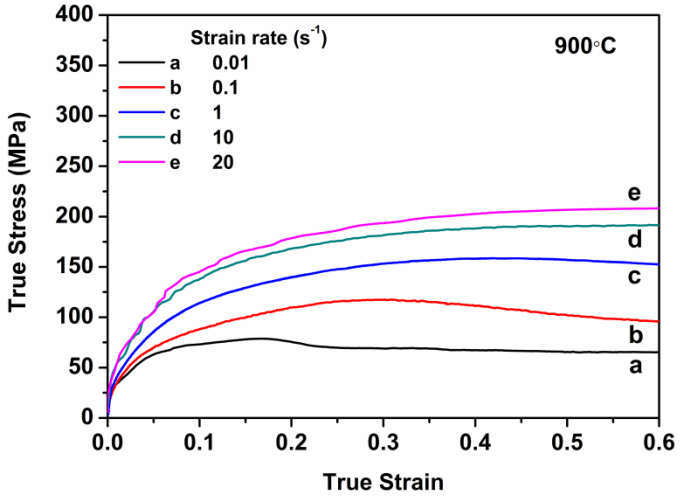

(d)

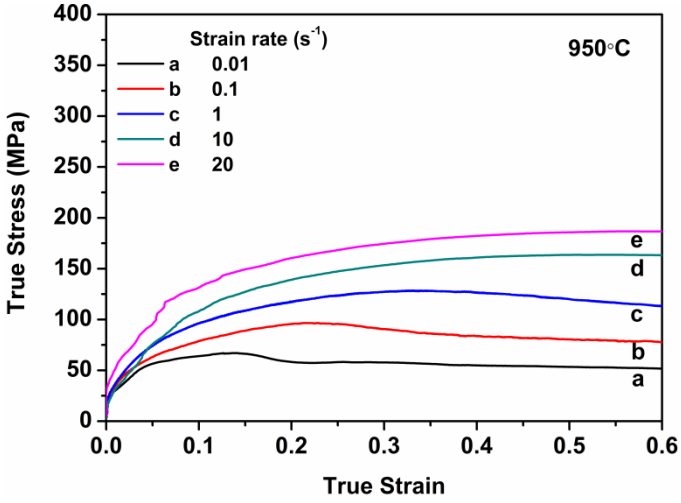

(e)

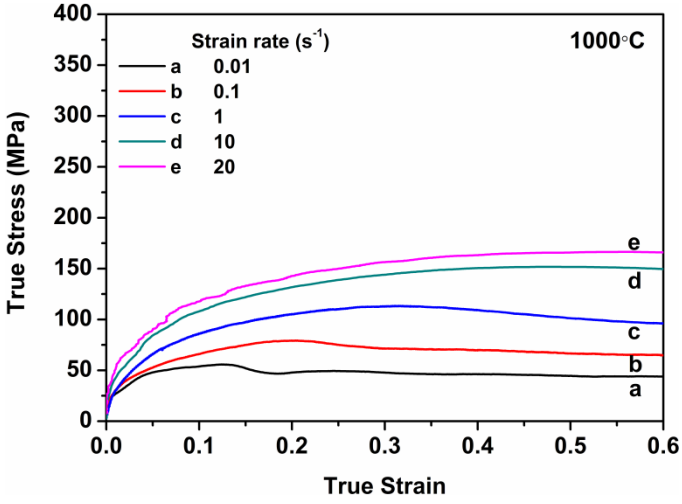

(f)

Fig. 5.4. Contd..

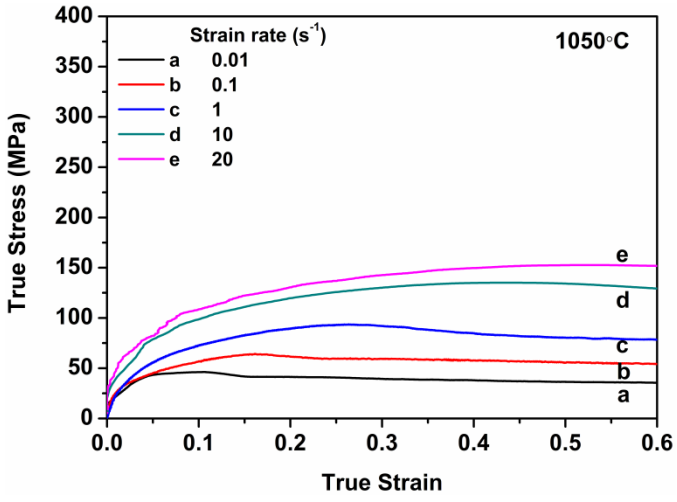

(g)

Fig. 5.4. Flow curves of AISI 1010 steel in compression obtained using different strain rates after austenitization at 1050°C during 5 minutes, and at deformation temperatures of (a) 750°C, (b) 800°C, (c) 850°C, (d) 900°C, (e) 950°C, (f) 1000°C, and (g) 1050°C.

Table 5.1. Maximum increment in temperature during hot compression of AISI 1010 steel.

Deformation Temperature (°C)	*dT* (°C) at the strain rate of (s^{-1})				
	0.01	0.1	1	10	20
750	10	13	13	19	18
800	12	13	19	28	26
850	8	16	14	25	24
900	14	20	11	21	22
950	11	17	6	18	19
1000	10	15	11	14	16
1050	13	19	8	6	8

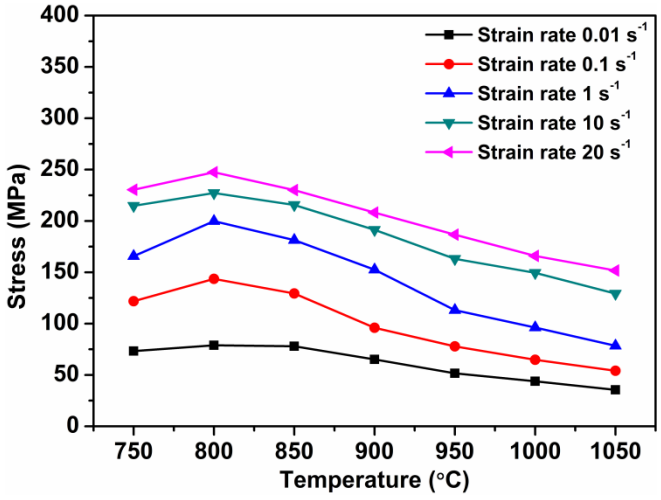

(a)

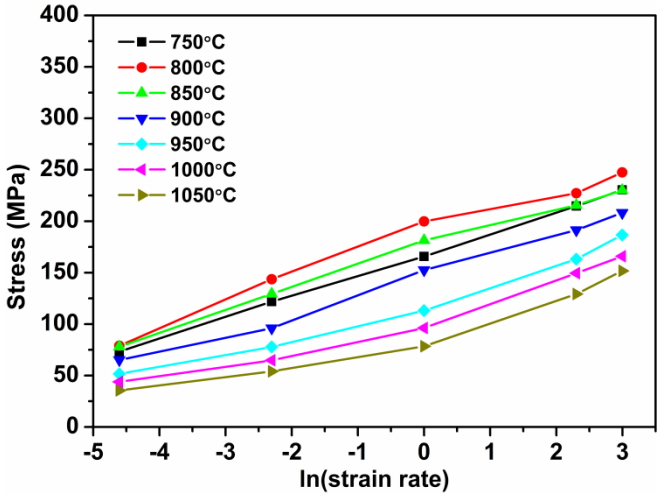

(b)

Fig. 5.5. Relationship between flow stress and (a) the deformation temperatures, (b) the logarithm of strain rate, for AISI 1010 steel at true strain of 0.6.

5.1.4. CHARACTERIZATION OF DEFORMED SPECIMENS

Each hot deformed specimen was cut along the center of the compression axis. One half of the specimen was mounted in resin for the metallographic procedures. A fixed region of all the specimens was selected for the microstructural examination in order to make microstructural analysis as systematic as possible. Schematic diagram of the cut specimen and the area of interest to gather microstructural information, are shown in figure 5.6. In order to minimize the sample-die friction effect that may result in dead metal zones at the ends of the deformed slightly barreled specimens, central region of the specimen was chosen for the analysis.

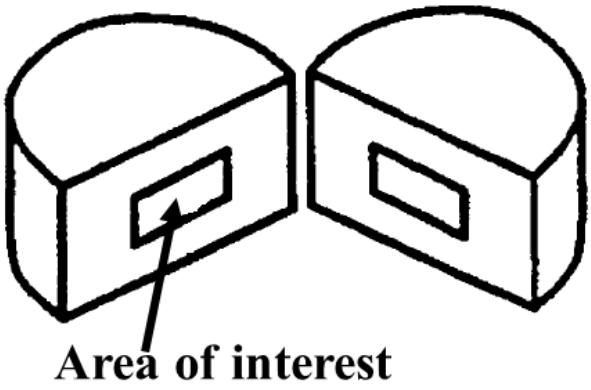

Fig. 5.6. Schematic diagram showing the region of the specimen from where the microstructural information was obtained. The direction of compression is vertical.

Light optical micrographs of water-quenched specimens of AISI 1010 steel after austenitization at 1050°C for 5 min followed by hot deformation at 750°C with the strain rates of 0.01, 1, 20 s^{-1}, are shown in figure 5.7. The applied total true strain was 0.7. All the specimens have martensitic microstructures (dark) with different amount of ferrite (bright) which was formed either before, during or after the hot deformation depending on the deformation temperature. From the transformation temperatures, one can see that at lower deformation temperature i.e. at 750°C, some pro-eutectoid ferrite was present before the deformation. Therefore, the largest amount of ferrite appeared after hot deformation at this temperature for all strain rates as shown in figures 5.7a, b, c. Additionally, some ferrite also formed during the deformation due to strain induced ferrite transformation. Figure 5.7b shows that the amount of ferrite (as shown by arrows) was the highest (about 74 pct) at 750°C and strain rate of 1 s^{-1}. Whereas, the amount of ferrite was about 70 pct both at the strain rates of 0.01 s^{-1} and 20 s^{-1}. Figures 5.8a, b, c show the light optical micrographs of the specimens deformed at 900°C using different strain rates. The specimen deformed at 900°C with the strain rate of 1 s^{-1} shows the highest amount of ferrite (about 62 pct) in this group. Whereas, the amount of ferrite was 46 pct and 53 pct for the strain rates of 0.01 s^{-1} and 20 s^{-1}, respectively. Since this hot deformation temperature is much higher than Ar_3 temperature, the ferrite most likely formed during cooling. The micrographs of the specimens deformed at 1050°C using the strain rates of 0.01 s^{-1}, 1 s^{-1} and 20 s^{-1},are shown in figure 5.9a, b, c respectively. The ferrite observed, probably formed during cooling, is acicular in nature and is formed at the grain boundaries.

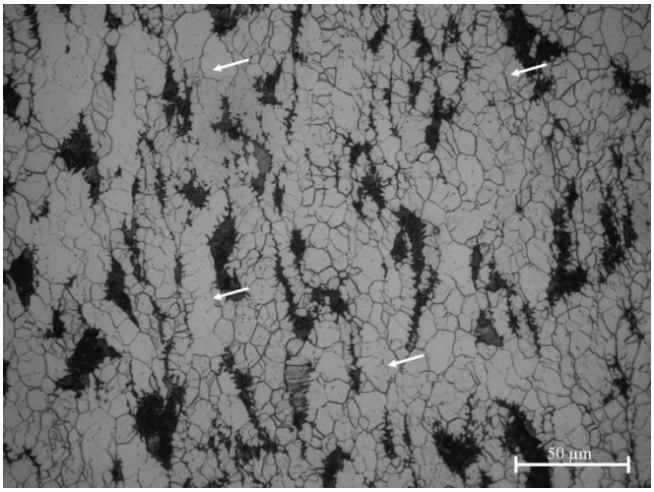

(a)

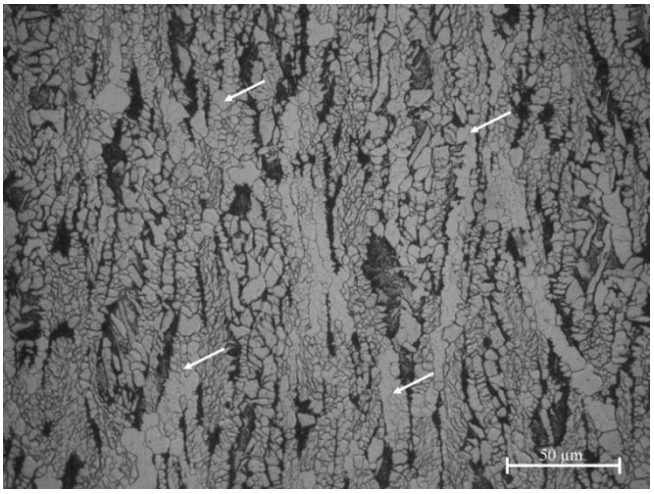

(b)

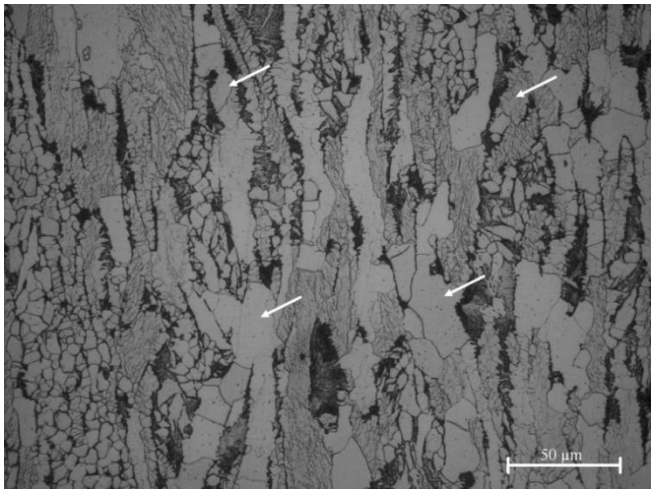

(c)

Fig. 5.7. Optical micrographs of AISI 1010 steel after hot deformation at 750°C using strain rate of (a) 0.01 s^{-1}, (b) 1 s^{-1}, and (c) 20 s^{-1}. The compression axis is horizontal.

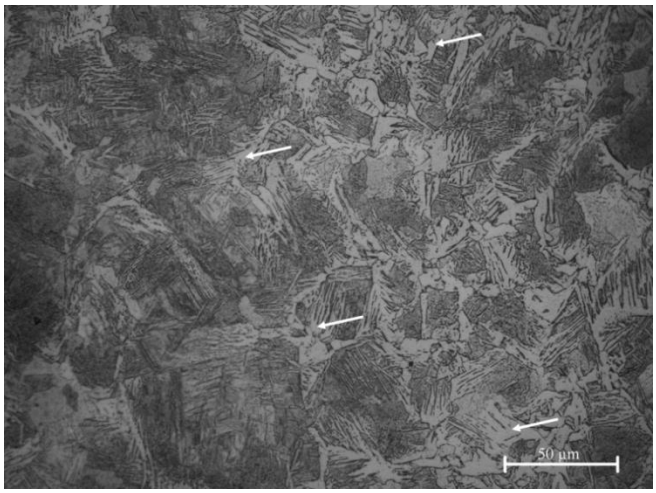

(a)

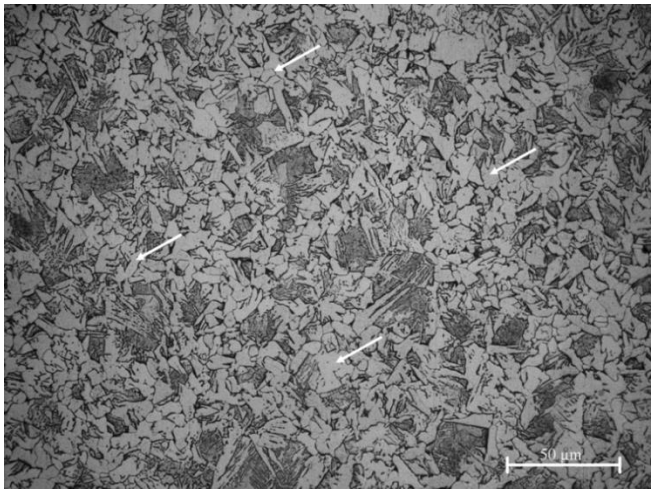

(b)

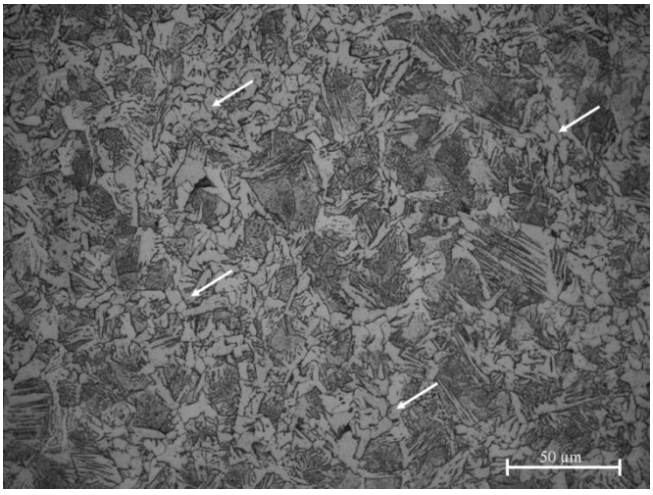

(c)

Fig. 5.8. Optical micrographs of AISI 1010 steel after hot deformation at 900°C using strain rate of (a) 0.01 s^{-1}, (b) 1 s^{-1}, and (c) 20 s^{-1}. The compression axis is horizontal.

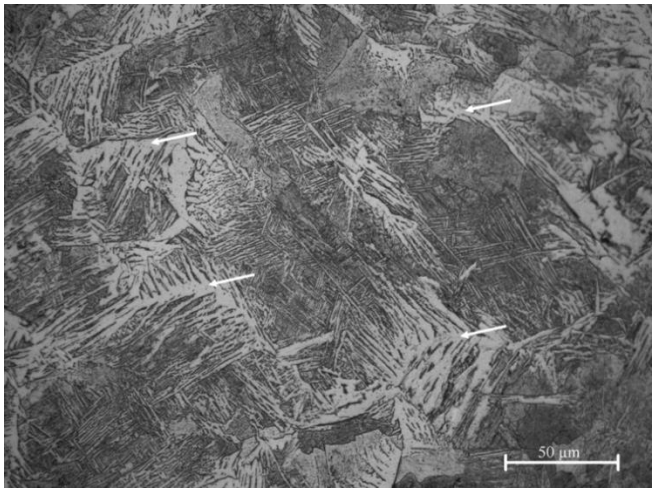

(a)

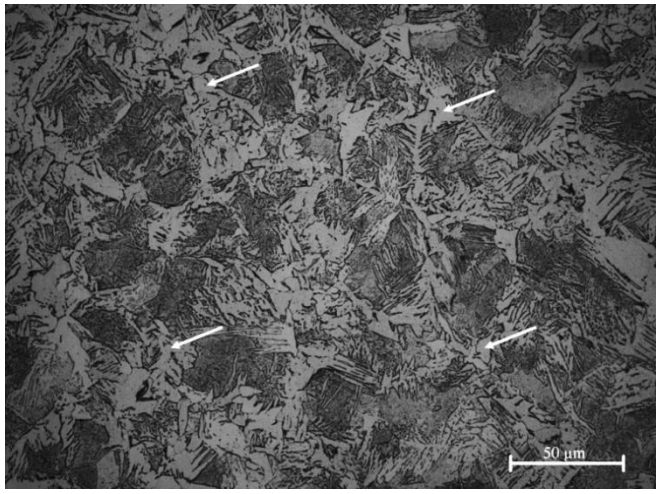

(b)

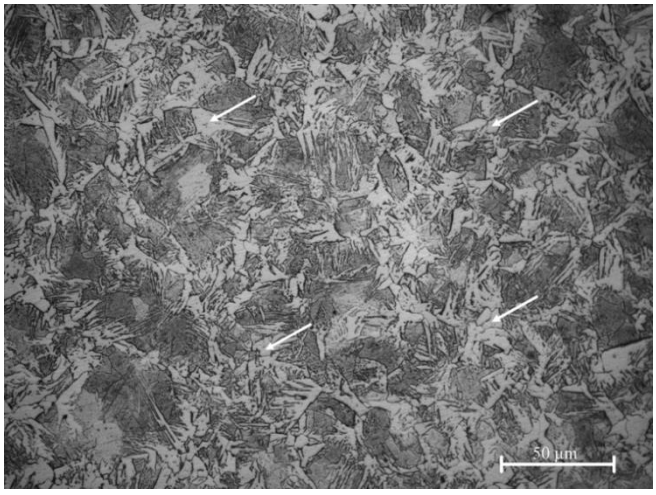

(c)

Fig. 5.9. Optical micrographs of AISI 1010 steel after hot deformation at 1050°C using strain rate of (a) 0.01 s^{-1}, (b) 1 s^{-1}, and (c) 20 s^{-1}. The compression axis is horizontal.

5.1.5. PROCESSING MAPS

The processing maps of AISI 1010 plain low carbon steel for the true strain of 0.3 and 0.6 are shown in figure 5.10. Processing map is the combination of superimposed maps viz. power dissipation efficiency, η and the instability parameter. The efficiency is shown by iso-efficiency lines whereas the instability parameter is shown by shaded area. Figures 5.10a and 5.10b show the strain-rate sensitivity maps and they show positive values of m over the entire test zone. This means that there is no instability predicted ($D = P$). High value of strain rate sensitivity, m is observed at the lower strain rate and low to moderate temperature zone. The high value of m is also observed at high temperature and higher strain rates region. The value of m decreases as the strain rate increases. In the range of lower temperature and low strain rates, the region of high value of m shrinks as the strain is increased from 0.3 to 0.6. Figure 5.11 shows the SEM micrograph of the specimens deformed at 800°C and 850°C, with the strain rate of 0.01 s^{-1}, which also represent the high m value, and shows that this is a crack/void free micrograph, consisting of ferrite and martensite phases as marked in figure.

The iso-efficiency lines of η_{Prasad} and the instability parameter, ξ of Prasad et al. are superimposed and are shown in figures 5.10c and d. The η_{Prasad} can be deduced from equation 4.2 and follows the same tendency as the strain rate sensitivity parameter, m. The iso-efficiency lines of $\eta_{Murty\ \&\ Rao}$ and the instability parameter, κ are shown in figures 5.10e and 5.10f. The large values of $\eta_{Murty\ \&\ Rao}$ are observed at lower temperatures and low to moderate strain rates. The κ instability domain predicts a larger instability domain as compared to the ξ instability domain. Figures 5.10g and 5.10h show the iso-efficiency lines of $\eta_{Murty\ \&\ Rao}$ and the instability parameter, κ_j (shaded area) as proposed by Poletti et al. [13]. The efficiency, $\eta_{Murty\ \&\ Rao}$ is high and corresponds to almost the same region as that given by strain rate sensitivity, m and η_{Prasad}, whereas the instability zone predicted by κ_j is smaller than that of κ.

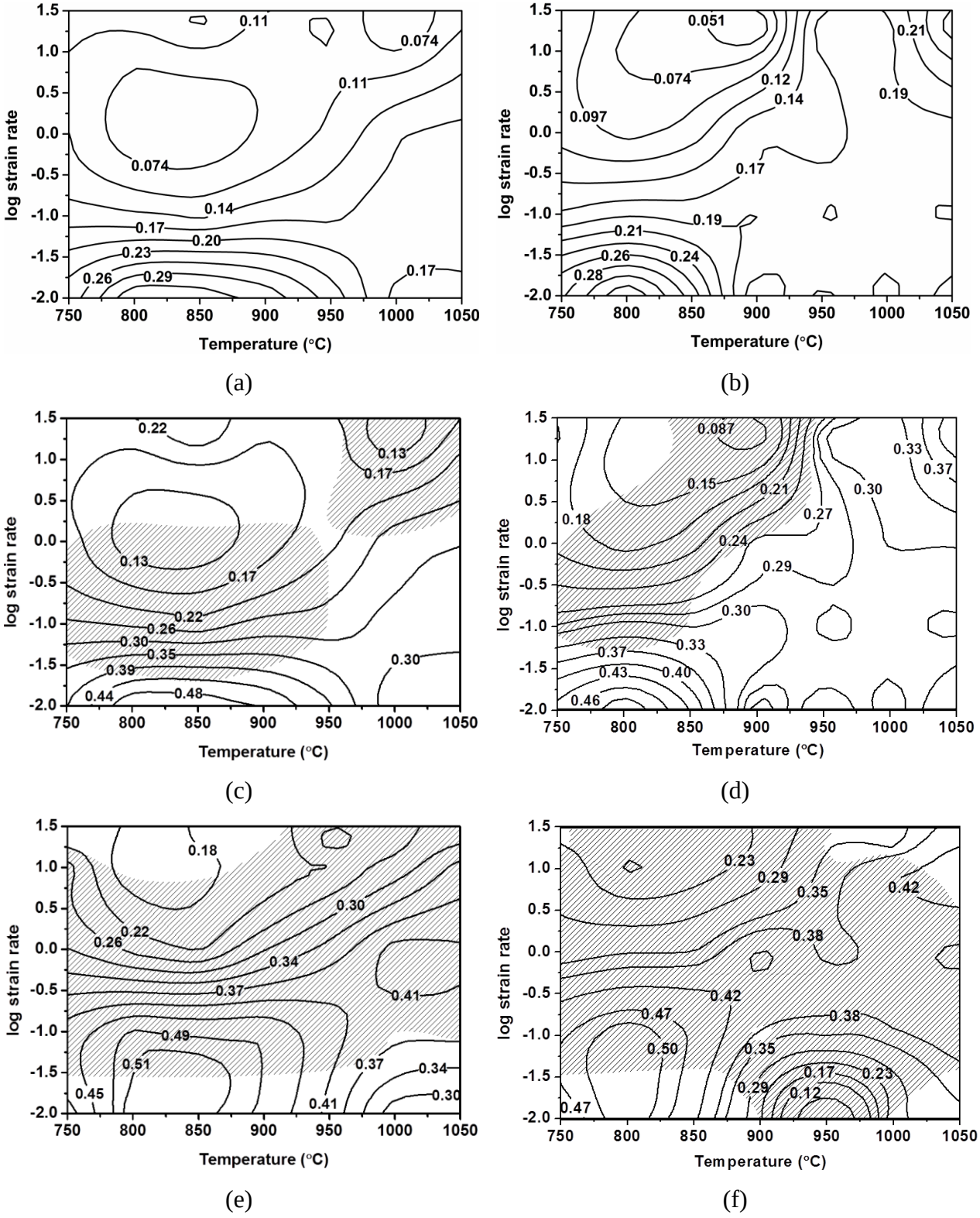

Fig. 5.10. Contd…

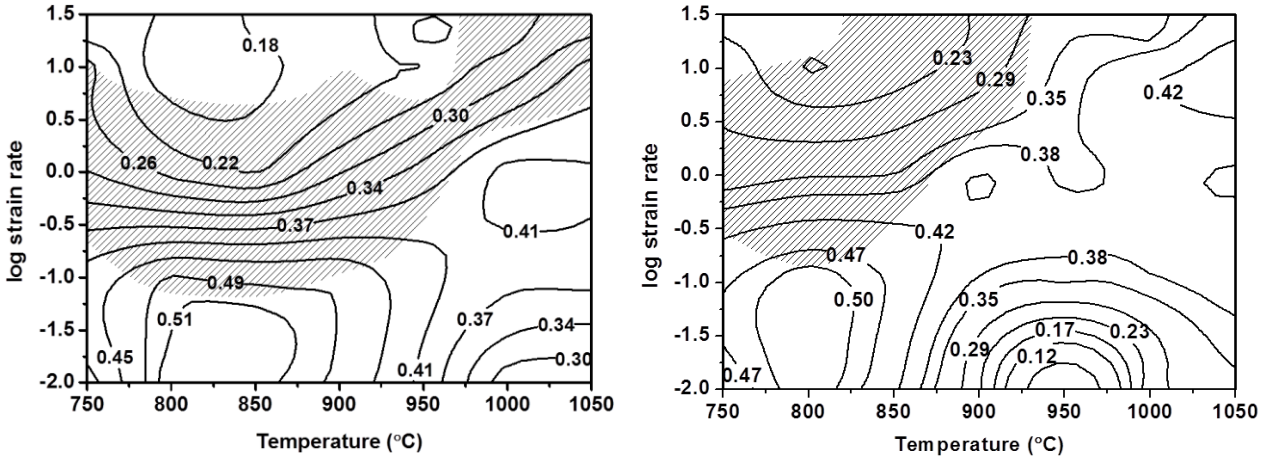

(g) (h)

Fig. 5.10. Processing maps constructed using different models to study the workability of AISI 1010 steel as a function of temperature and strain rate for strain of 0.3 (left) and 0.6 (right). (a),(b) strain rate sensitivity m, (c),(d) η and ξ using DMM of Prasad et al. [10] (e),(f) η and κ using modified DMM of Murty and Rao et al. [12] (g),(h) $\eta_{Murty\ \&\ Rao}$ and κ_j model of Poletti et al. [13].

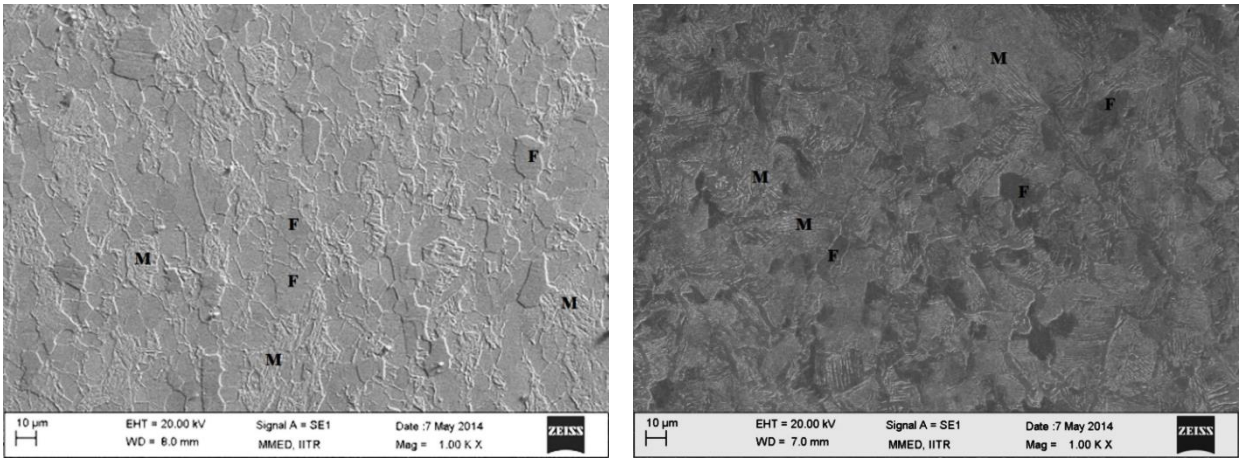

(a) (b)

Fig. 5.11. SEM micrographs of the AISI 1010 steel specimen deformed at (a) 800°C and (b) 850°C, with the strain rate of 0.01 s^{-1}. F and M, represent the ferrite and martensite phases, respectively.

Figure 5.12 shows the instability parameter, α for true strain of 0.6, calculated using equation 4.10. The entire test zone shows the negative values of α, which means that no flow

localization takes place. Figure 5.13 shows the Zener-Hollomon parameter, *Z*, which was determined from the flow stress data obtained from the hot deformation tests, on the axis of temperature and strain rate. It is obvious that with increasing temperature and decreasing strain rate, *Z* decreases. *Z*, is lower in the stable region where the power dissipation efficiency is high, and is higher in the flow instability regions depicted in figure 5.10.

Figures 5.4, 5.10 and 5.13 show the relationships among flow stress, dynamic recrystallization phenomenon, flow instability, and Zener-Hollomon parameter. Evidently, the flow stress decreases with decreasing Zener-Hollomon parameter for AISI 1010 steel. Lower the Zener-Hollomon parameter, larger the flow softening and more easily the DRX occurs.

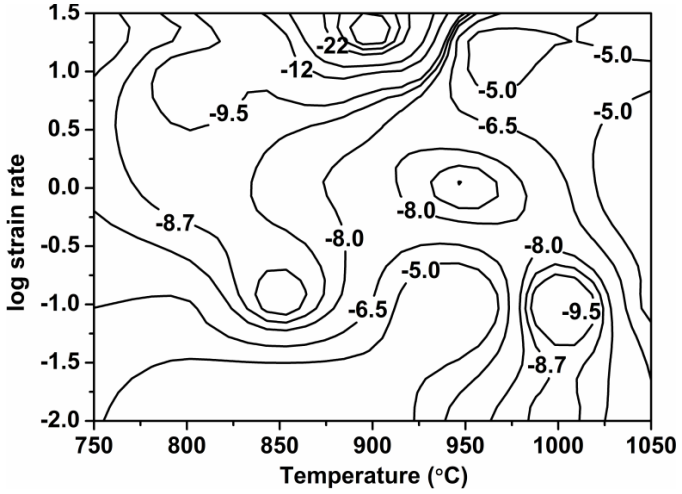

Fig. 5.12. Instability parameter, α, of AISI 1010 steel as a function of strain rate and temperature for a true strain of 0.6.

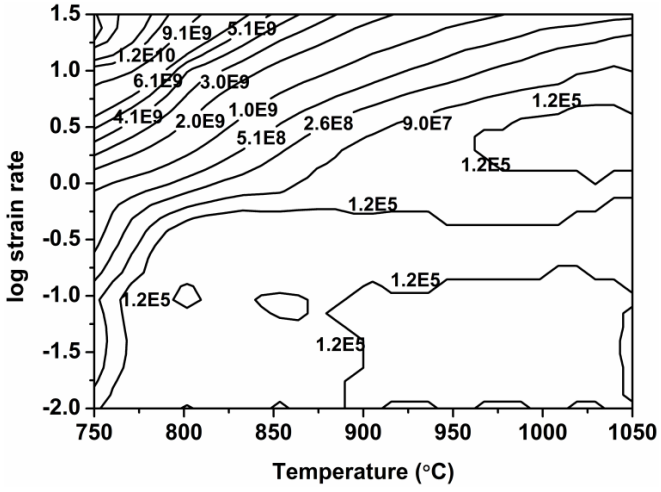

Fig. 5.13. Zener-Hollomon parameter, *Z* of AISI 1010 steel as a function of strain rate and temperature.

5.2. DISCUSSION

The values of Ar_1 and Ar_3 temperatures determined with the help of CCT dilatometry are lower as compared to those obtained from the CCC test as shown in figure 5.3. This is because as the deformation accompanies cooling in the CCC test it shifts the critical temperatures of phase transformation to the higher values [47]. This is due to the plastic deformation which results in the increase in the Gibbs energy of austenite phase [198] and/or refinement of austenite due to DRX. The presence of high density of dislocations increases sites for heterogeneous nucleation of ferrite and also enhances the diffusion of carbon [199] which alters the kinetics of transformation. Refinement from DRX of austenite has similar effect in terms of increased sites for heterogeneous nucleation. Therefore, the diffusion dependent ferrite transformation occurs and thus increase in the Ar_3 temperature is observed. In the present study, most of the hot deformation tests were performed above Ar_3 temperature except deformation at temperatures of 750°C and possibly 800°C. These two hot deformation tests were performed in the inter-critical region.

5.2.1. MICROSTRUCTURAL EVOLUTION AND PROCESSING MAPS

The deformation mechanisms in AISI 1010 steel are studied as a function of strain rate and temperature. The DRX of austenite takes place at low strain rates and high temperatures. Moreover, the value of stress increases continuously to a peak followed by softening towards a steady state region as shown in figure 5.4. This behavior is observed typically during DRX. In the beginning of deformation, the work hardening dominates over dynamic softening, due to the rapid multiplication of dislocations resulting in the increase in the flow stress. The flow stress peaks are shifted towards higher strains with the increase in strain rates and decreasing the temperature. As the strain increases, with dislocation accumulation the dynamic softening mechanisms such as DRX and dynamic recovery start. When the rate of work hardening is lower than the rate of dynamic softening, the flow stress gradually decreases and finally a steady state is reached [66]. At the lower values of Zener-Hollomon parameter, Z (i.e. low strain rates and/or higher temperatures) the tendency for nucleation and growth of new grains is increased [200] as shown by figures 5.7, 5.8, 5.9, and 5.13. Under these conditions, the parameters such as m and η are moderate to high, and flow stability is predicted.

In Table 5.2, comparisons of domains of power dissipation efficiency and instability for hot deformation of AISI 1010 steel obtained from the processing maps of figure 5.10 is presented. It describes the different workability zones according to their power dissipation efficiency and instability parameters.

Table 5.2. Comparisons of domains of efficiency and instability for hot deformation of AISI 1010 steel, obtained from the processing maps of figure 5.10.

	η_{Prasad} and ξ	$\eta_{Murty\ \&\ Rao}$ and κ	$\eta_{Murty\ \&\ Rao}$ and κ_j
Large η and no instability	• T < 950°C and $\dot{\varepsilon}$ < 0.018s^{-1} at 0.3 of strain and decreased to 875°C whereas $\dot{\varepsilon}$ increased to 0.03s^{-1} at 0.6 strain • 1025°C< T < 1050°C and 5.6 s^{-1} < $\dot{\varepsilon}$ < 20 s^{-1} at strain of 0.6. η values increases with strain.	• T < 950°C and $\dot{\varepsilon}$ < 0.03s^{-1} at 0.3 of strain and decreased to 850°C at strain of 0.6. • T > 1025°C and 3.16 s^{-1}< $\dot{\varepsilon}$ < 17.78 s^{-1} at strain of 0.6.	• T <950°C and $\dot{\varepsilon}$ < 0.1s^{-1} & T > 950°C and 0.18 < $\dot{\varepsilon}$ < 1 s^{-1} at strain of 0.3. • T < 850°C and $\dot{\varepsilon}$ < 0.18 s^{-1} & T > 1000°C and 3.2 s^{-1} < $\dot{\varepsilon}$ < 10 s^{-1} at strain of 0.6.
Low η and no instability	• T < 925°C and 1.78 s^{-1} < $\dot{\varepsilon}$ < 10 s^{-1} at 0.3 of strain • 775°C < T < 825°C and 3.2 s^{-1} < $\dot{\varepsilon}$ < 20 s^{-1} at 0.6 of strain. The value of η increases strain.	• T < 900°C and $\dot{\varepsilon}$ > 10 s^{-1} at 0.3 of strain. • T < 775°C and $\dot{\varepsilon}$ >17.8s^{-1} at 0.6 of strain.	• T <925°C and $\dot{\varepsilon}$ >5.6s^{-1} at 0.3 of strain • T < 825°C and $\dot{\varepsilon}$ > 5.6s^{-1} & 900°C < T < 1000°C and $\dot{\varepsilon}$ < 0.056 s^{-1} at strain of 0.6.
Large η and instability	• T < 950°C and 0.018 s^{-1} < $\dot{\varepsilon}$ < 0.056 s^{-1} at 0.3 of strain • T < 850°C and 0.056 s^{-1} < $\dot{\varepsilon}$ < 0.1 s^{-1} at strain of 0.6.	• T < 950°C and 0.032 s^{-1} < $\dot{\varepsilon}$ < 0.18 s^{-1} & T > 975°C and 0.18 s^{-1} < $\dot{\varepsilon}$ < 1 s^{-1} at strain of 0.3. • T > 875°C and 0.032 s^{-1} < $\dot{\varepsilon}$ < 0.32 s^{-1} & T > 1000°C and 3.2 < $\dot{\varepsilon}$ < 10 s^{-1} at strain of 0.6.	• T < 925°C and 0.056 s^{-1} < $\dot{\varepsilon}$ < 0.18s^{-1} at strain of 0.3. • T < 850°C and 0.018 s^{-1} < $\dot{\varepsilon}$ < 0.32s^{-1} at strain of 0.6.
Low η and instability	• T < 925°C and 0.32< $\dot{\varepsilon}$ <1.77 s^{-1} at 0.3 of strain • T < 850°C and 0.56 s^{-1} < $\dot{\varepsilon}$ <5.6 s^{-1}, & 850°C < T < 925°C with 5.6< $\dot{\varepsilon}$ <20s^{-1} at 0.6 strain	• 775°C < T < 850°C and 3.2 s^{-1} < $\dot{\varepsilon}$ < 10 s^{-1} at 0.3 of strain • 900°C < T < 975°C and $\dot{\varepsilon}$ < 0.032 s^{-1} at 0.6 of strain	• 775°C < T < 900°C and 1 s^{-1} < $\dot{\varepsilon}$ <1.78 s^{-1} at strain of 0.3. • 775°C < T < 875°C and $\dot{\varepsilon}$ >5.6s^{-1} at strain of 0.6

The use of DMM is expanded to different materials and conditions since the flow data obtained from compression tests results in a visual workability map. These maps can give an opinion of deformation mechanisms along with the processing window that can be used for the industrial applications. η_{Prasad} is directly related to the strain rate sensitivity parameter, m, whereas the correlation of $\eta_{Murty\ \&\ Rao}$ and m is insignificant. It is clear from figure 5.10 that the maximum values of these parameters (m, η_{Prasad}, $\eta_{Murty\ \&\ Rao}$) fall on the same region. This suggests that these parameters are closely related with the microstructural behavior and in visco-plastic materials diffusive process governs the deformation mechanisms. The instability parameters, ξ, κ, are also linked with the strain rate sensitivity parameter,m, whereas the instability parameter, κ_j, developed by Poletti et al. is directly associated with the dissipative function related to microstructural changes, J. Thus, κ_j is more accurate mathematically as it eliminates m from its calculations and also supported by figure 5.14 [184].

At deformation temperature of 750°C and for all strain rates, the prior austenite grains are elongated and ferrite was formed at the grain boundary, which is different from the pro-eutectoid ferrite (seen as blocky ferrite) as shown in figure 5.15a. After hot deformation, ferrite forms as a function of both the grain size and the stored energy developed as shown in figures 5.7, 5.8, and 5.9. Austenite grain refinement (i.e. smaller austenite grains) shifts the nose of CCT diagram towards the left, resulting in the ferrite formation during cooling. In this range, the value of m and η are high to moderate. At low temperature and high strain rates the values of m and η are moderate which supports the fact that the diffusion cannot takes place in this region. The ferrite observed in the micrographs was formed during cooling at temperatures 900°C for all strain rates. At deformation temperature of 900°C and low strain rate, the ferrite is formed at the prior austenite grain boundaries (Figure 5.8a), whereas as the strain rate increases the ferrite is formed within the prior austenite grain along with in the boundary. The moderate to low values of m and η are observed in this range.

Figure 5.10 shows the processing maps obtained using different DMM models. In general, the calculated values of m and η decrease as the strain rates increase. The influence of the strain rate in the deformability is related to the strain rate sensitivity. The large values of m and η were observed at low to moderate temperatures which are related to diffusion controlled processes resulting in better workability. The formation of ferrite is due to diffusive processes and the dynamic recovery of ferrite occurs concurrently in the low temperature and low strain

rate range. Furthermore, the values of m and η increase with increasing strain, indicating progress of the diffusion controlled process during deformation. There is no instability predicted for the low strain rate range. At high temperatures and all strain rates, the moderate values of m and η are related to diffusion controlled phenomena i.e. the DRX of austenite and no stability is predicted.

For all DMM models, the instability zones lie within low to moderate temperatures and moderate to high strain rates regions for the true strain of 0.6. The representative SEM micrographs of the specimens deformed at temperature 800°C with a strain rate of 10 s^{-1}, and at 900°C with a strain rate of 20 s^{-1} are shown in figure 5.14. In these specimens pores/voids are observed in (shown by arrows) the micrograph. The formation of pores/void in the specimen is the reflection of strain localization. The flow softening occurs locally due to adiabatic heating during the hot working at high strain rates [189]. At high strain rates, the microstructural restoration phenomena like DRX and DRV cannot take place due to short time of deformation and therefore the damage (pores/voids) occurs. The low restoration of the microstructure is supported by the low values of strain rate sensitivity, m and the efficiency parameters.

In general the negative values of calculated instability parameters of DMM except the flow localization parameter, α, are observed in the moderate to high strain rates region, where the austenite is deformed by fragmentation and deformation bands i.e. less restoration in the material [201]. Whereas, the flow localization parameter α is negative for entire range of testing, which shows the stability over the region and no flow localization takes place. Past studies on several materials show that the maximization of m and η reduced the tendency of flow localization [13].

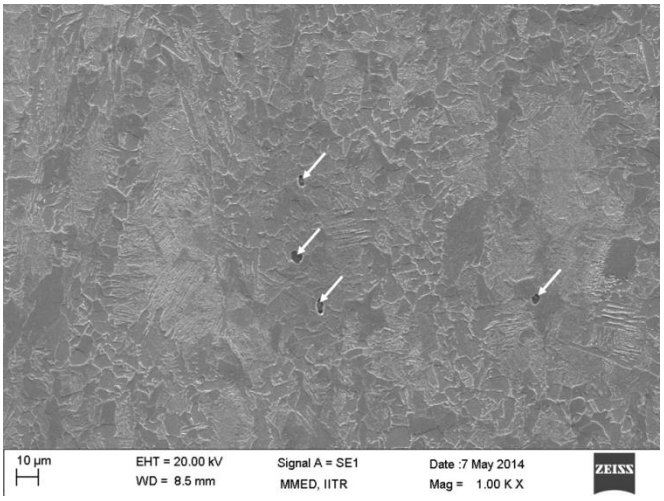

(a)

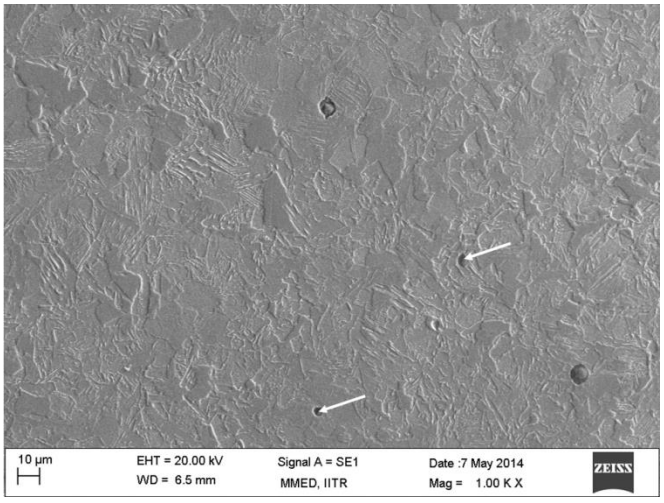

(b)

Fig. 5.14. SEM micrographs of the specimens deformed at (a) 800°C with strain rate 10 s^{-1}, and (b) 900°C at strain rate of 20 s^{-1}. Pores/voids observed are shown by arrow. The compression axis is horizontal.

In the EBSD measurements, the low angle grain boundaries (LAGB) are shown with the misorientation angle from 2 to 15° and are represented by white lines whereas high angle grain boundaries (HAGB) are with misorientation angles greater than 15° and represented by black colored lines. The proeutectoid ferrite (blocky in shape) and the DIFT ferrite are present in the low temperatures range as shown in figure 5.15a. The ferrite forms during the deformation because of DIFT and produces the softening which was reflected in the flow curves. This is also seen in the high values of m and η, and this region is always in the stable flow. This

microstructure also contains the sub-grains in the ferrite phase which was reflected in terms of low angle grain boundaries (LAGB) as shown in figure 5.15b, suggesting recovery of ferrite during deformation.

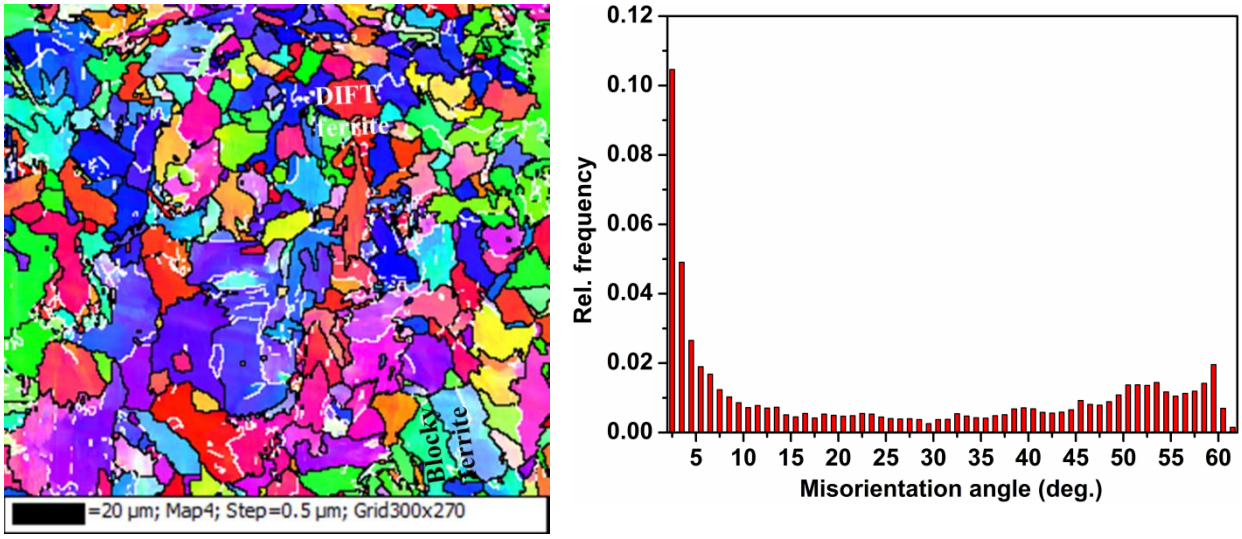

(a) (b)

Fig. 5.15. (a) Inverse pole figure, and (b) boundary misorientation angle distribution, obtained from EBSD analysis of AISI 1010 steel specimen deformed at temperature 850°C with strain rate of 0.1 s^{-1}. HAGBs are black and the LAGBs are white. Compression axis is horizontal.

5.2.2. CONSTITUTIVE EQUATIONS ANALYSIS

In order to know the deformation mechanisms, the constitutive equations can also be used. In this study, universal constitutive sinh type equation 4.13 is used to determine the apparent activation energy. To incorporate the experimental data in the universal constitutive sinh type equation, the mathematical treatment is applied by taking natural logarithm of equation 4.13.

$$\ln A + n \ln \sinh(c\sigma) = \ln \dot{\varepsilon} + \frac{Q}{RT}$$

$$\ln \sinh(c\sigma) = \frac{1}{n}(\ln \dot{\varepsilon}) + \frac{1}{n}\left(\frac{Q}{RT} - \ln A\right) \qquad (5.1)$$

From equation 5.1, the stress exponent is calculated as:

$$n = \left[\frac{\partial \ln \dot{\varepsilon}}{\partial \ln \sinh(c\sigma)} \right]_T \tag{5.2}$$

The plot of ln σ vs ln $\dot{\varepsilon}$ is used to determine the value of the stress exponent, *n*. Whereas the plot of ln σ vs *1/T* is used for calculating the value of apparent activation energy, *Q*, using sinh type laws for the true strain of 0.6 of AISI 1010 steel. These are shown in figures 5.16a and 5.16b, respectively. The value of c = 0.014 MPa^{-1} is used in sinh type equation [202]. Thus, the apparent activation energy for isothermal deformation at constant strain rate is determined using equation 5.3 as follows:

$$Q = Rn \left[\frac{\partial \ln \sinh(c\sigma)}{\partial \left(\frac{1}{T} \right)} \right]_{\dot{\varepsilon}} \tag{5.3}$$

The value of stress exponent is 3.5, which is consistent to the dislocation creep behavior [203] and is controlled by dislocation climb process [204]. The calculated average apparent activation energy is 177 kJ/mol using the sinh type equation, which suggests that the hot deformation is controlled by boundary/ core diffusion [205]. The constitutive equation obtained for AISI 1010 steel using sinh type law in the temperature range of 750ºC to 1050°C and strain rate ranging from of 0.01-20 s^{-1} is given by equation 5.4.

$$Z = 1.4 \times 10^6 \left[\sinh(0.014\sigma) \right]^{3.5} = \dot{\varepsilon} \exp\left(\frac{177000}{RT} \right) \tag{5.4}$$

Figure 5.17 shows the variation of Zener-Hollomon parameter as a function of peak flow stress. The peak flow stress data obtained from the different hot deformation conditions are fitted well with the Zener-Hollomon parameter, with the good linear correlation of regression coefficient (R^2=0.97) as obtained from the figure, and is given by equation 5.5.

$$\ln Z = 3.695 \ln \left[\sinh(c\sigma_p) \right] + 13.218 \tag{5.5}$$

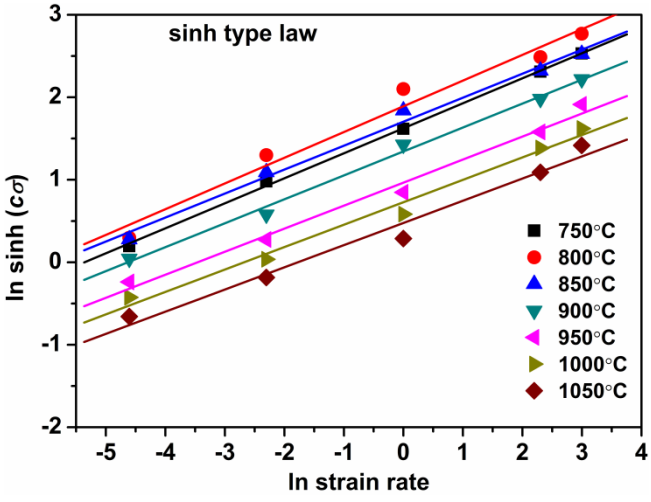

(a)

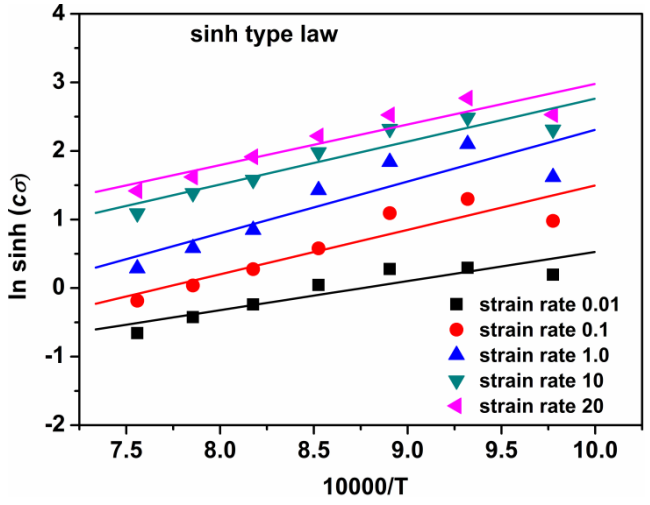

(b)

Fig.5.16. (a) Flow stress versus strain rate plot for all deformation temperatures, (b) flow stress versus temperature plot for all strain rates, using sinh type law at true strain of 0.6 for AISI 1010 steel.

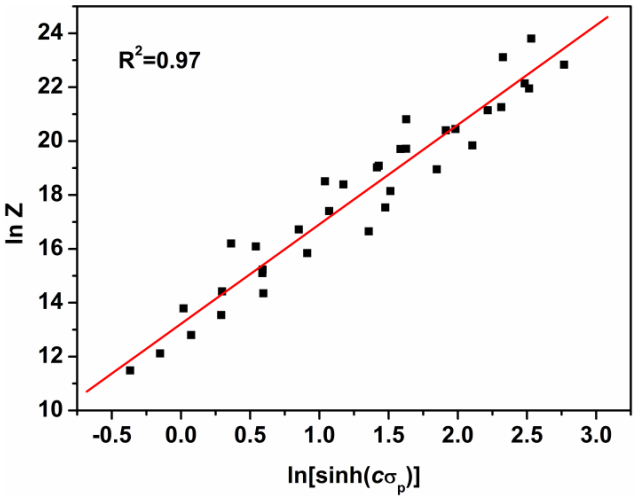

Fig. 5.17. Variation of the Zener-Hollomon parameter with peak flow stress.

5.3. SUMMARY

The hot deformation behavior of AISI 1010 steel is studied in the temperature range of 750°C to 1050ºC and the strain rate range of 0.01-20 s^{-1}. Processing maps are developed using the DMM and modified DMM and deformation is also analyzed by means of constitutive equations. The following conclusions are drawn from this work.

1. High values of strain rate sensitivity, m, and power dissipation efficiency, η are at low to moderate temperatures and low to moderate strain rates. This is due to the ferrite formation and the DRV of ferrite. The high values of m and η at moderate temperature and low to moderate strain rates are due to the DRX of austenite. Flow stability is predicted in either condition. The instability parameter, κ_j predict the more accurate deformation behaviour.
2. Smaller the Zener-Hollomon parameter, larger is the amount of softening and the more easily DRX/DRV occurs.
3. The flow is unstable at the high strain rates. In this region, the Zener-Hollomon parameter is higher and the values of m and η were lower. This is also confirmed by the metallographic investigations where the damage occurs at the high strain rates due to less restoration of microstructure due to possible adiabatic heating from short deformation times.
4. To analyse the relation between flow stress and Zener-Hollomon parameter, the sinh type equation is used over the entire deformation zone. The values of the peak flow stress, and Zener-Hollomon parameter show good correlation, and the pertaining equation is proposed.
5. The value of stress exponent, n is 3.5 shows that dislocation gliding and climb controlled the hot deformation process. Apparent activation energy for hot deformation of AISI 1010 steel was found to be 177 kJ/mol, which suggests that the deformation is controlled by boundary/core diffusion.

B. AISI 1016 STEEL

AISI 1016 steel was selected for hot deformation in order to study the effect of carbon content in the low carbon steels on hot deformation behavior, and microstructural evolution as compared to AISI 1010 steel. The hot deformation behavior of AISI 1016 is divided into two sub-divisions named as (i) results, and (ii) discussion.

5.4. RESULTS

5.4.1. AS-RECEIVED MICROSTRUCTURE

To determine the microstructural evolution occurring during hot deformation, it is necessary to understand the as-received microstructure of the materials. Thus, the microstructure of the AISI1016 steel was studied using LOM, SEM and EBSD. Figure 5.18a shows the light optical microstructure in as-received condition. It consists of light colored ferrite phase and dark etched pearlite (marked by the arrows). Figure 5.18b shows the SEM micrograph in secondary electron mode. It reveals banded pearlite in the ferrite matrix. The inverse pole figure (EBSD map) is shown in Figure 5.18c, reveals nearly random orientation of the ferrite grains in the as-received condition. The unindexed white region (shown by arrows) represents either a grain boundary region or a non-ferritic phase.

The microstructure of the non-deformed steel specimen heated up to 1050°C, soaked for 5 minutes and followed by water quenching is shown in figure 5.19a. It consists almost entirely of martensite in agreement with the average microhardness value of 395±8 VHN that is close to the value of Vickers hardness of martensite containing C-0.15wt% [196]. Figure 5.19b shows the LOM of the non-deformed steel specimen water quenched from 750°C after austenitization. It shows a two-phase structure: pro-eutectoid ferrite phase (bright and marked by arrows) and martensite phase (grey) formed from non-transformed austenite during cooling. The average micro-hardness value of ferrite phase is 220±12 VHN and that of the martensitic phase is 412±10 VHN. Pro-eutectoid ferrite is visible along the prior austenite grain boundaries. It has a blocky morphology at the triple junctions and needle like morphology along the rest of prior austenite grain boundaries. The blocky ferrite is also called as allotriomorphic ferrite and it is formed at high transformation temperature. Its growth is reduced as cooling proceeds because of shorter range of diffusion of carbon atoms and extremely retarded movement of iron atoms. Thus, side plates of acicular ferrite are nucleated and grow into austenite [197].

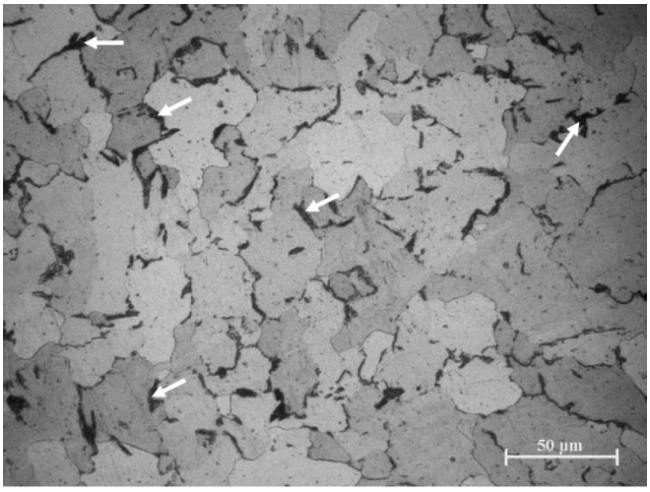

(a)

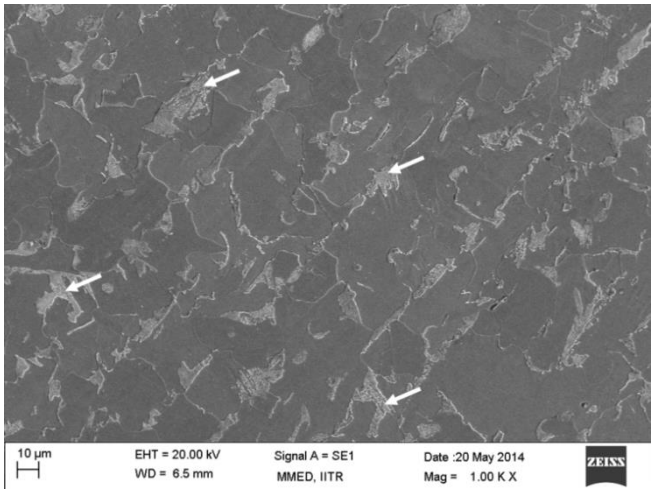

(b)

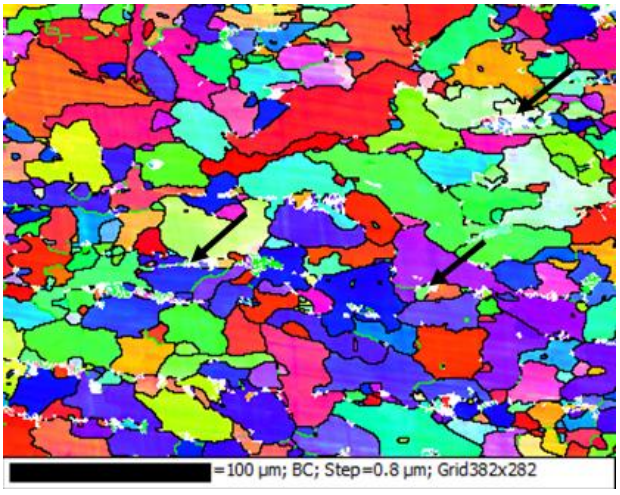

(c)

Fig. 5.18. Microstructure of AISI 1016 steel in as-received condition using (a) light optical microscopy (b) scanning electron microscopy (c) EBSD. Pearlite is shown by arrows.

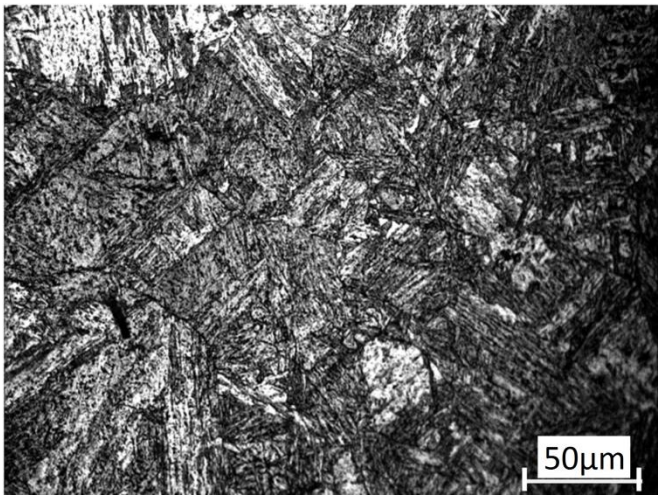

(a)

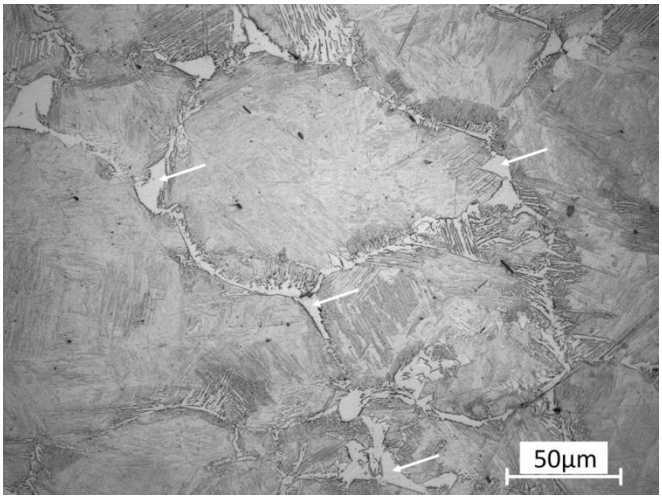

(b)

Fig. 5.19. Optical micrographs of AISI 1016 steel specimens heated to 1050°C for 5 min followed by (a) water quenching, and (b) cooling at 1°C s^{-1} to 750°C and water quenching.

5.4.2. CHARACTERIZATION OF PHASE TRANSFORMATION

The continuous cooling transformation (CCT) curve and compressive stress versus temperature curve obtained from the CCC test are shown in figures 5.20a and 5.20b, respectively. The inflection points during cooling, represents the phase transformation in the material and are denoted as the Ar_1 and Ar_3 temperatures. The Ar_3 and Ar_1 temperatures are estimated to be 753°C and 678°C using CCT curve and 786°C and 741°C using CCC curve, respectively.

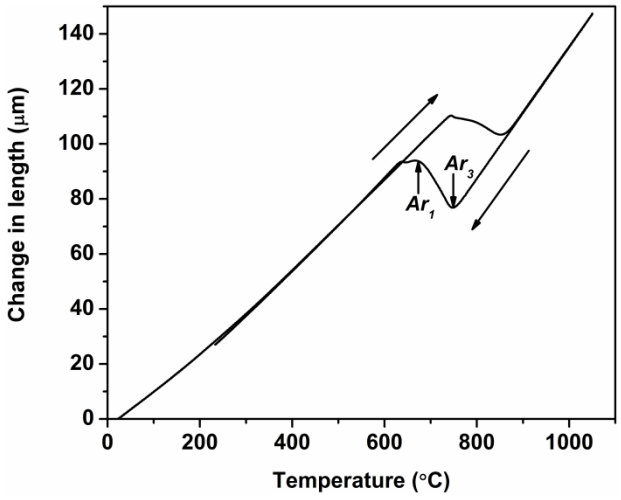

(a)

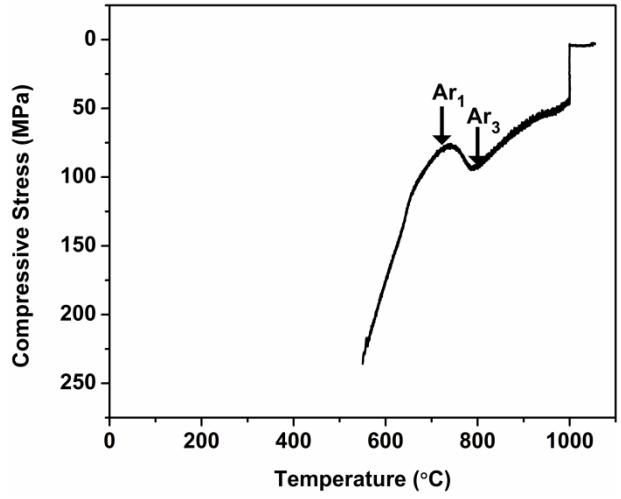

(b)

Fig. 5.20. (a) Results of the dilatometry test and (b) the continuous cooling compression curve obtained from CCC test, performed on AISI 1016 steel. Inflection points correspond to the Ar_1 and Ar_3 temperatures.

5.4.3. TRUE STRESS-TRUE STRAIN CURVES

Figure 5.21 shows flow curves corresponding to the test temperatures of 750°C, 800°C, 850°C, 900°C, 950°C, 1000°C, and 1050°C using different strain rates ranging from 0.01 to 80 s^{-1}. The true flow stress showed to be a function of strain rate and temperature. For a fixed strain rate, as the temperature increased, the values of flow stress progressively decreased. Whereas, for a particular temperature, the value of flow stress increases as the strain rate increased. All the stress-strain curves determined by compression testing at low strain rates

(0.01-0.1 s^{-1} for all test temperatures, and 0.01-1 s^{-1} for test temperatures 900°C onwards) showed a peak stress after hardening. For moderate strain rates and at low temperatures, a slight hardening is observed. At higher strain rates, the flow stress gradually increased over the whole strain of testing. Figure 5.21 also shows that the stress peaks seen at lower strain rates are shifted to higher strains with increasing the strain rate. That is because at lower temperatures and higher strain rates, the rate of work softening due to DRX slows down than the work hardening rate. Thus, the flow stress gradually increases, as the strain rate increases or the temperature decreases, over the entire strain range of testing. The stress strain curves without the stress peak, represents DRV behavior in that temperatures and strain rates region. When the Zener-Hollomon parameter, Z is high the DRV occurs whereas when it is low the DRX phenomenon occurs. Figure 5.22a shows that the value of flow stress progressively increases as the temperature decreases for a fixed strain rate because the work hardening phenomena plays a dominating role. Additionally, for a fixed temperature, as the strain rate increases the value of flow stress also increases (Figure 5.22b).

Table 5.3. Maximum increment in temperature during compression of AISI 1016 steel.

Deformation Temperature (°C)	*dT* (°C) at the strain rate of				
	0.01 s^{-1}	0.1 s^{-1}	1 s^{-1}	10 s^{-1}	80 s^{-1}
750	8	10	14	25	29
800	3	8	11	23	23
850	3	13	7	21	22
900	6	9	8	17	18
950	4	28	6	18	19
1000	4	8	8	16	20
1050	8	7	8	14	22

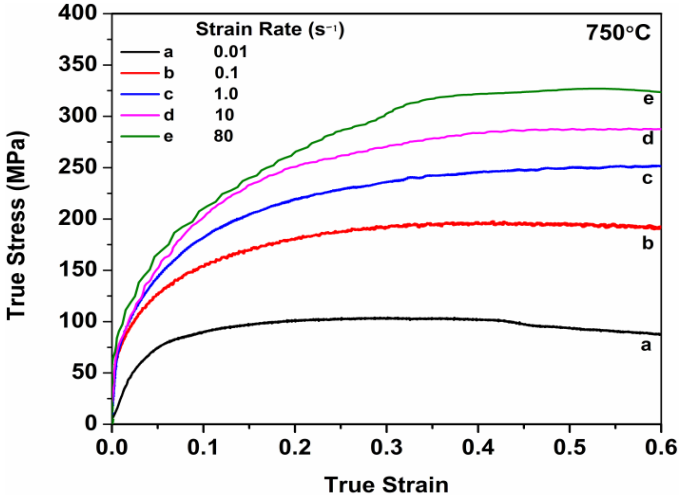

(a)

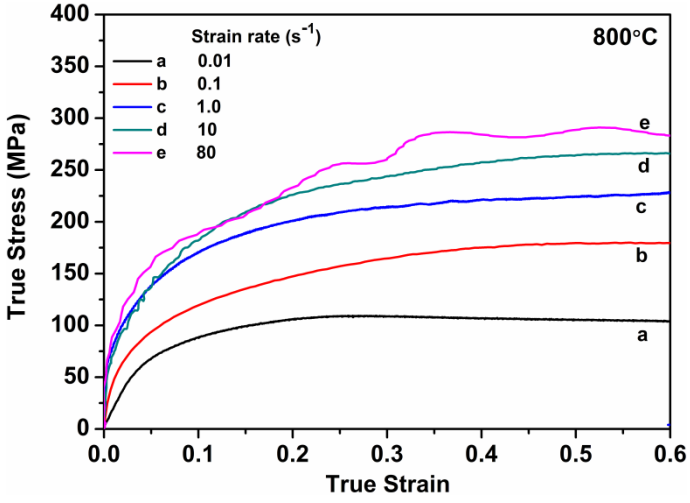

(b)

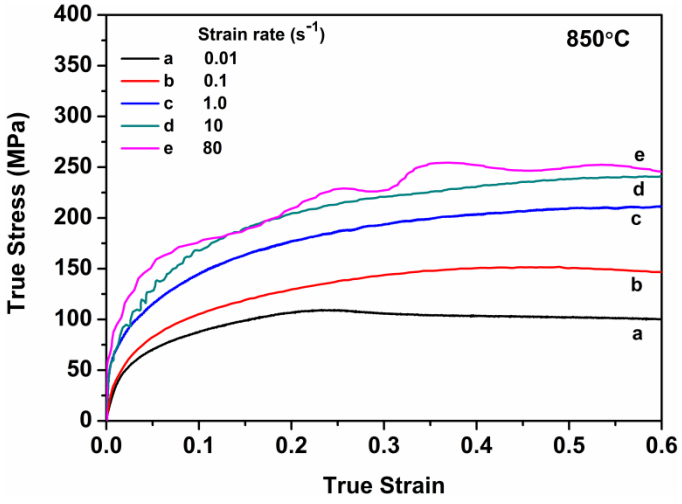

(c)

Fig. 5.21. Contd..

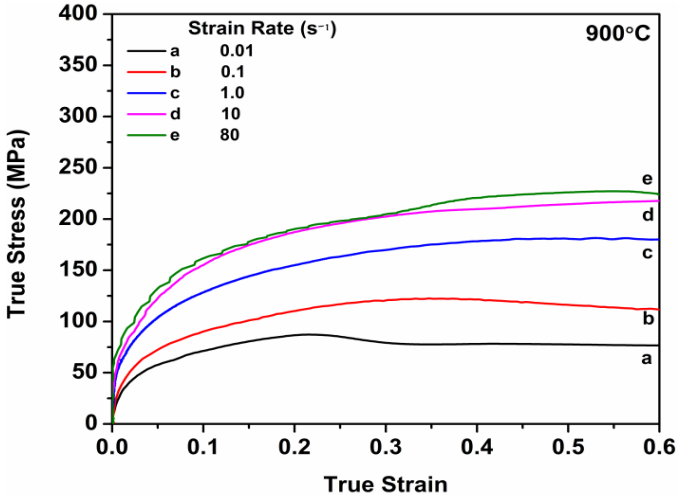

(d)

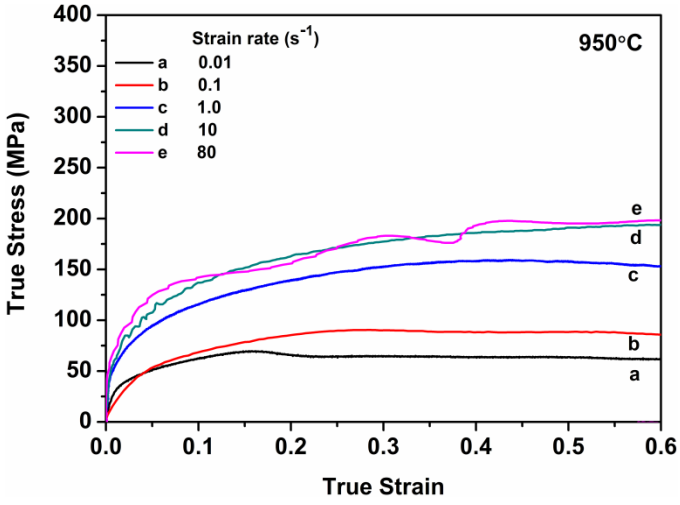

(e)

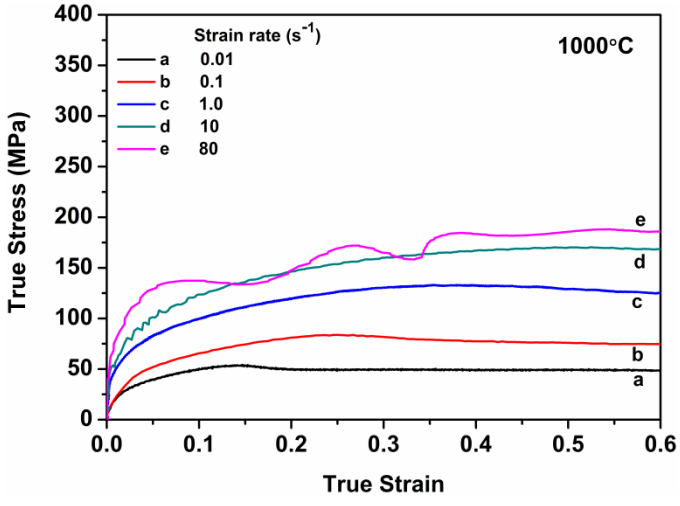

(f)

Fig. 5.21. Contd..

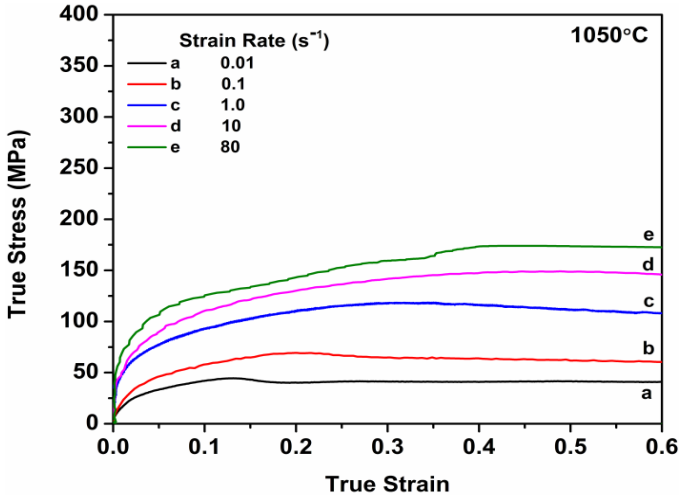

(g)

Fig. 5.21. Flow curves of AISI 1016 steel in compression obtained using different strain rates after austenitization at 1050°C during 5 minutes, and deformed at temperatures of (a) 750°C, (b) 800°C, (c) 850°C, (d) 900°C, (e) 950°C, (f) 1000°C, and (g) 1050°C.

The maximum increment of temperature (dT) measured due to adiabatic heating is summarized in Table 5.3 as a function of the strain rate and the temperature. At low strain rates and high deformation temperatures, the dT values are small because longer deformation time allows dissipation of heat generated from deformation. The largest values of dT are observed at low temperatures and high strain rates. In the calculation of flow instability parameter α in equation 4.11 these values of dT are used.

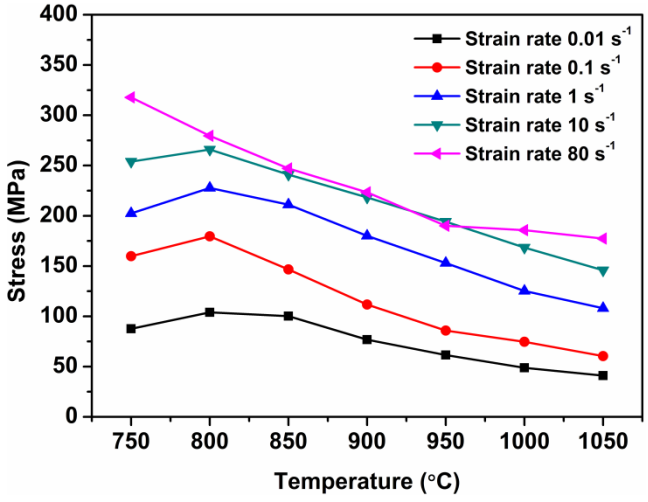

(a)

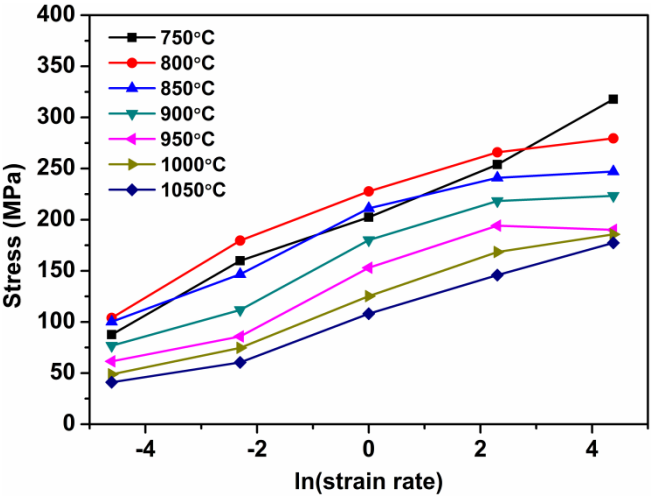

(b)

Fig. 5.22. Relationship between flow stress and (a) the deformation temperatures, (b) the logarithm of strain rate, of AISI 1016 steel at true strain of 0.6.

5.4.4. DEFORMED SPECIMEN CHARACTERIZATION

The hot deformed specimens were cut along the center of the compression axis and mounted on the resin for the metallographic preparations. In order to minimize the sample-die friction effect, a fixed region at the center of the specimen was selected for the microstructural examination (Figure 5.6).

LOM of water-quenched specimens deformed after austenitization at 1050°C and 5 minutes soaking, followed by hot compression to a true strain of 0.7 at test temperatures of 750°C, 900°C, and 1050°C and strain rates are shown in figures 5.23, 5.24, and 5.25, respectively. All the specimens show a martensitic microstructure with different amounts of ferrite (bright in color and marked by arrows) formed before, during, and after deformation. At 750°C, pro-eutectoid ferrite exists before deformation. The amount of ferrite is the largest for this temperature and is obtained at all the strain rates as shown in figures 5.23a, b, c. Furthermore, some ferrite was formed during hot deformation in the lower temperatures range. Finally, at 900°C (Figures 5.24a, b, c) there is no pro-eutectoid ferrite before deformation and the ferrite observed is formed during cooling. In this case, the amount of ferrite (21.80 vol%) is the highest for the strain rate of $1s^{-1}$ (Figure 5.24b) and is significantly lower for the other strain rates used in this work; these are 14.8 and 3.3 vol% for the strain rates of 0.01 and 80 s^{-1}, respectively. At 1050°C and strain rate of 0.01 s^{-1}, only martensite is observed (Figure 5.25a). Additionally for deformations at 1050ºC and at strain rates of 1 and 80 s^{-1}, a small amount of ferrite is formed at the grain boundaries during cooling (Figures 5.25b, c).

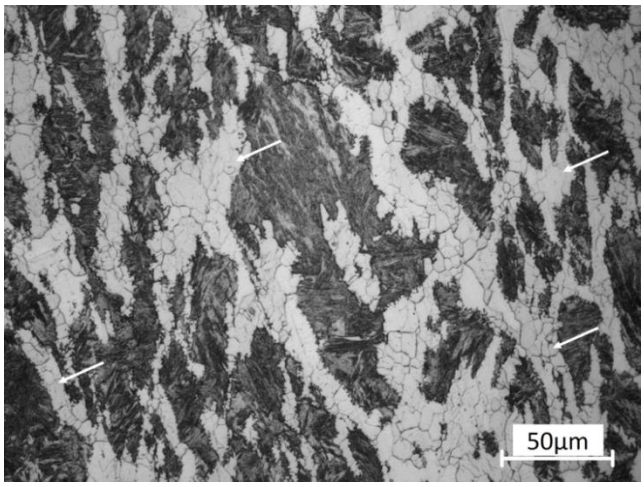

(a)

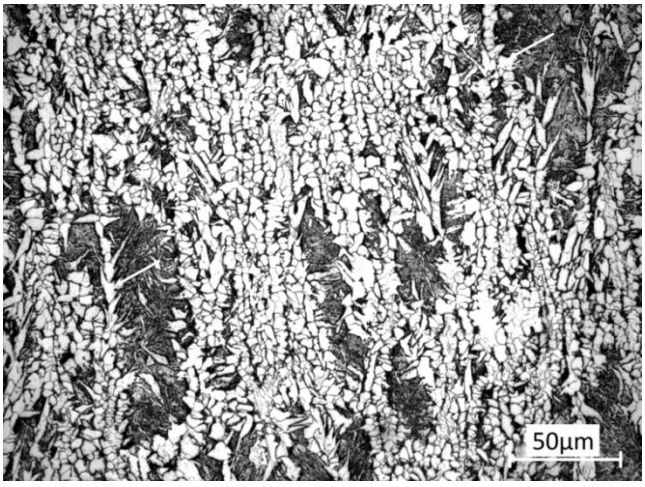

(b)

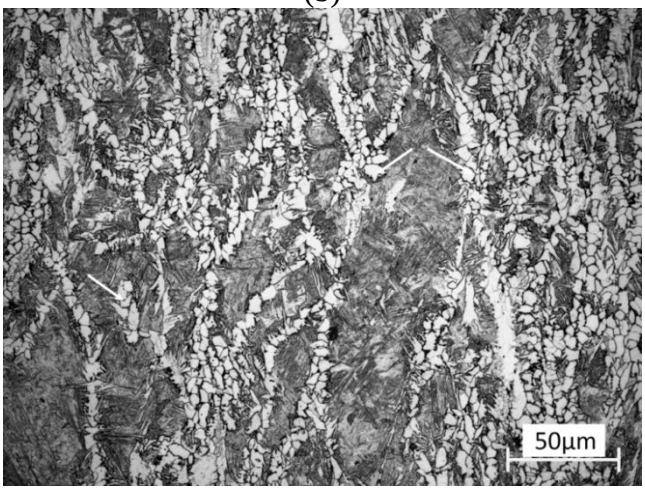

(c)

Fig. 5.23. Optical micrographs of AISI 1016 steel after hot deformation at 750°C using strain rate of (a) 0.01 s^{-1}, (b) 1 s^{-1}, and (c) 80 s^{-1}. The compression axis is horizontal.

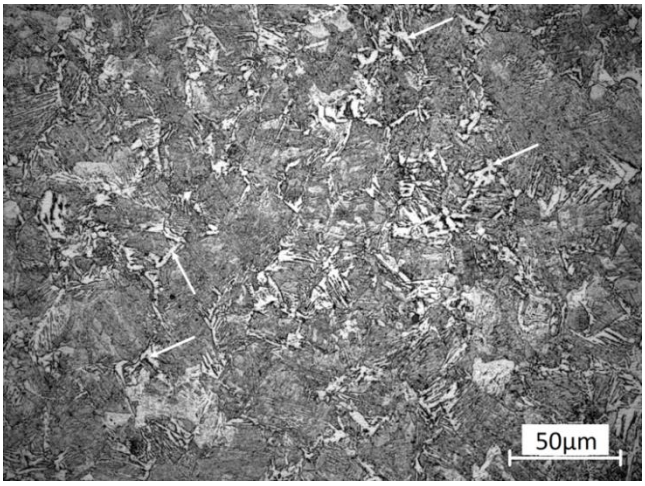

(a)

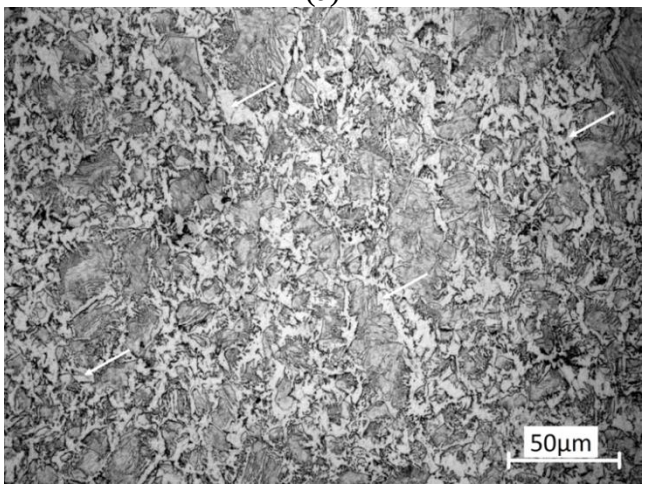

(b)

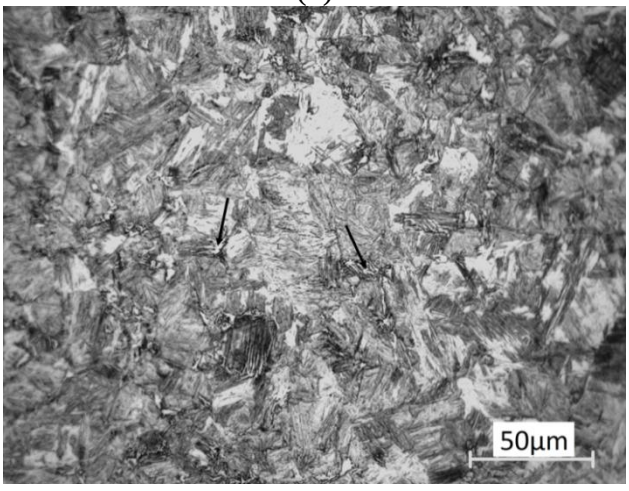

(c)

Fig. 5.24. Optical micrographs of AISI 1016 steel after hot deformation at 900°C using strain rate of (a) 0.01 s^{-1}, (b) 1 s^{-1}, and (c) 80 s^{-1}. The compression axis is horizontal.

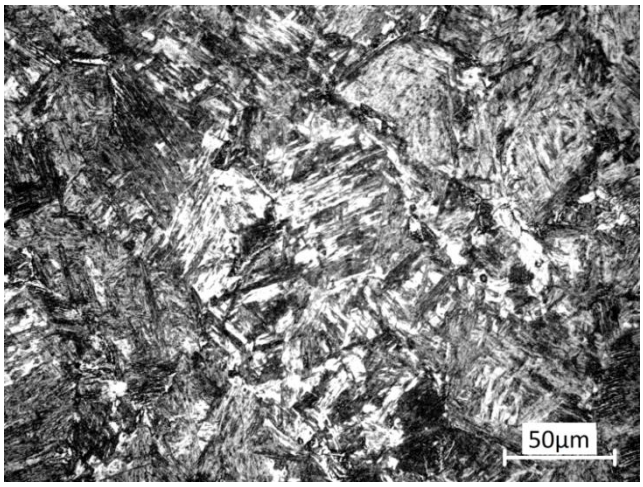

(a)

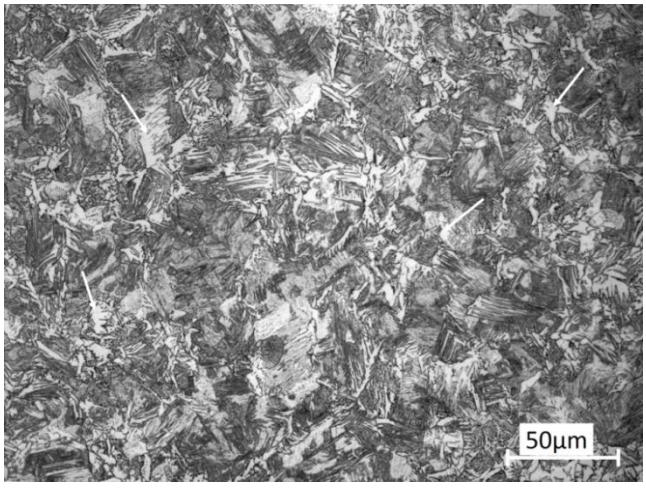

(b)

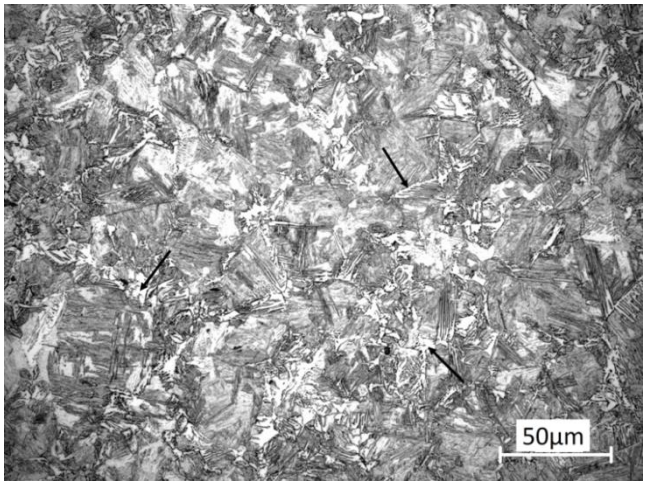

(c)

Fig. 5.25. Optical micrographs of AISI 1016 steel after hot deformation at 1050°C using strain rates of (a) 0.01 s^{-1}, (b) 1 s^{-1}, and (c) 80 s^{-1}. The compression axis is horizontal.

5.4.5. PROCESSING MAPS

Processing maps for 0.3 and 0.6 strains are shown in figure 5.26. The iso-efficiency (η) lines are shown in the plot of $\log \dot{\varepsilon}$ vs T and the instability parameter (shaded area) is superimposed. The strain rate sensitivity maps (Figures 5.26a, and 5.26b) show positive values of m in the entire testing zone, i.e. no instability is predicted when $D = P$. Large m values are observed at lower strain rates, especially at very high and very low temperatures. In the range of low temperatures and low strain rates, m increases as a function of the strain.

Figures 5.26c and 5.26d show iso-efficiency lines for η_{Prasad}. Instability (ξ) domains are shown by the shaded area. Figures 5.26e and 5.26f depict the iso-efficiency lines for $\eta_{Murty\ \&\ Rao}$ and corresponding κ instability domains are shown by the shaded area. The η_{Prasad} values follow the same tendency as the m values, which can be inferred from the corresponding equation ($\eta_{Prasad} = 2m/(m+1)$). On the other hand, the instability areas predicted by ξ and κ are similar. Iso-efficiency lines for $\eta_{Murty\ \&\ Rao}$ and the κ_j instability domains (shaded area) are shown in figures 5.26g and 5.26h. The values of $\eta_{Murty\ \&\ Rao}$ follow a similar trend as η_{Prasad} and m. In this steel too, the instability zones shown by κ_j are smaller than the ones depicted by ξ and κ.

The instability parameter α calculated using equation 4.10 is shown in figure 5.27 for true strain of 0.6. Instabilities denoted by positive values of the parameter α occur at high temperatures and high strain rates. Figure 5.28 shows the Zener-Hollomon parameter, Z on the axis of temperature and strain rate, which was determined from the flow stress data obtained from the hot compression tests. The Zener-Hollomon parameter, Z decreases with increasing the temperature and/or decreasing the strain rates. Z is lower in the stable region where the power dissipation efficiency is high, and higher in the flow instability region as shown in figures 5.26 and 5.28.

Figures 5.21, 5.26 and 5.28 show the relationships among flow stress, DRX, flow instability and Z. Evidently, the flow stress decreases with decreasing Z for AISI 1016 steel. Lower the Z, larger the flow softening and more easily the DRX occurs.

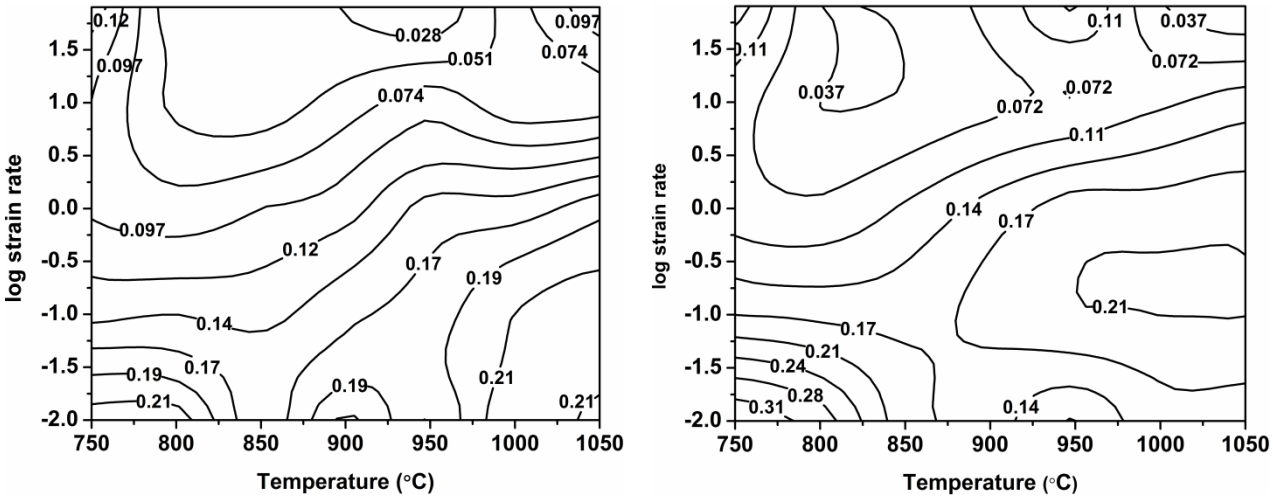

(a)

(b)

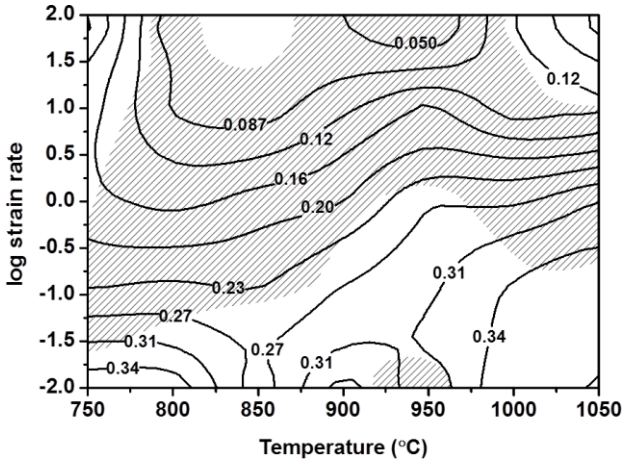

(c)

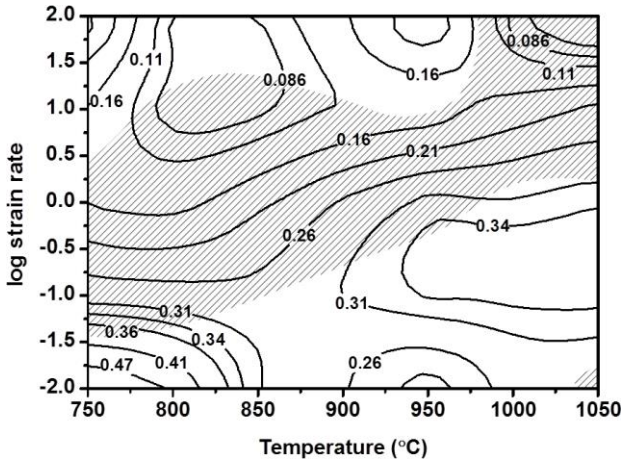

(d)

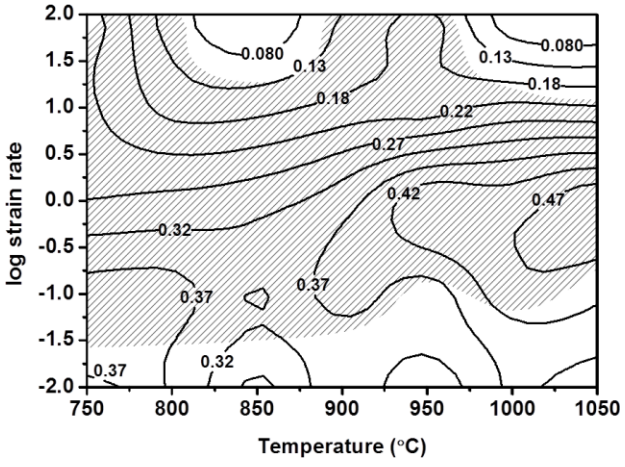

(e)

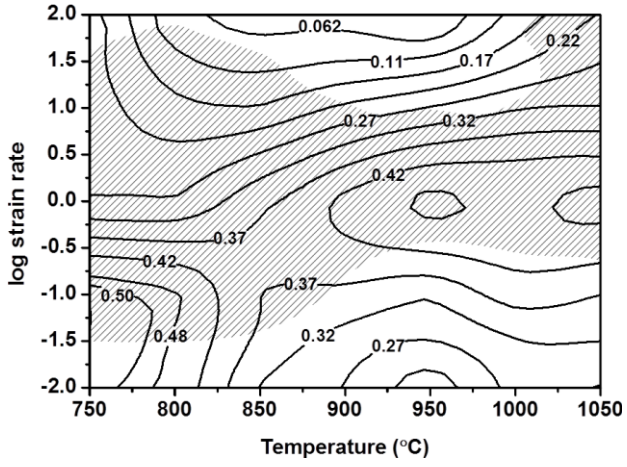

(f)

Fig. 5.26. Contd…

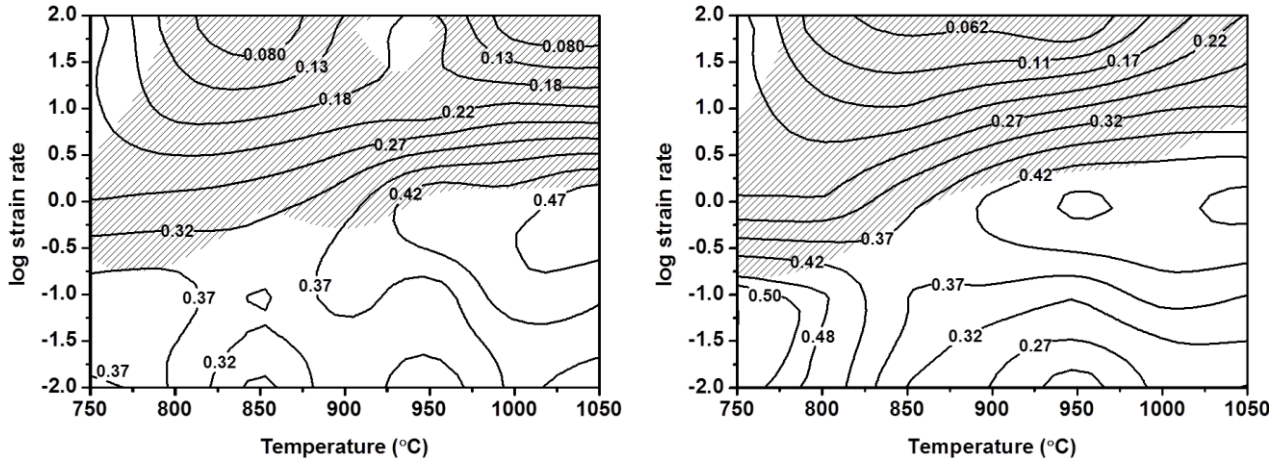

(g) (h)

Fig. 5.26. Processing maps constructed using different models to study the workability of AISI 1016 as a function of temperature and strain rate for strain of 0.3 (left) and 0.6 (right). (a),(b) strain rate sensitivity m, (c),(d) η and ξ using DMM of Prasad et al. [10] (e),(f) η and κ using modified DMM of Murty and Rao et al. [12] (g),(h) $\eta_{Murty\ \&\ Rao}$ and κ_j model of Poletti et al. [13].

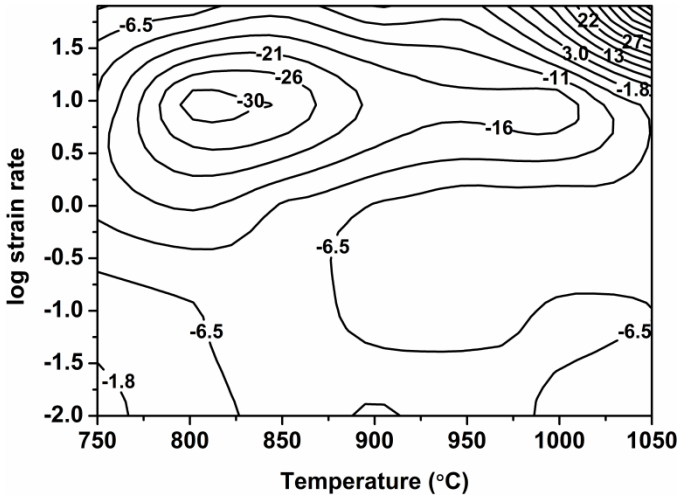

Fig. 5.27. Instability parameter α of AISI 1016 steel as a function of strain rate and temperature for a true strain of 0.6.

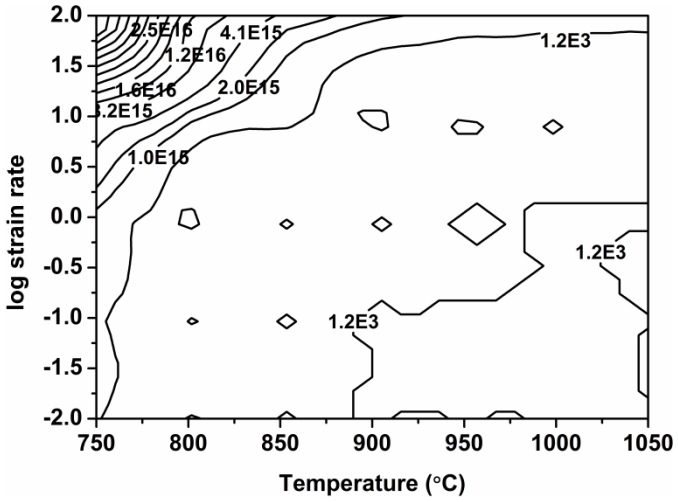

Fig. 5.28. Zener-Hollomon parameter, *Z* of AISI 1016 steel as a function of strain rate and temperature.

5.5. DISCUSSION

The following chapter discusses the microstructure of the studied alloy developed after thermomechanical treatments, its correlation with the deformation mechanisms taking place and the usability of the processing maps and constitutive equations.

5.5.1. PHASE TRANSFORMATION

The Ar_3 and Ar_1 temperatures determined from the CCC curves are higher than that determined from the CCT dilatometry (Figure 5.20). If the deformation accompanies cooling [47], the critical temperatures of the phase transformations shift to higher values. This effect can be explained by three phenomena, which can be superimposed: 1) the increment in the Gibbs energy of the austenite phase due to plastic deformation [198], 2) the presence of dislocations that increases the number of sites for heterogeneous nucleation, changing the kinetics of transformation, and 3) refinement of the austenite grains by DRX. In the second case, the high density of dislocations increases both the nucleation sites of ferrite and the diffusion of carbon [199]. Thus, the diffusion-dependent ferrite transformation is facilitated and provokes an increment in the Ar_3 temperature. The changes in the CCC curve (stress-temperature curve) are also related to the DRX of austenite which produces grain refinement and thus, an acceleration in the phase transformation kinetics by the increment in the nucleation sites [172, 206]. Finally, it should be noted that most of the hot compression experiments performed in this work are performed above the Ar_3 temperature. At 750°C, the deformation is performed in the intercritical region, and in this case, the curve obtained in figure 5.20a without deformation is used to determine the microstructure before deformation.

Deformation induced ferrite transformation (DIFT) occurs at low temperatures and low strain rates. Some DIFT can take place at 750°C, forming a ferrite which is distinguishable from the “blocky” pro-eutectoid ferrite formed before deformation. Finally, after deformation ferrite forms during cooling as a function of both the grain size and the stored energy developed during the hot deformation, as observed at 900°C in Figure 5.24. Smaller austenite grains (promoted by austenite grain refinement) shift the “nose” in the CCT diagram to the left and thus the ferrite forms during the cooling of steel.

5.5.2. MICROSTRUCTURE EVOLUTION AND PROCESSING MAPS

The deformation mechanisms will be analyzed as a function of temperature and strain rate in the single and two phases range. From the microstructural studies it can be determined that DRX of austenite takes place at high temperatures and low strain rates. Furthermore, the stress values increase steadily to a peak followed by softening towards a steady state region (Figure 5.21), typically observed during DRX. This is also in agreement with the shifting of these peaks to higher strains by increasing the strain rate and decreasing the temperature (Figure 5.21). Thus, the tendency for nucleation and growth of new grains is reduced [200] as the temperature decreases (i.e. high Z value). Parameters such as m and η are large in this range, and stability of the flow is predicted**.** On the other hand, austenite fragmentation takes place at moderate temperature, for almost all strain rates. This range is characterized by low and moderate values of η and m, since diffusion is retarded drastically due to the combination of low temperatures and high strain rates. Finally, at very high strain rates, pores are formed during deformation at the ferrite/austenite interface, as shown in figure 5.29.

As mentioned before, low temperature deformation range is characterized by the presence of both pro-eutectoid ferrite and DIFT ferrite. The formation of ferrite during deformation results in softening shown in the flow curves and which is reflected in high values of m and η, always through stable flow. Furthermore, both the ferrites are further deformed by dynamic recovery as observed in the formation of subgrains in the ferritic phase after EBSD measurements (Figure 5.30).

Processing maps in figure 5.26 show that in general, as the strain rate increases, the values of m and all η calculated with different models decrease. Both parameters are related to diffusion controlled processes and thus, to a better workability. Large values are observed at low and high temperatures. In the low temperature/low strain rate range, the diffusive processes that take part are the formation of ferrite and the dynamic recovery of ferrite occurring simultaneously. At high temperatures it is related to DRX of austenite. Furthermore, the value of m and η increase when increasing strain, indicating progress of the diffusional controlled process during deformation. There is no instability predicted for the low strain rate range.

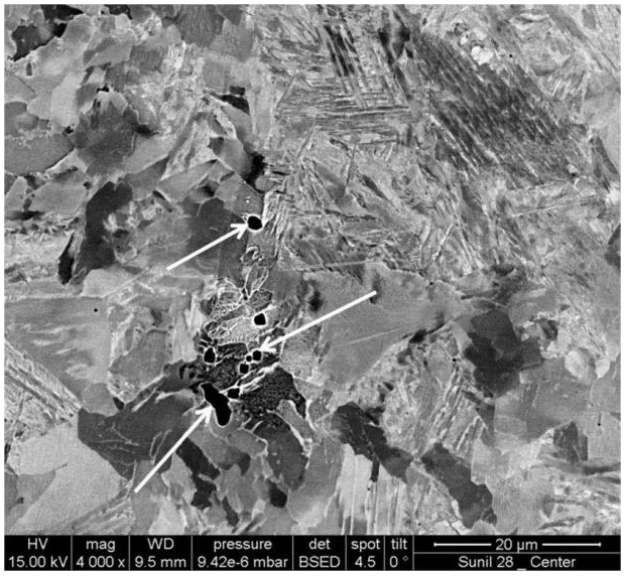

(a)

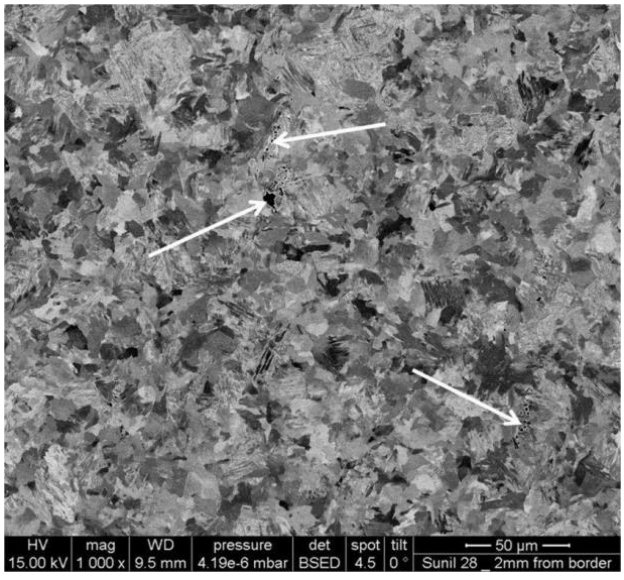

(b)

Fig. 5.29. FEG SEM (BSE mode) micrographs of AISI1016 steel after hot compression at 1050°C using a strain rate of 10 s^{-1} and true strain of 0.7. Pores are observed (shown by arrows) (a) at the center, and (b) at the edge of the deformed specimen.

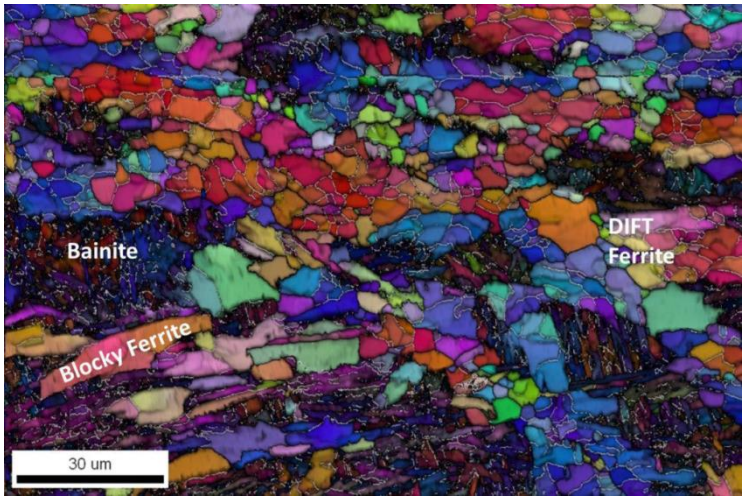

Fig. 5.30. EBSD orientation map of AISI 1016 steel specimen deformed at 750°C using a strain rate 0.1 s^{-1}. Grain boundaries are black and the sub grain boundaries are white. Load axis is vertical.

Concerning to the instability parameters, it can be observed that the instability zones predicted by all the parameters derived from DMM are spread in a wide range of strain rates and temperatures, which cannot be correlated with the microstructure since damage or flow localization was not determined, with only one exception (Figure 5.29). In general the negative values of instability parameters are calculated for the moderate/high strain rates range, characterized by less restoration in the material, where austenite is deformed by fragmentation and small deformation bands. On the other hand, α is large positive (unstable flow) at large strain rate and high temperature, which can be interpreted as a large softening produced by damage.

A representative micrograph of the specimen deformed at 10 s^{-1} up to 0.7 of strain is shown in figure 5.29, in which formation of pores is observed both at the center and near to the edge. During hot working at high strain rates, flow softening arises locally because of adiabatic heating [185,186,199], that is also shown in Table 5.3. Damage then takes place due to less restoration caused by the short times of deformation. The low restoration of the microstructure is corroborated by low values of both strain rate sensitivity and efficiency parameters. From the work on several materials, it is known that the tendency for flow localisation is reduced upon the maximisation of η and m [207]. Thus, it is found that the α parameter can predict the

damage clearly by using this concept: softening produced by either temperature increment or strain softening (large) will produce damage, if restoration (large *m*) is not enough.

5.5.3. CONSTITUTIVE EQUATIONS ANALYSIS

The constitutive equations can also be used to obtain some information about the deformation mechanisms. The flow data at true strain of 0.6 were treated using the power law (equation 4.14) and the sinh constitutive equations (equation 4.13) in order to determine the apparent activation energy. A constant parameter c = 0.014 is used for the sinh equation [63, 208]. The plots of ln σ vs ln $\dot{\varepsilon}$ and ln σ vs *1/T* [209] for both equations are shown in figures 5.31 and 5.32, respectively. The mean stress exponent *n* was found to be 8.1 for the power law equation. Due to this large value, the sinh type equation is used with a correlation coefficient (R^2=0.9702) of linear regression. Furthermore, an exponent *n* value of 3.8 is obtained, which is consistent to the dislocation creep behavior [203], meaning dislocation climb controlled [204]. The apparent activation energy calculated using the sinh type equation is 290kJ/mol, which is close to the bulk self-diffusion activation energy of austenite (reported as 270kJ/mol [210]). The constitutive equation obtained using power creep law and sinh type law over a temperature range of 750ºC to 1050°C and a strain rate range of 0.01 to 80 s^{-1} for AISI 1016 steel is given by equations 5.6 and 5.7 respectively:

$$Z = 7.17\times10^{-7}\left(\sigma_{0.6}\right)^{8.1} = \dot{\varepsilon}\exp\left(\frac{238656}{RT}\right) \tag{5.6}$$

$$Z = 2.29\times10^{10}\left[\sinh\left(0.014\sigma_{0.6}\right)\right]^{3.8} = \dot{\varepsilon}\exp\left(\frac{290000}{RT}\right) \tag{5.7}$$

Due to the large values of stress obtained during hot compression, the constitutive equation obtained using sinh type law results in more realistic values of stress exponent *n*. The results in the *n* exponent as well as in the apparent activation energy *Q* are related to dislocation controlled mechanisms, in which diffusion is needed to allow dislocations to climb. Such mechanism can be related to dynamic recovery. As observed, the constitutive equations as calculated are not sensitive to the deformation parameters of temperature and strain rate and as presented, they cannot distinguish changes in the deformation mechanisms as can be done, for example, by using strain rate sensitivity maps.

Figure 5.33 shows the variations of Zener-Hollomon parameter as a function of peak flow stress. The peak flow stress data obtained from the different hot deformation conditions are very well fitted with the Zener-Hollomon parameter with linear correlation of regression coefficient (R^2=0.98), as indicated by the figure, and is represented by equation 5.8.

$$\ln Z = 3.757 \ln\left[\sinh\left(c\sigma_p\right)\right] + 23.752 \tag{5.8}$$

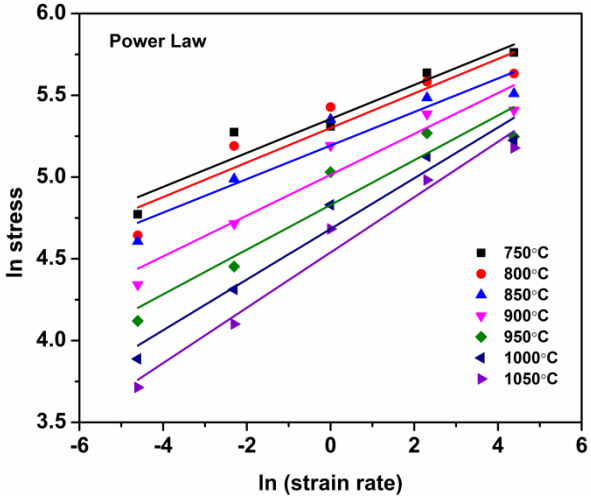

(a)

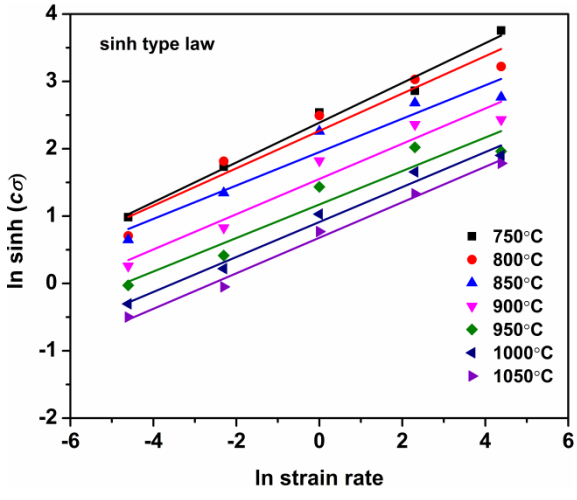

(b)

Fig. 5.31. Flow stress and strain rate plots of AISI 1016 steel for all temperatures using (a) power law, and (b) sinh type law (c = 0.014 for steel).

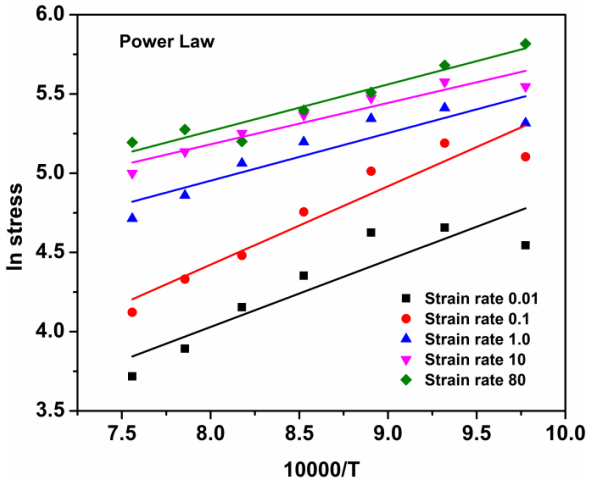

(a)

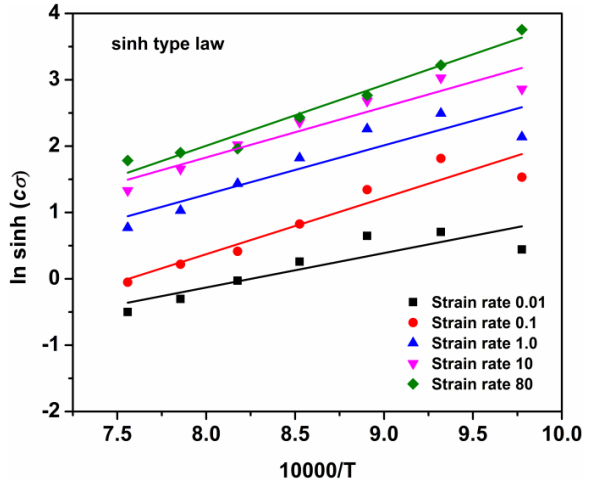

(b)

Fig. 5.32. Flow stress and temperature plots of AISI 1016 steel for all strain rates using (a) power law and (b) sinh type law (c = 0.014 for steel).

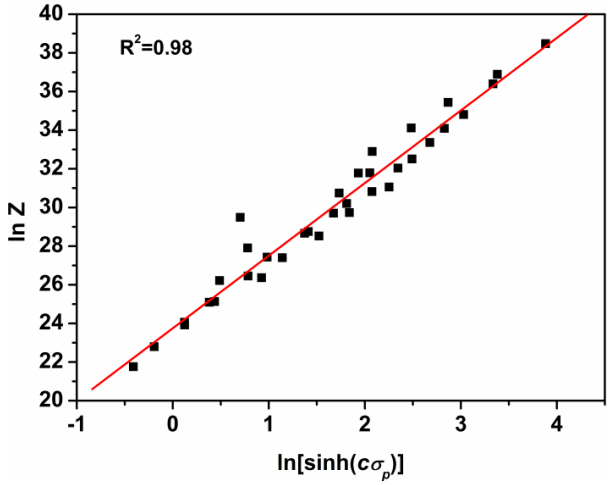

Fig. 5.33. Variation of the Zener-Hollomon parameter with peak flow stress of AISI 1016 steel.

5.6. SUMMARY

Hot deformation behavior of AISI 1016 steel is studied over wide range of temperatures and strain rates. The processing maps are developed by using dynamic materials model and modified dynamic materials model and compared with the strain rate sensitivity and the instability parameter based on the strain and temperature softening as a function of the temperature and the strain rate. Following conclusions are drawn from this work.

1. High values of η and m at low strain rates and high temperature result from dynamic recrystallization of austenite. Furthermore, high values of η and m at low strain rates and low temperatures is the result of ferrite formation and dynamic recovery of ferrite. Under these conditions, flow stability is predicted.
2. The prediction of flow instabilities is unclear for the DMM, since they predict instability in a very wide range of temperatures and strain rates. In this region, the Zener-Hollomon parameter, Z is higher, and the values of m and η were lower. Metallographic investigations have shown, that at high strain rates, damage occurs at the austenite triple grain boundary by a combination of adiabatic heating and inhibited restoration phenomena due to short deformation times.
3. It was found that the sinh type equation correlates better the flow stresses with temperature and strain rate than the power law. From the earlier, it was found that the apparent activation energy of AISI 1016 steel is 290kJ/mol, which is close to that for bulk self-diffusion in austenite meaning that deformation is controlled by diffusional processes. Furthermore, the value of the stress exponent n is 3.8, which suggests that the hot deformation is controlled by dislocation gliding and climb.
4. Smaller the Zener-Hollomon parameter, bigger amount of softening and the more easily DRX/DRV may occurs.
5. To analyse the relation between Zener-Hollomon parameter and flow stress, the sinh type equation is used over the entire deformation zone. The values of the peak flow stress, and Zener-Hollomon parameter was well related, and the pertaining equation was proposed.

EFFECT OF CARBON CONTENT (AISI 1010 AND AISI 1016 STEEL) ON MICROSTRUCTURE EVOLUTION AND PROCESSING MAPS

The stacking fault energy is decreased with the increasing carbon content of austenite [211]. This is an important factor for controlling the cross slip of dislocations. Due to low stacking fault energy higher stresses are required for cross slip. There are two significant mechanisms for restoration by DRV viz. cross slip and climb processes [211]. It is anticipated that cross slip plays an important role in DRV as compared to the climb process for high *Z* value deformations. Thus, at high *Z* conditions the low carbon steel shows higher softening rate. This results in the lower flow stress values in low carbon steel as compared to high carbon steel as reported by the researchers [212, 213]. Similar results were found in this study in the case of AISI 1010 steel and AISI 1016 steel. The peak flow stress increases as the amount of the carbon content increased as shown in figure 5.4 and figure 5.21. At low *Z* conditions, the kinetics of DRV is improved as the carbon content increased, since the climb is controlled by the diffusion process [214]. The DRX rate is increased with increasing the carbon content due to the increasing rate of diffusion of carbon. Therefore, the thermally activated processes like nucleation and growth of the recrystallized phase are supported with the increasing carbon content i.e. the kinetics of DRX would be increased with the carbon content as shown in figures 5.7-5.9 and 5.23-5.25.

The value of the strain rate sensitivity parameter, *m* is increased along with the workability region with the increase in carbon content. The same trends are followed by the η_{Prasad} and $\eta_{Murty\ \&\ Rao}$ as shown in figures 5.10 and 5.26. The apparent activation energy for AISI 1010 steel and AISI 1016 steel are 177kJ/mol and 290kJ/mol, respectively. This shows that the apparent activation energy increased with the increase in the carbon content. It is evident that the value of the Zener-Hollomon parameter, *Z* is also high for the higher carbon content steel (Figures 5.13 and 5.28). Laasaoui et al. [215] reported that at high *Z* parameter, the critical strain required for the DRX would be very high, thus DRV would be the dominant softening mechanism.

C. LOW CARBON Ti-Nb MICROALLOYED STEEL

After studying the hot deformation behavior of plain carbon steels with their ferrite pearlite microstructures, a low carbon Ti-Nb microalloyed steel was selected for study. The addition of precipitate forming elements such as Ti, Nb, and V, individually or in combination will strengthen the steel by a combination of precipitation strengthening and grain refinement. Therefore, for the higher strength steel it is economical to replace the heat treated steel plate or strip with the equivalent strength microalloyed steel without the requirement of heat treatment. In automotive application, hot rolled steels are used rather than the quenched and tempered steels, not only due to energy and cost factors, but also inherent metallurgical demerits such as retained austenite, quench cracking, distortion and residual stresses [216].

The as-cast microstructure of low carbon Ti-Nb microalloyed steel (Ti-Nb MA) is relatively finer with the fine precipitates. The microstructural evolution is significantly influenced due to the presence of precipitates in the microstructure during hot working. The pinning effect prevents the grain growth and might retard the evolution of UFG structure. To study these aspects, a low carbon Ti-Nb microalloyed steel with carbon content close to that of AISI 1016 steel is selected for the hot deformation tests. Therefore, the microstructural evolution during hot deformation can be compared with the presence or absence of precipitates. The hot deformation behavior of Ti-Nb MA steel is divided into two sections namely: (i) results, and (ii) discussion.

5.7. RESULTS

5.7.1. AS-CAST MICROSTRUCTURE

Figure 5.34 shows the light optical microstructure of low carbon Ti-Nb microalloyed steel in as-received condition. It consists of two phases viz. ferrite phase lighter in color, and cementite phase darker in color (as marked by the arrows). The SEM micrograph in secondary electron mode is shown in figure 5.34b. The EBSD map of microalloyed steel in as-received condition is shown in figure 5.34c. The unindexed white region (shown by arrows) represents either a grain boundary region or a non-ferritic phase. The compression axis is horizontal and the average grain size is 15 μm.

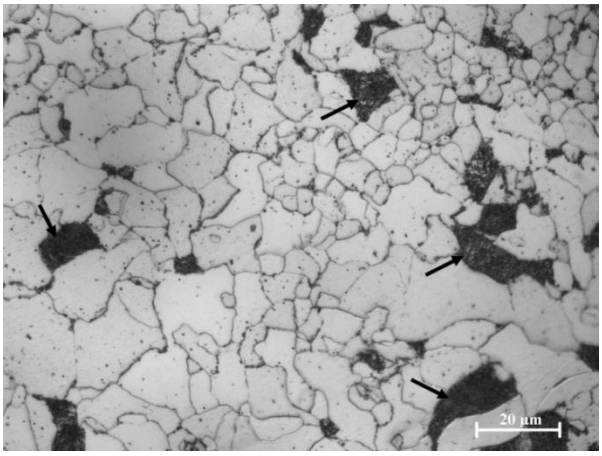

(a)

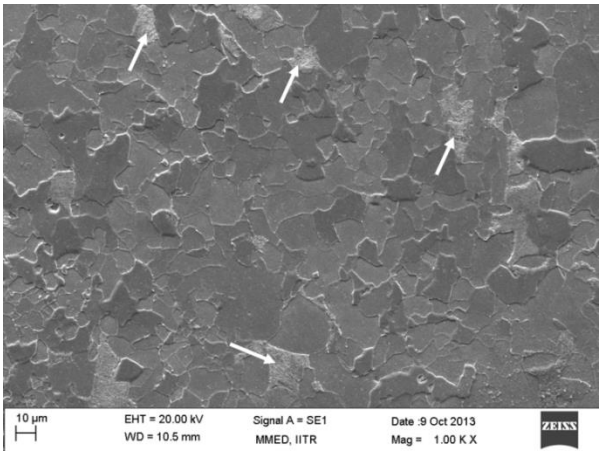

(b)

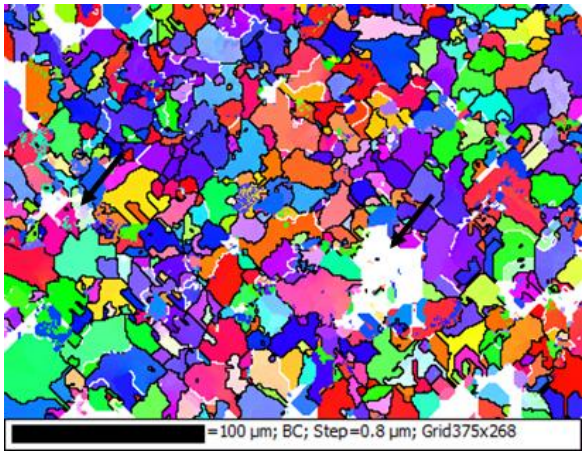

(c)

Fig. 5.34. As-received microstructure of low carbon Ti-Nb microalloyed steel using: (a) light optical microscopy, (b) scanning electron microscopy, and (c) EBSD. Pearlite is shown by arrows.

The microstructure of undeformed steel specimen heated to 1050°C, soaked for 2 minutes and followed by water quenching is shown in figure 5.35a. It consists entirely of martensite which is confirmed from its average micro-hardness value of 568 VHN. Figure 5.35b shows the light optical micrograph of the undeformed steel specimen water quenched from 750°C after austenitization. It also shows martensite phase formed from austenite during cooling. Thus, in this work, most of the hot compression tests of SAILMA grade microalloyed steel were carried out in single austenite phase field, except the ones carried out at 750°C.

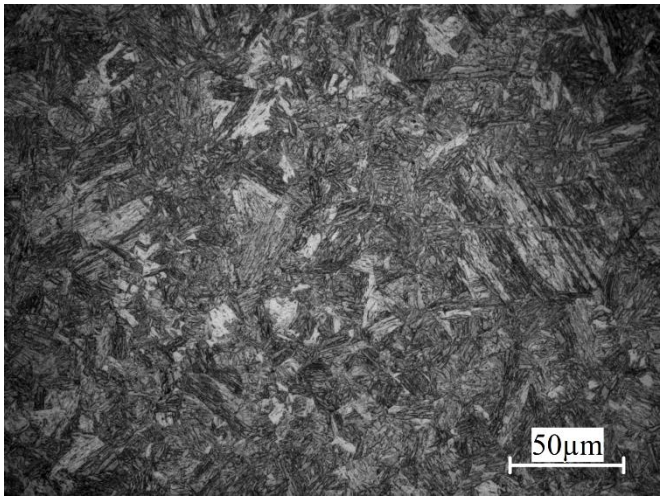

(a)

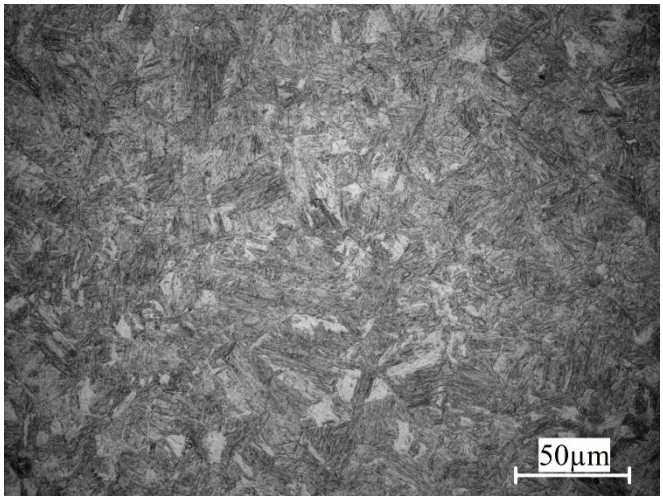

(b)

Fig. 5.35. Optical micrographs of microalloyed steel specimens heated to 1050°C for 2 minute followed by (a) water quenching, (b) cooling at $1°Cs^{-1}$ to 750°C followed by water quenching.

All the specimens were heated at the rate of 5°Cs^{-1} up to austenitization of temperature 1050°C and soaked for 2 minutes. They were then cooled down at the rate of 1°Cs^{-1} to deformation temperatures in the range of 750°C-1050°C with 50°C intervals. Specimens were deformed at constant strain rates of 0.01 s^{-1}, 0.1 s^{-1}, 1 s^{-1}, 10 s^{-1} and 80 s^{-1}. Total true strain was 0.7. After deformation, in-situ water quenching was employed immediately in order to freeze the microstructure and avoid any metadynamic or static phenomena that could happen at the test temperature or during slower cooling.

Typically, workers have used 1150°C to 1300°C as austenitizing temperature in order to dissolve the Nb carbides, Nb carbonitrides. Towards the lower end of this range, there is incomplete dissolution of carbides, as reported in many studies [60, 61, 72]. The austenitizing temperature chosen in the present work is 1050°C which is also lower than the temperatures required for complete dissolution of Nb(C,N) and TiC. In fact, the amount of Nb dissolved at 1050°C is calculated using the formulae [217]:

$$\log[Nb][C] = -\frac{6770}{T} + 2.26 \qquad (5.9)$$

$$\log[Ti][C] = -\frac{7000}{T} + 2.75 \qquad (5.10)$$

The values for dissolved Nb and Ti in the present work as determined using equations 5.9 and 5.10 are 0.01 and 0.022, respectively.

5.7.2. PHASE TRANSFORMATION CHARACTERIZATION

The compressive stress versus temperature curve obtained from the CCC test and the continuous cooling transformation (CCT) curve are drawn from the data obtained from the hot deformation experiments and are shown in figure 5.36. The phase transformation in the material is represented by the variation in the slope of the curve. The inflection points during cooling represents the Ar_1 and Ar_3 temperatures. The Ar_3 and Ar_1 temperatures for microalloyed steel are estimated to be 732°C and 634°C using the CCT curve (figure 5.36a) whereas 751°C and 710°C using the CCC curve (figure 5.36b).

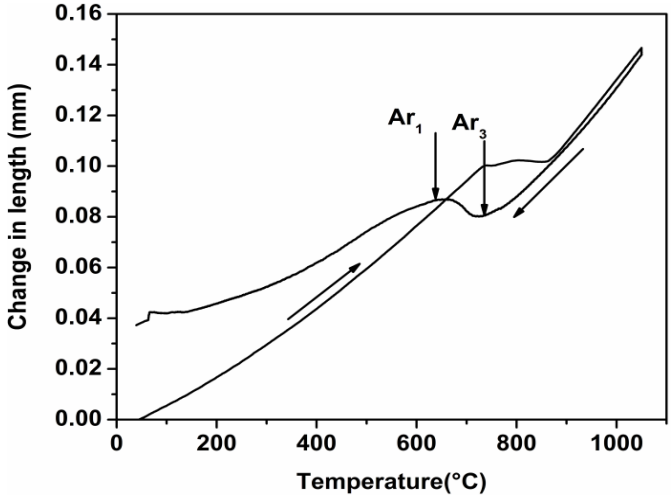

(a)

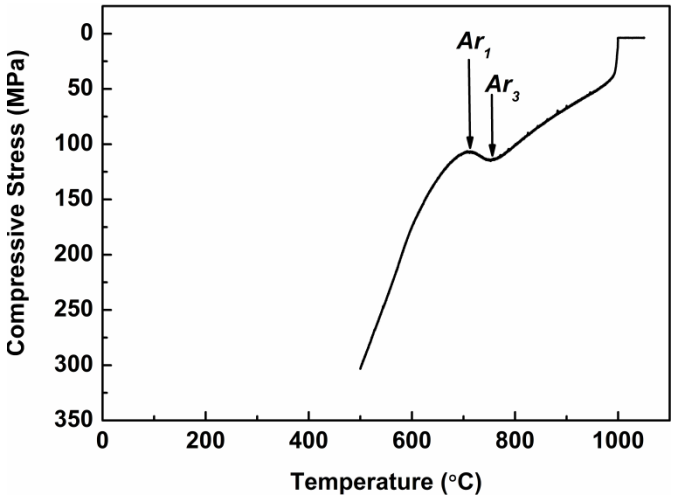

(b)

Fig. 5.36. (a) Results of the dilatometry test and (b) the continuous cooling compression curve obtained from CCC test, performed on low carbon Ti-Nb microalloyed steel. Inflection points correspond to the Ar_1 and Ar_3 temperatures.

5.7.3. TRUE STRESS-TRUE STRAIN CURVES

The flow curves (true stress vs true strain) corresponding to the test temperatures of 750°C, 800°C, 850°C, 900°C, 950°C, 1000°C, and 1050°C are shown in figure 5.37. At very high strain rate of 80 s^{-1}, load cell shows ringing effect because of high speed testing when the deformation is carried out which leads to an oscillating flow curve for testing at very high strain rate [218]. The true flow stress showed dependence on the strain rate and temperature. The stress-strain curves determined by hot compression testing at lower strain rates (0.01 s^{-1}) at low temperatures (750°C-850°C), lower to moderate strain rates (0.01-0.1 s^{-1}) at moderate

temperatures (900°C-950°C), and lower to higher strain rates (0.01-10 s^{-1}) at high temperatures (1000°C-1050°C) show a peak after hardening, which is followed by softening. At higher strain rates the flow stress gradually increases over the entire strain range of testing. The stress-strain curves show that the stress peaks seen at lower strain rates are shifted to higher strains with increasing the strain rate. With an increase in deformation temperature, peak in the flow curve is observed even at higher strain rates. At high temperature of 1050°C and lowest strain rate of 0.01 s^{-1} used in this work, two stress peaks are seen in the flow curve. These correspond to the multiple peaks DRX wherein grain coarsening results [219]. Figure 5.38a shows that for a fixed strain rate, as the temperature decreases work hardening dominates and the values of flow stress progressively increase. Further, for fixed temperature the flow stress increases with an increase in strain rate (Figure 5.38b).

The maximum increment of temperature (*dT*) measured due to adiabatic heating are summarized in Table 5.4 as a function of the strain rate and the temperature. The largest values of *dT* are observed at low temperatures and high strain rates. These values are used in the calculation of flow instability parameter *c* in equation 4.11.

Table 5.4. Maximum increment in temperature during compression of AISI 1010 steel.

Deformation Temperature (°C)	dT (°C) at the strain rate of				
	0.01 s^{-1}	0.1 s^{-1}	1 s^{-1}	10 s^{-1}	80 s^{-1}
750	4	11	8	9	18
800	9	12	10	25	26
850	7	11	10	20	22
900	10	11	6	23	25
950	9	10	6	21	21
1000	8	12	7	19	16
1050	12	14	11	15	19

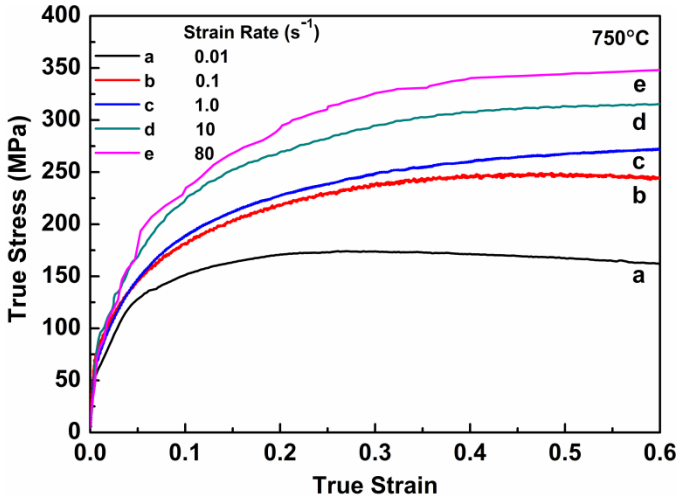

(a)

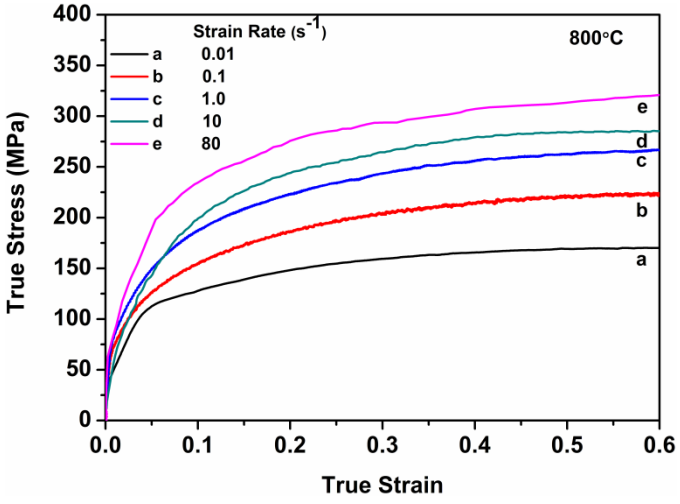

(b)

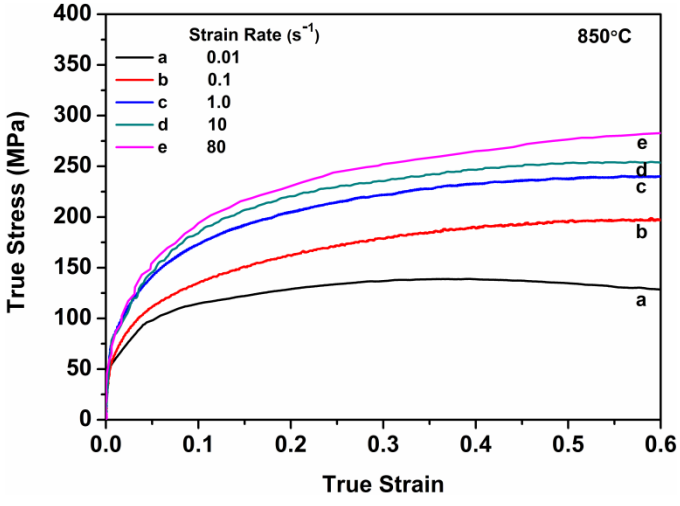

(c)

Fig. 5.37. Contd…

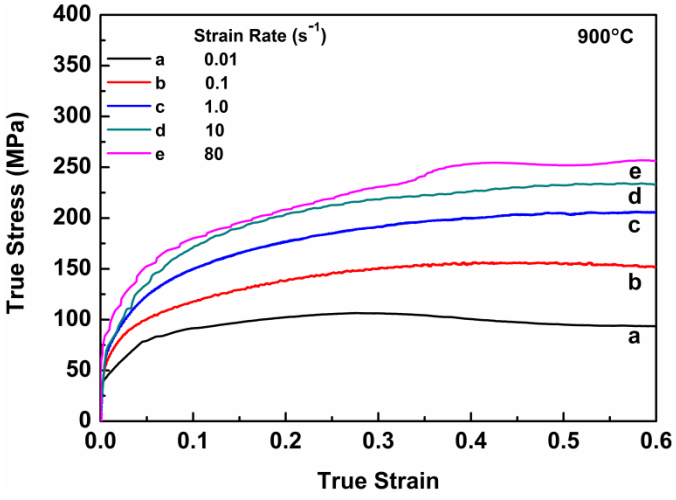

(d)

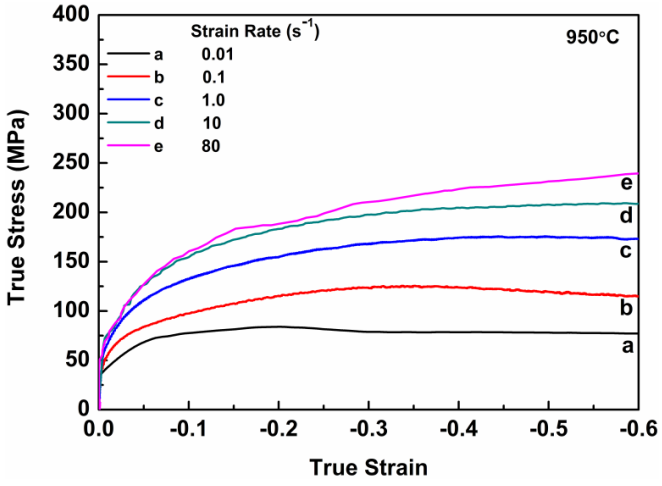

(e)

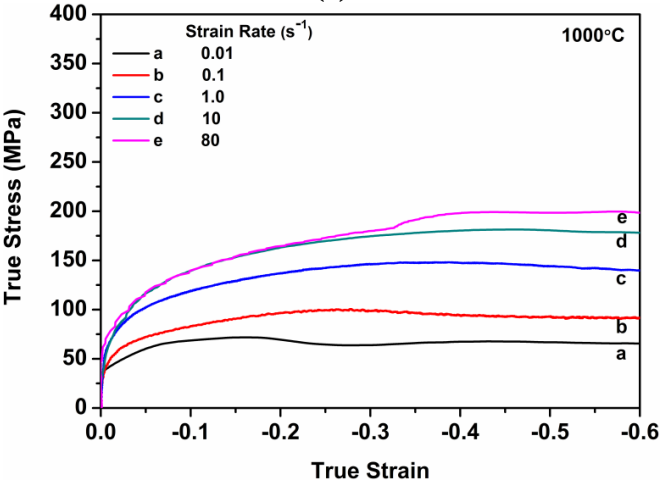

(f)

Fig. 5.37. Contd…

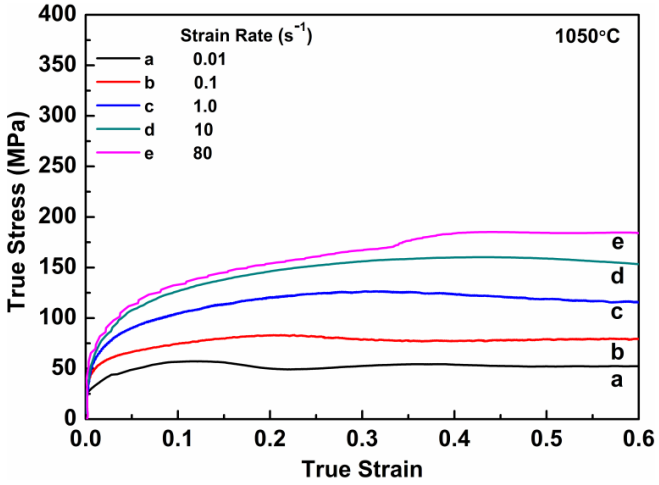

(g)

Fig. 5.37. Flow curves of Ti-Nb microalloyed steel in compression obtained using different strain rates after austenitization at 1050°C during 5 minutes, and at deformation temperatures of (a) 750°C, (b) 800°C, (c) 850°C, (d) 900°C, (e) 950°C, (f) 1000°C, and (g) 1050°C.

5.7.4. DEFORMED SPECIMEN CHARACTERIZATION

The hot deformed specimens were cut along the center of the compression axis and mounted on the resin to ease for the metallographic procedures. A constant of the specimen was selected for the microstructural examination in order to make microstructural analysis as systematic as possible in the light optical microscopy. To minimize the sample-die friction effect the central region of the specimen was chosen for the analysis because the dead metal zones are exhibited at the ends of the deformed barreled specimens.

The optical micrographs of water-quenched specimens of microalloyed steel after hot deformation at temperature of 750°C and at different strain rates are shown in figure 5.39. All the specimens show a martensitic microstructure (grey) with different amounts of ferrite (bright) formed during, and after deformation. At 750°C and at a strain rate of 0.01 s^{-1}, the amount of ferrite (shown by arrow) is the highest (about 27%) as shown in figure 5.39a, and is significantly lower for other strain rates. It is about 15% and 2% for strain rates of 1 s^{-1} and 80 s^{-1}, respectively. There is no pro-eutectoid ferrite before deformation and almost entire ferrite formed during the hot deformation and is strain induced ferrite.

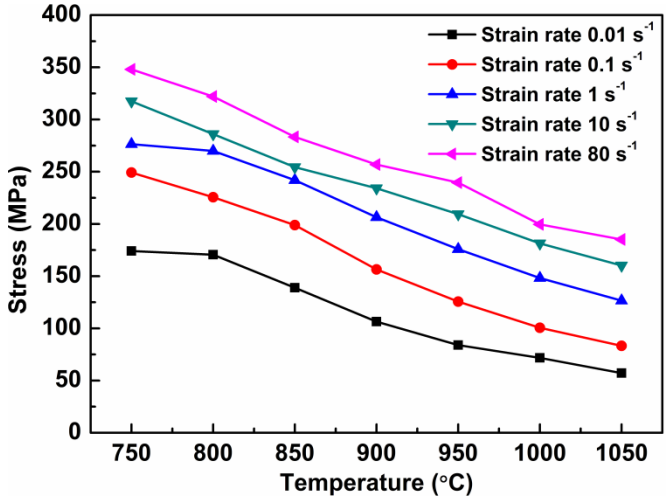

(a)

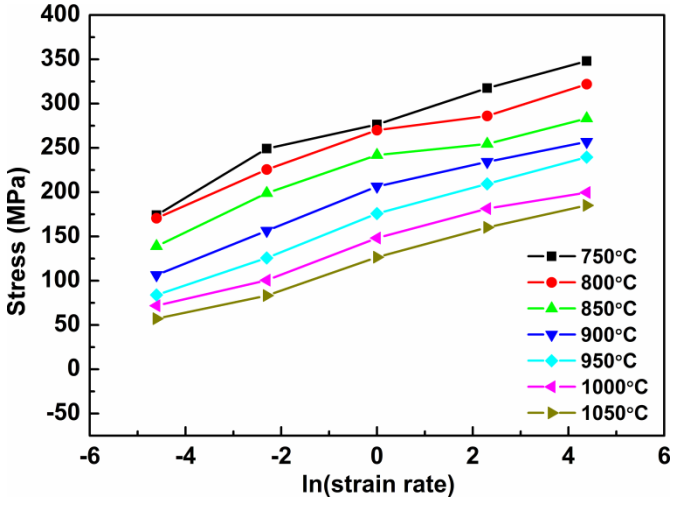

(b)

Fig. 5.38. Relationship between flow stress and (a) the deformation temperatures, (b) the logarithm of strain rate at true strain of 0.6.

The ferrite observed at 900°C (Figures 5.40a, b, c) possibly formed during cooling. In this case, the amount of ferrite (shown by arrow) is high (about 17%) for intermediate strain rate of 1 s^{-1} and is significantly lower for the other strain rates used. At deformation temperature of 1050°C, and at strain rate extremities of 0.01 s^{-1} and 80 s^{-1}, only martensite is observed in the microstructures (Figures 5.41a, c). The formation of about 7% acicular ferrite (shown by arrow) is observed, at the grain boundaries at intermediate strain rate of 1 s^{-1} (Figure 5.41b).

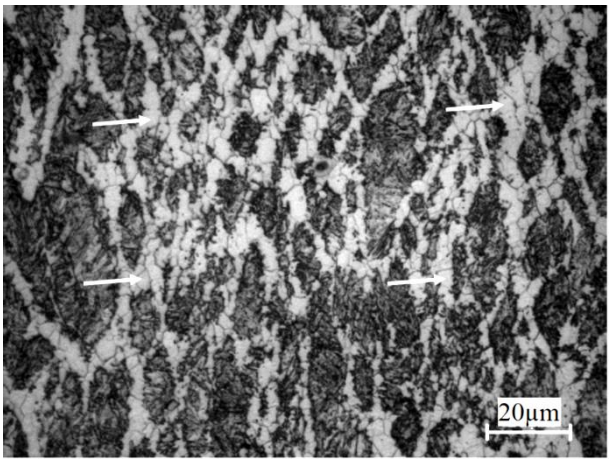

(a)

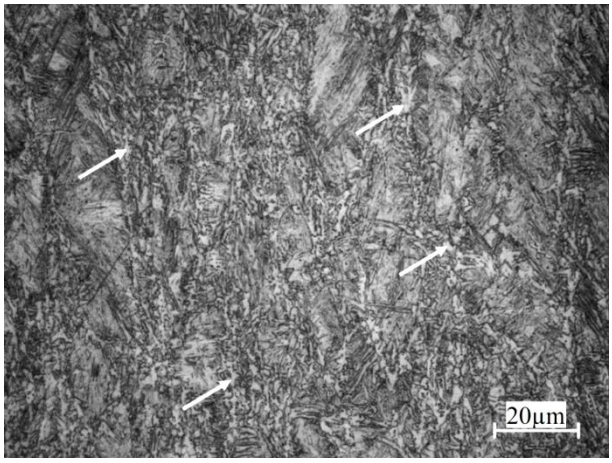

(b)

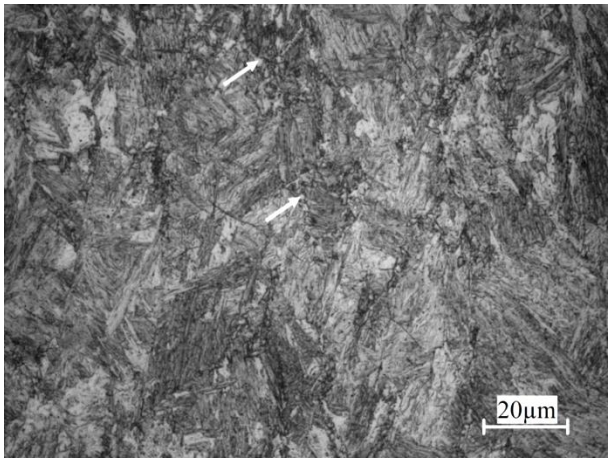

(c)

Fig. 5.39. Optical micrographs of water quenched Ti-Nb microalloyed steel specimens after hot deformation at 750°C and strain rates of (a) 0.01 s^{-1} (b) 1 s^{-1} (c) 80 s^{-1}. Axis of compression is horizontal.

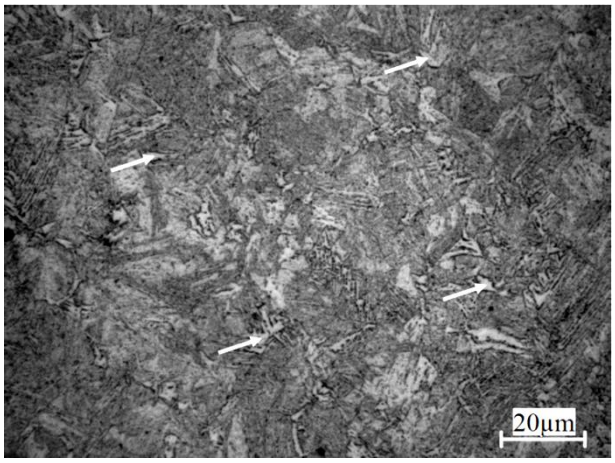

(a)

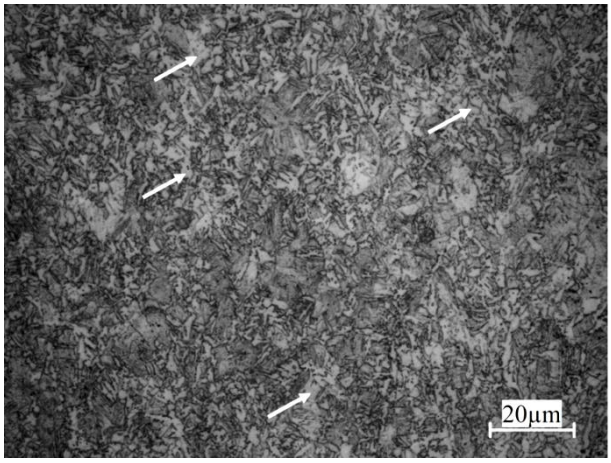

(b)

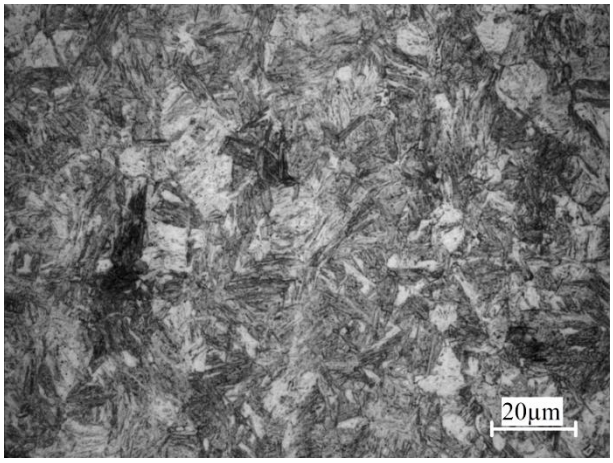

(c)

Fig. 5.40. Optical micrographs of water quenched Ti-Nb microalloyed steel specimens after hot deformation at 900°C using strain rates of (a) 0.01 s^{-1} (b) 1 s^{-1} (c) 80 s^{-1}. Axis of compression is horizontal.

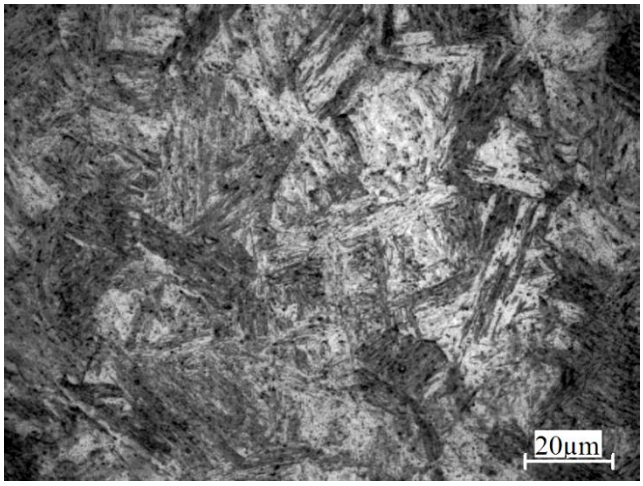

(a)

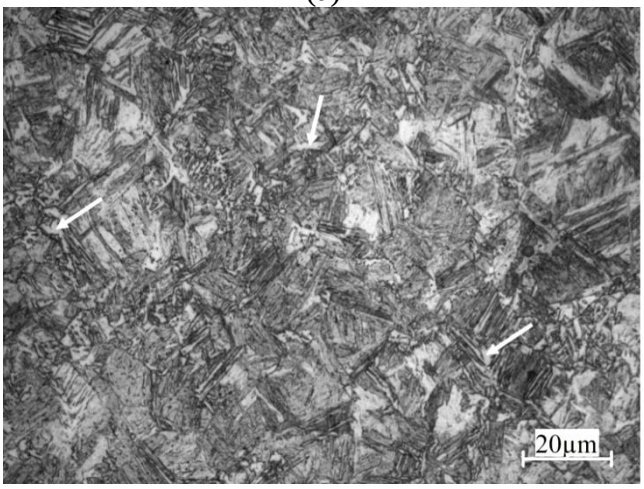

(b)

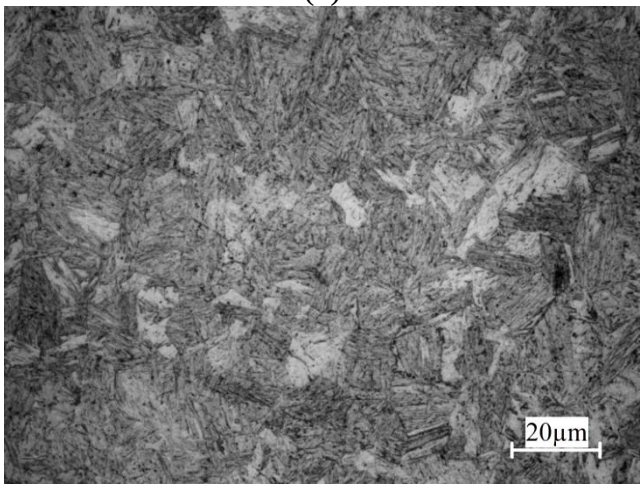

(c)

Fig. 5.41. Optical micrographs of water quenched Ti-Nb microalloyed steel specimens after hot deformation at 1050°C and strain rates of (a) 0.01 s^{-1} (b) 1 s^{-1} (c) 80 s^{-1}. Axis of compression is horizontal.

5.7.5. PROCESSING MAPS

Processing maps for strain values of 0.3 and 0.6 are shown in figure 5.42. The iso-efficiency (η) lines are shown in the plot of log $\dot{\varepsilon}$ vs T and the domain of instability parameter shown by shaded area is superimposed. In entire test zone, the strain rate sensitivity maps (Figures 5.42a, b) show positive values of m i.e. no instability is predicted when $D = P$. Large m values are observed at lower strain rates as represented by SEM micrograph of figure 5.43a which shows crack/void free SEM microstructures consisting of ferrite and martensite phases. The value of m decreases as the strain rates increase for all deformation temperatures. The iso-efficiency lines of η_{Prasad} are shown in figures 5.42c and 5.42d. Instability parameter (ξ) of Prasad et al. is shown by the superimposed shaded area. The η_{Prasad} values follow the same tendency as the m values, which can be inferred from the equation 4.2. This is confirmed by the fully recrystallized microstructure of figure 5.43b and from the flow behavior of (900°C, 0.01 s^{-1}) specimen shown in figure 5.37d. The value and the domain size of η_{Prasad} increased with the strain. Figures 5.42e and 5.42f depict the iso-efficiency lines and corresponding κ instability domains as shown by shaded area for $\eta_{Murty\ \&\ Rao}$. Large values of $\eta_{Murty\ \&\ Rao}$ are observed at low to moderate strain rates and for all deformation temperatures. Instability areas predicted by ξ are smaller than those predicted by κ. As the strain increases, the predicted expanse and the values of $\eta_{Murty\ \&\ Rao}$ increase. Iso-efficiency lines for $\eta_{Murty\ \&\ Rao}$ and the κ_j instability domains (shaded area) are shown in figures 5.42g and 5.42h. The region shown by the values of $\eta_{Murty\ \&\ Rao}$ is almost similar to that of strain rate sensitivity m and η_{Prasad}, while the instability zones predicted by κ_j are smaller than those predicted by either ξ or κ parameters.

Figure 5.44 shows the instability parameter, α for true strain of 0.6, calculated using the equation 4.10. The entire test zone shows the negative values, represents no flow localization takes place. Figure 5.45 shows the Zener-Hollomon parameter, Z, on the axis of temperature and strain rate, which was determined from the flow stress data obtained from the hot deformation tests. It is obvious that with increasing the temperature and decreasing the strain rate, the Z decreases. The Z is lower in the stable region where the power dissipation efficiency is high, and higher in the flow instability region as shown in figures 5.42 and 5.45.

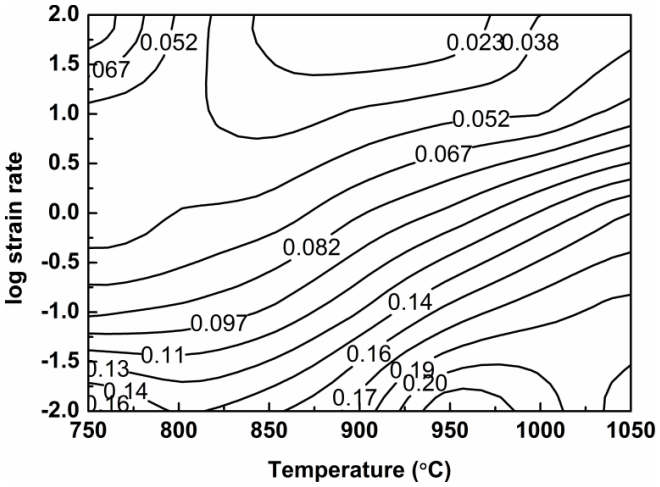

(a)

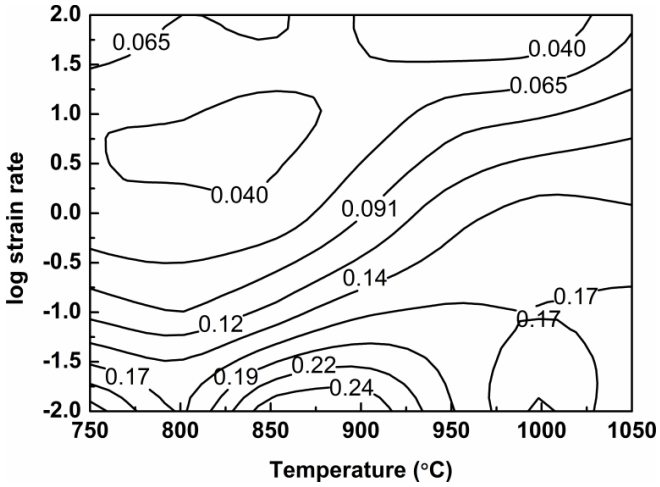

(b)

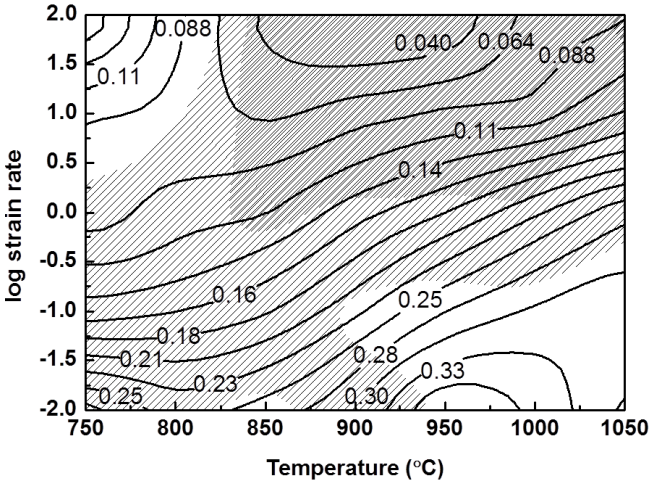

(c)

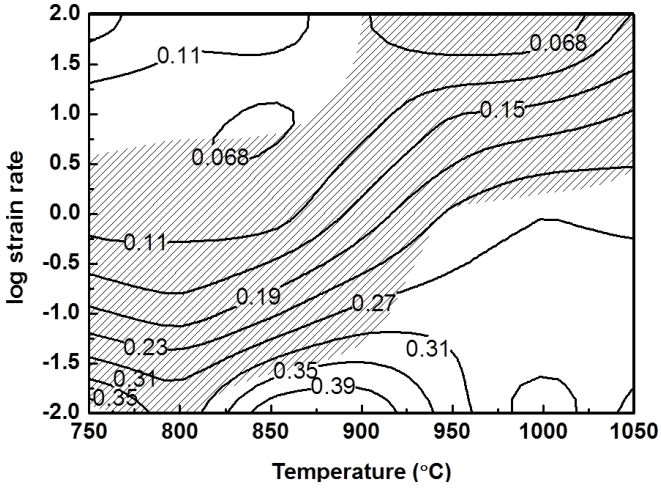

(d)

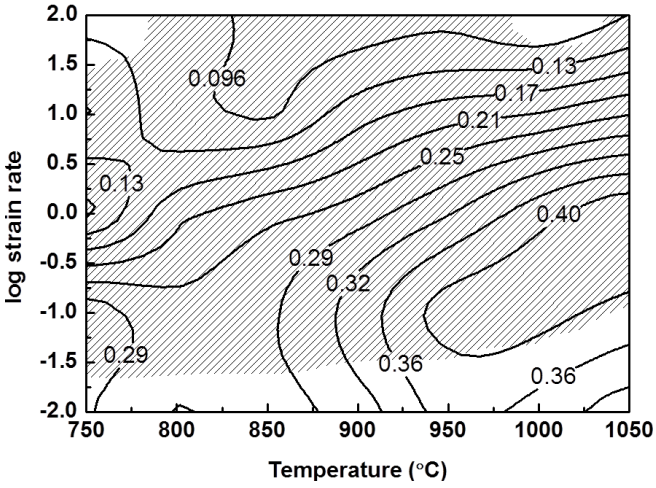

(e)

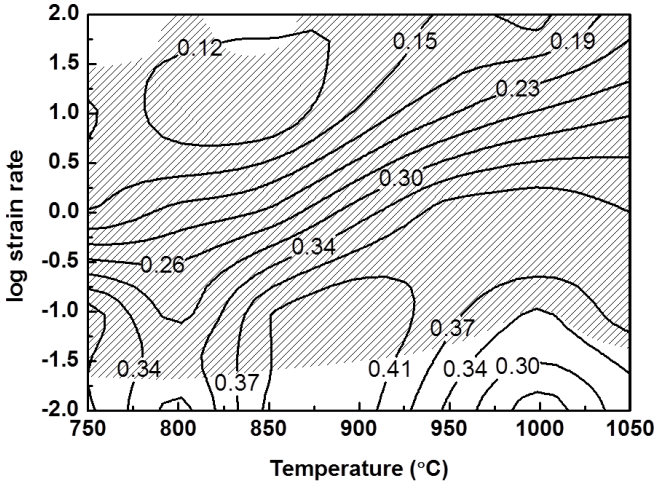

(f)

Fig. 5.42. Contd…

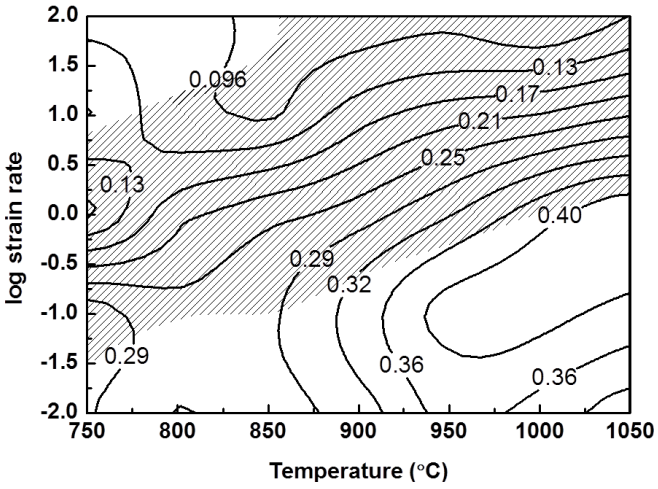

(g)

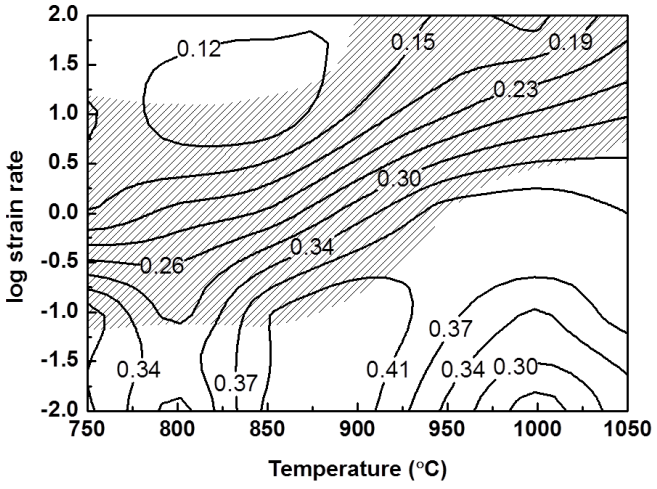

(h)

Fig. 5.42. Processing maps constructed using different models to study the workability of Ti-Nb microalloyed steel as a function of temperature and strain rate for strain of 0.3 (a,c,e,g) and 0.6 (b,d,f,h). (a),(b) strain rate sensitivity m, (c),(d) η and ξ using DMM of Prasad et al. [10] (e),(f) η and κ using modified DMM of Murty and Rao et al. [12] (g),(h) $\eta_{\text{Murty \& Rao}}$ and κ_j model of Poletti et al. [13].

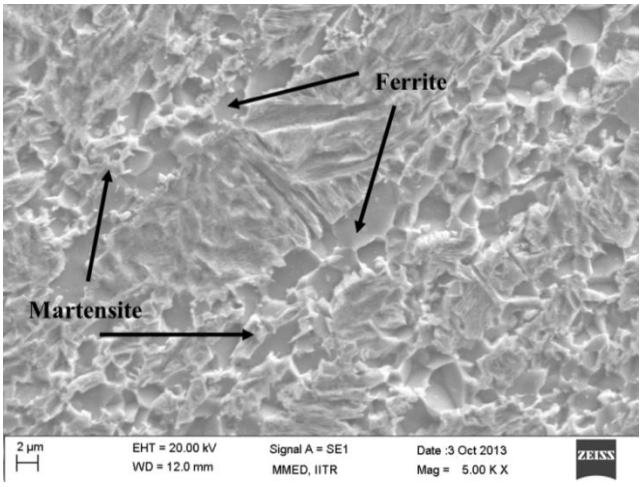

(a)

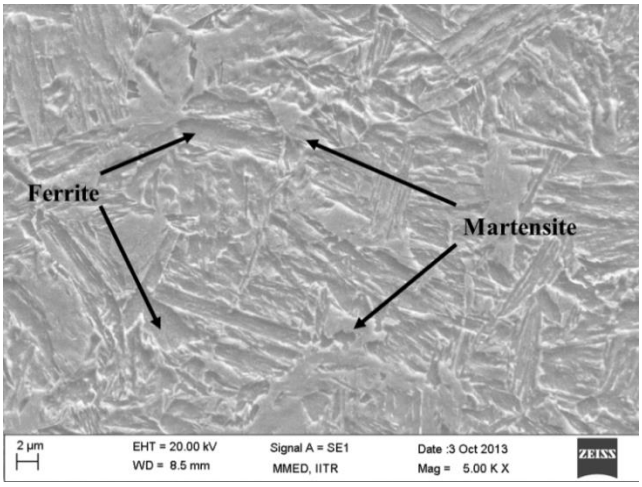

(b)

Fig. 5.43. SEM (SE mode) micrographs of Ti-Nb microalloyed steel after hot compression up to true strain of 0.7 at (a) 750°C and strain rate of 0.01 s^{-1} (b) 900°C and strain rate of 0.01 s^{-1}. Ferrite and martensite are observed (shown by arrows).

Figures 5.37, 5.42 and 5.45 show the relationships among flow stress, DRX, DRV, flow instability and Zener-Hollomon parameter. It can be observed that the flow stress decreases with decreasing the Zener-Hollomon parameter for Ti-Nb microalloyed steel. Lower the Zener-Hollomon parameter, larger the flow softening and more easily the DRX occurs.

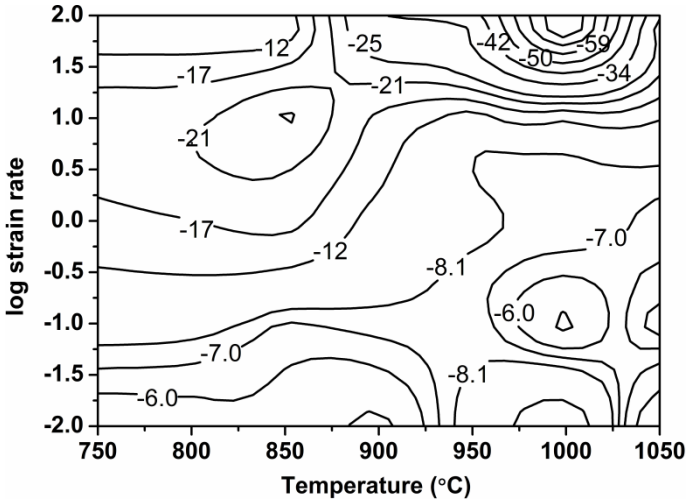

Fig. 5.44. Instability parameter, α of Ti-Nb microalloyed steel as a function of strain rate and temperature for a true strain of 0.6.

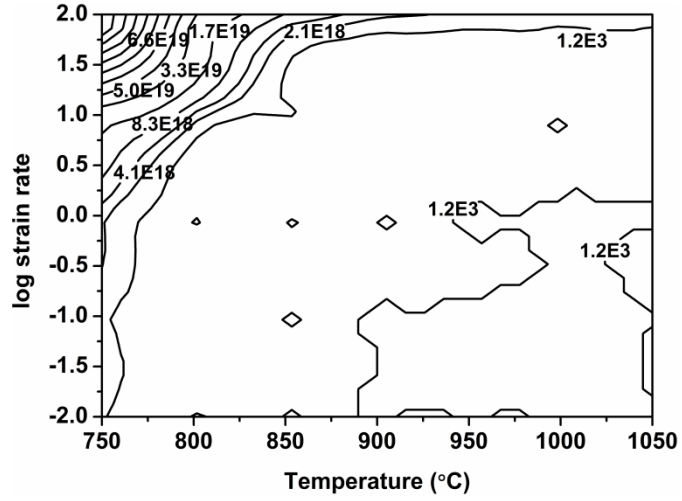

Fig. 5.45. Zener-Hollomon parameter, *Z* of Ti-Nb microalloyed steel as a function of strain rate and temperature.

5.8. DISCUSSION

Ar_3 and Ar_1 temperatures determined from the CCC curves are higher as compared to that determine with the help of CCT dilatometry as shown in figure 5.36. The changes in the CCC curve (stress-temperature curve) are related to the γ / α transformation [61, 206]. If the deformation accompanies cooling [47], the critical temperatures of the phase transformations shift to higher values. The reasons for this difference are discussed earlier for low carbon steels. Finally, it should be noted that all the hot compression experiments were performed above the Ar_3 temperature in this work.

5.8.1. MICROSTRUCTURE EVOLUTION AND PROCESSING MAPS

From the microstructural studies it can be determined that DRX of austenite takes place at high temperatures and low strain rates. At high temperatures and low strain rates, stress values increase steadily to a peak followed by softening towards a steady state region (Figure 5.37). This type of flow behavior can be related with DRX. The onset of DRX was observed when the critical strain (ε_c) was reached, which is 0.70 to 0.83 times of peak strain [77]. The work hardening exceeds the dynamic softening at the beginning of deformation, due to the rapid multiplication of dislocations. This leads to an increase of flow stress. This is also in agreement with the shifting of these peaks to higher strains with increasing the strain rate and or decreasing the temperature (Figure 5.37). This is due to the addition of Nb and Ti, which retard the DRX due to dynamic precipitation of complex Nb-Ti carbonitrides [78, 220]. Dynamic softening mechanisms such as DRX and dynamic recovery start as the strain increases. If the rate of the dynamic softening is higher than that of work hardening, the flow stress gradually decreases and finally a steady state is reached [66]. The tendency for nucleation and growth of new grains is reduced [200] as the strain rate increases or the temperature decreases which corresponds to a high Z value. Parameters such as m and η are moderate in this range, and the flow is stable**.** As compared to low plain carbon steels [221], the flow behavior is significantly altered due to the addition of Nb and Ti, which produce the strong retardation of DRX. It is observed that the values of peak stress and steady state stress are also increased due to addition of Nb and Ti as compared to the similar plain low carbon steel.

Strain induced ferrite transformation occurs at low temperature of 750°C and at all strain rates. In this range the prior austenite grains remained elongated and the necklace ferrite was formed in the austenite grain boundary. Because of a combination of low temperatures and high strain rates (80 s^{-1}), diffusion is relatively restricted as compared to other test conditions employed in the work. This is reflected in moderate values of *m* and η. At intermediate temperature of 900°C and low strain rate of 0.01 s^{-1} high values of *m* and η are obtained along with stable flow. However, at deformation temperature of 1000°C and strain rate of 10 s^{-1} and 1050°C and strain rate of 80 s^{-1}, pores/voids are formed during hot deformation. These can be seen in the SEM micrographs of figure 5.46a and 5.46b, respectively. To avoid the formation of pores/voids, the strain rate sensitivity, η of Prasad et al. and η of Murty and Rao values should be high together with positive values for the instability parameters (stable flow). When the specimen deformed at 1000°C with the strain rate of 10 s^{-1}, the value of strain rate sensitivity *m* is 0.084, η of Prasad el al. is 0.15, and η of Murty and Rao is 0.26, respectively. However, the instability parameters, ξ, κ, κ_j show negative values which represent the unstable flow. Whereas at the deformation temperature of 1050°C and strain rate of 80 s^{-1}, the values of strain rate sensitivity *m* is 0.059, η of Prasad el al. is 0.11, and η Murty and Rao is 0.21, respectively but all the instability parameters are negative that show unstable flow.

For the hot deformation at 750°C, amount of ferrite (about 27%) is highest for lowest strain rate of 0.01 s^{-1} (Figure 5.39a) and is significantly lower for the other strain rates used in this work because of deformation induced ferrite transformation (DIFT). After deformation, ferrite forms as a function of both the grain size and the stored energy developed during the hot deformation. Thus, small grains and high stored energy accelerate the formation of ferrite during cooling. When the hot deformation is performed at 900°C and strain rate of 1 s^{-1}, the austenite refinement promotes the ferrite nucleation at their grain boundaries (Figure 5.40b) as the CCT curve is shifted towards the left and the nose is intercepted during cooling. Whereas, when the hot deformation is performed at the very high strain rate of 80 s^{-1}, DRX of austenite is not observed as is evident from the absence of a peak in the flow curve (Figure 5.37d). Therefore, there is no ferrite formation during cooling as shown in figure 5.40c.

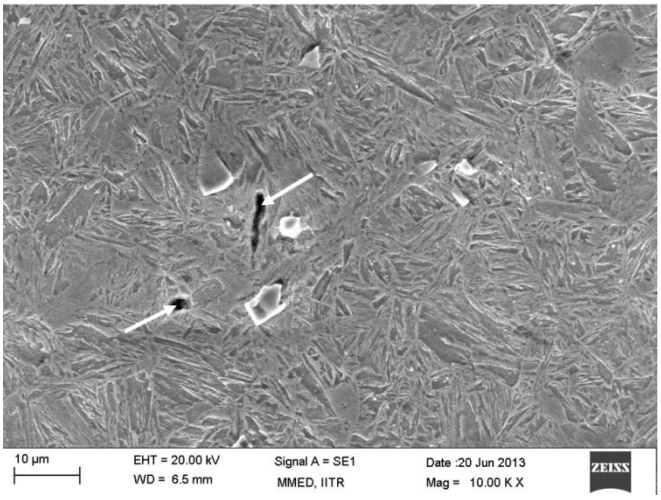

(a)

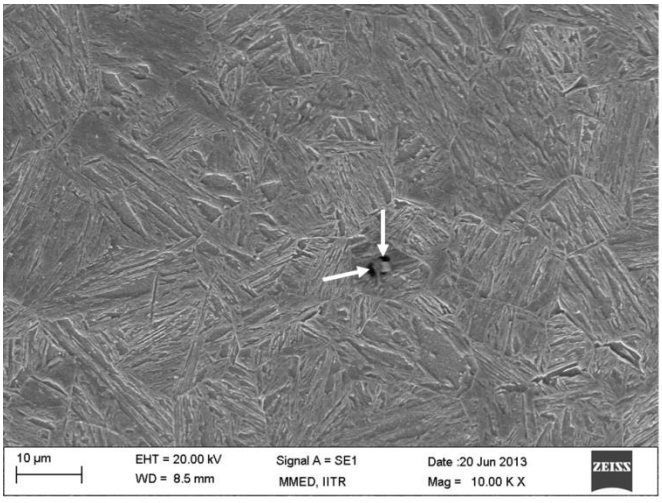

(b)

Fig. 5.46. SEM (SE mode) micrographs of Ti-Nb microalloyed steel after hot compression up to true strain of 0.7 at (a) 1000°C and strain rate of 10 s^{-1}, and (b) 1050°C and strain rate of 80 s^{-1}. Pores are observed (shown by arrows).

Processing maps in figures 5.42a to 5.42f show, in general that, as the strain rate increases, the values of *m* and all the η values calculated from different models decrease. The strain rate sensitivity corresponds to the influence of the strain rate on the deformability of material. Larger *m* values result in better workability as these are related to diffusion controlled processes at lower strain rates. Furthermore, these large values are observed at intermediate temperatures. In the low temperature-low strain rate range, the diffusive processes take part in

the formation of ferrite and the occurrence of dynamic recovery of ferrite simultaneously. At high temperatures and high strain rates the higher efficiency values are related to DRX of austenite which is a diffusion controlled phenomena. Furthermore, the value of m and η are high at moderate temperatures and low strain rates, indicating the occurrence of the diffusion controlled processes during deformation. There is no instability predicted in this range.

The instability zones predicted by all these models for both strains of 0.3 and 0.6 are mostly confined to high strain rates. Representative micrographs of the steel deformed at 1000°C and strain rate of 10 s^{-1} and 1050°C and strain rate of 80 s^{-1} with strain of 0.7, are shown in figure 5.46. It shows formation of pores/voids in the specimen caused by strain localization. During hot working at high strain rates, flow softening arises locally as a result of adiabatic heating [189]. In the present work too, the highest value of ΔT obtained during deformation was calculated as 26°C at high strain rate of 80 s^{-1}. If restoration phenomena viz. dynamic recovery and DRX cannot take place due to the short times of deformation, then damage takes place. The low values for both strain rate sensitivity and efficiency parameters support the fact that there is less restoration of microstructure.

In order to investigate the microstructural evolution further, the grain boundary misorientation was determined by EBSD analysis. In figures 5.47a and 5.47b the inverse pole figures superimposed with grain boundary maps are shown for the as-received and deformed specimens (at temperatures 900°C and strain rate of 0.01 s^{-1}) of microalloyed steel, respectively. Evidently, there are differences between the as-received and hot compressed samples with regard to both the grain boundaries and the grain sizes. The grain boundary with misorientation angle from 2 to 15° is low angle grain boundary (LAGB) and larger than 15° is taken as high angle boundary (HAGB). The fraction of both HAGB and LAGB are comparable in both the hot deformed specimen and in the as-received specimen. This is shown in figure 5.48. The fraction of LAGB should increase in deformed specimens due to dislocation multiplication. However, at the deformation conditions representing the depicted microstructure, restoration mechanism involving DRX is operating. This is a possible reason for the comparable fractions of HAGB and LAGB. This domain corresponds to highest values for power dissipation efficiency η and strain rate sensitivity m, and positive values of ξ, κ, and κ_j, all of which imply good workability. However, it may also be noted that figure 5.48b shows absence of misorientations in the range of 20-45° and a relatively high intensity peaks in range of 50-60°. A massive transformation like martensite formation generates characteristic peaks in

the misorientation distribution. EBSD results obtained with bainite/martensite microstructures follow this tendency following more or less the Kurdjumow–Sachs crystallographic relationships [222].

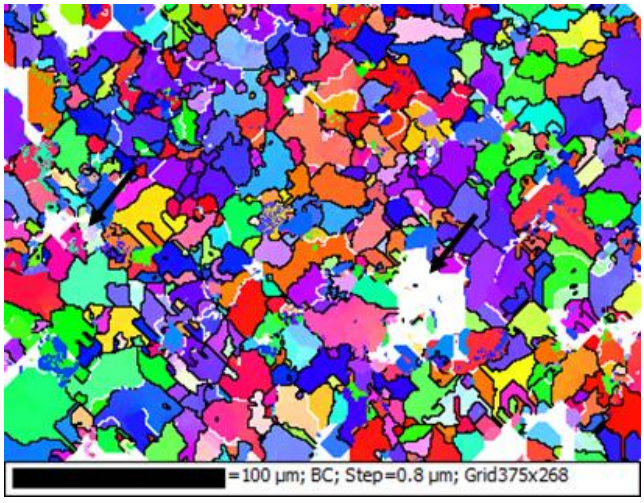

(a)

(b)

Fig. 5.47. Inverse pole figure map and superimposed grain boundary map of Ti-Nb microalloyed steel specimen (a) as received (b) hot deformed at 900°C using strain rate of 0.01 s^{-1}. High angle grain boundaries are dark, while the low angle grain boundaries are gray.

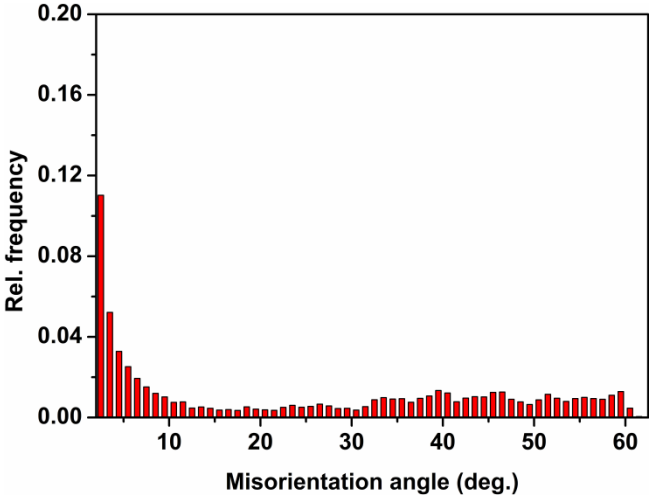

(a)

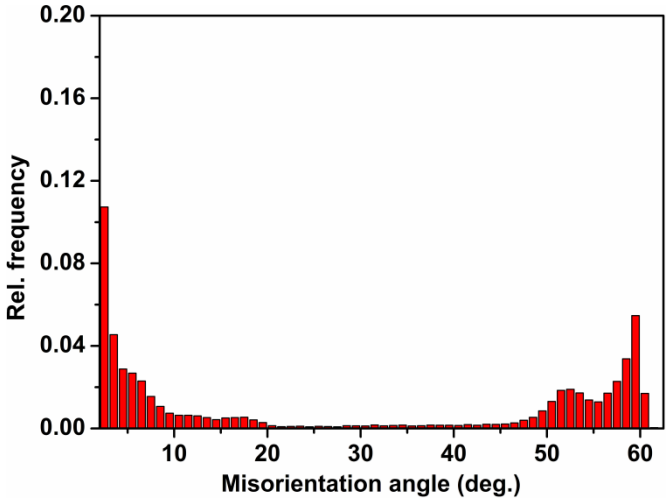

(b)

Fig. 5.48. Distribution of boundary misorientation angle obtained from EBSD analysis of Ti-Nb microalloyed steel. (a) As-received specimen (b) hot deformed at temperature 900°C and strain rate of 0.01 s^{-1}.

5.8.2. CONSTITUTIVE EQUATIONS ANALYSIS

Some information about the deformation mechanisms can also be obtained by using the constitutive equations (4.13, 4.14). The flow data at true strain of 0.6 were treated using the sinh constitutive equation (4.13) and power law equation (4.14) in order to determine the apparent activation energy. The plots of ln σ versus ln $\dot{\varepsilon}$ using power law and sinh type law are shown in figures 5.49a and 5.49b, respectively. The plot of ln σ vs *1/T* using power law and sinh type laws are shown in figures 5.49c and 5.49d, respectively [209]. In the power law

equation, the mean stress exponent *n* is obtained as 9.7. The power law breaks down because the flow conditions are beyond the applicable stress range. Therefore, because of this large n value, the sinh type equation is used by employing a value of 0.012 MPa^{-1} for *c* [202]. The correlation coefficient (R^2=0.9969) of linear regression shows that the sine hyperbolic equation (4.13) has better fit with the experimental data as compared to power law. Furthermore, value of exponent *n* using sinh equation is 4.6, which is consistent to the dislocation glide behavior [221] that it is controlled by dislocation climb [204] at low strain rate, where dislocation climb is significant. However, at moderate and high strain rates, the mechanism is likely to be controlled by cross-slip [67, 204]. The apparent activation energy calculated using the sinh type equation is 359 kJ/mol. This value is about 24% higher than the corresponding value of 290 kJ/ mol for plain low carbon steel of similar composition except the microalloying elements [221]. In Nb microalloyed steels, Nb can be present either in dissolved form where it exhibits a strong solute drag effect, or as NbC precipitates which effectively pin the grain boundaries [45]. Depending upon the temperature of deformation used in the present work, Nb can be present in either form although dissolved Nb is more effective in retarding DRX than the NbC precipitates [45]. Drag exerted on the migrating grain boundaries by Zener pinning effect of the NbC/TiC precipitates or by the presence of dissolved Nb solute can retard the progress of recrystallization. This therefore resulted in the observed high apparent activation energy for the microalloyed steel. The constitutive equation obtained for microalloyed steel using power creep law and sinh type law over a temperature range of 750ºC to 1050°C and strain rate range of 0.01 - 80 s^{-1} are given by equations 5.11 and 5.12, respectively. The sinh type law results in more realistic value of stress exponent *n*.

$$Z = 3.6\times10^{-7}\left(\sigma\right)^{9.7} = \dot{\varepsilon}\exp\left(\frac{340158}{RT}\right) \tag{5.11}$$

$$Z = 9.2\times10^{12}\left[\sinh\left(0.012\sigma\right)\right]^{4.6} = \dot{\varepsilon}\exp\left(\frac{359000}{RT}\right) \tag{5.12}$$

The variations of Zener-Hollomon parameter, *Z* as a function of peak flow stress is shown in figure 5.50. The peak flow stress data obtained from the different hot deformation conditions are very well fitted with the Zener-Hollomon parameter, with the good linear

correlation of regression coefficient (R^2=0.99) as indicated by the figure, and is given by equation 5.13.

$$\ln Z = 4.728 \ln\left[\sinh\left(c\sigma_p\right)\right] + 29.358 \qquad (5.13)$$

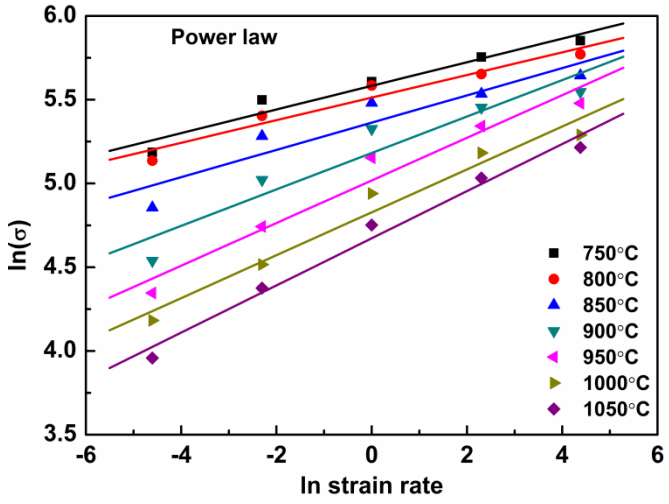

(a)

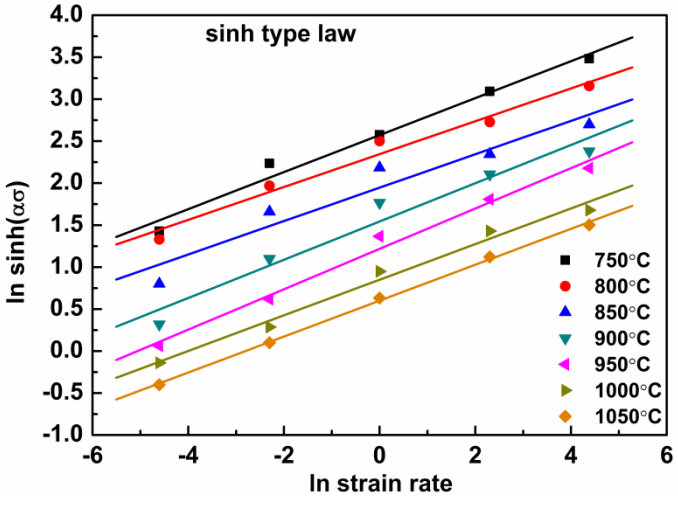

(b)

Fig. 5.49. Contd…

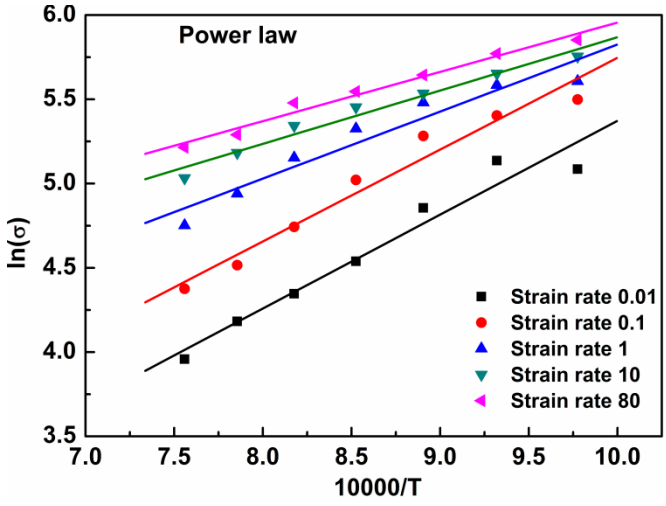

(c)

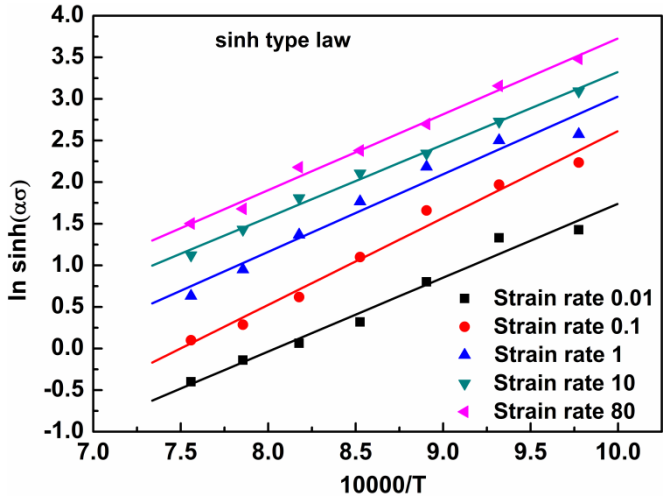

(d)

Fig. 5.49. Flow stress versus strain rate diagrams using (a) power law and (b) sinh type law, and flow stress versus temperature plots using (c) power law and (d) sinh type law (c = 0.012 for microalloyed steel), for Ti-Nb microalloyed steel.

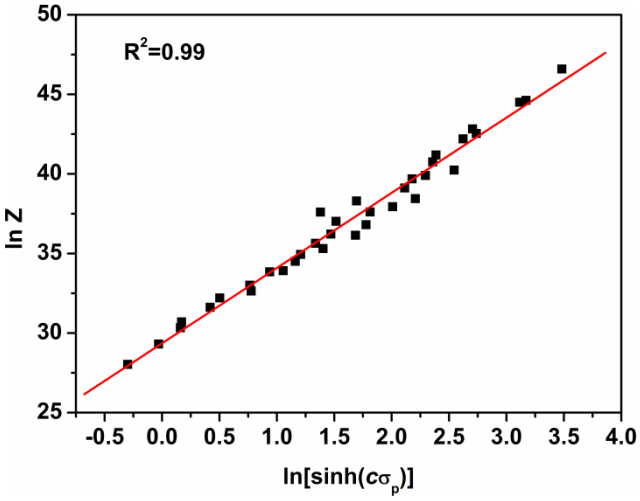

Fig. 5.50. Variation of the Zener-Hollomon parameter with peak flow stress of Ti-Nb microalloyed steel.

5.9. SUMMARY

Hot deformation processing maps are developed for SAILMA grade microalloyed steel by using DMM and modified DMM. The deformation behavior is studied over a wider temperature range of 750ºC to 1050°C and strain rate range of 0.01 - 80 s^{-1}. Following conclusions are drawn from this work.

6. High values of η and m at low strain rates and moderate temperatures result from dynamic recrystallization of austenite. A moderate value of η and m at low strain rates and low temperatures is a result of ferrite formation and dynamic recovery of ferrite through stable flow. Metallographic investigations show that the damage at high strain rates occurs by a combination of limited restoration of microstructure due to short deformation times and possible adiabatic heating.
7. It was found that the sinh type equation correlates the flow stresses with temperature and strain rate better than the power law. It is found that the apparent activation energy for hot deformation of microalloyed steel is 359 kJ/mol, which is higher than the corresponding value of 290 kJ/mol for plain low carbon steel of similar composition without the microalloying elements. Solute drag effect and Zener pinning of grain boundaries by TiC/NbC precipitates is responsible for higher apparent activation energy.
8. The value of the stress exponent, n is 4.6, which suggests that the mechanism of hot deformation is dislocation glide controlled by dislocation climb at lower strain rates.
9. To analyse the relation between flow stress and Zener-Hollomon parameter, the sinh type equation is used over the entire deformation zone and pertaining equation was proposed. The values of the peak flow stress, and Zener-Hollomon parameter was well related.
10. Lower the Zener-Hollomon parameter, larger the amount of softening and the more easily DRX/DRV occurs.

EFFECT OF MICRO-ALLOYING ELEMENTS ON MICROSTRUCTURE EVOLUTION AND PROCESSING MAPS (COMPARISON OF LOW CARBON Ti-Nb MICROALLOYED STEEL AND PLAIN LOW CARBON STEEL AISI 1016)

The main difference in the studied steel is the presence or absence of the microalloying elements such as Ti and Nb. The critical temperatures Ar_3 and Ar_1 of Ti-Nb MA steel are lower as compared to the plain carbon steel (AISI 1016). Also, the peak flow stresses of the Ti-Nb MA steel are higher than that of AISI 1016. This is due to the presence of Nb and Ti, which retard the DRX due to dynamic precipitation of complex Nb-Ti carbonitrides [78]. Also, the peak stress shifted towards the higher strain as compared to the plain low carbon steel. It is observed that the values of peak stress and steady state stress are also increased due to addition of Nb and Ti as compared to the similar plain low carbon steel.

The value of strain rate sensitivity parameter, *m* is reduced with the addition of Ti-Nb MA as compared to the plain low carbon steel. The region of the high value of *m* is shifted towards the higher temperature zone in the case of microalloyed steel. In Nb microalloyed steels, Nb can be present either in dissolved form where it exhibits a strong solute drag effect, or as NbC precipitates which effectively pin the grain boundaries [45]. Depending upon the temperature of deformation used in the present work, Nb can be present in either form although dissolved Nb is more effective in retarding DRX than the NbC precipitates [45]. Drag exerted on the migrating grain boundaries by Zener pinning effect of the NbC/TiC precipitates or by the presence of dissolved Nb solute can retard the progress of recrystallization. The same trends were followed by the power dissipation efficiency, η_{Prasad} and $\eta_{Murty\ \&\ Rao}$ as shown in figures 5.26 and 5.42. The apparent activation energy, *Q*, for Ti-Nb MA steel and AISI 1016 steel are 359kJ/mol and 290kJ/mol, respectively. This is due to the presence of Ti and Nb that affects the dislocation movement and subgrain boundaries, results strong retardation for the onset of DRX and DRV [223]. The value of the Zener-Hollomon parameter, Z is also higher in the Ti-Nb MA steel as evident from the figures 5.28 and 5.45.

Chapter 6

RESULTS AND DISCUSSION: GRAIN REFINEMENT BY THERMOMECHANICAL PROCESSING

The objective of the present chapter is to use thermomechanical processing for achieving grain refinement in plain low carbon and low carbon Ti-Nb microalloyed (MA) steels. The effect of different processing parameters such as strain, prior austenite grain size, deformation temperatures etc. on the deformation induced ferrite transformation (DIFT) are analyzed. Also, the processing conditions are optimized in the safe working zone to obtain the ultra-fine ferritic (UFF) microstructure.

6.1. RESULTS

6.1.1. PRIOR AUSTENITE GRAIN SIZE AND TRANSFORMATION START TEMPERATURES

The transformation start temperature for particular austenitization conditions, Ar_3 was determined by continuous cooling transformation (CCT) tests from the dilation of the specimen during cooling with the cooling rate of $1°Cs^{-1}$. The austenite grain sizes and corresponding transformation start temperatures thus determined for AISI 1010 plain low carbon steel and low carbon Ti-Nb microalloyed steel are summarized in Table 6.1.

Table 6.1. Summary of prior austenite grain size and transformation start temperature with respective austenitization conditions for the two steels.

Steel	**Austenitization temperature, T_γ (°C)**	**Holding time (s)**	**Prior austenite grain size, d_γ (µm)**	**Ar_3 (°C)**
AISI 1010 plain C steel	950	10	41	821
	1050	10	58	813
	1050	60	87	801
Ti-Nb microalloyed steel	950	10	11	753
	1050	10	27	740
	1050	120	39	732

The prior austenite grain size, d_γ, increased with the reheating temperature. The prior austenite grain size of AISI 1010 steel increased from 41 μm to 58 μm as the reheating temperature increased from 950°C to 1050°C for the holding time of 10 s. It also increased from 58 μm to 87 μm as the holding time increased from 10 s to 60 s at the austenitization temperature of 1050°C. The Ar_3 temperatures varied with the prior austenite grain size, and for AISI 1010 steel with austenite grain size of 41 μm and 87 μm these are 821°C and 801°C, respectively. The dilatometry test results of AISI 1010 steel after different austenitization conditions are shown in figure 6.1. These results reflect rapid coarsening of the prior austenite grains by grain growth due to the increasing the reheating temperature from 950°C to 1050°C.

In the case of low carbon Ti-Nb microalloyed steel the prior austenite grain was 11 μm after reheating at 950°C for 10 s. The prior austenite grain size increased from 11 μm to 27μm, when the reheat temperature was increased from 950°C to 1050°C for the same austenitization time. Also, when the austenitization time is increased from 10 s to 2 min for the same reheat temperature of 1050°C, the prior austenite grain size increased from 27μm to 39μm. It is clear from the figures 6.1 and 6.2, that Ar_3 temperature is higher in the case of AISI 1010 steel as compared to Ti-Nb MA steel. The prior austenite grain size of Ti-Nb microalloyed steel at the austenitization temperature of 1050°C for 2 min is much smaller as compared to the plain low carbon steel for the same austenitization temperature and for short holding time of 10 s. Thus, as seen from figures 6.1 and 6.2, ferrite formation is delayed due to the strong effects of Nb present in the form of Nb(C,N) precipitates that retarded growth of prior austenite grain. The effect of Nb was more pronounced when the austenitization temperature increased from 950°C to 1050°C, thereby increasing the amount of Nb in solution, which results in larger prior austenite grain size. The results show that for both the steels, as the prior austenite grain size decreases the Ar_3 temperature increases.

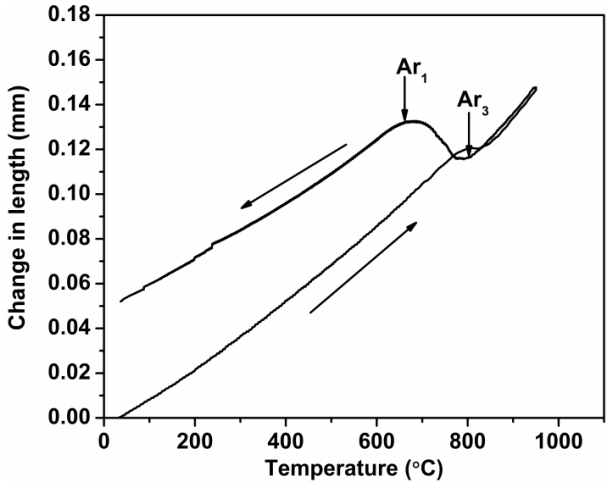

(a)

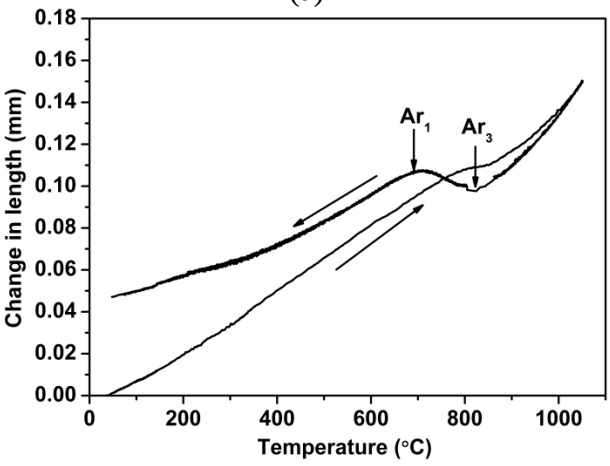

(b)

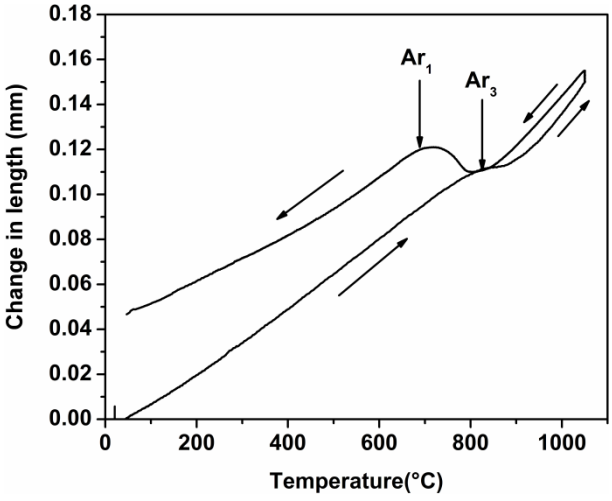

(c)

Fig. 6.1. Dilatometry test results of AISI 1010 steel after austenitization at (a) 950°C for 10 s, (b) 1050°C for 10 s, and (c) 1050°C for 60 s. Inflection points correspond to the Ar_1 and Ar_3 temperatures.

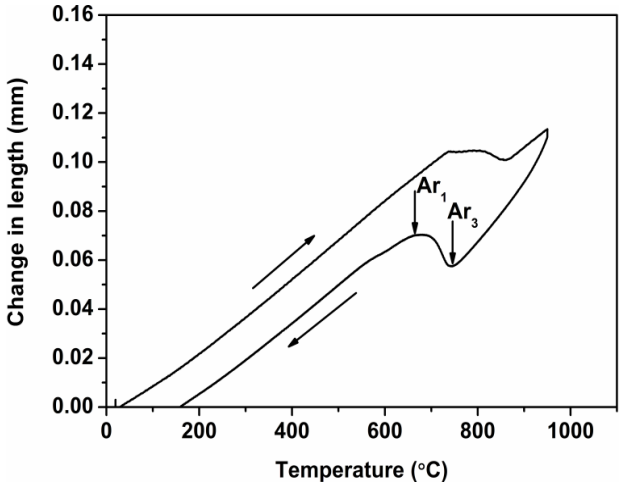

(a)

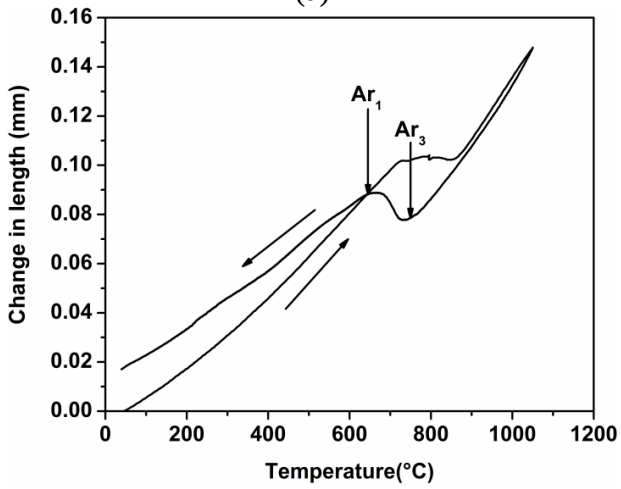

(b)

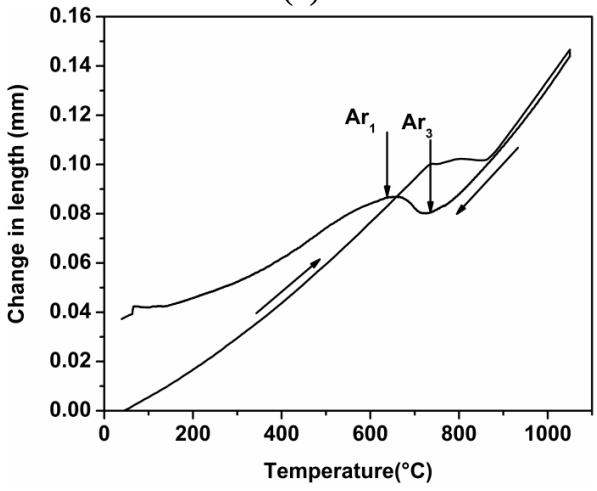

(c)

Fig. 6.2. Dilatometry test results of low carbon Ti-Nb microalloyed steel after austenitization at (a) 950°C for 10 s, (b) 1050°C for 10 s, and (c) 1050°C for 120 s. Inflection points correspond to the Ar_1 and Ar_3 temperatures.

6.1.2. EFFECT OF DIFFERENT PROCESSING PARAMETERS ON DIFT

The different processing parameters that influence the DIFT are the amount of strain, prior austenite grain size, strain rate, and the deformation temperature. In this work, the effect of various processing parameters on the DIFT is studied systematically. From the experimental studies (given in chapter 5) on hot deformations of AISI 1010 plain carbon and Ti-Nb MA steels, it was observed that a finer ferritic microstructure is obtained when a strain rate of 1 s^{-1} is employed. Therefore, the strain rate was kept constant at 1 s^{-1} in this study. The test details are explained in section 3.6 for both the materials. The total applied true strain was 1.4. UFF microstructure is encouraged by finer austenite grains [79]. Therefore, austenitization conditions corresponding to finer prior austenite grain size of 41 µm and 11 µm were selected for plain low carbon steel and Ti-Nb MA steel, respectively (Table 6.1). The austenitization was followed by two-step compression at different deformation temperatures, above the Ar_3 temperature. The deformed samples were in-situ water quenched immediately after the hot compression in order to freeze the microstructure.

EFFECT OF STRAIN ON DIFT

To obtain the DIFT, the deformation temperature is usually 25°C to 100°C above the Ar_3 temperature [23, 94, 166]. Thus, the deformation temperature 875°C was selected for first hit in the case of plain low carbon steel. At the deformation temperature of 875°C, applied true strain was varied. It was 0.2, 0.4 and 0.6 and the optical micrographs of corresponding specimens are shown in figures 6.3a, 6.3b and, 6.3c respectively. Deformation above Ar_3 temperature increases the γ free energy, which results in an increase in the $\gamma \rightarrow \alpha$ transformation temperature [47]. The specimen deformed at 875°C with true strain 0.2 shows the ferrite in the prior austenite grain boundaries along with some ferrite within the grain. As the applied true strain increased to 0.6, the amount of ferrite is increased within the prior austenite grains. From the micrographs, it is observed that the amount of ferrite fraction increased from 56.6 to 85.8% as the strain increased from 0.2 to 0.6 and its grain size reduced from 11 µm to 7.0 µm. The increase in ferrite fractions also confirmed from the stress-strain curves of AISI 1010 steel at strain of 0.2, 0.4 and 0.6 as shown in figure 6.4. Figures 6.4a and 6.4b show continuous strain hardening that means the dislocation density increased and whereas figure 6.4c shows flow softening after reaching peak stress probably due to the increase in ferrite fraction, when the specimen was deformed up to strain of 0.6. At the deformation temperature 875°C with true

strain of 0.6, the prior austenite grain (41 μm) is converted in to the finer austenite grains (12 μm) as shown in figure 6.3c. This provides the larger nucleation sites for the ferrite. Therefore to obtain a fine ferritic structure in AISI 1010 steel the strain of 0.6 is required.

To study the effect of strain on DIFT in the low carbon Ti-Nb microalloyed steel, the deformation temperature of 850°C corresponding to the fine prior austenite grain size of 11 μm was selected (Table 6.1) [23, 94, 166]. Figures 6.5a, 6.5b and 6.5c show the light optical micrographs of Ti-Nb MA steel deformed at 850°C with the true strain of 0.2, 0.4 and 0.6 respectively. The specimen deformed at 850°C with true strain of 0.2 shows ferrite predominantly in the prior austenite grain boundaries whereas as the true strain increases to 0.6 the ferrite was observed within the grains as well as along the prior austenite grain boundaries. The amount of ferrite also increased from 25.4 to 54.2% as the true strain increased from 0.2 to 0.6, and also the ferrite grain size decreased from 7 μm to 3 μm. This is also reflected in figure 6.6 that shows flow softening due to increased amount of DIFT. This indicates that in order to obtain fine ferritic structure a true strain of 0.6 is required to produce the fine ferritic structure. Thus, this amount of strain is required to increase the γ free energy and that plays an important role to produce the fine DP microstructure [47]. Thus, the amount of fine ferrite increased as the amount of applied strain increased in the DIFT tests, for both the studied materials.

The effect of strain is almost similar for the both chemistries. For plain low carbon steel, with increasing the amount of strain predominantly large ferrite grained (11 μm) structure was converted into a relatively fine-grained ferrite (7 μm) along with larger amount of ferrite microstructure and also the austenite grain size was decreased. Same trend is followed in the case of Ti-Nb microalloyed steel, with increasing strain the ferrite is formed within the grains along with the austenite grain boundaries and also equiaxed ferritic structure was formed.

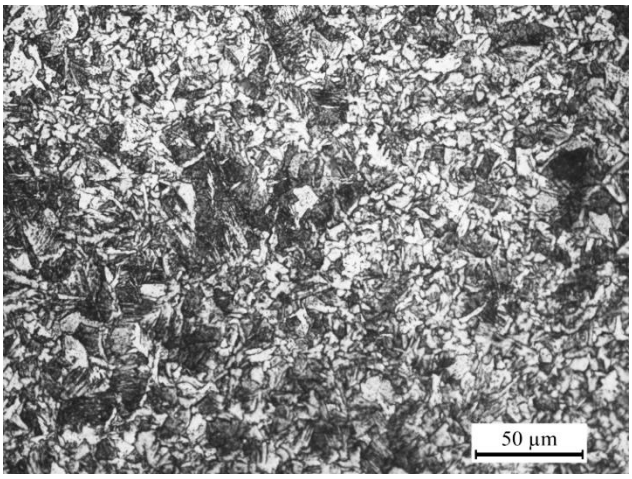

(a)

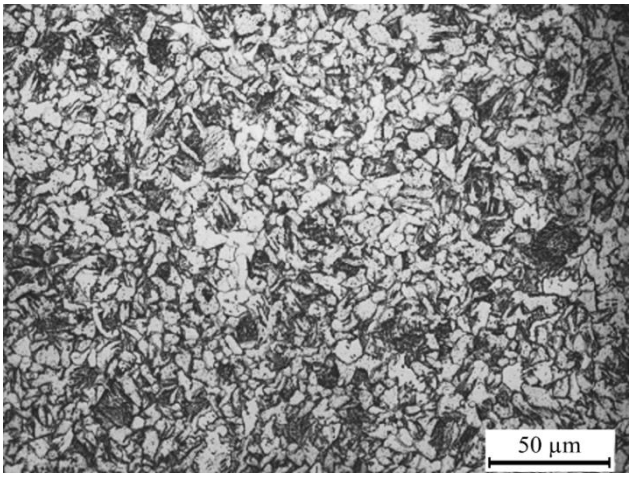

(b)

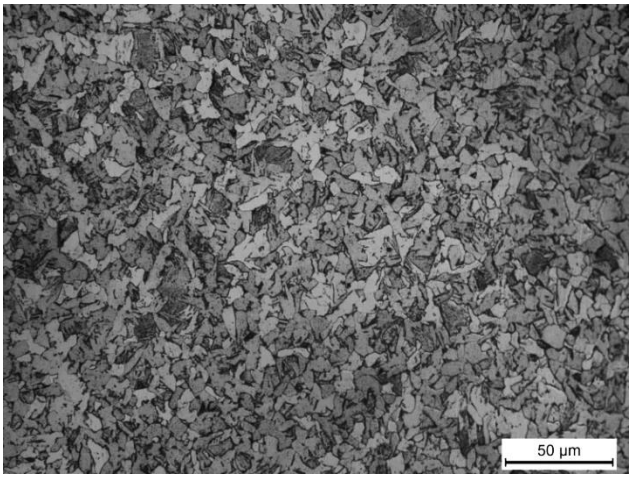

(c)

Fig. 6.3. Optical micrographs to show the effect of strain on DIFT for plain low carbon steel (AISI 1010), for initial austenite grain size d_γ= 41µm, and deformed at 875°C using a true strain of (a) 0.2, (b) 0.4, and (c) 0.6.

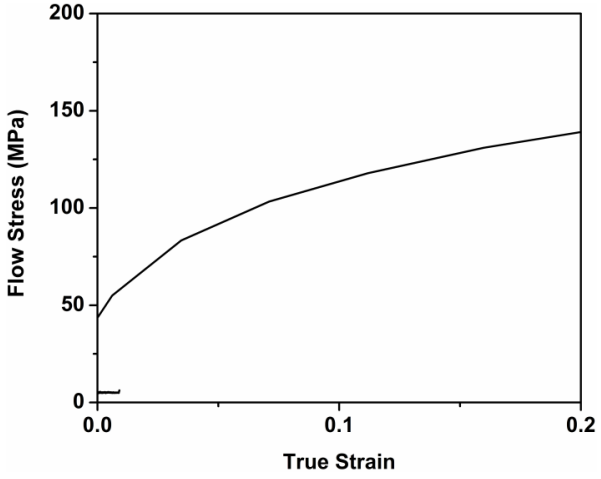

(a)

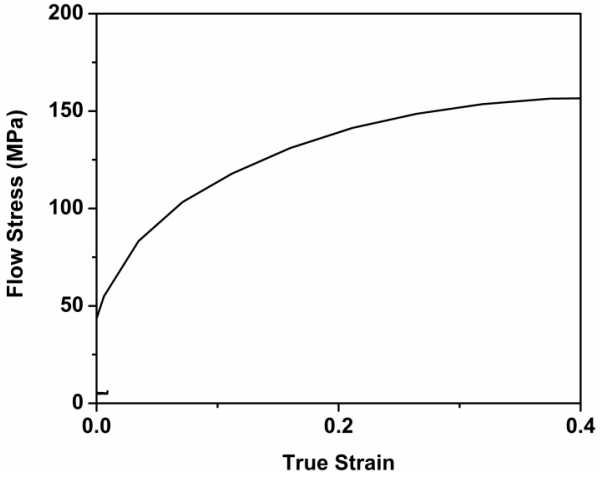

(b)

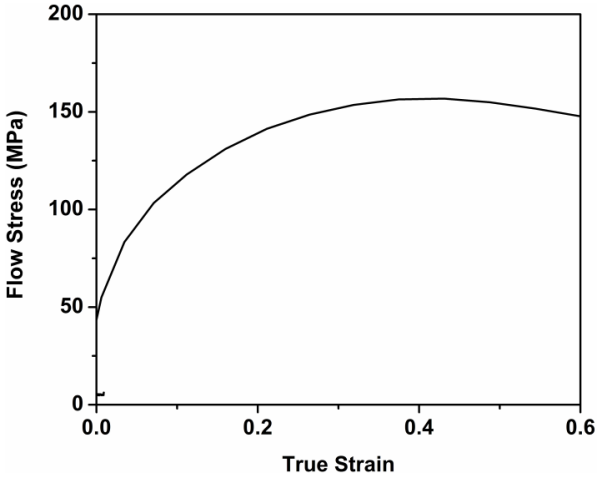

(c)

Fig. 6.4. Flow stress-strain curves of AISI 1010 steel, compressed at 875°C with the strain rate of 1 s^{-1} using a true strain of (a) 0.2, (b) 0.4, and (c) 0.6, after austenitization at 950°C for 10 s.

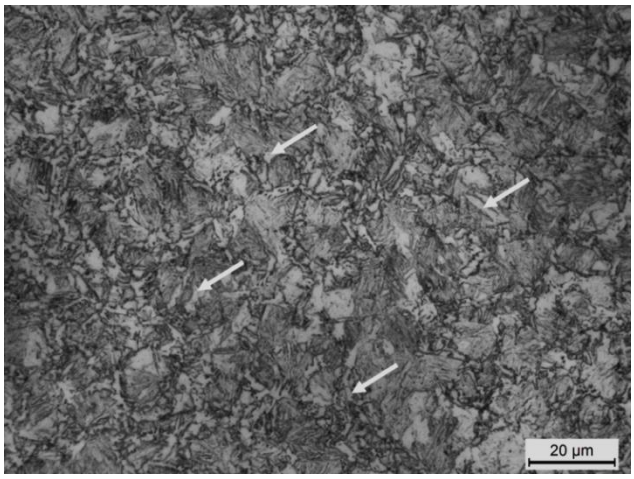

(a)

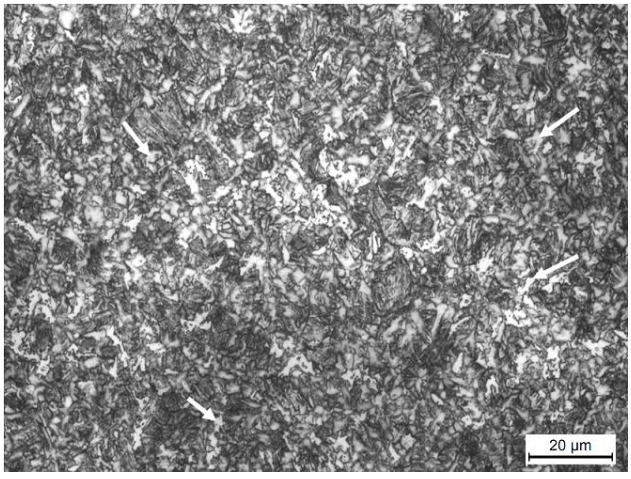

(b)

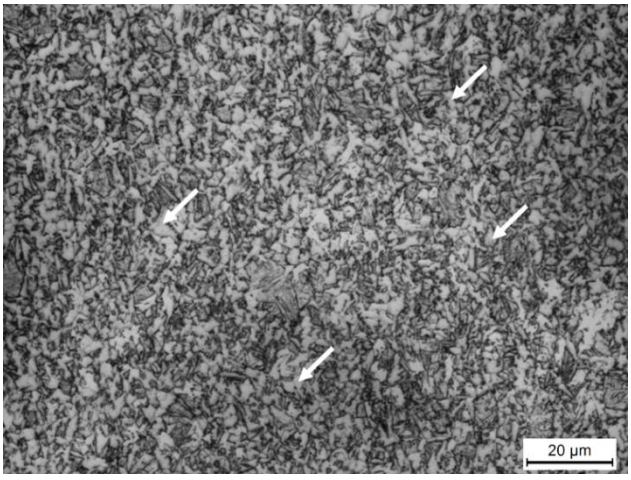

(c)

Fig. 6.5. Optical micrographs to show the effect of strain on DIFT for low carbon Ti-Nb microalloyed steel, for initial austenite grain size d_γ = 11µm, and deformed at 850°C using the true strain of (a) 0.2, (b) 0.4, and (c) 0.6.

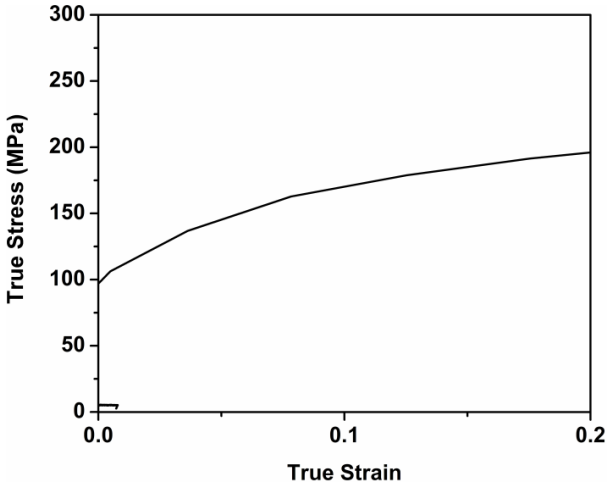

(a)

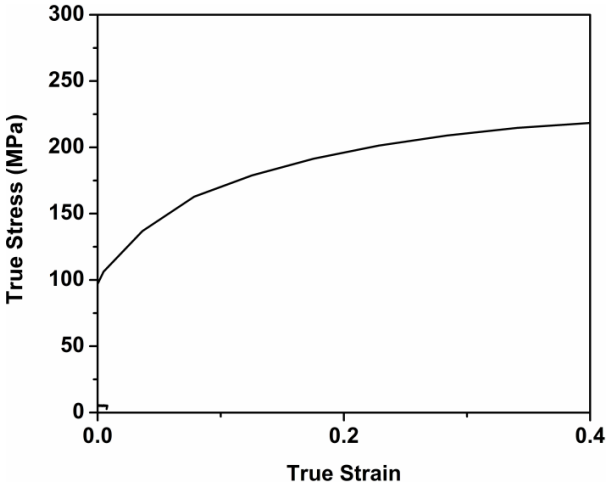

(b)

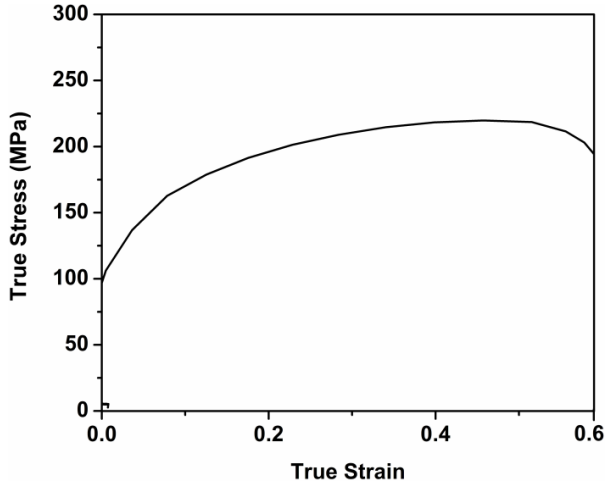

(c)

Fig. 6.6. Flow stress-strain curves of Ti-Nb MA steel, compressed at 850°C with the strain rate of 1 s^{-1} using true strain of (a) 0.2, (b) 0.4, and (c) 0.6 after austenitization at 950°C for 10 s.

In the first step deformation the true strain of 0.6 produced the fine austenite as depicted by figure 6.3c. Further straining will not affect the austenite grain. Again, in order to decrease the ferrite grain size and to obtain the equiaxed fine ferritic structure it is necessary to further deform the specimen just above the Ar_3 temperature with appropriate amount of strain. Figure 6.7 shows the optical micrographs of AISI 1010 steel that shows the effect of strain at different deformation temperatures in the two step deformation performed with the constant strain rate of 1 s^{-1}. Specimen S1 is deformed at 875°C in the first hit with true strain of 1.0 followed by second hit at 825°C with true strain of 0.4. Specimen S2 is deformed at the same temperatures but the applied true strains are 0.6 and 0.8, respectively. Whereas, the specimens deformed at 875°C in the first step and deformed at 840°C in second step, with the true strains of 1.0 and 0.4, and 0.6 and 0.8 are termed as S3 and S4, respectively. As the amount of applied true strain decreased from 1 to 0.6 in the first step deformation at constant temperature of 875°C and increased the true strain from 0.4 to 0.8 in the second step deformation at temperature of 825°C, the amount of ferrite increased and the grains became finer (figures 6.7 a,b). Same trend is followed with the second step deformation at 840°C as shown in figures 6.7 c and 6.7d. Thus, in the second step deformation, the true strain of 0.8 sufficient to refine the ferrite, because at temperature close to Ar_3 and with high dislocation density this amount strain is sufficient to produce the DIFT along with fine ferritic grains. Therefore the second step deformation with true strain of 0.8 is beneficial to produce fine grained equiaxed microstructure as compared to the deformation in one step either at 875°C or at 825°C.

To study the effect of temperatures on DIFT in two step deformations, AISI 1010 steel was deformed in two steps at different temperatures with a total true strain of 1.4 after reheating 950°C for 10 s. The first step deformation temperature was 875°C with applied strain of 0.6, whereas the second step deformation temperatures were 825°C and 840°C with true strain of 0.8, and with a constant strain rate of 1 s^{-1}, was represented in figures 6.7b and 6.7d, respectively. The effect of deformation temperature and applied strain on DIFT in terms of grain size and the ferrite volume fraction is summarized in Table 6.2. The amount of ferrite fraction decreases as the temperature of the second step deformation increases from 825°C to 840°C. Thus, the second step deformation at 825°C is advantageous to produce Dual-phase (DP) steel with sufficient amount of ferrite fraction along with fine ferrite grain size.

Table 6.2. Summary of volume fraction and average grain size of AISI 1010 steel specimens deformed in two steps at different processing conditions.

S. No.	Test Specimen	Ferrite fraction (pct)	Martensite fraction (pct)	Avg. grain size (μm)
1	S1	65.76	34.24	4.3
2	S2	77.87	22.13	3.2
3	S3	61.19	38.81	5.6
4	S4	65.32	34.68	3.7

Figures 6.7a - 6.7d show the optical micrographs of the S1, S2, S3, and S4 specimens, respectively. All specimens consist of ferrite (light color) and martensite (dark color) phase. Specimens S1 and S3 show the non-uniform distribution of bigger size of ferrite and martensite. The average grain size of specimens S1 and S3 are 4.3 μm and 5.6 μm, respectively as shown by figures 6.7a and 6.7c. While the figures 6.7a and 6.7d show the specimens S2 and S4, consist of fine ferrite but the microstructure of specimen S4 (average grain size 3.7 μm) is not equiaxed and consists of larger martensite grains. Among all micrographs, the micrograph S2 shows the equiaxed and finest structure and the average grain size of 3.2 μm (Figure 6.7b).

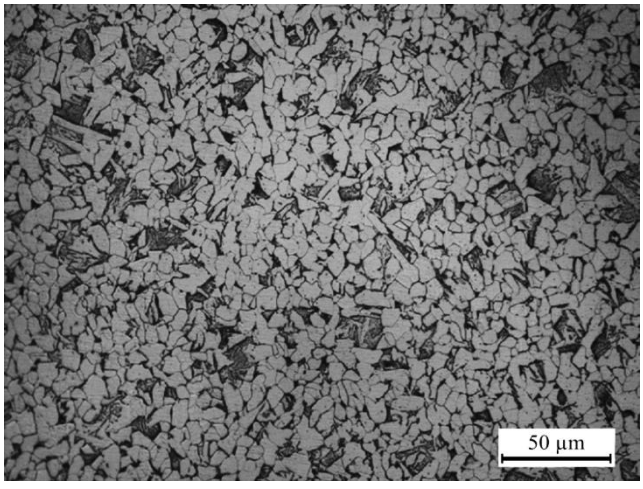

(a)

Fig. 6.7. Contd…

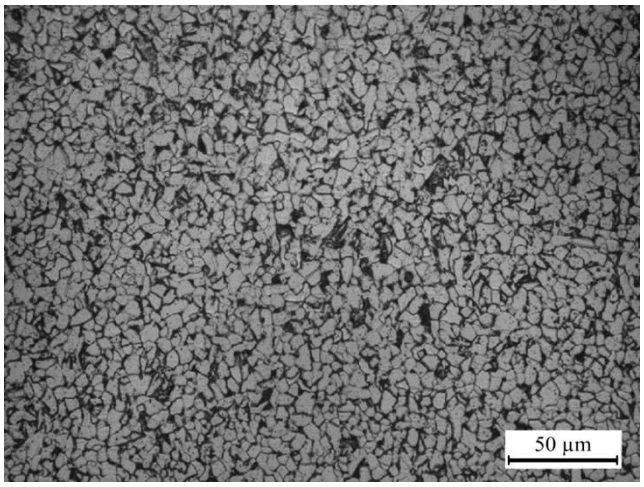

(b)

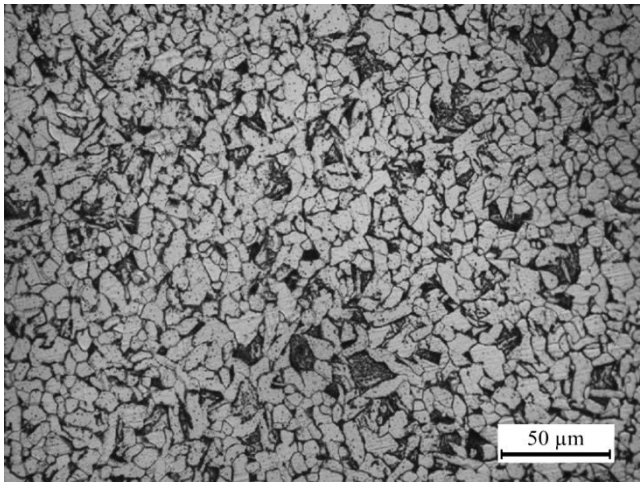

(c)

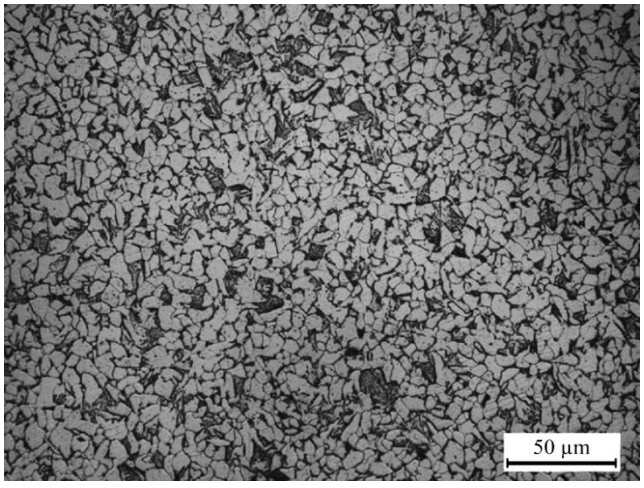

(d)

Fig. 6.7. Optical micrographs to show the effect of strain in two step deformations in AISI 1010 steel after reheating to 950°C for 10 s (a) S1, (b) S2, (c) S3, (d) S4 specimens.

The optical micrographs of Ti-Nb MA steel specimens deformed in two step compressions are shown in figure 6.8. To study the effect of temperatures on DIFT in two step deformations, Ti-Nb MA steel specimens were deformed at different deformation temperatures after reheating 950°C for 10 s and the total applied true strain was 1.4. The first step deformation temperatures were 850°C and 875°C with applied strain of 0.6, whereas the second step deformation temperatures were 760°C and 790°C with true of 0.8. The ferrite fraction decreased as the deformation temperature in first step increased from 850°C to 875°C with the same applied strain conditions. The effect of deformation temperatures on DIFT in terms of grain size and the ferrite volume fraction is shown in Table 6.3. The light optical micrographs of the specimens M1, M2, and M3 are shown in figures 6.8a to 6.8c, respectively. All specimens consist of ferrite (white color) and martensite (dark color) phase. Figure 6.8c shows the specimen M3 (First step deformation at 875°C with true strain of 0.6 and second step deformation at 760°C with true strain of 0.8) consists of approx. 80 pct ferrite phase and 20 pct martensite, with the average grain size of 2 µm. Whereas, the specimens M1 (First step deformation at 850°C with true strain of 0.6 and second step deformation at 760°C with true strain of 0.8) and M2 (First step deformation at 850°C with true strain of 0.6 and second step deformation at 790°C with true strain of 0.8) have the average grain size of 1.1 µm and 1.3 µm, respectively but the martensite fraction in specimen M2 is much high (39 pct) as compared to specimen M1 (19 pct). With increasing the temperature of the second step deformation from 760°C to 790°C, keeping first step deformation temperature same (850°C), the amount of ferrite fraction decreases from 81 pct to 61 pct. This is due to the working in the single austenite phase field (790°C). In this temperature the ferrite is formed in the grain boundaries. This occurs due to the DIFT and/ or during cooling. Thus specimen M1 shows the finer and equiaxed ferrite microstructure of average grain size of 1.1 µm with the good amount of martensite for DP steel. The obtained microstructures of Ti-Nb MA steel are finer as compared to that of plain low carbon steel; this is due to the presence of Nb which retards the ferrite formation.

The figure 6.9 shows the power dissipation efficiency map of the AISI 1010 steel according to the method followed by Murty and Rao et al. [176]. The result shows that the deformation at the temperatures 875°C and 825°C at the constant strain rate of 1 s^{-1} have been in the moderate power dissipation efficiency, η region. These conditions promote the ferrite

formation during deformation due to DIFT, which results softening as shown in the flow curve (Figure 6.10) [221]. As the temperature decreased from 875°C to 825°C, the dislocation density and the degree of work hardening increased; the defect structure increased within the grains for a given amount of true strain and strain rate. This promotes the grain refinement.

The power dissipation efficiency map of the Ti-Nb MA steel according to the method followed by Murty and Rao et al. [176] is shown in figure 6.11. The moderate value of the power dissipation efficiency, η promotes the ferrite formation during deformation due to DIFT, and results in softening as shown in the flow curve (Figure 6.12) [221]. The two step deformation of Ti-Nb MA steel were performed at deformation temperatures of 850°C and 760°C at the constant strain rate of 1 s^{-1}. In this region the value of η is moderate.

Table 6.3. Summary of volume fraction and average grain size of Ti-Nb microalloyed steel specimens deformed in two steps at different processing conditions.

S.No.	**Test specimen**	**Ferrite fraction (pct)**	**Martensite fraction (pct)**	**Avg. grain size (μm)**
1	M1	81.2	18.8	1.1
2	M2	60.8	39.2	1.3
3	M3	80.4	19.6	2.0

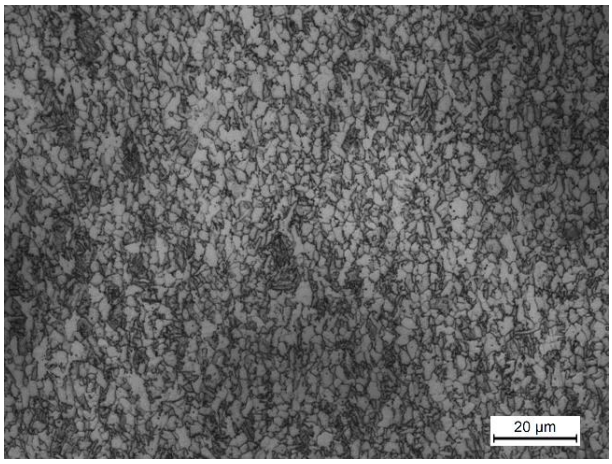

(a)

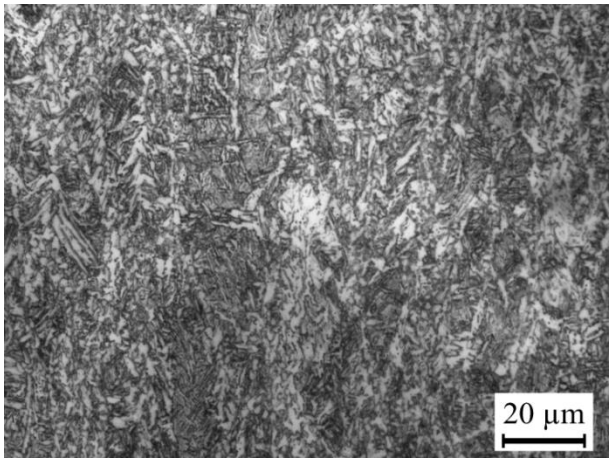

(b)

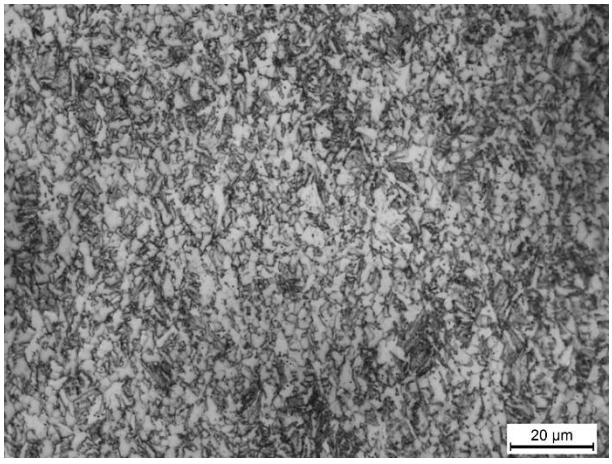

(c)

Fig. 6.8. Optical micrographs to show the effect of strain in two step deformations in Ti-Nb microalloyed steel after reheating to 950°C for 10 s (a) M1, (b) M2, and (c) M3 specimens.

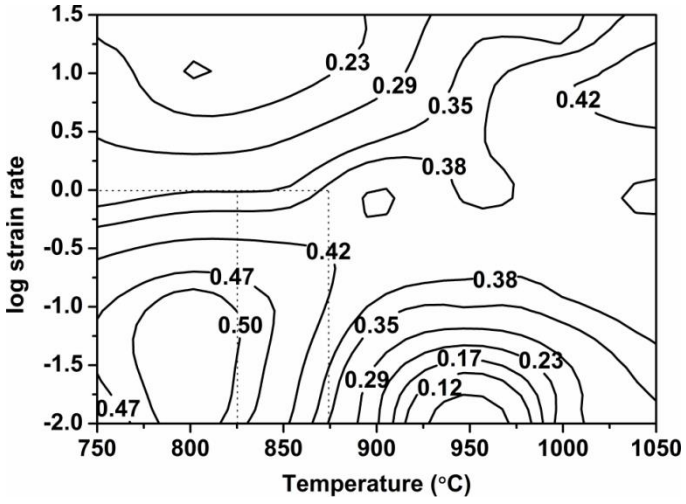

Fig. 6.9. Power dissipation efficiency map of AISI 1010 according to Murty and Rao et al., showing the working region (dotted lines) to obtain the fine grained ferritic microstructure.

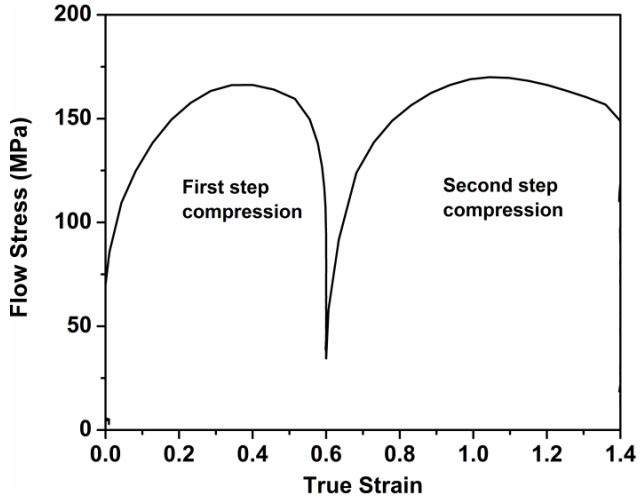

Fig. 6.10. Flow curve of the specimen of AISI 1010 steel deformed according to process S2, at the constant strain rate of $1s^{-1}$ after austenitizing at 950°C for 10 s.

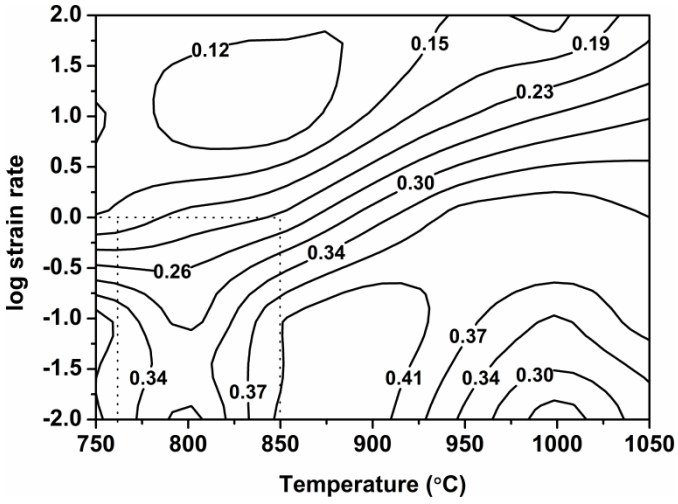

Fig. 6.11. Power dissipation efficiency map of Ti-Nb MA steel according to Murty and Rao et al., shows the working region (dot lines) to obtain the fine grained ferritic microstructure.

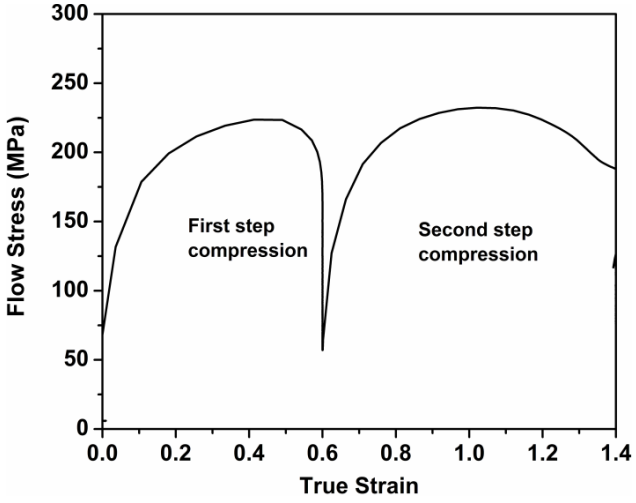

Fig. 6.12. Flow curve of the specimen of Ti-Nb MA steel deformed according to process M1, at the constant strain rate of $1s^{-1}$ after austenitizing at 950°C for 10 s.

6.1.3. EBSD ANALYSIS

To determine the grain size, phase fraction and grain boundary misorientation distribution, EBSD analysis of the selected specimens were performed. The EBSD maps of the AISI 1010 steel specimens deformed at two different temperatures (two steps) with different true strains (S1, S2, S3, and S4) at a constant strain rate of 1 s^{-1} are shown in figure 6.13. The compression axis of the deformed specimen is horizontal and colours indicate the crystal orientation. The low angle grain boundaries (LAGB) are with misorientation angle of 2° to 15°

and the high angle grain boundaries (HAGB) are with misorientation angle of 15° or more. The misorientation angle of 2° has been taken as lower limit of measurable grain boundary. The LAGB's are represented by white lines whereas HAGB's by black lines. Mukherjee et al. reported that the ferrite grain size determined using the critical misorientation angle of 2° to define the grains by EBSD analysis, were similar to that of conventional SEM studies [79]. The step size used during the EBSD analysis limits the accuracy of the grain size measurement but the grain size itself becomes a function of critical misorientation angle. In the present study the step size 0.5 μm was used. Also, the presence of two phases, ferrite and martensite makes EBSD analysis complicated because of minor difference in the lattice parameter of c-axis. To separate the ferrite from the martensite, a threshold level can be introduced using the pattern quality [79]. The specimen preparation influences the pattern quality. The initial grains of the material are equiaxed and LAGB are introduced with the early stage of deformation. The initial grain is subdivided into the sub-grains (formation of LAGB). These sub-grains are converted into very fine grains surrounded by generated HAGB along with the initial ferrite grain boundaries. This shows that these fine grains are formed by a process of fragmentation/subdivision of initial grains and the fraction of HAGB's increased. The distribution of grain boundary misorientation angle of specimens S1, S2, S3, and S4 were shown in figure 6.14 for the above four EBSD maps. The specimen S4 has highest amount of LAGB which is probably due to the formation on sub-grains, whereas specimen S2 has lowest amount of LAGB with the finest equiaxed ferritic structure of average grain size of 3.2 μm.

Figures 6.15 and 6.16 shows the EBSD map and the misorientation angle distribution of Ti-Nb MA steel specimens designated as M1 and M3, respectively. The non-ferritic phase or a grain-boundary region was indicated by the unindexed white pixels as shown in figure 6.15. The results confirmed that M1 specimen has higher proportion of HAGB than the other specimens of Ti-Nb MA steel and plain low carbon steel specimens. The average grain size (1.1 μm) of the Ti-Nb MA steel was smaller than that of plain low carbon steel due to presence of Nb(C,N). Thus, the increased fraction of HAGB confirmed the equiaxed fine microstructure with the help of EBSD studies.

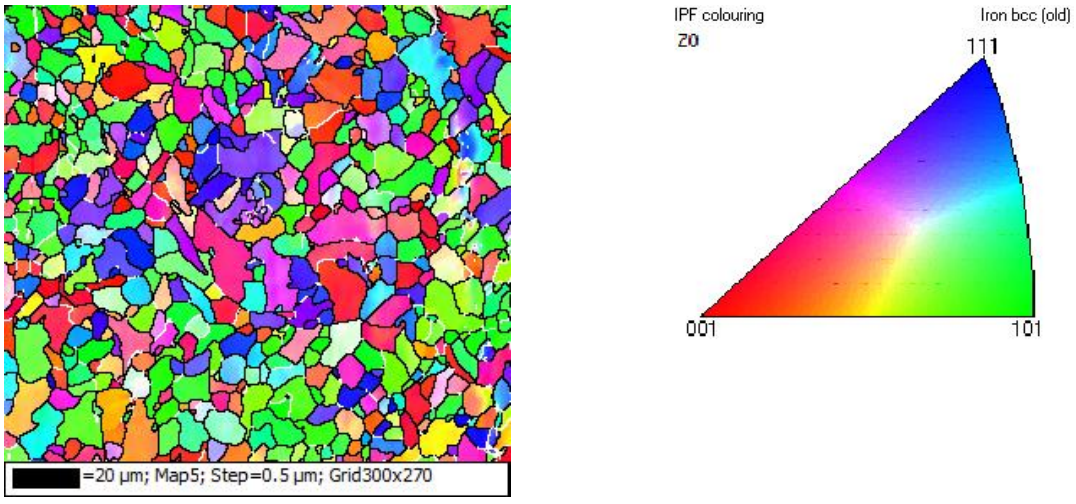

(a)

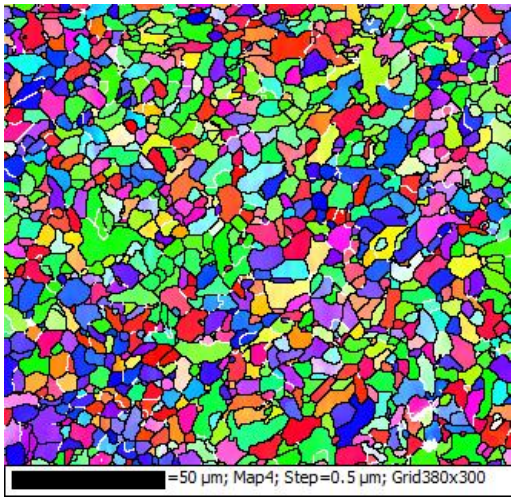

(b)

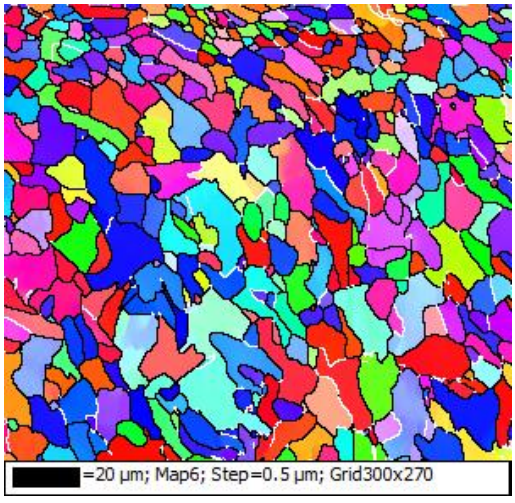

(c)

Fig. 6.13 Contd...

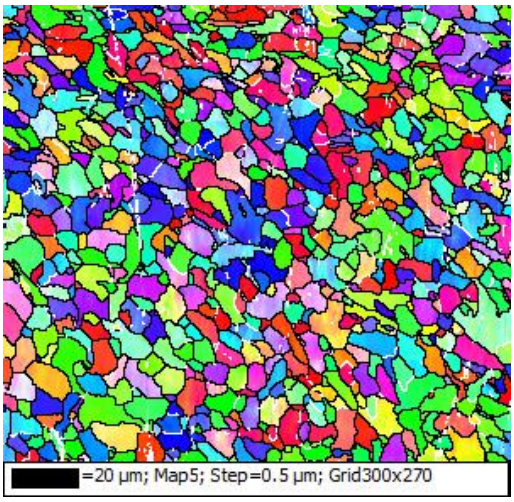

(d)

Fig. 6.13. EBSD (Inverse pole figure) maps of deformed specimens of AISI 1010 steel at constant strain rate of $1s^{-1}$ according to the processing conditions (a) S1, (b) S2, (c) S3, and (d) S4, after reheating at 950°C for 10 s.

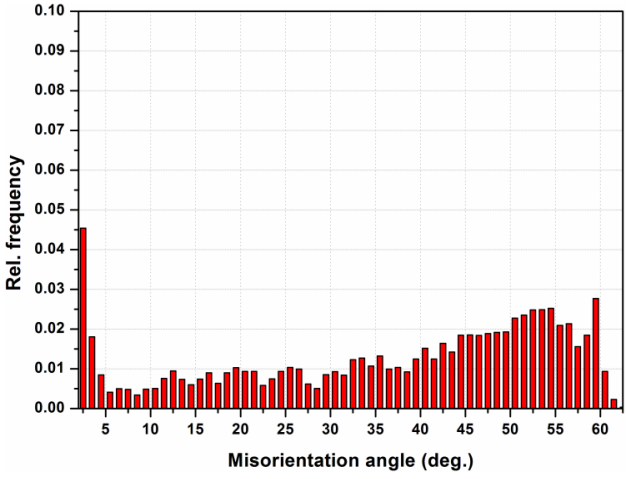

(a)

Fig. 6.14. Contd…

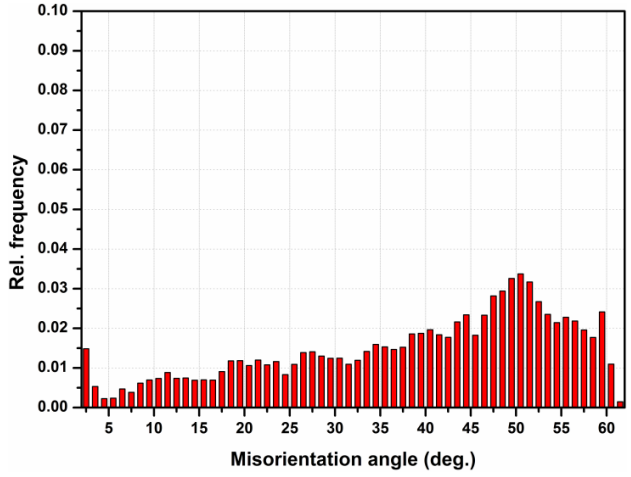

(b)

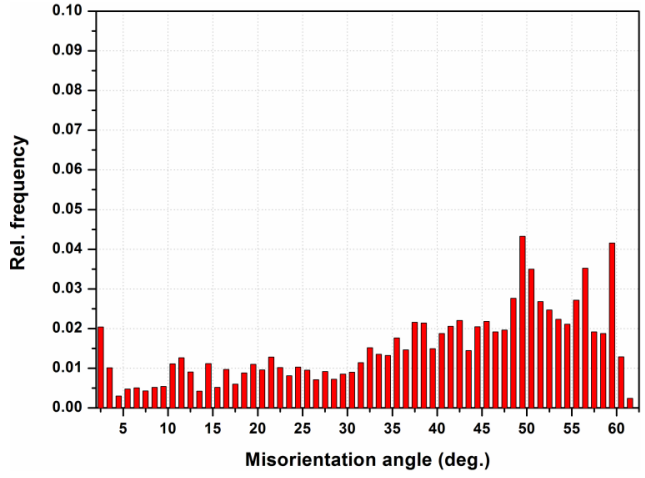

(c)

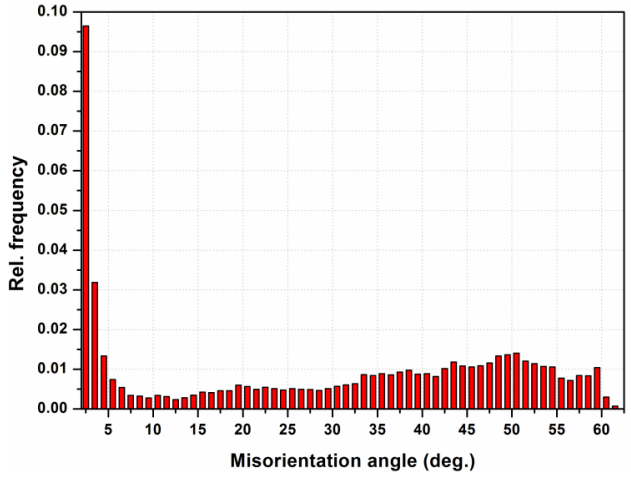

(d)

Fig. 6.14. Misorientation grain boundaries distribution of AISI 1010 steel specimens after the hot deformation at constant strain rate of 1 s^{-1} according to the processing conditions of (a) S1, (b) S2, (c) S3, and (d) S4, after reheating at 950°C for 10 s.

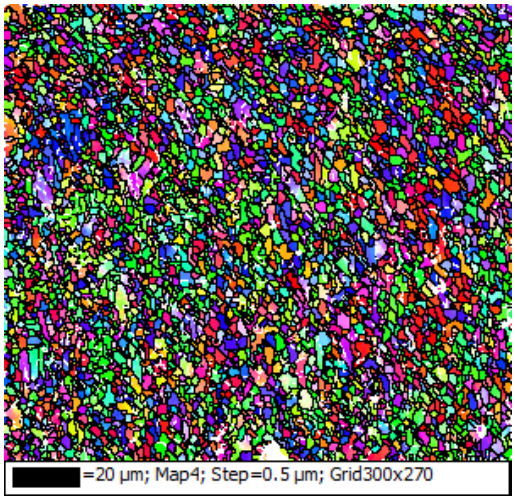

(a)

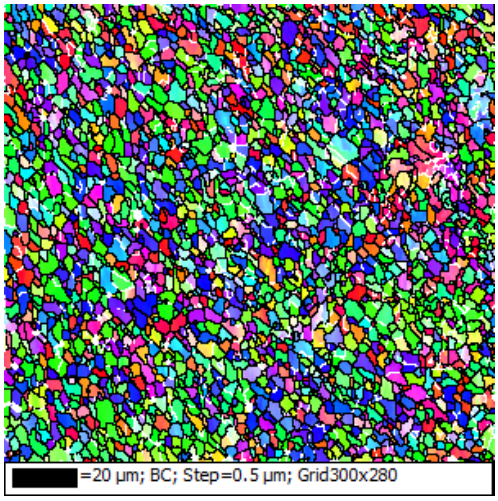

(b)

Fig. 6.15. EBSD (Inverse pole figure) maps of deformed specimens of Ti-Nb MA steel at constant strain rate of $1s^{-1}$ according to the processing conditions (a) M1, (b) M3, after reheating at 950°C for 10 s.

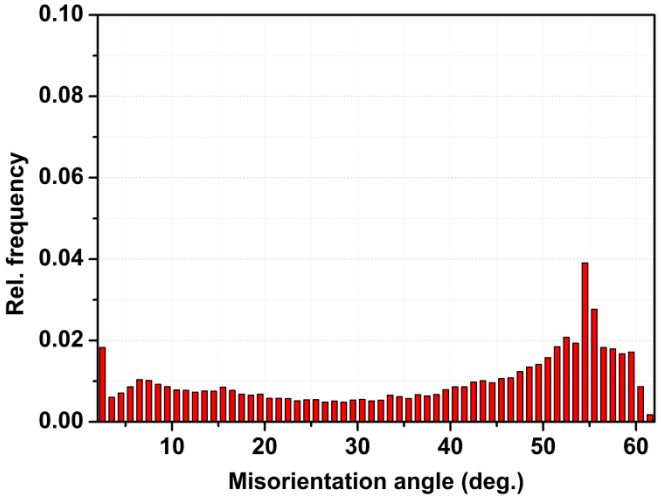

(a)

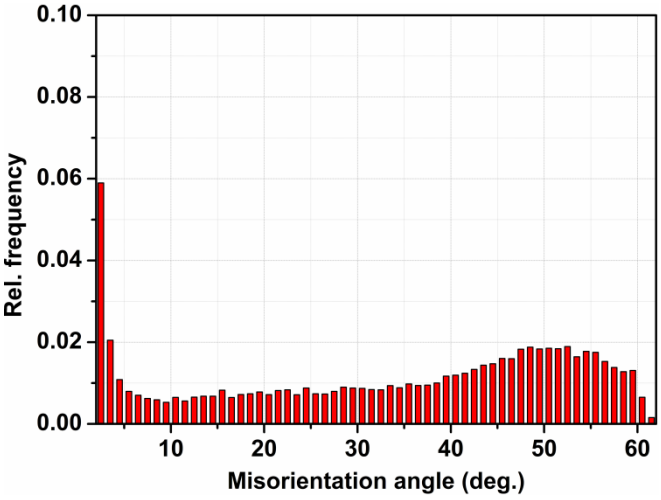

(b)

Fig. 6.16. Misorientation grain boundaries distribution of Ti-Nb MA steel specimens after the hot deformation at constant strain rate of $1s^{-1}$ according to the processing conditions of (a) M1, (b) M3, after reheating at 950°C for 10 s.

6.1.4. MECHANICAL PROPERTIES

The specimens after the compression test in Gleeble are small and tensile test specimens could not be prepared from it [79]. To obtain the mechanical properties of selected specimens, hardness measurements are performed. The hardness data and the predicted flow stress data of AISI 1010 steel at 8 pct strain ($\sigma_{0.08}$) as estimated by Tabor's relation are summarized in Table 6.4 [224].

$$H_V = 3\sigma_{0.08} \tag{6.1}$$

where H_V is the Vicker's hardness number. To obtain the flow stress in MPa a unit conversion factor is introduced in equation 6.1 (i.e. 1 H_V =9.81 MPa). Similarly, the predicted flow stress data and the hardness value of Ti-Nb MA steel are summarized in the Table 6.5.

Table 6.4 Summary of Vickers's hardness and the predicted flow stress data of AISI 1010 steel.

Specimen name	H_V	Predicted $\sigma_{0.08}$ (MPa)
S1	295±6	965±20
S2	350±8	1145±26
S3	224±8	733±26
S4	298±7	974±23

Table 6.5 Summary of Vickers's hardness and the predicted flow stress data of Ti-Nb MA steel.

Specimen name	H_V	Predicted $\sigma_{0.08}$ (MPa)
M1	557±10	1821±33
M2	525±7	1717±23
M3	398±8	1301±26

The predicted flow stress values are much high than that of DP steel (600MPa) which are most widely used. This supports the potential of fine grained microstructures [79]. With the decrease in average grain size, the hardness values increased and corresponding predicted flow stress also increased as shown in Table 6.4 and 6.5. This confirmed the trend that strength levels are increased with refining the microstructure.

6.2. DISCUSSION

6.2.1. FACTORS THAT AFFECT DIFT

Applying the two step deformations to the finest prior austenite grain size (41 μm of AISI 1010 steel, 11 μm of Ti-Nb MA steel) at different deformation temperatures, results the predominantly fine ferrite microstructure in both plain low carbon steel and the Ti-Nb MA steel. However, the steel chemistries along with strain also influence the evolution of microstructure. The path to the formation of fine grained ferrite by DIFT can be described after studying the microstructural evolution at different strain levels.

The potential for DIFT increases with the increase in the amount of strain. The increase in the amount of strain affects the final microstructure in one of the following ways: (1) most of the coarse-grained ferrite microstructures converted into fine-grained ferrite microstructures or (2) it increases the ferrite fraction. In this study, it was observed that with increasing the strain, gradually the coarse grained ferrite was replaced with fine grained ferrite in both the studied steels (AISI 1010 and Ti-Nb MA steel), also the ferrite volume fraction increased as shown in figures 6.3, and 6.5. At all levels of applied strain dynamic ferrite nucleation occurred in the plain carbon steel. The lower strain leads to the larger ferrite grains, resulting in lower nucleation density. The deformations were performed in the γ region which is in metastable state. The heavy deformation increases the γ free energy, resulting metastable γ to unstable γ and the DIF transformation is possibly induced [47]. In Ti-Nb MA steel the velocity of austenite-ferrite interface is much lower as compared to that of AISI 1010 steel. This happens due to the presence of Nb which slows down the ferrite transformation rate [79].

In Ti-Nb MA steel, the DIFT potential was retarded with increasing the prior austenite grain size. This was the similar findings as reported by the Hong et al. [47] with the final microstructure of ferrite of about 4.1 μm and about ferrite fraction of 75 pct in the case of plain carbon steel. In this study, a finer ferrite microstructure of 3.2 μm was observed with the ferrite fraction of about 78 pct in plan carbon steel. Whereas, UFF microstructure with the average grain size of 1.1 μm with the ferrite fraction of 81 pct in the case of Ti-Nb MA steel, may be good for dual phase steel. On the contrary, Hurley et al. reported that DIFT potential was increased with the increasing of prior austenite grain size [37]. The reason behind this contradiction may be due to the fact that the Ar_3 temperature changed with the changing of prior austenite grain size, which influenced the deformation temperature during the DIFT

schedule. Higher austenitization temperature is employed to obtain the larger prior austenite grain size, and also the significant amount of Nb dissolves in the solution. The combined effect of more Nb in solution and larger prior austenite grain size results the distinct delay in the ferrite formation. Thus, in DIFT process the prior austenite grain size cannot be considered as an independent parameter. Figures 6.17 and 6.18 show S2 specimen of AISI 1010 steel and M1 specimen of Ti-Nb MA steel, respectively, in which the DIF was transformed uniformly at both austenite grain boundary and in austenite matrix. This means that in smaller prior austenite grains, the DIF propagates more uniformly in the austenite grains due to deformation. Therefore, more DIF was observed due to the smaller austenite grain and more austenite grain boundaries.

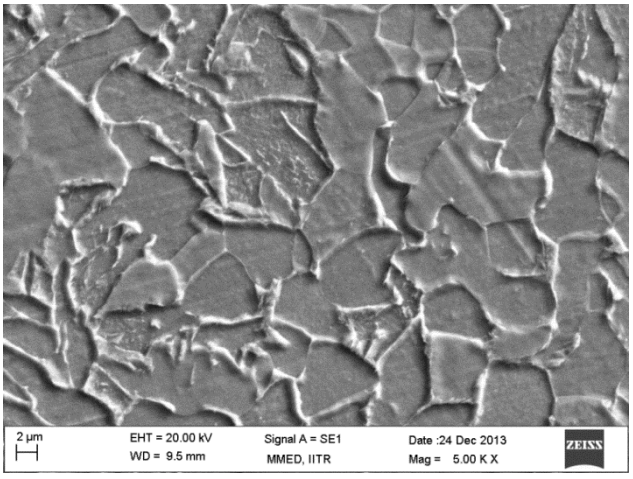

Fig. 6.17. SEM micrograph of the AISI 1010 steel specimen deformed according to the processing conditions of S2 at constant strain rate of $1s^{-1}$.

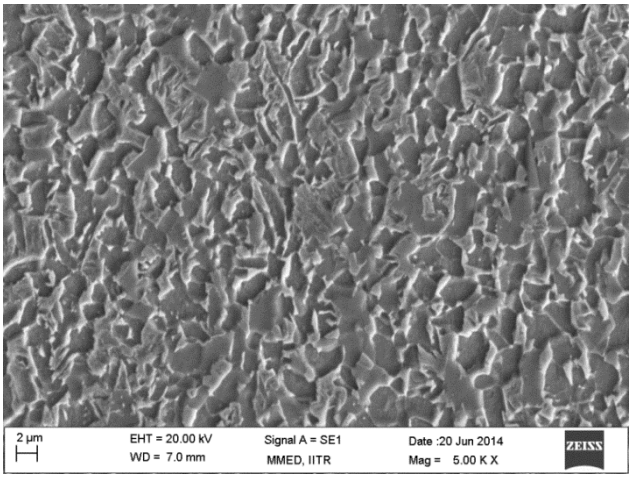

Fig. 6.18. SEM micrograph of the Ti-Nb MA steel specimen deformed according to the processing conditions of M1 at constant strain rate of 1 s^{-1}.

6.2.2. OPTIMUM CONDITIONS FOR FERRITE GRAIN REFINEMENT BY DIFT

Under static condition the acceleration of ferrite transformation depends upon the following factors such as large austenite grain boundary as ferrite nucleation site, deformation band density, adequate strain rate and sufficient amount of deformation before austenite to ferrite transformation [47]. In the present study, it was observed that the required true strain in the second step deformation to form deformation induced ferrite was 0.8, just above the Ar_3. This shows that γ free energy will increase if the deformation is performed at lower temperature. The DIFT occurs at the lower temperatures in the non-recrystallization region of austenite i.e. the temperature above Ar_3 and below Ad_3, where Ad_3 is the upper limiting temperature of DIFT at a certain deforming condition. Ad_3 depends upon the deformation stored energy, and it increases as the deformation temperature decreases [225]. DIFT occurs more easily in the fine grained austenite owing to increase in the austenite grain boundaries. In the present study, large amount of DIF was observed from the finer austenite grain size of AISI 1010 and Ti-Nb MA steel. Hence, DIFT results from a large number of lattice defects in austenite grain boundary, dislocation, vacancy, twin boundary, interstitial atom and stacking fault. With spreading the dislocations in the boundaries is the starting of their absorption and is connected with diffusion. Thus, the grain boundary diffusion is accelerated with the increasing rate of spreading of dislocations in both the materials. Accelerated absorption of lattice dislocations and enhanced diffusion by grain boundaries in the region of small grain sizes, the basic character of mechanical properties is quite understandable. For example, multi-axial deformation as a complex strain mode to obtain fine grains of submicron level [226]. The DIF was formed at the austenite grain boundary at the lower strain rate. The only thin ferrite film was formed because when the deformations were performed in the temperature range of Ae_3-Ar_3 with low strain rate, the deformation concentrates only at the austenite grain boundary as reported by Mintz et al. [227].

Generally, ferrite grain size and martensitic island size have to be refined to achieve suitable combination of strength-ductility and formability in DP steels, with the martensite volume fraction in the range of 20-30 pct. The heavy deformation (true stain 1.4) results fine austenite and fine ferrite and achieved the average grain size of 3.2 μm with ferrite fraction of 78 pct in the case of plain low carbon steel, whereas 1.1 μm with ferrite fraction of 81 pct in the case of Ti-Nb MA steel. Thus, such thermomechanical processing approach can be employed to produce fine grained DP steels.

6.3. SUMMARY

1. DIFT can be successfully used to form fine to ultra-fine ferrite microstructure with appropriate processing conditions and produced equiaxed fine grained DP microstructure with appropriate amount of martensite for both AISI 1010 and Ti-Nb MA steel.
2. The potential for DIFT increases as the amount of applied strain increases. A dual phase (ferrite + martensite) microstructure with the average grain size of 3.2μm along with martensite of volume fraction of 22 pct is obtained, even though the prior austenite grain size of AISI 1010 steel was large (41μm). Whereas, in Ti-Nb MA steel the average grain size of 1.1μm with the ferrite fraction of 81 pct was obtained.
3. Fine-grained DP microstructure was processed in the moderate power dissipation efficiency η region which validated by the ferrite formation due to DIFT and it is supported by the flow curves. This would be well suited to design a suitable processing window for industrial purpose.

Chapter 7

CONCLUSIONS

In the present work three steels viz. AISI 1010, AISI 1016 (plain low carbon steels) and low carbon Ti-Nb microalloyed steel have been selected to study the hot deformation behavior, and also to develop the optimize conditions for grain refinement using thermomechanical processing. The objective of the present work was to obtain to establish the better understanding of the material behavior, metallographic structure, involved mechanisms and the safe workability zone.

HOT DEFORMATION AND MICROSTRUCTURAL EVOLUTION

(1) HOT DEFORMATION OF PLAIN LOW CARBON STEEL

The hot deformation behavior of AISI 1010 steel is studied in the temperature range of 750°C to 1050ºC and the strain rate range of 0.01-20 s^{-1} whereas AISI 1016 steel are studied in same temperature range with strain rate ranging from 0.01-80 s^{-1}. Processing maps are developed using the DMM and modified DMM and deformation is also analyzed by means of constitutive equations. The following conclusions are drawn from this work.

1. High values of strain rate sensitivity, m, and power dissipation efficiency, η are at low to moderate temperatures and low to moderate strain rates in AISI 1010 steel. Also some region of high m and η is shown in the moderate strain rate and at high temperature. As the amount of carbon content increased the values of strain rate sensitivity, m, and power dissipation efficiency, η increased and also the workability region increased.
2. The instability parameter, κ_j predict the more accurate deformation behaviour. The workability zone is decreased as the carbon contents increased.
3. The peak value of flow stress increased as the carbon contents in the steel are increased. The stacking fault energy is decreased with the increasing carbon content of austenite. Due to low stacking fault energy higher stresses are required for cross slip.
4. Smaller the Zener-Hollomon parameter, larger is the amount of softening and the more easily DRX/DRV occurs. This is true for both studied plain carbon steels. But the value

Zener-Hollomon parameter increased with the increase in carbon contents.

5. The flow is unstable at the high strain rates. In this region, the Zener-Hollomon parameter is higher and the values of m and η were lower. This is also confirmed by the metallographic investigations where the damage occurs at the high strain rates due to less restoration of microstructure in both plain carbon steels due to possible adiabatic heating from short deformation times.
6. The peak stress is shifted towards the higher strain for a particular deformation temperature and strain rate with increasing the amount of carbon contents.
7. To analyse the relation between flow stress and Zener-Hollomon parameter, the sinh type equation is used over the entire deformation zone. The values of the peak flow stress, and Zener-Hollomon parameter show good correlation, and the pertaining equation is proposed.
8. The value of stress exponent, n is 3.5 shows that dislocation gliding and climb controlled the hot deformation process. As the amount of carbon content increased the value of stress exponent, n is increased.
9. Apparent activation energy for hot deformation of AISI 1010 steel was found to be 177 kJ/mol, and 290 kJ/mol for AISI 1016 steel. This means as the carbon content is increased the amount of carbon in the solid solution is increased and thus apparent activation energy increased.
10. At low Z conditions, the kinetics of DRV is improved as the carbon content increased, since the climb is controlled by the diffusion process.

(2) HOT DEFORMATION OF LOW C Ti-Nb MICROALLOYED STEEL

Hot deformation processing maps are developed for SAILMA grade microalloyed steel by using DMM and modified DMM. The deformation behavior is studied over a wider temperature range of 750ºC to 1050°C and strain rate range of 0.01 - 80 s^{-1}. Following conclusions are drawn from this work.

1. The critical temperatures Ar_3 and Ar_1 of Ti-Nb MA steel are lower as compared to the plain carbon steel (AISI 1016). Also, the peak flow stresses of the Ti-Nb MA steel are higher than that of AISI 1016. This is due to the presence of Nb and Ti, which retard the DRX due to dynamic precipitation of complex Nb-Ti carbonitrides.

2. The peak stress shifted towards the higher strain as compared to the plain low carbon steel. It is observed that the values of peak stress and steady state stress are also increased due to addition of Nb and Ti as compared to the similar plain low carbon steel.
3. The value of strain rate sensitivity parameter, *m* is reduced with the addition of Ti-Nb MA as compared to the plain low carbon steel. The region of the high value of *m* is shifted towards the higher temperature zone in the case of microalloyed steel. The same trends were followed by the power dissipation efficiency, η_{Prasad} and $\eta_{Murty\ \&\ Rao}$.
4. The apparent activation energy, *Q*, for Ti-Nb MA steel is higher as compared to AISI 1016 steel and is 359 kJ/mol. This is because that in Ti-Nb microalloyed steel Nb can be present either in dissolved form where it exhibits a strong solute drag effect, or as NbC precipitates which effectively pin the grain boundaries. Drag exerted on the migrating grain boundaries by Zener pinning effect of the NbC/TiC precipitates or by the presence of dissolved Nb solute can retard the progress of recrystallization.
5. The value of the stress exponent, *n* is 4.6, which suggests that the mechanism of hot deformation is dislocation glide controlled by dislocation climb at lower strain rates.
6. The value of the Zener-Hollomon parameter, Z is also higher in the Ti-Nb MA steel as compared to the plain carbon steel.

GRAIN REFINEMENT USING DIFT TECHNIQUE

1. DIFT can be successfully used to form fine to ultra-fine ferrite microstructure with appropriate processing conditions and produced equiaxed fine grained DP microstructure with appropriate amount of martensite for both AISI 1010 and Ti-Nb MA steel.
2. The potential for DIFT increases as the amount of applied strain increases. A dual phase (ferrite + martensite) microstructure with the average grain size of 3.2 μm along with martensite of volume fraction of 22 pct is obtained, even though the prior austenite grain size of AISI 1010 steel was large (41μm). Whereas, in Ti-Nb MA steel the average grain size of 1.1μm with the ferrite fraction of 81 pct was obtained.
3. Fine-grained DP microstructure was processed in the moderate power dissipation efficiency η region which validated by the ferrite formation due to DIFT and it is supported by the flow curves. This would be well suited to design a suitable processing window for industrial purpose.

Chapter 8

FUTURE SCOPE OF THE WORK

In the present work hot deformation behavior of Ti-Nb microalloyed steel is studied in the temperature range where carbides are partially dissolved. In continuation of this work, the hot deformation behavior of Ti-Nb microalloyed steel can be further analyzed in the wide range of temperatures and strain rates, after austenitizing at the temperature where the completely dissolution of Ti and Nb takes place. The processing maps of complete dissolved Ti, Nb and partially dissolved Ti, Nb should be compared and determine the effect of these micro alloying elements can be clearly explained. This will be useful and important contribution for this type of materials. The safe workable region obtained from the processing maps should be used to obtain the defect free forming process.

REFERENCES

1. Chowdhury S. G., Rajinikanth V., Thermomechanical processing of metals and alloys, Special Metal Casting and Forming Processes, 78-81, 2008.
2. Roberts W., McQueen H. J. et al., (Eds.), Strength of Metals and Alloys, Pergamon Press,Oxford, Vol. 3, 1859-1892, 1985.
3. Ryan N. D., McQueen H. J., Effects of alloying upon the hot workability of carbon, microalloyed, tool, and austenitic stainless steels, J. Mech. Work. Tech., 12, 279-296, 1986.
4. Ryan N. D., McQueen H. J., Mean pass flow stresses and interpass softening in multistage processing of carbon, HSLA, tool and γ-stainless steels, J. Mech. Work. Tech., 12, 323-349, 1986.
5. McQueen H. J., Metal forming: Industrial, mechanical computational and microstructural, J. Mater. Process. Technol., 37, 3-36, 1993.
6. Venugopal P., Optimisation of workability and control of microstructures in deformation processing of austenitic stainless steels: Development and application of processing maps for stainless steels type AISI 304 and 316 L, Ph D thesis, Indian Institute of Technology Madras, Chennai, 1981.
7. Khun H. A., Lee P. W., Erturk T., A fracture criterion for cold forming, J. Eng. Mater. Technol., 213-218, 1973.
8. Frost H. J., Ashby M. F., Deformation mechanism maps, Pergamon, NewYork, vol. 1, 1982.
9. Raj R., Development of processing maps of use in warm forming and hot forming processes, Metall. Trans. A, 12, 1089-1097, 1981.
10. Prasad Y. V. R. K., Gegel H. L., Doraivelu S. M., Malas J. C., Morgan J. T., Lark K. A., Barker D. R., Modelling of Dynamic Material Behavior in Hot Deformation: Forging of Ti-6242, Metall. Trans. A, 15, 1883-1892, 1984.
11. Prasad Y. V. R. K., Seshacharyulu T., Modelling of hot deformation for microstructural control, Int. Mater. Rev., 43, 243-258, 1998.

12. Narayana Murty S. V. S., Rao B. N., Kashyap B. P., On the hot working characteristics of 6061Al-SiC and 6061-Al_2O_3 particulate reinforced metal matrix composites, Comp. Sci. Tech., 63, 119-135, 2003.
13. Poletti C., Six J., Hochegger M., Degischer H. P., Ilie S., Hot Deformation Behaviour of Low Alloy Steel, Steel Research Inter., 82, 710-718, 2011.
14. Hodgson P. D., Hickson M. R., Gibbs R. K., Ultrafine ferrite in low carbon steel, Scripta Mater., 40(10), 1179-1184, 1999.
15. Hong S. C., Lim S. H., Lee K. J., Shin D. H., Lee K. S., Effect of Undercooling of Austenite on Strain Induced Ferrite Transformation Behavior, ISIJ International, 43, 394-399, 2003.
16. Calcagnotto M., Ponge D., Raabe D., Effect of grain refinement to 1 μm on strength and toughness of dual-phase steels, Mater. Sci. Eng. A, 527, 7832-7840, 2010.
17. Sellars C. M., Tegart W. J. M., Hot Workability, Int. Metall. Rev., 17, 1-24, 1972.
18. Ahlblom B., Sandström R., Hot workability of stainless steels: influence of deformation parameters, microstructural components, and restoration processes, Int. Metals Rev., 27(1), 1-27, 1982.
19. Semiatin S. L., ed. Introduction to Bulk-Forming Processes, Metalworking: Bulk Forming, Vol 14A, ASM Handbook, ASM International, 3-10, 2005.
20. Brooks J. W., Forging of superalloys, Mater. Design, 21, 297-303, 2000.
21. Rao K. P., Prasad Y. K. D. V., Hawbolt E. B., Hot deformation studies on a low-carbon steel: Part 1 - Flow curves and the constitutive relationship, J. Mater. Process. Technol., 56, 897-907, 1996.
22. Baragar D. L., The high temperature and high strain-rate behaviour of a plain carbon and an HSLA steel, J. Mech. Work. Tech., 14, 295-307, 1987.
23. Matsumura Y., Yada H., Evolution of Ultrafine-grained Ferrite in Hot deformation, Trans. ISIJ, 27, 492-498, 1987.
24. Eghbali B., Abdollah-Zadeh A., Beladi H., Hodgson P. D., Characterization on ferrite microstructure evolution during large strain warm torsion testing of plain low carbon steel, Mater. Sci. Eng. A, 435-436, 499-503, 2006.
25. Eghbali B., Abdollah-Zadeh A., Hodgson P. D., Dynamic softening of ferrite during large strain warm deformation of a plain C steel, Mater. Sci. Eng.A, 462, 259-263, 2007.

26. Fan J., Dai X., Xie R., Zhang W., Wang Z., Surface Ferrite Grain Refinement and Mechanical Properties of Low Carbon Steel Plates, J. Iron Steel Research, International, 13(4), 35-39, 2006.
27. Yang Z., Wang R., Formation of Ultra-fine grain structure of plain low carbon steel through deformation induced ferrite transformation, ISIJ International, 43(5), 761-766, 2003.
28. Cai M., Ding H., Lee Y., Dynamic strain-induced ferrite transformation during hot compression of low carbon Si-Mn Steels, Materials Transactions, 52(9), 1722-1727, 2011.
29. Kim S., Lee C., Choi I., Lee S., Effects of Heat Treatment and Alloying Elements on the Microstructures and Mechanical Properties of 0.15 wt pct C Transformation-Induced Plasticity-Aided Cold-Rolled Steel Sheets, Metall. Mater. Trans. A, 32, 505-514, 2001.
30. Zhang J., Kwon H., Kim H., Byon S., Park H., Im Y., Micro-cracking of low carbon steel in hot-forming processes, J. Mater. Process. Technol., 162-163, 447-453, 2005.
31. Sarkar B., Jha B. K., Kumar V., Chaudhuri S. K., Jha S., Development and Characterization of Steel Containing Very Fine Ferrite Grains, J. Mater. Eng. Perform., 14, 219-222, 2005.
32. Huang Y. D., Froyen L., Important factors to obtain homogeneous and ultrafine ferrite-pearlite microstructure in low carbon steel, J. Mater. Process. Technol., 124, 216-226, 2002.
33. Chung J. H., Park J. K., Kim T. M., Ok S. Y., Study of deformation-induced phase transformation in plain low carbon steel at low strain rate, Mater. Sci. Eng. A, 527, 5072-5077, 2010.
34. Calcagnotto M., Adachi Y., Ponge D., Raabe D., Deformation and fracture mechanisms in fine and ultrafine-grained ferrite/martensite dual-phase steels and the effect of aging, Acta Mater., 59, 658-670, 2011.
35. Song R., Ponge D., Raabe D., Improvement of the work hardening rate of ultrafine grained steels through second phase particles, Scripta Mater., 52, 1075-1080, 2005.
36. Hickson M. R., Hurley P. J., Gibbs R. K., Kelly G. L., Hodgson P. D., The Production of Ultrafine Ferrite in Low-Carbon Steel by Strain-Induced Transformation, Metall. Mater. Trans. A, 33, 1119-1126, 2002.

37. Hurley P. J., Hodgson P. D., Formation of ultra-fine ferrite in hot rolled strip: potential mechanisms for grain refinement, Mater. Sci. Eng. A, 302, 206-214, 2001.
38. Lee K., Lee H., Grain refinement and mechanical properties of asymmetrically rolled low carbon steel, J. Mater. Process. Technol., 210, 1574-1579, 2010.
39. Choi J., Seo D., Lee J., Um K., Choo W., Formation of Ultrafine Ferrite by strain-induced dynamic transformation in Plain Low Carbon Steel, ISIJ International, 43(5), 746-754, 2003.
40. Escobar F., Cabrera J. M., Prado J. M., Effect of carbon content on plastic flow behaviour of plain carbon steels at elevated temperature, Mater. Sci. Tech., 19, 1137-1147, 2003.
41. Xiao F., Liao B., Qiao G., Zhang C., Shan Y., Zhong Y., Yang K., Effects of chemical composition and hot deformation on continuous cooling transformation behavior of acicular ferrite pipeline steels, Multidiscipline Modeling in Mat. Str., 2, 389-410, 2006.
42. Saxena A., Kumar V., Datta R., Influence of Cooling Rate on Transformation Behavior of 0.15% V Microalloyed Steel, J. Mater. Eng. Perform., 20, 1481-1483, 2011.
43. Deva A., Jha B. K., Mishra N. S., Influence of boron on strain hardening behaviour and ductility of low carbon hot rolled steel, Mater. Sci. Eng. A, 528, 7375-7380, 2011.
44. Kwon O., DeArdo A. J., Suppression of static recrystallization by Nb(C,N) precipitation in HSLA steels, Proc. Int. Conf. on Processing, Microstructure and properties of HSLA steels, ed. A.J. DeArdo, TMS, Pittsburg, USA, 63-68, 1987.
45. Xiao F., Cao Y., Qiao G., Zhang X., Liao B., Effect of Nb Solute and NbC Precipitates on Dynamic or Static Recrystallization in Nb Steels, J. Iron Steel Research, International, 19(11), 52-56, 2012.
46. Guo Z. X., The deformation and processing of structural materials, Woodhead Publishing limited, Cambridge, England, 2005.
47. Hong S. C., Lee K. S., Influence of deformation induced ferrite transformation on grain refinement of dual phase steel, Mater. Sci. Eng. A, 323, 148-159, 2002.
48. Lin Y. C., Liu G., Effects of strain on the workability of a high strength low alloy steel in hot compression, Mater. Sci. Eng. A, 523, 139-144, 2009.
49. Lin Y. C., Chen M., Study of microstructural evolution during static recrystallization in a low alloy steel, J. Mater. Sci., 44, 835-842, 2009.

50. Deva A., Jha B. K., Mishra N. S., Silicon as grain refiner in niobium microalloyed hot rolled steel, Mater. Sci. Tech., 27, 710-712, 2011.
51. Wei H., Liu G., Xiao X., Zhao H., Ding H., R. Kang R., Characterization of hot deformation behavior of a new microalloyed C-Mn-Al high-strength steel, Mater. Sci. Eng. A, 564, 140-146, 2013.
52. Wei H., Liu G., Zhao H., Zhang M., Effect of carbon content on hot deformation behaviors of vanadium microalloyed steels, Mater. Sci. Eng. A, 596, 112-120, 2014.
53. Wei H., Liu G., Effect of Nb and C on the hot flow behavior of Nb microalloyed steels, Mater. Design, 56, 437-444, 2014.
54. Momeni A., Arabi H., Rezaei A., Badri H., Abbasi S. M., Hot deformation behavior of austenite in HSLA-100 microalloyed steel, Mater. Sci. Eng. A, 528, 2158-2163, 2011.
55. Momeni A., Abbasi S. M., Badri H., Hot deformation behavior and constitutive modeling of VCN200 low alloy steel, Applied Mathematical Modelling, 36, 5624-5632, 2012.
56. Jorge Junior A. M., Guedes L. H., Balancin O., Ultra Grain refinement during the simulated thermomechanical-processing of low carbon steel, J. Mater. Res. Technol., 1(3), 141-147, 2012.
57. Mirzaee M., Keshmiri H., Ebrahimi G. R., Momeni A., Dynamic recrystallization and precipitation in low carbon low alloy steel 26NiCrMoV 14-5, Mater. Sci. Eng. A, 551, 25-31, 2012.
58. Ueki M., Horie S., Nakamura T., High Temperature Deformation and Thermomechanical Treatment of Low Carbon Steel and Vanadium-Niobium Microalloyed Steel, Trans. ISIJ, 27, 453-459, 1987.
59. Eghbali B., Abdollah-Zadeh A., The influence of thermomechanical parameters in ferrite grain refinement in a low carbon Nb-microalloyed steel, Scripta Mater., 53, 41-45, 2005.
60. Eghbali B., Abdollah-Zadeh A., Influence of deformation temperature on the ferrite grain refinement in a low carbon Nb-Ti microalloyed steel, J. Mater. Process. Technol., 180, 44-48, 2006.
61. Eghbali B., Abdollah-Zadeh A., Strain-induced transformation in a low carbon microalloyed steel during hot compression testing, Scripta Mater., 54, 1205-1209, 2006.

62. Eghbali B., Abdollah-Zadeh A., Deformation-induced ferrite transformation in a low carbon Nb-Ti microalloyed steel, Mater. Design, 28, 1021-1026, 2007.
63. Eghbali B., Study on the ferrite grain refinement during intercritical deformation of a microalloyed steel, Mater. Sci. Eng. A, 527, 3407-3410, 2010.
64. Kwon O., Ardo A. J. D., Interactions between recrystallization and precipitation in hot-deformed microalloyed steels, Acta Metall. Mater., 39, 529-538, 1991.
65. Cao J., Liu Q., Yong Q., Sun X., Effect of niobium on isothermal transformation of austenite to ferrite in HSLA low-carbon steel, J. Iron Steel Res. Inter., 14(3), 51-55, 2007.
66. Opiela M., Grajcar A., Hot deformation behavior and softening kinetics of Ti-V-B microalloyed steels, Archives of Civil and Mech. Eng., 12, 327-333, 2012.
67. Zhao H., Liu G., Xu L., Rate-controlling mechanisms of hot deformation in a medium carbon vanadium microalloy steel, Mater. Sci. Eng. A, 559, 262-267, 2013.
68. Cho S., Kang K., Jonas J. J., The Dynamic, Static and Metadynamic Recrystallization of a Nb-microalloyed Steel, ISIJ International, 41, 63-69, 2001.
69. Cho S. H., Kang K. B., Jonas J. J., Effect of manganese on recrystallisation kinetics of niobium microalloyed steel, Mater. Sci. Tech., 18, 389-395, 2002.
70. Xu Y. B., Yu Y. M., Xiao B. L., Liu Z. Y., Wang G. D., Modelling of microstructure evolution during hot rolling of a high-Nb HSLA steel, J. Mater. Sci., 45, 2580-2590, 2010.
71. Medina S. F., Hernandez C. A., The influence of chemical composition on peak strain of deformed austenite in low alloy and microalloyed steels, Acta Mater., 44(1), 149-154, 1996.
72. Medina S. F., Hernendez C. A., Modelling of the dynamic recrystallization of austenite in low alloy and microalloyed steels, Acta Mater., 44(1) 165-171, 1996.
73. Zhang Z., Liu Y., Liang X., She Y., The effect of Nb on recrystallization behavior of a Nb micro-alloyed steel, Mater. Sci. Eng. A, 474, 254-260, 2008.
74. Bao S., Zhao G., Yu C., Chang Q., Ye C., Mao X., Recrystallization behavior of a Nb-microalloyed steel during hot compression, Applied Mathematical Modelling, 35, 3268-3275, 2011.

75. Shaban M., Eghbali B., Characterization of austenite dynamic recrystallization under different Z parameters in a microalloyed steel, J. Mater. Sci. Technol., 27(4), 359-363, 2011.
76. Maruyama N., Uemori R., Sugiyama M., The role of niobium in the retardation of the early stage of austenite recovery in hot-deformed steels, Mater. Sci. Eng. A, 250, 2-7, 1998.
77. Fernández A. I., Uranga P., López B., Rodriguez-Ibabe J. M., Dynamic recrystallization behavior covering a wide austenite grain size range in Nb and Nb-Ti microalloyed steels, Mater. Sci. Eng. A, 361, 367-376, 2003.
78. Ma L., Liu Z., Jiao S., Yuan X., Wu D., Effect of Niobium and Titanium on dynamic recrystallization behavior of low carbon steels, J. Iron Steel Research, International, 15(3), 31-36, 2008.
79. Mukherjee K., Hazra S. S., Militzer M., Grain refinement in Dual phase steels, Metall. Mater. Trans. A, 40, 2145-2159, 2009.
80. Priestner R., Hodgson P. D., Ferrite grain coarsening during transformation of thermomechanically processed C-Mn-Nb austenite, Mater. Sci. Tech., 8, 849-854, 1992.
81. Bakkaloğlu A., Effect of processing parameters on the microstructure and properties of an Nb microalloyed steel, Materials Letters, 56, 263-272, 2002.
82. Wang Z., Mao X., Yang Z., Sun X., Yong Q., Li Z., Weng Y., Strain-induced precipitation in a Ti micro-alloyed HSLA steel, Mater. Sci. Eng. A, 529, 459-467, 2011.
83. Hong S. G., Kang K. B., Park C. G., Strain induced precipitation of NbC in Nb and Nb-Ti microalloyed HSLA steels, Scripta Mater., 46, 163-168, 2002.
84. Cao Y., Xiao F., Qiao G., Zhang X., Liao B., Quantitative research on effects of Nb on hot deformation behaviors of high-Nb microalloyed steels, Mater. Sci. Eng. A, 530, 277-284, 2011.
85. Kostryzhev A. G., Shahrani A., Zhu C., Ringer S. P., Pereloma E. V., Effect of deformation temperature on niobium clustering, precipitation and austenite recrystallization in a Nb-Ti microalloyed steel, Mater. Sci. Eng. A, 581, 16-25, 2013.
86. Ma L., Liu Z., Jiao S., Yuan X., Wu. D., Dynamic Recrystallization Behaviour of Nb-Ti Microalloyed Steels, Journal of Wuhan University of Technology-Mater. Sci. Ed., 23(4), 551-557, 2008.

87. Hong S. C., Lim S. H., Hong H. S., Lee K. J., Shin D. H., Lee K. S., Effects of Nb on strain induced ferrite transformation in C-Mn steel, Mater. Sci. Eng. A, 355, 241-248, 2003.
88. Vervynckt S., Verbeken K., Thibaux P., Houbaert Y., Recrystallization-precipitation interaction during austenite hot deformation of a Nb microalloyed steel, Mater. Sci. Eng. A, 528, 5519-5528, 2011.
89. Abdollah-Zadeh A., Eghbali B., Mechanism of ferrite grain refinement during warm deformation of a low carbon Nb-microalloyed steel, Mater. Sci. Eng. A, 457, 219-225, 2007.
90. Yao S., Du L., Li G., Jiao X., Wang G., Microstructure Evolving Behaviors of Undercooled Ultrafine Austenite Grains During deformation, J. Iron Steel Research, International, 18(6), 43-48 and 53, 2011.
91. Liu Q., Deng S., Sun X., Dong H., Weng Y., Effect of dissolved and precipitated Niobium in microalloyed steel on deformation induced ferrite transformation (DIFT), J. Iron Steel Research, International, 16(4), 67-71, 2009.
92. Beladi H., Kelly G. L., Shokouhi A., Hodgson P. D., The evolution of ultrafine ferrite formation through dynamic strain-induced transformation, Mater. Sci. Eng. A, 371, 343-352, 2004.
93. Beladi H., Kelly G. L., Shokouhi A., Hodgson P. D., Effect of thermomechanical parameters on the critical strain for ultrafine ferrite formation through hot torsion testing, Mater. Sci. Eng. A, 367, 152-161, 2004.
94. Beladi H., Kelly G. L., Hodgson P. D., The Effect of Multiple Deformations on the Formation of Ultrafine Grained Steels, Metall. Mater. Trans. A, 38, 450-463, 2007.
95. Lin Y. C., Chen M., Study of microstructural evolution during metadynamic recrystallization in a low-alloy steel, Mater. Sci. Eng. A, 501, 229-234, 2009.
96. Ashby M. F., A First Report on Deformation-Mechanism Maps, Acta Metall., 20, 887-897, 1972.
97. Honeycombe R. W. K., The Plastic Deformation of Metals, Edward Arnold Publishers Ltd, London, England, 128-176, 1968.
98. Kocks U. F, Laws for Work-Hardening and Low-Temperature Creep, J. Eng. Mater. Tech., 98(1), 76-85, 1976.

99. Saada G., Cross-Slip and Work Hardening of F. C. C. Crystals, Mater. Sci. Eng. A, 137, 177-183, 1991.

100. Roberts W., Dynamic changes that occur during hot working and their significance regarding microstructural development and hot workability, in Deformation, Processing and Structure, Ed. G. Krauss, ASM International, Materials Park, Ohio 44073, 109-189, 1982.

101. Sakai T., Jonas J. J., Dynamic Recrystallization: Mechanical and Microstructural Considerations, Acta Metall., 32(2), 189-209, 1984.

102. Dieter G. E., Workability Testing Techniques, ASM International, Materials Park, Ohio 44073, 1- 19, 1984.

103. Kuhn H. A., Dieter G. E., Workability in Bulk Forming Processes, in Fracture 1977, Vol. 1, IFC4, Waterloo, Canada, 307-324, 1977.

104. Rao K. P., Doraivelu S. M., Gopinathan V., Flow Curves and Deformation of Materials at Different Temperatures and Strain Rates, J. Mech. Work. Tech., 6, 63-88, 1982.

105. Dieter G. E., Evaluation of Workability, in Forming and Forging, Vol. 14, Metals Handbook, 9th Edition, ASM International, Materials Park, Ohio 44073, 363-387, 1988.

106. McQueen H. J., Jonas J. J., Hot Workability Testing Techniques, in Metal Forming: Interrelation Between Theory and Practice, Ed. A.L. Hoffmanner, Plenum Pub. Corp., NY 10011, 393-427, 1970.

107. Schey J. A., Venner T. R., Takoman S. L., The Effect of Friction on Pressure in Upsetting at Low Diameter-to-Height Ratios, J. Mech. Work. Tech., 6, 23-33, 1982.

108. Baragar D. L., Crawley A. F., Frictional Effects on Flow Stress Determination at High Temperatures and Strain Rates, J. Mech. Work. Tech., 9, 291-299, 1984.

109. Rao K. P, Hawbolt E. B., McQueen H. J., Baragar D., Constitutive Relationships, for Hot Deformation of a Carbon Steel: A Comparison Study of Compression Tests and Torsion Tests, Canadian Metall. Quaterly, 32 (2), 165-175, 1993.

110. Malas III J. C., Frazier W. G., Venugopal S., Medina E. A., Medeiros S., Srinivasan R., Irwin R. D., Mullins W. M., Chaudhary A., Optimization of Microstructure Development during Hot Working Using Control Theory, Metall. Mater. Trans. A, 28, 1921-1930, 1997.

111. Venugopal S., Medina E. A., Malas III J. C., Medeiros S., Frazier W. G., Mullins W. M., Srinivasan R., Optimization of microstructure during deformation processing using control theory principles, Scripta Mater., 36, 347-353, 1997.
112. Kuhn H. A., Metals handbook, 9th edn, Metals Park, OH, American Society for Metals, Vol. 14, 388-408, 1988.
113. Kobayashi S., Oh S. I., Altan T., Forming and the finite element method, New York, Oxford, Oxford University Press, 1989.
114. Brown S. B., Kim K. H., Anand L., An Internal Variable Constitutive Model for Hot Working of Metals, Int. J. Plast., 5, 95-130, 1989.
115. Prasad Y. V. R. K., Recent advances in the science of mechanical processing, Indian J. Technol., 28, 435-451, 1990.
116. Rao V. V. K., Rajagopalachary T., Recent developments in modeling the hot working behavior of metallic materials, Bull. Mater. Sci., 19, 677-698, 1996.
117. Jonas J. J., Sellars C. M., Tegart W.J., Strength and structure under hot-working conditions, Metall. Rev., 14(1), 1-24, 1969.
118. Raj R., Deformation processing maps, unpublished work, Dept. Materials Science and Engineering, Cornell University, Ithaca, NY, 1982.
119. Ziegler H., Progress in solid mechanics, (ed. I.N. Sneddon and R. Hill), New York, Wiley, 4, 91-193, 1965.
120. Progogine I., Time, Structure, and Fluctuations, Science, 201, 777-787, 1978.
121. Wellstead P. E., Introduction to physical systems modelling, London, Acad. Press, 1979.
122. Hillborn R.C., Chaos and nonlinear dynamics: An introduction for scientists and engineers, New York, Oxford, Oxford University Press, 1994.
123. Hill R., Constitutive dual potentials in classical plasticity, J. Mech. Phys. Solids, 35, 23-33, 1987.
124. Prakash N. A., Gnanamoorthy R., Kamaraj M., Surface nanocrystallization of aluminium alloy by controlled ball impact technique, Surface Coatings Tech., 210, 78-89, 2012.
125. Manna R., Mukhopadhyay N.K., Sastry G.V.S., Effect of Equal Channel Angular Pressing on Microstructure and Mechanical Properties of Commercial Purity Aluminium, Metall. Mater. Trans. A, 39, 1525-1534, 2008.

126. Pant B. K., Sundar R., Kumar H., Kaul R., Pavan A. H. V., Ranganathan K., Bindra K. S., Oak S. M., Kukreja L. M., Prakash R. V., Kamaraj M., Studies towards development of laser peening technology for martensitic stainless steel and titanium alloys for steam turbine applications, Mater. Sci. Eng. A, 587, 352-358, 2013.

127. Prakash N. A., Gnanamoorthy R., Kamaraj M., Fretting wear behavior of fine grain structured aluminium alloy formed by oil jet peening process under dry sliding condition, Wear, 294-295, 427-437, 2012.

128. Roumina R., Sinclair C. W., Deformation Geometry and Through-Thickness Strain Gradients in Asymmetric Rolling, Metall. Mater. Trans. A, 39, 2495-2503, 2008.

129. Morimoto T., Chikushi I., Kurahashi R., Yanagimoto J., Proc. of TMP 2004, 2nd Intl. Conf. on Thermomechanical Processing of Steels, Stahleisen Verlag GmbH, Düsseldorf, Germany, 415-422, 2004.

130. Manna R., Agrawal P., Joshi S., Mudda B. K., Mukhopadhyay N. K., Sastry G. V. S., Physical modeling of equal channel angular pressing using plasticine, Scripta Mater., 53, 1357-1361, 2005.

131. Manna R., Mukhopadhyay N. K., Sastry G.V.S., Strengthening behavior of Bulk Ultra-Fine Grained Aluminum Alloys, Mater. Sci. Forum, 710, 241-246, 2012.

132. Lu F., Ma A., Jiang J., Yang D., Song D., Yuan Y., Chen J., Effect of multi-pass equal channel angular pressing on microstructure and mechanical properties of $Mg_{97.1}Zn_1Gd_{1.8}Zr_{0.1}$ alloy, Mater. Sci. Eng. A, 594, 330-333, 2014.

133. Shin D. H., Kim I., Kim J., Park K., Grain refinement mechanism during equal-channel angular pressing of a low-carbon steel, Acta Mater., 49, 1285-1292, 2001.

134. Zhang L., Ma A., Jiang J., Yang D., Song D., Chen J., Sulphuric acid corrosion of ultrafine-grained mild steel processed by equal-channel angular pressing, Corrosion Science, 75, 434-442, 2013.

135. Zhang L., Ma A., Jiang J., Jie X., Effect of processing methods on microhardness and acid corrosion behavior of low-carbon steel, Mater. Design, 65, 115-119, 2015.

136. Hwang B., Kim Y. G., Lee S., Hwang D. Y., Shin D. H., Dynamic Torsional Deformation Behavior of Ultra-Fine-Grained Dual-Phase Steel Fabricated by Equal Channel Angular Pressing, Metall. Mater. Trans. A, 38, 3007-3013, 2007.

137. Son Y. I., Lee Y. K., Park K. T., Lee C. S., Shin D. H., Ultrafine grained ferrite–martensite dual phase steels fabricated via equal channel angular pressing: Microstructure and tensile properties, Acta Mater., 53, 3125-3134, 2005.
138. Ueji R., Tsuji N., Minamino Y., Koizumi Y., Ultragrain refinement of plain low carbon steel by cold-rolling and annealing of martensite, Acta Mater., 50, 4177-4189, 2002.
139. Ueji R., Tsuji N., Minamino Y., Koizumi Y., Effect of rolling reduction on ultrafine grained structure and mechanical properties of low-carbon steel thermomechanically processed from martensite starting structure, Sci. Tech. Advanced Mater., 5, 153-162, 2004.
140. Tyagi R., Nath S. K., Ray S., Development of wear resistant medium carbon dual phase steels and their mechanical properties, Mater. Sci. Tech., 20, 645-652, 2004.
141. Tyagi R., Nath S. K., Ray S., Dry Sliding Friction and Wear in Plain Carbon Dual Phase Steel, Metall. Mater. Trans. A, 32, 359-367, 2001.
142. Tyagi R., Nath S. K., Ray S., Effect of Martensite Content on Friction and Oxidative Wear Behavior of 0.42 Pct Carbon Dual-Phase Steel, Metall. Mater. Trans. A, 33, 3479-3488, 2002.
143. Karmakar A., Sivaprasad S., Nath S. K., Misra R. D. K., Chakrabarti D., Comparison Between Different Processing Schedules for the Development of Ultrafine-Grained Dual-Phase Steel, Metall. Mater. Trans. A, 45, 2466-2479, 2014.
144. Karmakar A., Karani A., Patra S., Chakrabarti D., Development of Bimodal FerriteGrain Structures in Low-Carbon Steel Using Rapid Intercritical Annealing, Metall. Mater. Trans. A, 44, 2041-2052, 2013.
145. Najafi-Zadeh A., Jonas J. J., Yue S., Grain refinement by dynamic recrystallization during the simulated warm-rolling of interstitial free steels, Metall. Trans. A, 23, 2607-2617, 1992.
146. Tsuji N., Saito Y., Utsunomiya H., Tanigawa S., Ultra-fine grained bulk steel produced by Accumulative roll-bonding (ARB) process, Scripta Mater., 40, 795-800, 1999.
147. Luo J., Acoff V. L., Using cold roll bonding and annealing to process Ti/Al multi-layered composites from elemental foils, Mater. Sci. Eng. A, 379, 164-172, 2004.
148. Zhang R., Acoff V. L., Processing sheet materials by accumulative roll bonding and reaction annealing from Ti/Al/Nb elemental foils, Mater. Sci. Eng. A, 463, 67-73, 2007.

149. Qu P., Zhou L., Xu H., Acoff V. L., Microtexture Development of Niobium in a Multilayered Ti/Al/Nb Composite Produced by Accumulative Roll Bonding, Metall. Mater. Trans. A, 45, 6217-6230, 2014.
150. Yada H., Matsumura Y., Nakazima K., Ferritic steel having ultra-fine grains and a method for producing the same, United States Patent No.-4466842, August 21, 1984.
151. Niikura M., Fujioka M., Adachi Y., Matsukura A., Yokota T., Shirota Y., Hagiwara Y., New concepts for ultra refinement of grain size in Super Metal Project, J. Mater. Process. Technol., 117, 341-346, 2001.
152. Hickson M. R., Hurley P. J., Gibbs R. K., Kelly G. L., Hodgson P. D., The production of ultrafine ferrite in low-carbon steel by strain-induced transformation, Metall. Mater. Trans. A, 33, 1019-1026, 2002.
153. Kelly G. L., Beladi H., Hodgson P. D., Ultrafine Grained Ferrite Formed by Interrupted Hot Torsion Deformation of Plain Carbon Steel, ISIJ International, 42, 1585-1590, 2002.
154. Hodgson P. D., Beladi H., The role of recrystallization and coarsening in the formation of ultrafine grained steels through thermomechanical processing, Mater. Sci. Forum, 467-470, 1137-1144, 2004.
155. Morimoto T., Yoshida F., Chikushi I., Yanagimoto J., Combined macro-micro modeling for rolling force and microstructure evolution to produce fine grain hot strip in tandem hot strip rolling, ISIJ International, 47, 1475-1484, 2007.
156. Patra S., Roy S., Kumar V., Haldar A., Chakrabarti D., Ferrite Grain Size Distributions in Ultra-Fine-Grained High-Strength Low-Alloy Steel After Controlled Thermomechanical Deformation, Metall. Mater. Trans. A, 42, 2575-2590, 2011.
157. Karmakar A., Misra R. D. K., Neogy S., Chakrabarti D., Development of Ultrafine-Grained Dual-Phase Steels: Mechanism of Grain Refinement During Intercritical Deformation, Metall. Mater. Trans. A, 44, 4106-4118, 2013.
158. Xiao F., Liao B., Shan Y., Yang K., Isothermal transformation of low-carbon microalloyed steels, Mater. Charact., 54, 417-422, 2005.
159. Cho J., Suh D., Kang J., Lee H., Ultrafine Grained Materials II, Y. T. Zhu, T. G. Langdon, R. S. Mishra, S. L. Semiatin, M. J. Saran, T. C. Lowe, (Eds.), TMS, 259-266, 2002.

160. Porter D. A., Easterling K. E., Phase Transformations in Metals and Alloys, Chapman and Hall, 1992.
161. Bengochea R., Lopez B., Gutierrez I., Microstructural evolution during the austenite-to-ferrite transformation from deformed austenite, Metall. Mater. Trans. A, 29, 417-426, 1998.
162. Hurley P. J., Muddle B. C., Hodgson P. D., Nucleation sites for ultrafine ferrite produced by deformation of austenite during single-pass strip rolling, Metall. Mater. Trans. A, 32, 1507-1517, 2001.
163. Suh D., Oh C., Kim S., Limit of Ferrite Grain Refinement by Severe Plastic Deformation of Austenite, Metall. Mater. Trans. A, 36, 1057-1059, 2005.
164. Suh D., Cho J., Nagai K., Effect of initial grain size of austenite on hot-deformed structure of Ni-30Fe alloy, Metall. Mater. Trans. A, 35, 3399-3408, 2004.
165. Li C. M., Yada H., Yamagata H., In situ observation of γ-α transformation during hot deformation in an Fe-Ni alloy by an X-ray diffraction method, Scripta Mater., 39, 963-967, 1998.
166. Dong H., Sun X., Deformation induced ferrite transformation in low carbon steels, Current Opinion in Solid State Mater. Sci., 9, 269-276, 2005.
167. Zheng C., Li D., Lu S., Li Y., On the ferrite refinement during the dynamic strain-induced transformation: A cellular automaton modelling, Scripta Mater., 58, 838-841, 2008.
168. Poliak E. I., Jonas J. J., A one-parameter approach to determining the critical conditions for the initiation of dynamic recrystallization, Acta Mater., 44, 127-136, 1996.
169. Hutchinson C. R., Zurob H. S., Sinclair C. W., Brechet Y. J. M., The comparative effectiveness of Nb solute and NbC precipitates at impeding grain-boundary motion in Nb steels, Scripta Mater., 59, 635-637, 2008.
170. Medina S. F., The influence of niobium on the static recrystallization of hot deformed austenite and on strain induced precipitation kinetics, Scripta Metall., 32, 43-48, 1995.
171. Hickson M. R., Gibbs R. K., Hodgson P. D., The effect of chemistry on the formation of UItrafine Ferrite in Steel, ISIJ International, 39(11), 1176-1180, 1999.
172. Hanzaki A. Z., Pandi R., Hodgson P. D., Yue S., Continuous cooling deformation testing of steels, Metall. Mater. Trans. A, 24, 2657-2665, 1993.

173. Day A. P. et al., Channel 5 User Manual, HKL Technology A/S, Hobro, Denmark, 2001.
174. Prasad Y. V. R. K., Author's reply: Dynamic materials model: Basis and principles, Metall. Trans. A, 27, 235-236, 1996.
175. Narayana Murty S. V. S., Rao B. N., Kashyap B. P., Development and validation of a processing map for zirconium alloys, Modelling Simul. Mater. Eng., 10, 503-520, 2002.
176. Narayana Murty S. V. S., Rao B. N., Kashyap B.P., On the hot working characteristics of 2014 Al-20 vol % Al_2O_3 metal matrix composite, J. Mater. Process. Technol., 166, 279-285, 2005.
177. Malvern L. E., Introduction to the mechanics of a continuous medium, Prentice-Hall, Inc., Englewood Cliffs, New Jersey, 1969.
178. Wang C. Y., Wang X. J., Chang H., Wu K., Zheng M. Y., Processing maps for hot working of ZK60 magnesium alloy, Mater. Sci. Eng. A, 464, 52-58, 2007.
179. Wang C. Y., Wu K., Zheng M. Y., Hot deformation and processing maps of $Al_{18}B_4O_{33}$w/ZK60 composite, Mater. Sci. Eng. A, 477, 179-184, 2008.
180. Ziegler H., Becker E., Budiansky B., Lauwerier H. A., Koiter T., An introduction to thermodynamics, North-Holland publishing company, 2nd ed., 1983.
181. Montheillet F., Jonas J. J., Neale K. W., Modeling of dynamic material behavior: A critical evaluation of the dissipator power co-content approach Metall. Trans. A, 27, 232-235, 1996.
182. Samantaray D., Mandal S., Kumar V., Albert S. K., Bhaduri A. K., Jayakumar T., Optimization of processing parameters based on high temperature flow behaviour and microstructural evolution of a nitrogen enhanced 316L(N) stainless steel, Mater. Sci. Eng. A, 552, 236-244, 2012.
183. Wang C., Wu K., Zheng M., Hot deformation behavior and processing map of squeeze cast ZK 60 magnesium alloy, Transactions of the Nonferrous Metals Society of China, 16, 1758-1761, 2006.
184. Dikovits M., Poletti C., Warchomicka F., Deformation Mechanisms in the Near-β Titanium Alloy Ti-55531, Metall. Mater. Trans. A, 45, 1586-1596, 2014.
185. Semiatin S. L., Jonas J. J., Formability and Workability of Metals: Plastic Instability and Flow Localization, American Society for Metals, Ohio, 1984.

186. Semiatin S. L., Lahoti G. D., The occurrence of shear bands in isothermal, hot forging, Metall. Trans. A, 13, 275-288, 1982.

187. Considère A.. Annales des Ponts et Chaussées, 9, 574-775, 1885.

188. Hart E. W., Theory of the tensile test, Acta Metall., 15, 351-355, 1967.

189. Jonas J. J., Holt R. A., Coleman C. E., Plastic stability in tension and compression, Acta Metall., 24, 911-918, 1976.

190. Gupta R. K., Narayana Murty S. V. S., Pant B., Agarwala V., Sinha P. P., Hot workability of $\gamma + \alpha_2$ titanium aluminide: Development of processing map and constitutive equations, Mater. Sci. Eng. A, 551, 169-186, 2012.

191. Warchomicka F., Poletti C., Stockinger M., Study of the hot deformation behaviour in Ti-5Al-5Mo-5V-3Cr-1Zr, Mater. Sci. Eng. A, 528, 8277-8285, 2011.

192. Poletti C., Warchomicka F., Degischer H. P., Local deformation of Ti6Al4V modified 1 wt% B and 0.1 wt% C, Mater. Sci. Eng. A, 527, 1109-1116, 2010.

193. Sellars C.M., McTegart W.J., On the mechanism of hot deformation, Acta Metall., 14, 1136-1138, 1966.

194. McQueen H. J., Yue S., Ryan N. D., Fry E., Hot working characteristics of steels in austenitic state, J. Mater. Process. Technol., 53, 293-310, 1995.

195. McQueen H. J., Elevated temperature deformation at forming rates of 10^{-2} to 10^{2} s^{-1}, Metall. Trans. A, 33, 345-362, 2002.

196. Callister W. D., Material Science and Engineering-An Introduction, Fourth ed., John Wiley and Sons Inc., Singapore, 1997.

197. Krauss G., Steels: Processing, Structure, and Performance, ASM International, Materials Park, Ohio, USA, 2005.

198. Verlinden B., Driver J., Samajdar I., Doherty R. D., Thermo-Mechanical Processing of Metallic Materials, Pergamon Materials Series, R.W. Cahn (series ed.), Elsevier, Amsterdam, ISBN 978-0-08-044497-0, 2007.

199. Zhao M. C., Yang K., Xiao F. R., Shan Y. Y., Continuous cooling transformation of undeformed and deformed low carbon pipeline steels, Mater. Sci. Eng. A, 355, 126-136, 2003.

200. Abbasi S. M., Momeni A., Hot working behavior of Fe-29Ni-17Co analyzed by mechanical testing and processing map, Mater. Sci. Eng. A, 552, 330-335, 2012.

201. Semiatin S. L., Staker M. R., Jonas J. J., Plastic instability and flow localization in shear at high rates of deformation, Acta Metall., 32(9), 1347-1354, 1984.
202. Mirzadeh H., Cabrera J. M., Prado J. M., Najafizadeh A., Hot deformation behavior of a medium carbon microalloyed steel, Mater. Sci. Eng. A, 528, 3876-3882, 2011.
203. Dowling N. E., Mechanical Behaviour of Materials: Engineering Methods for Deformation, Fracture and Fatigue, 3rd edition, Pearsons Prentice Hall, 2007.
204. Cabrera J. M., Omar A., Jonas J. J., Prado J. M., Modeling the flow behavior of a medium carbon microalloyed steel under hot working conditions, Metall. Trans. A, 28, 2233-2244, 1997.
205. James D. W., Leak G. M., Grain boundary diffusion of iron, cobalt and nickel in alpha-iron and of iron in gamma-iron, Philosophical Magazine, 12, 491-503, 1965.
206. Bai D. Q., Yue Y., Maccagno T. M., Jonas J. J., Continuous cooling transformation temperatures determined by compression tests in low carbon bainitic grades, Metall. Trans. A, 29, 989-1001, 1998.
207. Narayana Murty S. V. S., Rao B. N., Kashyap B. P., Instability criteria for hot deformation of materials, Int. Mater. Rev., 45(1), 15-26, 2000.
208. Liu J., Chang H., Wu R., Hsu T. Y., Ruan X., Investigation on hot deformation behavior of AISI T1 high-speed steel, Mater. Charact., 45, 175-186, 2000.
209. Smolej A., Skaza B., Fazarinc M., Determination of the strain-rate sensitivity and the activation energy of deformation in the superplastic aluminium alloy Al-Mg-Mn-Sc, Mater. Geoenv., 56(4), 389-399, 2009.
210. Mitchell T. E., Hirth J. P., Misra A., Apparent activation energy and stress exponent in materials with a high Peierls stress, Acta Mater., 50, 1087-1093, 2002.
211. Honeycombe R. W. K., Steels microstructure and properties, Ed. Arnold, London, 1981.
212. Collinson D. C., Hodgson P. D. , Davies C. H. J., The effect of carbon on the hot deformation and recrystallization of austenite, Proc. of Inter. Conf. on Thermomechanical Process. of Steels, and other Materials, Wollongong, 7-11 July 1997.
213. Jaipal J., Davis C. H. J., Wynne B. P., Collinson D. C., Brownrig A., Hodgson P. D., Effect of carbon content on the hot flow stress and dynamic recrystallization behaviour of plain carbon steels, Proc. of Inter. Conf. on Thermomechanical processing of Steels, and other Materials, Wollongong, 539-545, 7-11 July 1997.

214. Serajzadeh S., Taheri A. K., An investigation on the effect of carbon and silicon on flow behavior of steel, Mater. Design, 23, 271-276, 2002.
215. Laasaoui A., Jonas J.J., Prediction of steel flow stress at high temperatures and strain rates, Met Trans A, 22, 1545-1558, 1991.
216. Misra R. D. K., Weatherly G. C., Hartmann J. E., Boucek A. J., Ultrahigh strength hot rolled microalloyed steels: microstructural aspects of development, Mater. Sci. Tech., 17, 1119-1129, 2001.
217. Ghosh A., Das S., Chatterjee S., Mishra B., Rao P. R., Influence of thermo-mechanical processing and different post-cooling techniques on structure and properties of an ultra low carbon Cu bearing HSLA forging, Mater. Sci. Eng. A, 348, 299-308, 2003.
218. Dynamic Systems Inc. Elimination of load cell ringing during high speed deformation by mathematical treatment, (Application note, New York), 2001.
219. Sakai T., Dynamic recrystallization microstructures under hot working conditions, J. Mater. Process. Technol., 53, 349-361, 1995.
220. Qiao G., Xiao F., Zhang X., Cao Y., Liao B., Effects of contents of Nb and C on hot deformation behaviors of high Nb X80 pipeline steels, Trans. Nonferrous Met. Soc. China, 19, 1395-1399, 2009.
221. Rajput S. K., Dikovits M., Chaudhari G.P., Poletti C., Warchomicka F., Pancholi V., Nath S. K., Physical simulation of hot deformation and microstructural evolution of AISI 1016 steel using processing maps, Mater. Sci. Eng. A, 587, 291-300, 2013.
222. Gourgues A. F., Flower H. M., Lindley T. C., Electron backscattering diffraction study of acicular ferrite, bainite, and martensite steel microstructures, Mater. Sci. Tech., 16, 26-40, 2000.
223. Cho S. H., Kang K. B., Jonas J. J., Mathematical Modeling of the Recrystallization Kinetics of Nb Microalloyed Steels, ISIJ International, 41(7), 766-773, 2001,.
224. ASTM E384-99 Standard Test Method for Microindentation Hardness of Materials, Annual Book of ASTM Standards, ASTM, West Conshohocken, PA, vol. 3.01, 437-460, 2000.
225. Huang Y.D., Yang W.Y., Sun Z.Q., Formation of ultrafine grained ferrite in low carbon steel by heavy deformation in ferrite or dual phase region, J. Mater. Process. Technol., 134, 19-25, 2003.

226. Valiev R. Z., Krasiinikov N. A., Tsenev N. K., Plastic deformation of alloys with submicron-grained structure, Mater. Sci. Eng. A, 137, 35-40, 1991.

227. Mintz B., Lewis J., Jonas J. J., Importance of deformation induced ferrite and factors which control its formation, Mater. Sci. Tech., 13, 379-388, 1997.

LIST OF PUBLICATIONS

International Journals (Refereed)

1. **S.K. Rajput**, M. Dikovits, G.P. Chaudhari, C. Poletti, F. Warchomicka V. Pancholi, S.K. Nath, Physical simulation of hot deformation and microstructural evolution of AISI 1016 steel using processing maps, Materials Science and Engineering A, 587, 291-300, 2013.
2. **S.K. Rajput**, G.P. Chaudhari, S.K. Nath, Physical Simulation of Hot Deformation of Low-Carbon Ti-Nb Microalloyed Steel and Microstructural Studies, Journal of Materials Engineering and Performance, 23(8), 2930-2942, 2014.

Conferences

1. Abhishek Kumar Singh, **S.K. Rajput**, S.K.Nath, M. Bhardwaj, Vivek Pancholi, G. P. Chaudhari, Thermomechanical processing of dual phase steel and its corrosion behavior, GUWI- 2011, September 16-17, 2011, JSW Ltd.,Toranagallu, Karnataka, India.
2. Pallavi Swaroop, **S.K. Rajput**, G.P. Chaudhari, S. K. Nath, Effect of heat treatment on mechanical properties and to study the wear behavior of Dual-Phase steels using Air-Jet Erosion Test, AMEET- 2012, April 7-8, 2012, KNIT, Sultanpur, India.
3. **S.K. Rajput**, G.P. Chaudhari, S.K. Nath, " Characterization of hot deformation behavior of a low carbon steel using processing maps, constitutive equations and Zener-Hollomon parameter" Materials Science & Technology 2014, (MS&T 2014) Conference, October 12-16, 2014, Pittsburgh, USA.